REPORT DOCUMENTATION PAGE

Form Approved
OMB No. 0704-0188

Public reporting burden for this collection of information is estimated to average 1 hour per response, including the time for reviewing instructions, searching existing data sources, gathering and maintaining the data needed, and completing and reviewing the collection of information. Send comments regarding this burden estimate or any other aspect of this collection of information, including suggestions for reducing this burden, to Washington Headquarters Services, Directorate for Information Operations and Reports, 1215 Jefferson Davis Highway, Suite 1204, Arlington, VA 22202-4302, and to the Office of Management and Budget, Paperwork Reduction Project (0704-0188), Washington, DC 20503.

1. AGENCY USE ONLY (Leave blank)	2. REPORT DATE	3. REPORT TYPE AND DATES COVERED
	Aug 96	

4. TITLE AND SUBTITLE
A Unified Design for the Image Processing, Tracking, and Control of a Real-Time Robotic Laser System for Ophthalmic Surgery

5. FUNDING NUMBERS

6. AUTHOR(S)
Cameron Harrold Greene Wright

7. PERFORMING ORGANIZATION NAME(S) AND ADDRESS(ES)
University of Texas at Austin

8. PERFORMING ORGANIZATION REPORT NUMBER
96-030D

9. SPONSORING/MONITORING AGENCY NAME(S) AND ADDRESS(ES)
DEPARTMENT OF THE AIR FORCE
AFIT/CI
2950 P STEET, BLDG 125
WRIGHT-PATTERSON AFB OH 45433-7765

10. SPONSORING/MONITORING AGENCY REPORT NUMBER

11. SUPPLEMENTARY NOTES

12a. DISTRIBUTION/AVAILABILITY STATEMENT
Unlimited

12b. DISTRIBUTION CODE

13. ABSTRACT *(Maximum 200 words)*

19960809 058

14. SUBJECT TERMS

15. NUMBER OF PAGES
273

16. PRICE CODE

17. SECURITY CLASSIFICATION OF REPORT	18. SECURITY CLASSIFICATION OF THIS PAGE	19. SECURITY CLASSIFICATION OF ABSTRACT	20. LIMITATION OF ABSTRACT

DTIC QUALITY INSPECTED 1

GENERAL INSTRUCTIONS FOR COMPLETING SF 298

The Report Documentation Page (RDP) is used in announcing and cataloging reports. It is important that this information be consistent with the rest of the report, particularly the cover and title page. Instructions for filling in each block of the form follow. It is important to *stay within the lines* to meet *optical scanning requirements*.

Block 1. Agency Use Only *(Leave blank)*.

Block 2. Report Date. Full publication date including day, month, and year, if available (e.g. 1 Jan 88). Must cite at least the year.

Block 3. Type of Report and Dates Covered. State whether report is interim, final, etc. If applicable, enter inclusive report dates (e.g. 10 Jun 87 - 30 Jun 88).

Block 4. Title and Subtitle. A title is taken from the part of the report that provides the most meaningful and complete information. When a report is prepared in more than one volume, repeat the primary title, add volume number, and include subtitle for the specific volume. On classified documents enter the title classification in parentheses.

Block 5. Funding Numbers. To include contract and grant numbers; may include program element number(s), project number(s), task number(s), and work unit number(s). Use the following labels:

C	- Contract	PR	- Project
G	- Grant	TA	- Task
PE	- Program Element	WU	- Work Unit Accession No.

Block 6. Author(s). Name(s) of person(s) responsible for writing the report, performing the research, or credited with the content of the report. If editor or compiler, this should follow the name(s).

Block 7. Performing Organization Name(s) and Address(es). Self-explanatory.

Block 8. Performing Organization Report Number. Enter the unique alphanumeric report number(s) assigned by the organization performing the report.

Block 9. Sponsoring/Monitoring Agency Name(s) and Address(es). Self-explanatory.

Block 10. Sponsoring/Monitoring Agency Report Number. *(If known)*

Block 11. Supplementary Notes. Enter information not included elsewhere such as: Prepared in cooperation with...; Trans. of...; To be published in.... When a report is revised, include a statement whether the new report supersedes or supplements the older report.

Block 12a. Distribution/Availability Statement. Denotes public availability or limitations. Cite any availability to the public. Enter additional limitations or special markings in all capitals (e.g. NOFORN, REL, ITAR).

DOD - See DoDD 5230.24, "Distribution Statements on Technical Documents."
DOE - See authorities.
NASA - See Handbook NHB 2200.2.
NTIS - Leave blank.

Block 12b. Distribution Code.

DOD - Leave blank.
DOE - Enter DOE distribution categories from the Standard Distribution for Unclassified Scientific and Technical Reports.
NASA - Leave blank.
NTIS - Leave blank.

Block 13. Abstract. Include a brief *(Maximum 200 words)* factual summary of the most significant information contained in the report.

Block 14. Subject Terms. Keywords or phrases identifying major subjects in the report.

Block 15. Number of Pages. Enter the total number of pages.

Block 16. Price Code. Enter appropriate price code *(NTIS only)*.

Blocks 17. - 19. Security Classifications. Self-explanatory. Enter U.S. Security Classification in accordance with U.S. Security Regulations (i.e., UNCLASSIFIED). If form contains classified information, stamp classification on the top and bottom of the page.

Block 20. Limitation of Abstract. This block must be completed to assign a limitation to the abstract. Enter either UL (unlimited) or SAR (same as report). An entry in this block is necessary if the abstract is to be limited. If blank, the abstract is assumed to be unlimited.

dissertation below this sheet

Copyright © 1996

by

Cameron Harrold Greene Wright

A Unified Design for the Image Processing, Tracking, and Control of a Real-Time Robotic Laser System for Ophthalmic Surgery

by

Cameron Harrold Greene Wright, B.S.E.E., M.S.E.E., P.E.

Dissertation

Presented to the Faculty of the Graduate School of

The University of Texas at Austin

in Partial Fulfillment

of the Requirements

for the Degree of

Doctor of Philosophy

The University of Texas at Austin

August 1996

A Unified Design for the Image Processing, Tracking, and Control of a Real-Time Robotic Laser System for Ophthalmic Surgery

Approved by
Dissertation Committee:

I dedicate this work to the one whose day-to-day patience, support, and understanding allowed me to persevere while retaining my sanity (I think!): to my wife, my love, my Apollonian Princess—*to Robin...*

Acknowledgments

This dissertation is an example of how closely engineering and science are often intertwined. In light of this, I'd like to begin these acknowledgments with a quotation I find apropos to engineering as well as science.

> Science has a simple faith, which transcends utility. Nearly all men of science, all men of learning for that matter, and men of simple ways too, have it in some form and in some degree. It is the faith that it is the privilege of man to learn to understand, and that this is his mission. If we abandon that mission under stress we shall abandon it forever, for stress will not cease. Knowledge for the sake of understanding, not merely to prevail—that is the essence of our being. None can define its limits, or set its ultimate boundaries.
>
> *Vannevar Bush (1890-1974), U.S. electrical engineer, physicist. During World War II, he led the U.S. Office of Scientific Research and Development.*

This quotation, coming from both an engineer and a scientist, captures perfectly[1] the feelings I have regarding the research outlined in this dissertation. Despite many times of "stress" during the last three years, it has always been my "privilege" to "learn to understand" about many things, with the untiring help and encouragement from both faculty and fellow students.

[1]Perfectly, that is, except I would have chosen a more gender-neutral way to say it ...

The success of this research would not have been possible without the contributions and cooperation of many people. At the risk of inadvertently omitting someone, I'd like to express my appreciation in particular to the following individuals. To begin, I can never thank my wife Robin enough for her patience and support during this endeavor, which is why this dissertation is dedicated to her.

I am grateful in a multitude of ways to my committee members: Dr. A. J. Welch, for his patience, wisdom, and many helpful suggestions in all aspects of this research; Dr. H. Grady Rylander III, for his invaluable insights as both a practicing ophthalmologist and electrical engineer; Dr. John A. Pearce, for his real-world understanding of image processing; Dr. Rebecca Richards-Kortum, for her expertise in optics and spectroscopy; Dr. Wilson S. Geisler, for his intimate understanding of the entire vision system; and to Dr. Steven F. Barrett (LtCol, USAF), for the excellent foundation of his prior research and his priceless help on moving forward with CALOSOS. Other particularly helpful people at UT whom I'd like to thank are: Chris Humphrey, Joni Burks, and Melanie Gulick, for keeping me straight on a plethora of administrative matters; Arthur Birdwell and Paul Landers, electronics technicians extraordinaire, for their ever-ready help with circuit parts and construction; and Dr. Jerry Fineg and the staff at the UT Animal Resource Center, for their support with the *in vivo* experiments.

I'm also indebted to people who helped me at the U.S. Air Force Academy before I came to UT: Dr. Alan R. Klayton (Col, USAF), head of the Electrical Engineering Department, who nominated me for the Academy-sponsored Ph.D. program; Dr. Randy L. Haupt (LtCol, USAF), my immediate supervisor and a truly inspiring research mentor; and Dr. Michael S. Markow (LtCol, USAF), who started the original project that a decade later would become CALOSOS, and who encouraged me to pursue that goal.

My appreciation is also extended to those at other organizations: Drs. Clarence Cain, Pat Roach, and Ben Rockwell, all of the Brooks AFB laser/optics laboratory,

who made available to me facilities for many critical experiments; Dr. Maya Jerath of Dartmouth University, whose knowledge of retinal lesion reflectance proved invaluable; Dan Ferguson of Physical Sciences Inc., who first came up with the analog dither tracking method; Kendall Bennett of SciTech Software, who showed me how to program ultrafast graphics routines in 32-bit protected mode; John Morrissey, Charles Wang, and Mike Paravasthu of MuTech Corporation, who helped me make the best use of their excellent frame grabber; and Dan Tevan, software consultant and former chief programmer at Rational Systems, whose knowledge of the DOS4G/W 32-bit protected-mode extender proved to be invaluable.

I'd also like to express my thanks to many friends and co-workers here at UT. While I certainly can't name them all, thanks especially go to my office-mates Colin Smithpeter, Wei-Chiang Lin, and Andy Dunn, for the moral support, stimulating conversations, deviant jokes, and shared appreciation for a good cup of coffee.

Finally, thanks go to my parents, who raised me in an intellectually stimulating environment and gave me the tools to reach my potential.

This work was funded in part by NIH grant 1R41EY10777, the Albert and Clemmie Caster Foundation, and the U.S. Air Force Academy.

CAMERON HARROLD GREENE WRIGHT
MAJOR, USAF

The University of Texas at Austin
August 1996

A Unified Design for the Image Processing, Tracking, and Control of a Real-Time Robotic Laser System for Ophthalmic Surgery

Publication No. _____

Cameron Harrold Greene Wright, Ph.D.
The University of Texas at Austin, 1996

Supervisor: Ashley J. Welch

The need has existed for many years to automate the therapeutic process of placing laser-induced lesions on a patient's retina at specific locations while protecting the critical vision anatomy. Furthermore, it is desirable for the lesions to be of consistent and controllable size (diameter and/or depth). Partial solutions have been designed with varying degrees of success, but no system has yet been developed which can both track the moving eye at clinically acceptable speeds and control the lesion formation in real time.

This dissertation describes research toward the development of a Computer Aided Laser Optics System for Ophthalmic Surgery (CALOSOS): a reliable, safe, cost-effective system which can control laser photocoagulators of the type found in an ophthalmologist's office. The system will safely create therapeutic retinal lesions of a specified number and location in minimal time with little or no human intervention.

The state of the system development described herein includes several capabili-

ties not previously available: track and compensate for eye movements at clinically acceptable speeds, automatically create user specified lesion patterns on the retina with optimized laser pointing movements, and obtain a real-time lesion reflectance signal during typical clinical coagulations.

Implementation details regarding the design and integration of the various functions for image processing, tracking, and control (both analog and digital) necessary for CALOSOS are given, as are quantifiable capabilities such as maximum tracking speed, position resolution, safety response time, and lesion placement accuracy. Operational validation of the system is documented from both *in vitro* tests using eye phantoms and *in vivo* tests using laboratory animals. Recommendations for commercialization and further research are included.

Contents

Acknowledgments v

Abstract viii

List of Tables xvi

List of Figures xvii

Chapter 1 Introduction 1
- 1.1 The Need for Automation . . . 1
- 1.2 CALOSOS Defined . . . 2
- 1.3 Previous Research . . . 2
- 1.4 Dissertation Overview . . . 3
- 1.5 Executive Summary . . . 4

Chapter 2 The Human Eye and Laser Surgery 5
- 2.1 Eye Anatomy . . . 5
  - 2.1.1 Internal Structure . . . 5
  - 2.1.2 The Retina . . . 7
- 2.2 Movement of a Fixated Eye . . . 11
- 2.3 Optical Properties of the Retina . . . 12
- 2.4 Photocoagulation of the Retina . . . 13
- 2.5 Retinal Pathology and Treatment . . . 15
  - 2.5.1 Diabetic Retinopathy . . . 15
  - 2.5.2 Macular Degeneration . . . 16
  - 2.5.3 Retinal Tears . . . 17
  - 2.5.4 Other Conditions . . . 17
- 2.6 Retinal Disorders Suitable for Robotic Surgery . . . 17

Chapter 3 CALOSOS System Design 19
3.1 Introduction . . . 19
3.2 Requirements Specifications . . . 19
3.3 Limitations of Previous Designs . . . 21
3.3.1 Barrett's Retinal Tracker and Lesion Placement System . . . 21
3.3.2 Jerath's Lesion Control System . . . 23
3.3.3 Incompatibilities Between Barrett's and Jerath's Systems . . . 24
3.3.4 Inderfurth's Lesion Control System . . . 25
3.3.5 Lessons Learned . . . 26
3.4 Improved Hardware Design for CALOSOS . . . 27
3.4.1 Alleviating the Video I/O Bottleneck . . . 27
3.4.2 Improving Control Signal I/O . . . 30
3.5 Improved Software Design for CALOSOS . . . 31
3.5.1 Determining the Optimal Software Environment . . . 31
3.5.2 Creating a High-Speed Graphical User Interface . . . 34
3.5.3 Creating a Customized 32-bit Data Acquisition Library . . . 38
3.5.4 Other Software Improvements . . . 38
3.6 Improved Optics Design for CALOSOS . . . 38
3.7 CALOSOS System Overview . . . 40
3.7.1 Digital Tracking Implementation of CALOSOS . . . 40
3.7.2 Hybrid Tracking Implementation of CALOSOS . . . 49
3.8 Ramifications of Improved Design . . . 49

Chapter 4 Retinal Image Formation and Image Processing 53
4.1 Estimating Retinal Distances . . . 53
4.2 Analyzing Retinal Image Formation . . . 55
4.3 Optical Resolution of Retinal Images . . . 56
4.3.1 Image Evaluation . . . 57
4.3.2 The Eye . . . 58
4.3.3 The Fundus Camera Optics . . . 59
4.3.4 The Eye and Fundus Camera Combination . . . 60
4.4 Retinal Image Pixelation . . . 62
4.4.1 The CCD Camera . . . 62
4.4.2 The Frame Grabber . . . 69
4.5 Effective Spatial Resolution of the Retinal Image . . . 71
4.6 Retinal Image Quantization . . . 73
4.6.1 Intensity Partitioning . . . 74
4.6.2 Gray Levels . . . 74
4.6.3 Quantization SNR . . . 74

4.7 Retinal Image Enhancement 75
4.7.1 Signal-to-Noise Ratio 75
4.7.2 Tracking SNR 77
4.7.3 Methods to Improve the Tracking SNR 78
4.8 Computer Detection of Critical Vision Anatomy 80
4.8.1 Safety Considerations 80
4.8.2 A New Technique 81

Chapter 5 Tracking the Moving Retina **85**
5.1 The Need to Track the Retina 85
5.2 Search Area Calculations for the Retina 86
5.3 Improvements to Barrett's Retinal Tracking Implementation 88
5.3.1 Overall Improvements 88
5.3.2 Improvements to Template Response Calculations 89
5.3.3 Improvements to Template Response Figure of Merit 89
5.3.4 Improvements to Tracking Relock Technique 90
5.4 System Optimizations for Digital Tracking 93
5.4.1 The Master Mode Dilemma 93
5.4.2 The Image Data Validity Dilemma 94
5.4.3 Digital Tracking Analysis of the New Design 95
5.4.4 Limitations of Digital Tracking 97
5.5 System Integration for Hybrid Tracking 98
5.5.1 Digital and Analog Tracking 99
5.5.2 Aspects of an Ideal Hybrid System 100
5.5.3 Specific Integration Obstacles 101
5.5.4 First Generation Hybrid Operation 104
5.6 Summary of Retinal Tracking 105

Chapter 6 Controlling and Pointing the Laser **106**
6.1 Laser Pointing and Control System Analysis 106
6.1.1 Data Acquisition I/O Card 107
6.1.2 Interface Control Unit 108
6.1.3 Laser Shutter 109
6.1.4 Beam Shaping Optics 110
6.1.5 Scan Coupling Lens and Beam Splitter Combination 110
6.1.6 Galvanometer Driver Modules 111
6.1.7 Galvanometer and Mirror Combination 112
6.1.8 Timing Accuracy 114
6.1.9 Summary of LPCS Analysis 115

6.2 Laser Pointing and Control System Alignment 115
6.3 Automated Generation of Lesion Patterns 116
6.4 Optimizing Galvanometer Movements 117
6.4.1 Optimizing a Uniformly-Spaced Lesion Pattern 117
6.4.2 Randomization of the Lesion Pattern 118
6.4.3 Finding an Optimized Path Through a Random Pattern . . . 119
6.5 Summary of Laser Pointing and Control 122

Chapter 7 Controlling Retinal Lesion Formation 124
7.1 The Need for Feedback Control 124
7.2 Obtaining a Lesion Reflectance Signal 125
7.2.1 Reflectance as an Indicator of Lesion Morphology 125
7.2.2 Lesion Reflectance from a Confocal Reflectometer 126
7.2.3 Lesion Consistency versus Calibrated Lesion Depth 129
7.2.4 Motion-Induced Reflectometer Signal Corruption 130
7.2.5 Lesion Reflectance Acquisition for CALOSOS 131
7.3 Monte Carlo Simulations of Lesion Reflectance 132
7.3.1 Improving the Simulation Fidelity 132
7.3.2 Implementing a Buried Lesion Model 133
7.3.3 Model Results 137
7.4 Lesion Reflectance Anomalies 139
7.4.1 Investigative Methods 139
7.4.2 Results 140
7.4.3 A Possible Explanation 143
7.4.4 Conclusions Regarding Anomalous Lesions 148
7.5 Summary of Reflectance as a Lesion Control Signal 148

Chapter 8 CALOSOS System Operation and Test Results 150
8.1 System Operation 150
8.2 System Test 153
8.2.1 Tests Using a Simulated Retina 153
8.2.2 Tests Using an Eye Phantom 169
8.2.3 Tests Using Animals 182
8.3 Observations 198

Chapter 9 Summary and Conclusions 200
9.1 Major Accomplishments 200
9.1.1 CALOSOS System Design 200
9.1.2 Publications and Presentations 201

9.2 Recommendations and Future Research 201
9.3 Conclusion 202

Appendix A Supporting Topics **203**
A.1 Determining Optical Resolution 203
A.1.1 Definitions and Assumptions 203
A.1.2 Diffraction-Limited Optics 204
A.1.3 Aberration Effects 209
A.2 Just Detectable Difference for Photodetectors 210
A.3 Chromatic Characteristics of Retinal Images 211
A.4 Barrett's Methods of Image Enhancement 212
A.4.1 Using Optics to Improve the Tracking SNR 212
A.4.2 Using LUTs to Improve the Tracking SNR 214
A.5 Overview of Digital Tracking 216
A.5.1 Image Transformations 217
A.5.2 Correlation-Based and Sequential Registration Methods . . . 218
A.6 Barrett's Digital Retinal Tracking Technique 222
A.6.1 Blood Vessel Templates 222
A.6.2 The Two Dimensional Tracking Template 224
A.7 Ferguson's Analog Retinal Tracking Technique 226
A.7.1 Generating Analog Tracking Signals 226
A.7.2 Analog Tracking Performance Metrics 228
A.7.3 Analog Tracking Implementation 231
A.8 Galvanometer Beam Steering Analysis 233
A.8.1 Sources of Error 233
A.8.2 Design Implications of Resonant Frequency 233
A.8.3 Other Performance Factors 240
A.9 Eye Phantoms 242
A.10 The Monte Carlo Method 243

Appendix B CALOSOS Equipment and Setup **247**
B.1 Computer and Electronics Hardware 247
B.2 Optics 249

Appendix C CALOSOS Software Organization **251**
C.1 Compiler 251
C.2 Support Libraries 251
C.3 Include Files 252
C.4 Source Code Files 252

References 257

Vita 272

List of Tables

3.1 Summary of primary CALOSOS design specifications, suitable for treatment of diabetic retinopathy and retinal tears. 20
3.2 Signals to/from the interface control unit. 42

7.1 Optical properties of an eye phantom when using an argon laser. Units for absorption and scattering coefficients are mm^{-1}. 135

8.1 Maximum overshoot of galvanometer steered laser beam, measured in mm at a target distance of 1 m, versus a given software delay inserted before opening the shutter. All measurements ± 0.5 mm. Distances of less than 1 mm were not measured. 168
8.2 Results of the hybrid tracking subsystem with an eye phantom located on an XY plotter at the conjugate retinal plane. Note: 9 Hz was the maximum XY plotter response. Retinal demagnification of 3:1 assumed. 172

A.1 Dimensions of mirrors used on G124 galvanometers. 234
A.2 Design factors determining galvanometer scanning performance. . . 237
A.3 Calculated maximum pointing error on the retina due to the galvanometers. Values have been rounded for clarity. 241

B.1 Interface Control Unit (ICU) pin assignments for connector and adapter. Pins marked with a * were separately wired. 248
B.2 Optical elements for digital tracking version. 250
B.3 Optical distances for digital tracking version. 250
B.4 Optical elements for hybrid tracking version. 250
B.5 Optical distances for hybrid tracking version. 250

List of Figures

2.1 Internal structures of the human eye. 6
2.2 Diagram and corresponding photo of a normal human retina. 8
2.3 A cross section of the human retina. 9
2.4 Safe exposure limits for staring into a collimated light beam in the visible and near infrared wavelengths. 10
2.5 Cross section of the human retina in the region of the fovea. 11
2.6 Basic laser-tissue interactions. 13
2.7 A laser-induced lesion forming in the human retina. 14

3.1 A comparison of camera FOVs used by Jerath and Barrett. 25
3.2 Opening screen of the graphical user interface for CALOSOS. 37
3.3 Computer and electronics hardware for the digital tracking version of CALOSOS. 41
3.4 Optics design for the digital tracking version of CALOSOS. 44
3.5 A comparison of laser beam shaping for use with CALOSOS. 45
3.6 An example of confocal light detection. 46
3.7 An example of laser beam coupling into the eye at two different steering angles. 47
3.8 Computer and electronics hardware for the hybrid tracking version of CALOSOS. 50
3.9 Optics design for the hybrid tracking version of CALOSOS. 51

4.1 The reduced eye model for simplified calculations of human retinal distances. 54
4.2 Convolution to obtain the combined PSF of the eye and fundus camera. 61
4.3 A rhesus monkey fundus image from CALOSOS. 65
4.4 A 2-D Fourier transform of Figure 4.3 with the DC component eliminated for enhanced detail. 66

4.5 Representation of a circular image on a 4:3 rectangular video frame buffer. 71
4.6 Tracking signal-to-noise ratio SNR_T versus blood vessel contrast. . . 78
4.7 A simulated retinal image with a 10×10 lesion pattern and no blood vessel masking. 83
4.8 The same image as Figure 4.7 , with automated detection of blood vessels. 84

5.1 Maximum retinal tracking capability for a given image search distance. 87
5.2 Flowchart of improved digital tracking with the "zoom-out, zoom-in" relock technique. 92
5.3 CALOSOS effective frame rate for a given search window size. . . . 96

6.1 Laser beam steering via two orthogonal galvanometers and mirrors. . 113
6.2 Comparison of paths through a uniformly-spaced lesion pattern: nonoptimized (a), and optimized (b). 118
6.3 Comparison of paths through a "randomized" lesion pattern: nonoptimized (a), and optimized (b). 122

7.1 The higher scattering coefficient of a retinal lesion increases its reflectance. 126
7.2 Reflectance profile of an albumen eye phantom, obtained with a CCD camera, showing the formation of a laser-induced lesion at several instants during irradiation. 127
7.3 Correlation of reflectance to diameter and depth of normal argon laser-induced lesions [1]. Reflectance diameter calculated from above-threshold pixel dimensions. 128
7.4 Typical signals obtained from a confocal reflectometer during photocoagulation of a rabbit retina. 129
7.5 The three layer model of an eye phantom with a buried lesion. . . . 134
7.6 A few possible photon paths in the eye phantom (top view). The dashed line indicates where the photon would pass through the buried lesion. 136
7.7 Monte Carlo simulation of buried cylindrical lesion in an albumen eye phantom. Gaussian laser beam (power is normalized) having a diameter of 750 μm and λ = 488 nm and 514 nm; 5000 photons simulated. 138

7.8 Monte Carlo simulation of buried hemispherical lesion in an albumen eye phantom. Gaussian laser beam (power is normalized) having a diameter of 750 μm and λ = 488 nm and 514 nm; 5000 photons simulated. 138
7.9 Anomalous lesion (900 μm diameter) formed in an albumen eye phantom. Bubbles at the center of the lesion result in a lower reflectance and hence an overall annular reflectance pattern. Gaussian beam profile, λ = 488 and 514 nm, 750 μm spot, irradiation time of 0.5 s at 195 mW. 141
7.10 Reflectance vs. depth of normal and anomalous lesions. Anomalous lesions were those exhibiting an annular reflectance pattern. Central reflectance was determined as the average of the central 300 μm of each lesion. Total size of each lesion ranged from 400–1500 μm in diameter. 142
7.11 A fundus camera 20° FOV showing anomalous lesions (having an annular reflectance pattern) in a rhesus monkey retina following argon laser photocoagulation. Gaussian beam profile, λ = 514 nm, 500 μm spot, irradiation time of 7 ms at 287 mW/cm^2. Used with permission from Walter Reed Army Institute of Research, U.S. Army Medical Research Department, Brooks AFB, TX. 143
7.12 Schematic for thermal model of an infinite composite solid. 145
7.13 Theoretical tissue temperature using the simplified thermal model of an infinite composite solid, consisting of tissue and glass. Note that the phase change of water and the pressure-dependent heat of vaporization is not reflected in this graph. 147

8.1 Flowchart of CALOSOS software during photocoagulation. 152
8.2 A simulated retina used for testing CALOSOS. Blood vessels were simulated using a fractal algorithm to enhance realism. 154
8.3 Results of the digital tracking tests for CALOSOS. Note: typical *in vivo* SNR_T seldom exceeds 20 dB. 158
8.4 Example of random movement for the digital tracking test. 159
8.5 Normalized target displacements (solid line) and tracking updates (dashed line) for a 1 Hz, 3 Hz, and 6 Hz sinusoid. Displacement amplitude was held constant. Only the x axis signal is shown. 160
8.6 Heat sensitive paper target irradiated at λ = 488 nm and 514 nm, 1.25 W, 400 ms at each location. The motion was 10 mm p-p at 5 Hz. 164

8.7 Response of the coagulating beam confocal reflectometer when small white dots on a black background target were passed slowly through the beam. The target was at the intended retinal plane. 166
8.8 Response of the coagulating beam confocal reflectometer when small white dots on a black background target were passed slowly through the beam. The target was 10 mm further away than the intended retinal plane. 167
8.9 Lesions created in an eye phantom during motion. 173
8.10 Closer view of lesions created in an eye phantom during motion. . . 174
8.11 Dynamic confocal reflectometer signals of the coagulating beam. . . 176
8.12 Comaprison of coagulating and tracking beam reflectometers. 177
8.13 Coagulating beam reflectometer signals when target is stationary, moving and locked, unlocked, and relocked. 178
8.14 Comparision of confocal reflectometer signals with analog tracking and digital tracking. Motion of target was 2 mm p-p, 6 Hz, for an equivalent retinal velocity of 40 deg/sec. 181
8.15 Fundus image of photocoagulation on rabbit fundus. Argon laser ($\lambda =$ 488 nm, 514 nm), 100 mW at the cornea, 291 ms average irradiation time. 183
8.16 Fundus image of lesions on the retina of a rhesus monkey due to a CW argon laser and an ultrashort pulsed laser. 186
8.17 Annotated fundus image of rhesus monkey following photocoagulation. 187
8.18 Photocoagulation on a rabbit fundus using hybrid operation. Argon laser ($\lambda = 488$ nm, 514 nm), 175 mW at the cornea, approximately 275 μm diameter spot on the retina. 191
8.19 Annotated version of Figure 8.18. 192
8.20 Unlocked and locked photocoagulation on a rabbit fundus using hybrid operation. Eye motion was up to 32 deg/sec. Argon laser ($\lambda = 488$ nm, 514 nm), 175 mW at the cornea, approximately 275 μm diameter spot on the retina. 193
8.21 Annotated version of Figure 8.20. 194
8.22 Confocal reflectometer signal for a 100 ms irradiation on a rabbit fundus during tracked motion of up to 14 deg/sec. 196

A.1 The point spread function (PSF) of an ideal circular lens. 204
A.2 The optical transfer function (OTF) of an ideal circular lens. 207
A.3 A comparison of the MTF (solid line) and CTF (dashed line) of an ideal circular lens. 208

A.4 Spectral ranges of optimal visibility for various structures in the human retina. 212
A.5 A comparison of illumination lamp filters for fundus camera imaging. 213
A.6 An arbitrary remapping of the frame grabber look up table (LUT) to modify the image. 215
A.7 A generic image shown with examples of rigid transformations. . . . 217
A.8 Schematic flow chart of Cideciyan's technique for image registration. 220
A.9 Template response in the vicinity of a retinal blood vessel. 223
A.10 A conceptualized view of templates on the fundus image. 225
A.11 Analog method of obtaining Δx and Δy tracking signals from a confocal reflectometer. 227
A.12 Resonant frequency derating curve. 234
A.13 Moment of inertia calculations for some basic shapes. 235
A.14 Mechanical drawing for mirror holders used on G124 galvanometers. 236
A.15 Transient response of an underdamped galvanometer and mirror combination to a step change in the position signal. 238
A.16 An eye phantom using a petri dish filled with egg white. The bottom of the petri dish has been painted black to simulate the RPE. 243
A.17 A photon encountering a scattering event. 244
A.18 Monte Carlo method of mapping probability distributions for simulation. 245
A.19 Flow chart of computer-based decisions for a Monte Carlo simulation of light-tissue interaction. 246

Chapter 1

Introduction

1.1 The Need for Automation

Retinal photocoagulation is the most widely used medical laser procedure employed today [2]. It is used to treat thousands of patients each year and is the recommended procedure for conditions such as diabetic retinopathy (requiring up to 3000 therapeutic lesions in each eye), retinal tears, and macular degeneration. Today, however, the procedure is performed manually and suffers from several drawbacks [3], including:

- It often requires many clinical visits.
- It is very tedious for both patient and ophthalmologist.
- The laser pointing accuracy and safety margin are limited by a combination of the ophthalmologist's manual dexterity and the patient's ability to hold their eye still.
- There is a large variability in lesion size even with identical irradiation parameters.

The need has existed for many years to somehow automate the actual process of placing lesions on a patient's retina at specific locations while protecting the critical

vision anatomy [4–6]. However, one of the main obstacles to achieving this task has been the ability to track the retina and compensate for any movement with sufficient speed during photocoagulation. Furthermore, it is desirable for the retinal lesions to have consistent and controllable size (diameter and/or depth). Partial solutions have been designed with varying degrees of success, but no system has yet been developed which can track the moving eye, direct the laser appropriately, and control the lesion formation.

1.2 CALOSOS Defined

This dissertation describes the research and development toward the goal of creating a reliable, safe, cost-effective system which can control a typical laser photocoagulator found in an ophthalmologist's treatment room. It makes use of a normal fundus camera (also found as standard equipment in the treatment room), and will create therapeutic retinal lesions of a specified number, location, and size in minimal time with little or no human intervention. This development system is known as **CALOSOS**, for **C**omputer **A**ided **L**aser **O**ptical **S**ystem for **O**phthalmic **S**urgery.

1.3 Previous Research

Work toward a system like CALOSOS has progressed for many years [7–15]. Markow [8] identified the preliminary requirements and feasibility of automated retinal surgery. Building on the early work of researchers such as Weinberg [16], Birngruber [4], Markow [8], Yang [13], and many others [17–20], Jerath [14] and Inderfurth et al. [21] independently demonstrated possible methods of using reflectance to control retinal lesion formation. Ghaffari [12] investigated the use of optical correlation for tracking the retina, and Barrett [15] demonstrated the feasibility of using digital computer control to track the retina and create a lesion array, although not fast enough for a typical clinical application.

Thus with much of the groundwork accomplished, the design, integration, development, and prototype testing of a real-time system was the objective of this dissertation.

1.4 Dissertation Overview

While many Ph.D. dissertations describe a very narrow subject area, this project is unusually eclectic. It includes aspects of image processing, signal processing, electronic communication systems, information theory, analog and digital control systems, biomedical instrumentation, analog and digital hardware design, software engineering, lasers, optics, thermodynamics, physiology, and ophthalmology. Due to this breadth, the treatment of background material and previous research is brief. The interested reader is directed to the appropriate source documents listed in the extensive References section for further detail. The key to this project is the selective integration of these diverse fields to fulfill the specific requirements of CALOSOS.

The organization of this dissertation is by subject area. Chapter 2 contains a brief review of the physiology and properties of the human eye, and how lasers are used to treat the retina. Chapter 3 discusses overall system design architecture developed for CALOSOS, and lays the foundation for the next four chapters. Chapter 4 focuses on the retinal image formation and image processing required by CALOSOS, whereas Chapter 5 describes how the system tracks the moving eye. Chapter 6 discusses the methods used to direct the laser to the correct spot on the retina, while Chapter 7 is concerned with retinal lesion formation and how to dynamically control the laser-induced retinal lesion. Chapter 8 discusses the experimental results, both *in vitro* and *in vivo*, with quantitative performance figures. Chapter 9 summarizes the project and offers recommendations for future work. The appendices contain extensive additional information that, due to subject or detail, would interrupt the flow of the main document.

1.5 Executive Summary

For those readers who wish to skip the detail of the main text, but for whom the abstract is insufficient, the major accomplishments of this research are listed in Section 9.1.

Chapter 2

The Human Eye and Laser Surgery

The research goal of this dissertation is to develop a biomedical instrument for ophthalmologists which can perform automated laser photocoagulation of the human retina. Therefore, in order to fully appreciate the following chapters, the reader needs a basic knowledge of the human eye. Presented below is a concise treatment of eye anatomy, eye movements, optical properties of the retina, the basics of laser photocoagulation, eye pathology and treatment, and the suitability of applying robotic techniques in some of these treatments.

2.1 Eye Anatomy

2.1.1 Internal Structure

The human eye is a complex sensor that responds to electromagnetic stimuli at wavelengths from approximately 400–700 nm [22]; for obvious reasons this band is called the *visible wavelengths*. The various internal structures that make up the human eye are depicted in Figure 2.1.

Ambient light enters the cornea, passes through the anterior chamber (containing the aqueous humor), through the pupil opening, through the crystalline lens, and then passes through the vitreous humor before striking the retina. The retina is

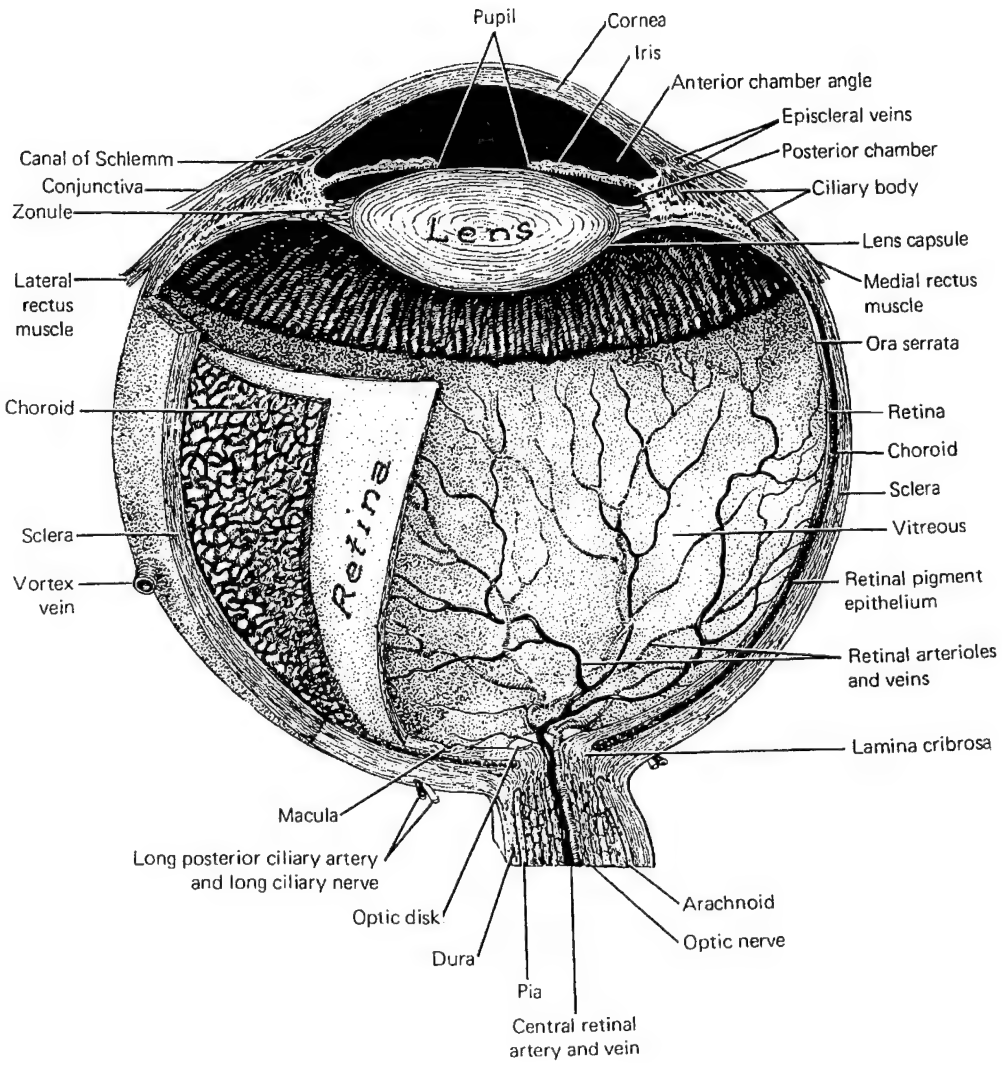

Figure 2.1: Internal structures of the human eye [23].

of primary interest for this discussion. It is a layer of neural tissue that contains, among other things, the actual visual receptors (rods and cones).

2.1.2 The Retina

When viewed through a fundus camera [24], the human retina has some prominent landmarks [25]. See Figure 2.2 for a diagram and corresponding fundus camera photo of a normal human retina. The most prominent of these landmarks is the optic disk, which is a nearly circular region of approximately 1800 μm diameter [26] where blood vessels and the optic nerve pass through to the inner eye (the optic disk is the "blind spot" of the retina). This region appears much lighter than the surrounding tissue at most wavelengths. Temporal to the optic disk (toward the left in Figure 2.2), is a small circular region of approximately 350 μm diameter called the fovea (the capillary-free area of the central retina). This is where our most acute vision takes place: when we look directly at an object we focus its image on our fovea. The area extending roughly 1500 μm radially beyond the boundaries of the fovea (representing an angle of about 5 degrees) is called the macula. The macula is used for vision less acute than the foveal region, but more acute than peripheral vision. Notice also the prominent blood vessels on the retina, to which I shall refer in later chapters. The major blood vessels are typically 150–180 μm wide [27]. This description of landmarks, while cursory, is sufficient to support the discussion in the remainder of this document.

The retina itself is made up of several layers as shown in Figure 2.3. As depicted, the incoming light would strike the top of the figure and pass downward. The retina is nearly transparent to visible light [28], so the light energy passes through these inner layers with very little attenuation, activates the visual receptors, and finally encounters the *retinal pigment epithelium* (RPE). The inner layers of the retina (those shown above the RPE in Figure 2.3) are sometimes grouped together and called the *neural retina*; this region is on average 150 μm thick [29]. The RPE is a

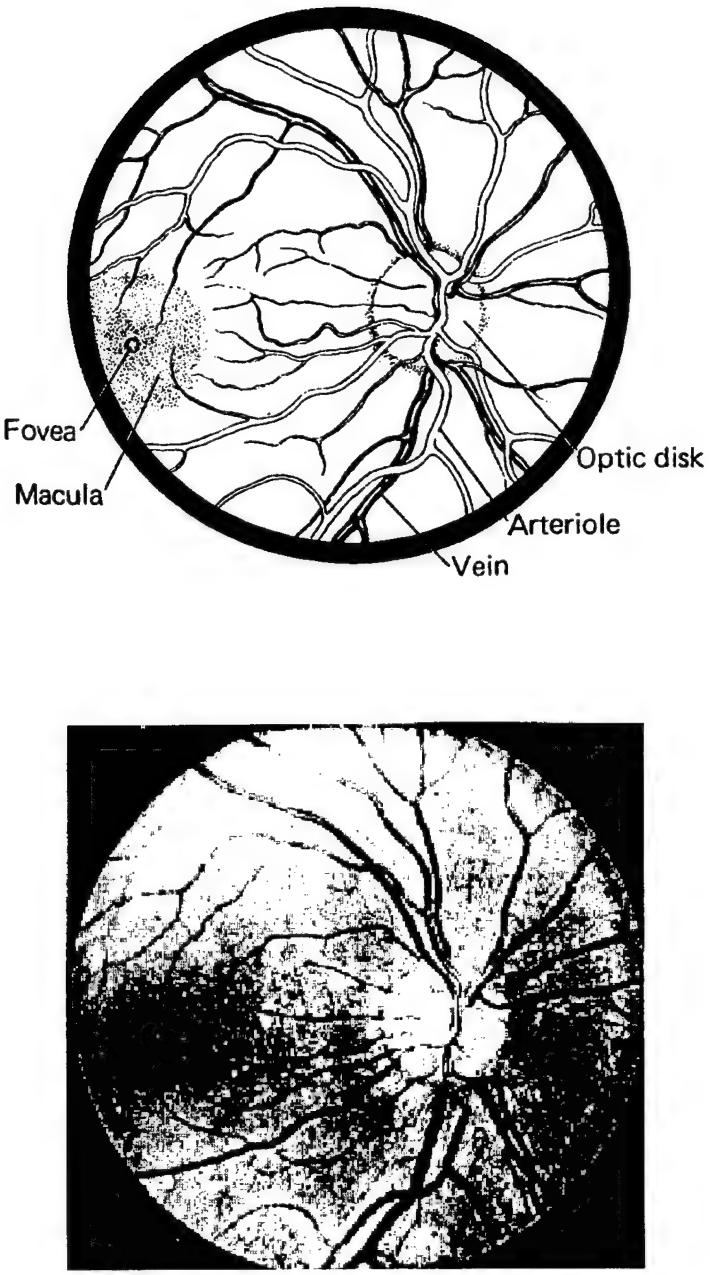

Figure 2.2: Diagram and corresponding photo of a normal human retina (right eye) at a 30° FOV [23].

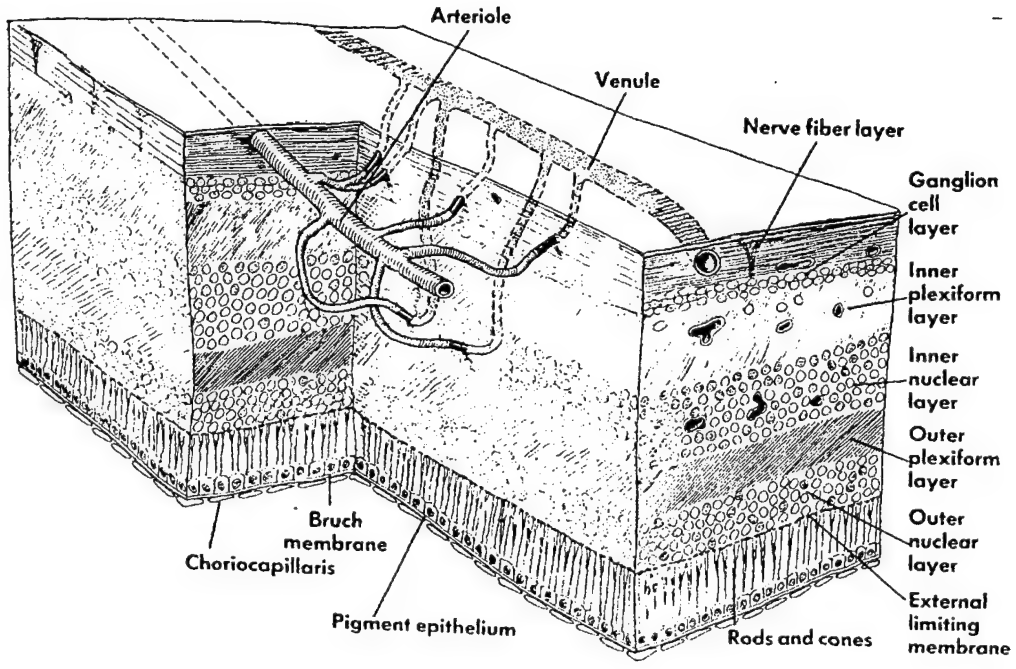

Figure 2.3: A cross section of the human retina [27].

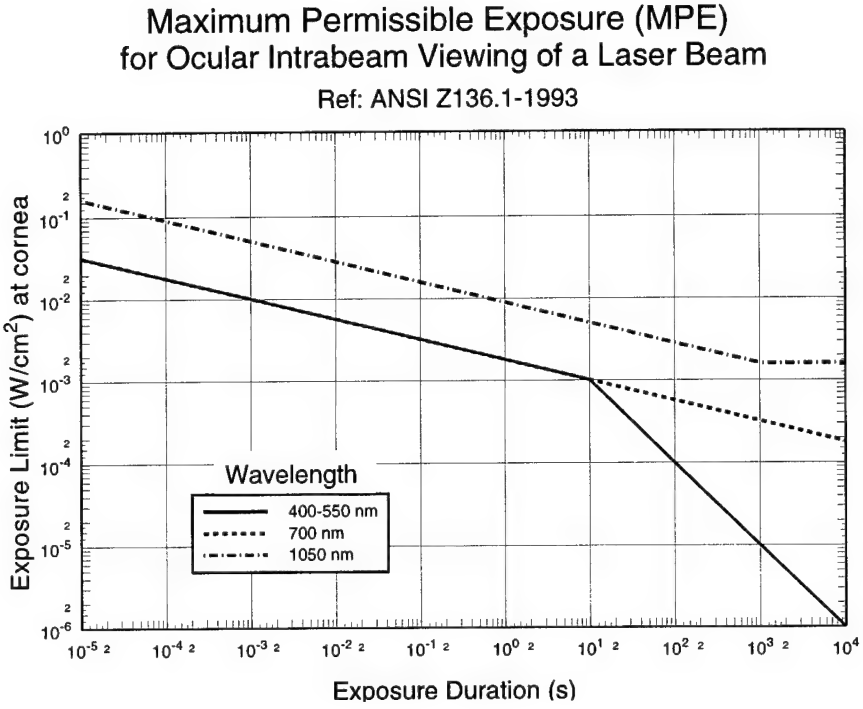

Figure 2.4: Safe exposure limits for staring into a collimated light beam in the visible and near infrared wavelengths.

highly absorbing layer roughly 12–15 μm thick [29]. If it weren't for the RPE, light would tend to scatter back toward the inner eye, greatly reducing our ability to see clearly. Beyond the RPE is Bruch's membrane and the highly vascular choroid.

The retina can be damaged by exposure to light beyond certain a intensity; the safe limit [30] is both time and wavelength dependent (see Figure 2.4). For therapeutic reasons, the retina is sometimes intentionally damaged by laser light; this procedure is called *retinal photocoagulation*, and is discussed in greater detail below.

Note that there are many objects (blood vessels, ganglions, etc.) that lie between the incoming light and the visual receptors. We don't "see" these objects for three reasons. First, the retina is at its thinnest directly over the fovea where critical vision

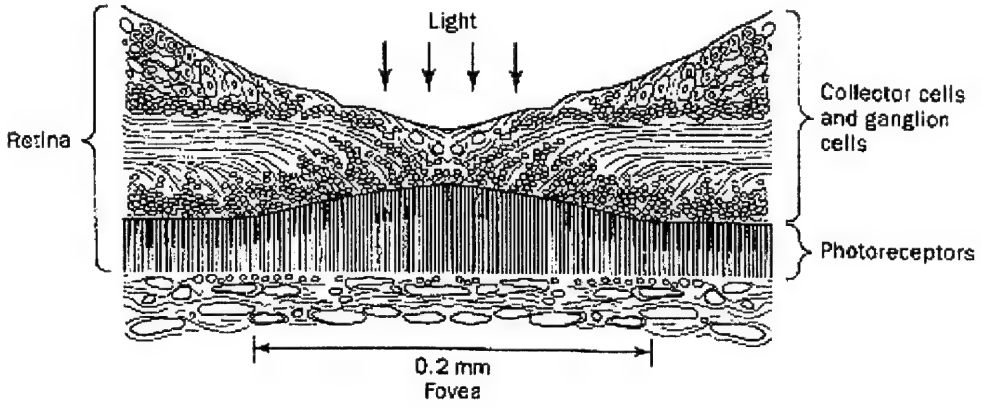

Figure 2.5: Cross section of the human retina in the region of the fovea [31].

takes place, as shown in Figure 2.5. Second, the blood vessel density is almost zero in the immediate region of the fovea. Third, and most important to this discussion, is the fact that the human visual system tends to eliminate any image or object which is stationary on the retina [31,32]. Since these objects within the retina itself are always stationary with respect to the retina, we don't see them. Objects in the outside world are visible because our eyes are *always* moving.

2.2 Movement of a Fixated Eye

Even when we are looking at a motionless object and might believe our eyes to be perfectly still (called "fixated"), there are tiny motions that occur continuously [3,9,23,27,31,33–36]:

- Physiologic nystagmus movements of roughly 5–30 seconds of arc[1] that oscillate back and forth at a rate of approximately 50–100 kHz which keep different regions of the fovea stimulated (this avoids image fading from cone saturation).

[1]Note: 30 sec of arc $\simeq$ 2.43 μm on the surface of the retina. For more detail, see Chapter 4.

- Micro-nystagmus movements of up to 1 minute of arc that tend to oscillate slowly back and forth at a rate of about 0.02 Hz; these movements can be considered "noise" from an engineering point of view.

- Micro-saccades of up to 5–10 minutes of arc which occur as often as once per second; as the object of fixation drifts to the boundary of the macula (i.e. due to micro-nystagmus oscillation), these movements will shift it back to the fovea.

Obviously a retinal laser surgery system must compensate for an eye that is always moving, a topic which will be discussed in later chapters. There are several other categories of eye movement, both voluntary and involuntary. For the purposes of this discussion, it is sufficient to summarize that a human eye can move up to 800 degrees per second when trying to acquire a moving object, and up to 50 degrees per second when following an object moving steadily at that speed.

2.3 Optical Properties of the Retina

Laser-tissue interactions follow the well-known rules of optics. When laser light strikes tissue it can be reflected, transmitted, absorbed, scattered, internally reflected, or some combination thereof [37–40]. This is shown graphically in Figure 2.6.

There are many factors that determine how light will behave in a given type of tissue [41, 42]. Some of the more important parameters, collectively called the optical properties, are functions of wavelength, so two lasers of different wavelengths may behave quite differently in the same tissue. The optical properties are: index of refraction n, coefficient of absorption μ_a, coefficient of scattering μ_s, and the anisotropy factor g. The last parameter, the anisotropy factor, characterizes the angular distribution of scattering (most tissue has been found to be highly forward scattering, so g would be close to 1). These parameters show up in most litera-

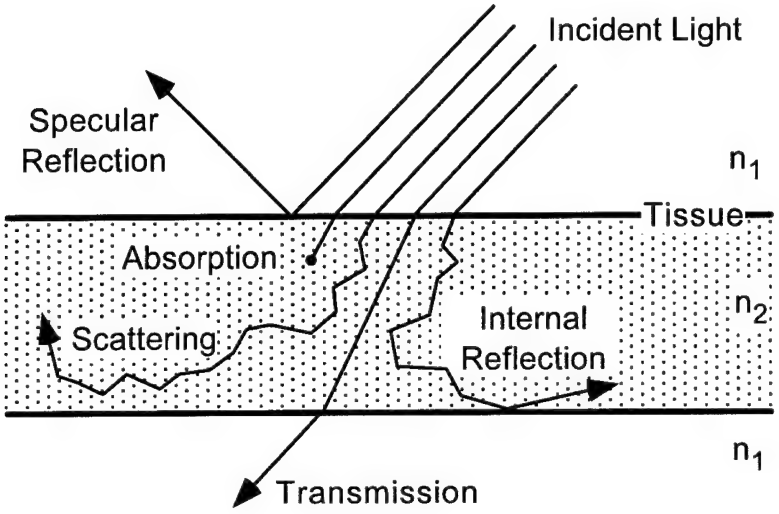

Figure 2.6: Basic laser-tissue interactions.

ture regarding propagation of electromagnetic fields in a scattering medium [41–43]. Other parameters, such as the total attenuation coefficient, the effective attenuation coefficient, and albedo can all be derived from the basic four optical properties.

For a typical photocoagulation wavelength of roughly 500 nm, the entire retina of a human has an n of approximately 1.4. The neural retina at this wavelength has a μ_a that is very low, while both the μ_s and g are essentially zero, making these layers nearly transparent. The pigment epithelium, on the other hand, is also low in scattering but has a very high μ_a. This situation is used to advantage in photocoagulation of the retina.

2.4 Photocoagulation of the Retina

Since visible wavelengths pass through the eye with little attenuation, laser light in the visible range easily reaches the retina. Typically, the patient's pupils are dilated and an argon laser ($\lambda = 488,\ 514$ nm) is used. As noted above, these wavelengths have been found to have the most desirable penetration depth through the neural

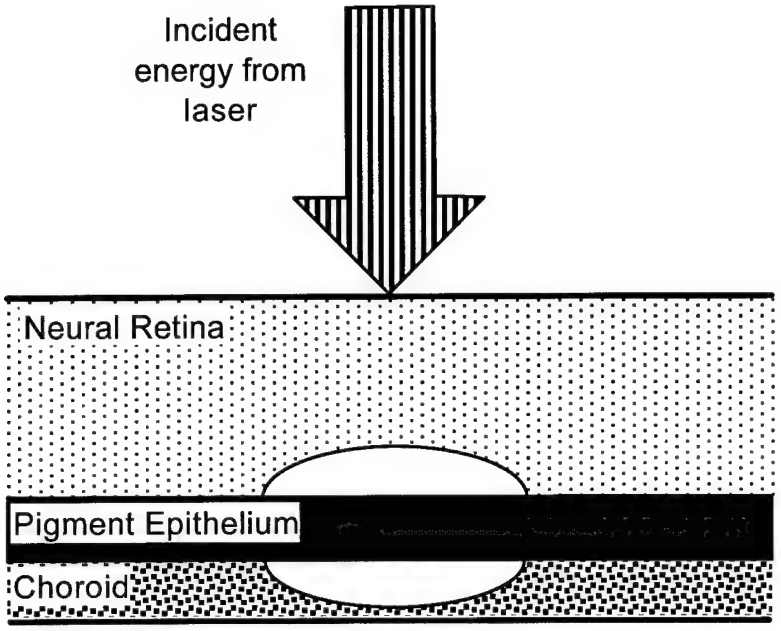

Figure 2.7: Highly conceptual illustration of a laser-induced lesion forming in the human retina.

retina and high absorption in the RPE [3, 23].

The primary mechanism behind laser treatment for retinal disorders is heat generation. That is, when laser light is absorbed by the RPE, the energy is converted to heat. Thus the area of the RPE being irradiated becomes a "hot spot" which transfers heat to the neural retina and to the choroid. The primary therapeutic effect comes from heating the neural retina, although the exact nature of the effect is still being investigated. Most researchers agree that a lesion forms in the neural retina due to denaturation of the tissue. The resulting lesion appears bright in fundus camera images since the denatured tissue has a much higher scattering coefficient compared to the normal tissue, and the incident light is thus backscattered. A conceptual picture of this lesion formation is shown in Figure 2.7.

One significant problem is that μ_a of the RPE is not uniform across the retina.

It has been shown that absorption of laser energy in the RPE typically varies up to 200% across the same eye [44]. This causes the rate of heat deposition to vary widely under identical irradiation parameters, which results in somewhat unpredictable lesion growth and makes consistent lesion formation difficult. If the RPE μ_a is much higher than expected at a particular irradiation site, a much larger and/or deeper lesion than expected will form. Note that if the lesion grows too close to the inner surface of the retina, the nerve fiber layer can be damaged which would adversely affect nonlocal areas of the retina and create arcuate scotoma. Excessive lesion growth can also result in hemorrhage into the vitreous chamber. If the RPE μ_a is much lower than expected at a particular irradiation site, either no lesion or a much smaller and/or shallower lesion than expected will form. The main problem in this case is a lack of therapeutic effect. Other variables can also affect lesion growth, such as opacities in the optical path of the laser. It has been shown that any change in the optical properties or laser parameters greatly influences lesion diameter and/or depth [10].

2.5 Retinal Pathology and Treatment

Photocoagulation is used to treat a variety of ophthalmic disorders. Three of the most common are diabetic retinopathy, macular degeneration, and retinal tears or breaks [3, 23, 27].

2.5.1 Diabetic Retinopathy

One of the leading causes of blindness in the Western hemisphere, diabetic retinopathy is a disease of the retina that progresses through several stages [23]. The *background* (sometimes called the non-inflammatory) stage is characterized by small aneurysms and hyperpermeability of the involved blood vessels accompanied by multiple hemorrhages throughout different levels of the retina. With increasing ischemia the *preproliferative* stage begins, caused by closure of retinal capillaries

surrounding the foveal avascular zone. The most severe ocular complications occur as the disorder progresses to the *proliferative* stage. This is when the increasing ischemia stimulates the formation of fragile, low quality blood vessels (called neovascularization) that leak serum and proteins profusely; these new vessels can grow into the posterior region of the vitreous. Massive vitreous hemorrhage can occur and the posterior vitreous tends to detach from the retina.

The indicated treatment for proliferative diabetic retinopathy is panretinal photocoagulation (PRP), in which thousands of lesions are placed all over the retina except for the macular region. This preserves acute vision but degrades peripheral vision. Given that the alternative is blindness, the trade-off is appropriate. Although the therapeutic mechanism is not precisely understood, PRP is believed to work by reducing the angiogenic stimulus from the ischemic retina [23].

2.5.2 Macular Degeneration

Age-related (also called "senile") macular degeneration is the most common cause of legal blindness in the United States for people over 60 years old [27]. After the age of 65, its prevalence increases greatly; it affects 28% of persons older than 75 years. Because it affects the critical vision area of the retina, macular degeneration can result in severe vision loss. There are two forms: nonexudative ("dry") and exudative ("wet"). Nonexudative macular degeneration has no generally acceptable treatment; supplemental zinc [23] and vitamin E [27] taken orally are recommended, but this form does not usually result in loss of central vision. More serious is the exudative form, where blood or serous fluid from the choroid leaks through defects in Bruch's membrane causing detachment of the RPE, and allowing ingrowth of new blood vessels from the choroid into the subretinal space (forming a neovascular membrane). The natural progression of this subretinal neovascularization is toward irreversible loss of central vision over a variable period of time.

In the absence of neovascularization, no treatment of RPE detachment is of

proved benefit [23]. However, if a subretinal neovascular membrane is present in a well-defined extrafoveal region (≥ 200 μm from the center of the fovea), photocoagulation can be used to ablate the membrane before it has time to reach the fovea. Some acuity is lost, but the fovea is spared. Recurrent neovascularization may occur in 50% of the cases within 2 years. Note that this procedure requires the laser spot to be placed with extreme precision to prevent inadvertent damage to the central fovea.

2.5.3 Retinal Tears

When a patient notices the sudden appearance of many "floaters" in their vision, it is often due to a retinal tear, break, or hole [23]. The most common cause is senile vitreous degeneration, but other causes include diabetic retinopathy and ocular trauma. The tear can cause retinal detachment (eventually leading to blindness), but if detected prior to the accumulation of subretinal fluid it can be sealed off by applying a double ring of laser-induced lesions around it. This creates adhesions of the adjacent attached retina to the pigment epithelium, preventing a buildup of subretinal fluid and the associated retinal detachment.

2.5.4 Other Conditions

Photocoagulation is also used for less frequently occurring conditions such as central retinal vein thrombosis, branch retinal vein thrombosis, certain cases of central serous chorioretinopathy, angioid streaks, occlusion due to central or branch arteries or veins, and certain cases of retinal arterial macroaneurysm [23].

2.6 Retinal Disorders Suitable for Robotic Surgery

Of the many disorders listed above that are treated by photocoagulation, the best candidates for automation are diabetic retinopathy and retinal tears [45]. The moderate precision required and the easily specified lesion patterns make automation of

these tasks both logical and possible with available technology. Furthermore, PRP treatments for diabetic retinopathy appear to have the most to gain from the application of robotics: a reduction of both patient and clinician fatigue, and an increase in the overall safety margin. Combining retinal tracking with computer-controlled lesion patterns would result in a highly useful system.[2] Additional functionality would result from improved control over lesion size and/or depth.

The following chapter outlines the overall design considerations for such a system.

[2]Tracking capabilities developed for this system could also be used for other areas. For example, tracking blood vessels of the conjuntiva could enhance photorefractive keratectomy (PRK) procedures. A non-ophthalmic medical application might be endoscopic laser surgery. Non-medical applications would also exist for this tracking technology.

Chapter 3

CALOSOS System Design

3.1 Introduction

This chapter begins the discussion of the design of CALOSOS. While the next four chapters specifically discuss the major functional elements of the system (image processing, retinal tracking, controlling the laser, and controlling lesion formation), this chapter is more general in nature. It addresses those aspects of the CALOSOS design which span more than one functional area, and lays an appropriate foundation for more detailed discussions in the following chapters.

3.2 Requirements Specifications

One of the first tasks in the engineering design process is to properly define the requirements specifications. For a system as complex as CALOSOS, there are a multitude of requirements which must be met. There are obvious ones, such as the need to track the moving retina, and less obvious ones, such as the need to incorporate an easy-to-use human-computer interface. Each has an associated priority, and each has an impact on the system design. If the anticipated design impact (in terms of cost, complexity, and/or reliability) outweighs the priority (in terms of performance or functionality), then that requirement should be reexamined. Entire

Function	Performance	
Retinal Tracking	$\geq$ 10 deg/sec	5 ms response time
Laser Pointing	100 μm resolution	5 ms response time
Lesion Control	uniform within 5%	5 ms response time

Table 3.1: Summary of primary CALOSOS design specifications, suitable for treatment of diabetic retinopathy and retinal tears.

books have been written on the requirements definition task [46–48], and if done properly the designer has as its output a coherent set of requirements which, when met, will result in a system with the desired capabilities for the desired cost.

Obviously the requirements task can be lengthy, and the specifications for the CALOSOS system are numerous. The requirements were determined through significant background research, discussions with experts in the field,[1] and the principles of sound engineering practice. Since most readers will be more interested in the end result rather than the process of this task, only the primary specifications for CALOSOS—those which have the greatest impact on the system design—are given here. Other specifications and an extended discussion of the requirements can be found in [49] for the interested reader.

The primary specifications cover three main areas: tracking the retina, pointing and controlling the laser, and controlling lesion formation. Recall from Chapter 2 that CALOSOS is being designed as an automated assistant for the photocoagulation treatments of two common disorders: diabetic retinopathy and retinal tears. See Table 3.1, which summarizes in one place the primary specifications for CALOSOS to fulfill this need.

Before ending the disussion of requirements specifications, three facts should be noted. First, the most important specification to meet from a safety standpoint is the response time of 5 ms. If the tracking algorithm loses lock, for example, it's not a serious problem if it can be detected within 5 ms so that the laser can

[1] In particular, ophthalmologists consulted were: Dr. H. G. Rylander, III (UT Austin), Dr. C. A. Toth (Duke University), and Dr. J. Gillis (Chief of Ophthalmology, U.S. Air Force Academy Hospital).

be immediately turned off until tracking lock is reestablished. The response time also has a direct impact on the tracking velocity versus pointing resolution trade-off discussed in Chapter 5. The need for a 5 ms response time is derived from the standard ophthalmological practice of using irradiation times of approximately 100 ms for retinal photocoagulation. A response time of 5 ms therefore allows the system to make adjustments to within 1/20 of a full irradiation, which is an acceptable safety margin according to practicing ophthalmologists.

Second, while the *minimum* tracking capability for a useable system is specified as 10 deg/sec (anything less would lose lock too often for convenient use), it should be emphasized that greater capability is highly desirable. Ophthalmologists typically specify 50 deg/sec as their "wish list" specification.

Third, the overall design philosophy of CALOSOS is "do no harm." That is, the basic advantage of using CALOSOS over manual operation will be to ensure that the patient's critical vision anatomy is not harmed during the photocoagulation procedure. The collateral increases in speed, comfort, and convenience that also will be provided by CALOSOS are secondary (albeit highly welcome) benefits.

3.3 Limitations of Previous Designs

Past attempts to provide some automation for photocoagulation procedures have met with limited success. Three recent approaches are briefly examined: Barrett's retinal tracking and lesion placement system [15,50], Jerath's lesion control system using diffuse white light reflectance feedback [14,51,52], and the Inderfurth et al. approach to lesion control using confocal reflectometry [21].

3.3.1 Barrett's Retinal Tracker and Lesion Placement System

The development system built by Barrett for *in vivo* testing on rabbits was a follow-on to Markow's earlier work [8,53] along similar lines. An argon laser, aimed using two orthogonal steering mirrors, provided the photocoagulation energy. The laser

shutter was under the control of a standard 33 MHz 486 PC, which processed a digitized fundus image provided via an internal ISA bus frame grabber and a standard RS-170 CCD camera attached to a fundus camera. The computer built a reference image template based on retinal blood vessel locations for tracking the retina and establishing a coordinate system for lesion patterns.

Barrett's work represented a significant advance in retinal tracking, laser pointing, and automatic lesion pattern generation. However, available technology limited the system to retinal velocities of less than 2 degrees per second at a 100 μm laser pointing resolution [15]. While the CCD camera could provide 30 frames per second of the fundus image, the system was only able to utilize a maximum of 7 frames per second. This means the system response time could be no better than 1/(7 fps) = 143 ms (plus time for processing overhead). Referring to Table 3.1, this is insufficient performance.

From an engineering development point of view, the algorithms and basic approach developed by Barrett are quite sound. When one examines the specific implementation, however, the need for redesign is evident. For example, the frame grabber used by Barrett transferred image data to main memory via an 8-bit interface over the 8 MHz ISA bus. This resulted in a critical system bottleneck.

All of Barrett's software was developed to run under 16-bit real-mode MS-DOS, bringing with it the unavoidable problems which that environment's segmented memory causes (such as the 64 kbyte contiguous block limit, 640 kbyte DOS memory space, small/medium/large memory model tradeoffs, and more—see [54]). This resulted in suboptimal performance, cramped memory limits, and software workarounds. In particular, the 64 kbyte contiguous block limit meant that the system could never load even a single entire image frame (of 512×512 pixels at 8 bits per pixel = 256 kbytes) into memory at one time. Barrett had to resort to loading and processing the image on a row by row basis. The memory limits had other significant performance ramifications. The search area for the initial tracking

lock had to be minimized, meaning that even slight movement of the retina between the time the tracking templates were established and the time photocoagulation was to begin could defeat the tracking algorithm. In addition to the memory problems, the software implementation was not well optimized for real-time processing. More use of in-line macros and less use of nested function calls (resulting in multiple stack pushes of all the CPU registers) in time-critical routines are recommended [55,56].

The CPU processing power, coupled with the memory limitations, was also insufficient for certain necessary functions. For example, the laser spot localization routine, which finds where the actual irradiating spot is on the retinal image during photocoagulation, had to be removed from Barrett's code during his tracking tests because of speed limitations. Note that this routine is the only way to ensure closed-loop control of the laser pointing subsystem.

Barrett's design, while outstanding for its time, does not meet the requirements of CALOSOS. The problems listed above and other more minor limitations must be overcome to meet the specifications of Table 3.1.

3.3.2 Jerath's Lesion Control System

Jerath's work was also a follow-on to Markow's, only her area of concentration was dynamic control of lesion formation. Her system used an RS-170 CCD camera to image the laser irradiation site as the lesion formed. She derived a feedback control signal based upon the central (5×5 pixels) area reflectance of the lesion, which seemed to correlate well with lesion depth. When the central reflectance reached a precalibrated level, the laser was shut off. Her system was able to create lesions in an albumen eye phantom that were within 5% of the desired depth [14].

One significant drawback to Jerath's approach was the system response time. The reflectance signal was only updated at the 30 frames per second rate of the CCD camera; thus only long irradiation times (over 1 minute) yielded acceptable results. Typical clinical irradiation times are on the order of 100 ms, which drive

the requirements of CALOSOS. Obviously Jerath's system, as designed, could not meet the response time requirements of Table 3.1. Jerath's system also needed a complex optical setup which included a chopping wheel synchronized to the camera frame rate to prevent the laser from washing out the CCD image.

3.3.3 Incompatibilities Between Barrett's and Jerath's Systems

Since the original concept for an integrated system was to combine the work of Barrett and Jerath, it is worthwhile to examine the incompatibilities between the two approaches.

- An obvious difference is the platform on which the systems were developed. Barrett used an IBM-compatible PC, an internal Matrox frame grabber, and the MS-DOS operating system; Jerath used a Sun workstation, an external ITI frame grabber, and the Unix operating system.

- Another problem is the use of automatic gain control (AGC) with the CCD camera. Barrett's retinal tracker required the use of AGC for the best performance, whereas Jerath's lesion controller used absolute gray levels and thus must be operated with AGC off.

- Jerath's system used a chopping wheel to ensure that the CCD camera never "saw" the laser to ensure the reflectance measured was due to the diffuse white light source; Barrett's system expected to see the laser spot for closed loop control of the laser pointing subsystem.

- The greatest incompatibility from an engineering design standpoint is the difference in camera FOV used by the two systems. Barrett's system used a FOV of 50° to obtain the best selection of blood vessels for template creation, and to minimize the number of patient fixation points needed for panretinal photocoagulation. Jerath's system, however, used a FOV of $\simeq 2°$ to ensure that the single lesion she was measuring would fill the video frame (see Figure

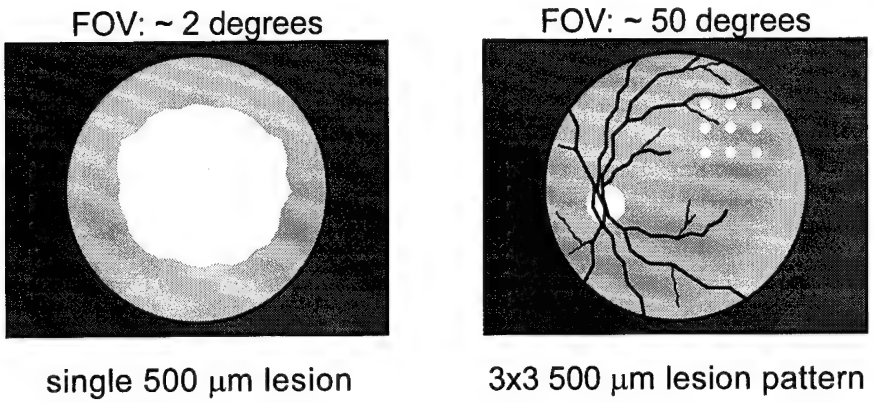

Figure 3.1: A comparison of camera FOVs used by Jerath (left) and Barrett (right).

3.1). At these extremes, tracking cannot be accomplished at a 2° FOV, yet at a 50° FOV the reflectance for a single lesion would be measured from an object only about 10 pixels across (assuming a 300 μm lesion), providing a questionable feedback signal.

The first three items above are not insurmountable, but the last item constitutes a significant design challenge. One solution would be to use two cameras, but the greater cost, complexity, and optical alignment problems would be hard to justify. Preliminary work toward finding a single compromise FOV is underway [57, 58]. However, a fundamental problem still remains concerning Jerath's approach: the unacceptably long response time of the feedback signal. To overcome this problem, a different method of lesion control was investigated.

3.3.4 Inderfurth's Lesion Control System

Recently, confocal reflectometry has been shown to have potential as a technique to obtain a feedback control signal for lesion formation [21]. Inderfurth et al. gathered data from both rabbits and from the clinical photocoagulation treatments of 68 patients (corresponding to $\simeq$12,000 retinal lesions) at the New England Eye Center

(Tufts University School of Medicine) by attaching a confocal reflectometer to a standard slit lamp microscope. The human data was gathered passively during normal photocoagulation treatments. The preliminary results on rabbits indicate that the latency time and initial slope of the reflectance signal may provide information that can be used to create repeatable lesions on the retina, as originally predicted by Weinberg [16]. Since the confocal setup has limited lateral spatial acceptance, the signal obtained can have similarities to the central reflectance measurement advocated by Jerath (see Chapter 7).

Unfortunately, this limited spatial acceptance is also a potential weakness of the confocal approach. Any relative movement between the reflectometer and the retina during lesion formation caused the reflectance signal to vary. The human data obtained by Inderfurth et al., due to normal minor eye movements while the patients were fixated, was rendered useless due to this motion-induced noise in the reflectance signal. While the technique can achieve a very fast response time (limited primarily by the data acquisition sample frequency), it can only be used when the eye is either imobilized or when the eye motion is tracked. Since another requirement of CALOSOS is to track the moving retina, a modified version of this confocal reflectometry seems promising since it overcomes the speed limitations of Jerath's approach.

3.3.5 Lessons Learned

While the systems reviewed above each had flaws, they represent a solid foundation from which CALOSOS can built. Barrett's basic approach was excellent, but the implementation and specifics of the design need considerable engineering work. Jerath demonstrated the viability of using a reflectance-based feedback control signal for lesion formation, while Inderfurth et al. found a way to acquire a very similar signal at a much faster rate, albeit one extremely sensitive to retinal motion. The challenge for this research was to design a system that takes the best of these pre-

vious approaches, overcome their limitations and drawbacks, and ultimitely create an entirely new system that meets or exceeds the clinically-derived requirements of Table 3.1.

3.4 Improved Hardware Design for CALOSOS

This section assumes a familiarity with computer engineering, digital electronics design, and the ubiquitous PC-compatible computer [59–61]. For its outstanding price/performance ratio, widespread use, and plethora of affordable hardware and software development tools, the PC was chosen over other computer types for the basic CALOSOS hardware platform.

Note that there are actually two hardware designs for CALOSOS. As will be discussed in Chapter 5, CALOSOS may be used either with all digital tracking of the retina or used in a hybrid implementation that uses both digital and analog control. The second approach requires some additional hardware for the analog tracking. Diagrams of the overall hardware designs are shown below in Section 3.7.

3.4.1 Alleviating the Video I/O Bottleneck

As indicated above, an engineering analysis of Barrett's original hardware design revealed a fundamental problem: it was I/O limited by the ISA data bus used by the frame grabber. This bus does not have the necessary bandwidth to accommodate real-time (30 fps) video. The ISA bus has a theoretical bandwidth of 16 Mbytes/sec (16-bit transfers, 8 MHz bus clock), but in actual use averages approximately 2 Mbytes/sec, due to an inefficient early-1980s design [62,63]. An RS-170 monochrome video signal (see Chapter 4 for more detail) configured for square pixels will create 640×480 8-bit pixel frames 30 times each second, and therefore needs a minimum bandwidth (not counting overhead) of 9.2 Mbytes/sec. To make matters worse, Barrett's design was limited by a frame grabber with an older 8-bit interface to the ISA bus, thus halving the possible throughput.

Selecting an Appropriate Data Bus

After analyzing both proprietary and open-standards alternatives, the peripheral connect interface (PCI) bus was selected to alleviate the I/O bottleneck. This open-standards bus, originally developed by Intel in 1993, combines high performance with very low cost [62]. It was designed to be platform independent, and can be found in both Pentium PCs and Power-PC Macintosh computers. The PCI bus has a maximum theoretical bandwidth of 132 Mbytes/sec (32-bit transfers, 33 MHz bus clock[2]), minus overhead. Actual sustained data throughput has been measured at more than 40 Mbytes/sec with first generation PCI controller chip sets (e.g. the Neptune chip set from Intel) and at more than 90 Mbytes/sec with second generation PCI controller chip sets (e.g. the Triton chip set from Intel). This is more than sufficient for real-time video. Thus the PC selected for the CALOSOS hardware platform was a 90 MHz Pentium which included a PCI bus; this was the fastest machine available at the time.

Selecting an Appropriate Frame Grabber

Choosing the bus is only half the solution: the other half is choosing a frame grabber that can take advantage of the PCI bus. For CALOSOS, the frame grabber is a key component and must meet stringent criteria. It must be capable of master mode transfers across the bus, which is a special type of direct memory access (DMA). During master mode transfers, the frame grabber becomes bus master and transfers data directly into main system memory without CPU intervention. The frame grabber must also be capable of interrupt-driven operation, since master mode is of little use without some efficient means to signal the CPU when new data is ready. Both capabilities are necessary for optimized retinal tracking. On-board dual-ported memory is also important for the frame grabber, so that data will not be lost if an unexpected bus latency delays data transfer. The frame grabber must

[2]The new PCI-2 bus uses a 66 MHz bus clock yielding twice the bandwidth.

be able to send video frames directly to the standard computer monitor, eliminating the need for separate, external television monitors. As explained below, the frame grabber software development library must support 32-bit protected mode extended-DOS operation. Other criteria include accepting a wide variety of standard and non-standard camera inputs (to allow CALOSOS to migrate to other cameras if needed); good video channel signal-to-noise ratio (SNR); a stable, jitter-free pixel sample clock with protection against aliasing; accurate 8-bit or better quantization; and flexible software control of the frame grabber features.

Few frame grabbers can meet even half of these criteria. After an in-depth review of over twenty companies' products, one clearly stood out. The MV-1000 PCI frame grabber by MuTech Corporation meets all the criteria above, and was selected for CALOSOS. See the MV-1000 technical reference manual [64] for more information. Further details regarding the programming and use of the frame grabber can be found in Chapters 4 and 5.

An additional video I/O speed increase was realized from the fact that the circular 50 degree FOV of the fundus camera only filled the central region of the 640×480 video frame (refer to Figure 3.1). This region was measured to be 450×450 pixels. By designating this area of the frame as a region of interest (ROI) and sending only those pixels across the PCI bus, a considerable increase in efficiency can be realized. The programmer must exercise caution, however, as the hardware specifics of the PCI bus can lead to subtle side effects. For example, setting the ROI to the central 450×450 pixels actually resulted in a transfer rate only 1/3 the full screen rate. After some investigation, it was determined that the 32-bit granularity of the PCI bus makes optimal transfers when an integer multiple of 32-bits are specified. There are four 8-bit pixels for every 32 bits, so adjusting the ROI to 452×452 pixels brought the PCI bus transfers back up to full speed. Using a 452×452 image rather than a 640×480 image yields an increase in both CPU and memory utilization efficiency of 34%, with no loss in retinal image detail.

Although published after the design decision was made, recent articles [65, 66] support the architectural choice of the PCI bus, and confirm the importance of the criteria which led to selection of the MuTech frame grabber.

3.4.2 Improving Control Signal I/O

In addition to the video signal, various control signals must be passed between the computer and the rest of the system. These include the analog output signals to drive beam-steering galvanometers, digital input signals for patient status and lesion completion status, and a digital output signal to control the laser shutter. The lesion control signal may be an analog input rather than a digital input, so flexibility is needed. The digital signals can be accomodated by a wide variety of I/O cards, but the capability of analog output to the beam-steering galvanometers is present on only a few multifunction data acquisition cards.

Barrett used a Data Translation DT2801 card for all his control signal I/O, but had experienced some ringing and lag in the analog galvanometer signals [67]. The fidelity of these signals is absolutely vital to the pointing accuracy and control system dynamics of CALOSOS. After analyzing the DT2801 and testing its capabilities, it was found that a potential contributing cause of Barrett's problem was the settling time (50 μs for a 20 V step) and slew rate (0.5 V/μs) of the analog output circuitry [68]. A review of boards with similar I/O capabilities was conducted. The National Instruments AT-MIO-16 contains superior analog out circuitry, with a settling time of 4 μs for a 20 V step, and a slew rate of 30 V/μs. Thus the signal to the galvanometers could settle to a new value 12.5 times faster, and respond to changes in value 60 times faster. Since the AT-MIO-16 met or exceeded all other requirements, and cost no more than a DT2801, it was selected for the CALOSOS design. See the AT-MIO-16 User Manual [69] for more information.

The data acquisition card is only one component affecting the dynamics of the laser pointing and control system. The galvanometers and beam steering mirrors

are major contributors to the control system performance and cannot be neglected; they are treated in detail in Chapter 6.

One significant problem was encountered with the data acquisition card selection process: the software support libraries were not available from any manufacturer for 32-bit protected mode extended-DOS operation. The solution to this problem is detailed in the section on software below.

3.5 Improved Software Design for CALOSOS

The software design for CALOSOS follows a highly structured approach proven to minimize errors in large, complex software projects [56, 70]. The C programming language was chosen for it's efficiency, suitability to image processing and data acquisition tasks, and the availability of sophisticated optimizing compilers which rival assembly code [55]. The algorithms and implementations were optimized for speed, but written in such a way as to facilitate maintenance and modifications by another programmer [71–76]. See Appendix C for details on the configuration of the source files.

3.5.1 Determining the Optimal Software Environment

With a PC as the hardware platform, the available software environments include DOS (16-bit), extended DOS (32-bit protected mode), Windows 3.11 (16-bit with some 32-bit extensions), Windows NT (32-bit), OS/2 (32-bit), Unix (32-bit), and specialized operating systems. Selecting the best environment for CALOSOS is vital to the project's success, so an extensive engineering review was performed. Windows95 was introduced after the design decision was made, but since it's code represents a "half-way" point between Windows 3.11 and Windows NT, the significant attributes of Windows95 were considered.

DOS

The 16-bit DOS environment suffers from an archaic segmented addressing scheme, with the associated 64 kbyte contiguous memory block limit, 640 kbyte DOS memory space, small/medium/large memory model tradeoffs, and no protection from errant pointers or other subtle software bugs [54, 76]. The user interface is command-line, unless a custom graphical user interface (GUI) is written for each program. No serious programs are now written for this environment.

Extended DOS

The 32-bit extended DOS environment overcomes nearly all the limitations of DOS [54]. It operates in the CPU's protected mode with virtualized memory and a linear 4 Gbyte address space. There are no memory block limits, no artificial memory models, no need to load two registers (segment and offset) for a memory access, and strict protection from invalid memory operations. While more challenging to program for than DOS, anecdotal evidence and personal experience show that a CPU-intensive program typically experiences a 4× to 5× speedup when ported from DOS to 32-bit extended DOS. Like DOS, the user interface is command-line, unless a custom GUI is written for each program. Extended DOS programs can coexist with DOS or Windows; a special program stub (the "extender") automatically loads when an extended DOS program is executed and unloads upon program exit. The major disadvantage of extended DOS is the relative scarcity of commercial software tools and libraries.

Windows 3.11

Nearly all new commercial software for PCs is being written to run in one of the Windows environments. CALOSOS, however, must operate as a real-time system, responding to tracking corrections or lesion control signals without significant delay—tasks unsuited to Windows 3.11. The programmer has very little control in

Windows over the CPU priority of individual tasks; the critical tracking code could get put on hold for something as trivial as a timer check for the screen saver! Some improvement can be realized if the specific hardware drivers (for the frame grabber and the data acquisition board) are implemented as Virtual Device Drivers (commonly referred to as VxD drivers). Drivers which are regular Windows executables or dynamic link libraries (DLLs) will be very slow due to priority contention and the virtualized hardware interrupts [77]. A VxD runs in Ring 0 of the CPU Virtual Machine Manager (VMM) and is the only way to talk directly to hardware in a Windows environment. However, a VxD is tricky to write, hard to debug, and part (sometimes all) of it has to be written in assembly language.

While an advantage of the Windows environment is a standardized GUI across all programs, the large associated overhead results in a significant performance penalty. A Windows program will typically run more slowly than an otherwise equivalent DOS program. For the programmer, Windows can be a time-intensive and extremely subtle software environment. Disastrous bugs can creep into seemingly flawless code, mainly due to residual bugs in Windows, compilers, or errors in documented Windows functions [78]. The unpredictable task latency, GUI overhead, and inherent instability have made programmers of real-time software avoid Windows.

Windows95, Windows NT, OS/2, Unix and Others

While some of the disadvantages (particularly with regard to stability) of Windows 3.11 were overcome with Windows95 and Windows NT, the GUI overhead is still present and the programming complexity is unimproved. These environments also require large amounts of user memory (typically 32 Mbytes RAM) to run efficiently, and many software tools and hardware drivers are not yet available. OS/2 has many similarities to Windows NT, no significant advantages, has a relatively small user base, and is not well supported. Unix has a very large user base, but is incompatible

with all other PC environments and was never intended for real-time programming. There are some highly specialized real-time operating systems for PCs, but they are expensive, incompatible with most other PC programs, and have limited available software tools.

The Final Choice

The primary requirement of the software environment for CALOSOS is speed. The software must execute quickly, respond to asynchronous events with predictably short latency, and allow efficient manipulation of large memory blocks (for video images). Secondary requirements include compatibility (or coexistance) with common PC programs, and low price. The only environment that meets these criteria is 32-bit extended DOS. The highly optimized Watcom C/C++ compiler was chosen since it supports extended DOS at no extra charge, and includes a free unlimited run-time license for the DOS4G/W 32-bit extender.

Performance is the greatest advantage of this choice. The greatest disadvantage is that complex parts of the CALOSOS software, readily available in some other environments but not in extended DOS, must be written from scratch. In particular, the entire graphical user interface and the data acquisition library had to be designed, programmed, and debugged.

3.5.2 Creating a High-Speed Graphical User Interface

As with DOS, extended DOS has only a command-line interface in it's native mode. Yet CALOSOS requires a graphical user interface (GUI) to meet its design goals of a single monitor solution and program control using a mouse. A single monitor solution implies the need to combine video images with command menus on one screen, preferably a standard computer monitor. This can only be accomplished with a GUI, where separate windows can be created. CALOSOS should also enable the ophthalmologist to use a mouse cursor directly on the video image of the retina

to select items such as lesion sites or lesion patterns, or to easily select program menu items and parameters. This represents a major advance in ease-of-use for the clinician, and requires a GUI. But any GUI designed for CALOSOS must be highly optimized for speed, and avoid the costly overhead from which other environments such as Windows suffer. To create this GUI for CALOSOS, significant obstacles were overcome.

In Windows (all variants), OS/2, or Unix (X-Windows), the software environment provides the necessary generalized function calls to access the built-in GUI. For DOS, standard software libraries are available with which a programmer can construct a custom GUI [79]. With its smaller potential for sales volume and greater complexity for programming, extended DOS has not attracted commercial software developers to create GUI frameworks. Thus the programmer must build a GUI from scratch. To further complicate the task, CALOSOS must display windows for a video image (nominally 640×480 pixels), for user menus, and for program information simultaneously. The recommended screen resolution for this is 800×600 [80], which is beyond the normal VGA resolution and is even more difficult to program [81]. For example, the frame grabber manufacturer had been working on this problem for over a year and had only developed a crude, single menu display without any mouse support. This was unacceptable for CALOSOS.

With so many challenges, a search was conducted via the Internet in an effort to find if other people were working on a similar problem. It was discovered that in Australia, the chief programmer for a small software company (SciTech Software[3]) had just started to create a collection of low-level graphics functions for protected mode extended DOS. The anticipated market was computer game programmers, so the functions were highly optimized for speed in order to support smooth animation of complex graphics. The good news was the high-speed animation requirements also matched the requirements of CALOSOS. The bad news was that development

[3]The company recently relocated to California, USA.

had just started, the functions were not debugged or documented, and the collection would not be available for at least one year. No other existing efforts were identified, so the author convinced SciTech to make him a member of their beta test software development team. This provided full access to the software-in-progress, in return for testing, identifying bugs, and helping with the documentation [82]. While the beta test duties consumed some time, it more than made up for the time saved by having the low-level graphics functions available as a foundation for the CALOSOS GUI.

The low-level graphics functions provided the means in 32-bit protected mode to write lines and characters, create and manipulate mouse cursors, and directly address the graphics screen in the fastest possible way. From this, the author created and debugged a library of higher-level GUI functions (define windows, build menus, display text, accept alphanumeric input, accept mouse selections, change mouse cursors, display CCD camera video, save/load files, etc.) uniquely tailored for CALOSOS and having minimal overhead. The final result is an extremely fast, flexible, and easy-to-use GUI that gives the ophthalmologist complete control over the photocoagulation procedure, using the standard computer monitor and a mouse. See Figure 3.2 for an example, with the CCD camera imaging a simulated retina. Note the central window contains the video from the CCD camera; the right window contains the various menus that can be selected via mouse or keyboard; the bottom window contains information, status messages and accepts user alphanumeric input; and the left window contains the present status of the various program and surgical procedure settings. The frame grabber manufacturer, upon hearing of the progress embodied in the CALOSOS GUI, expressed interest in using some of this new software as a basis for their own developments.

Just as extended DOS presented a challenge for creating a GUI, it was found that software support for data acquisition boards was also nonexistant.

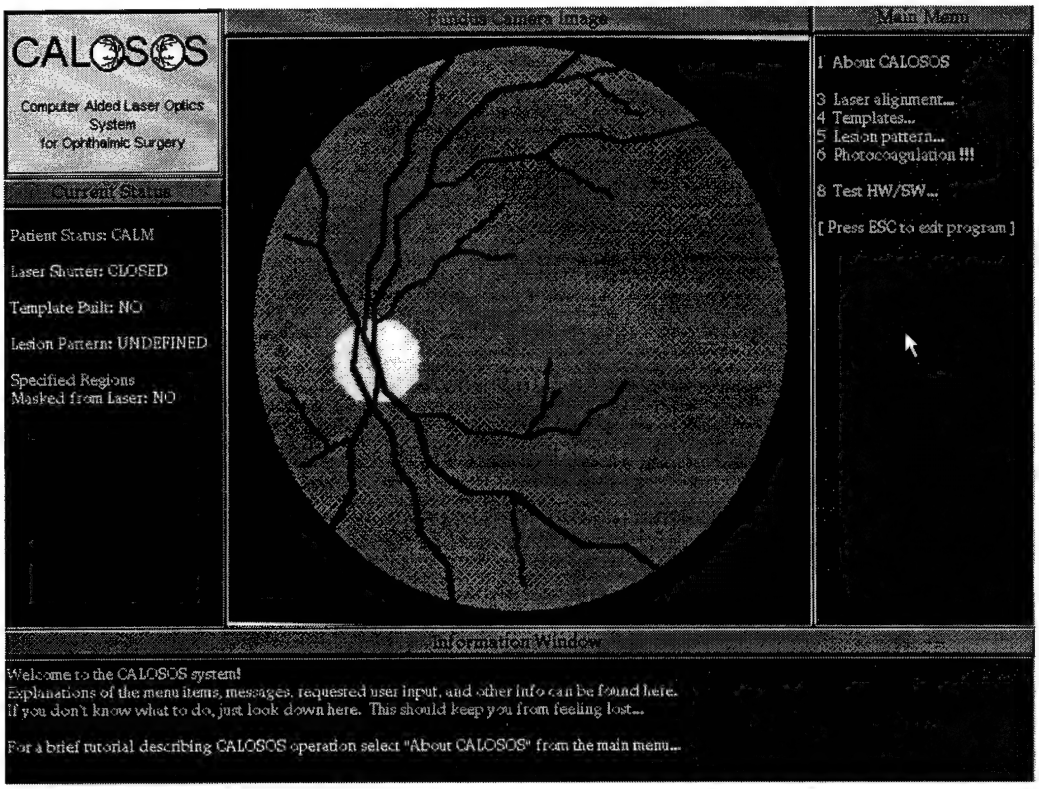

Figure 3.2: Opening screen of the graphical user interface for CALOSOS.

3.5.3 Creating a Customized 32-bit Data Acquisition Library

While 32-bit extended-DOS yields outstanding performance, it is a low sales volume and unforgiving programming environment which no data acquisition board manufacturer supports. After weeks of fruitless discussions with engineers from the major data aqcuisition companies, it became evident that this would not change.

With the data acquisition board selected on the basis of its performance alone, the internal hardware register definitions and addresses were obtained from the manufacturer (National Instruments). A complete data acquisition function library (including initialization, setup, analog-out, analog-in with software controllable sampling, digital-out, and digital-in) was then written, tested, and debugged by the author specifically for the 32-bit protected mode extended-DOS environment. The data acquisition board manufacturer then expressed considerable interest in this software, and the author donated it free of charge in the hopes of saving others the effort.

3.5.4 Other Software Improvements

Many other parts of the overall software for CALOSOS were improved over previous approaches. For example, the automated detection of retinal blood vessels is over three orders of magnitude faster than Barrett's previous method, the retinal tracking algorithm was converted to integer math and optimized for faster execution, and the lesion pattern software now minimizes the needed galvonometer movements for any given pattern. These and other specific improvements are discussed in greater detail in the appropriate chapters following this one.

3.6 Improved Optics Design for CALOSOS

The optics for CALOSOS are the result of a complete redesign from previous approaches, with the intent of combining a variation of both Jerath's lesion control

signal (using Inderfurth's technique) and Barrett's laser pointing subsystem. The optics for Jerath's lesion control system required six lenses, a turning mirror, two beam splitters, and a chopping wheel synchronized to the camera frame rate [14]. The optics for Barrett's original laser pointing subsystem required six lenses, a beam splitter, and two galvanometer-driven steering mirrors [15]. Due to the angular limitations of the galvanometers used and some subtle optical design issues, Barrett's system needed nearly a meter of space between the steering mirrors and the fundus camera.

The optical redesign for CALOSOS achieved multiple goals:

- it combined the ability to point and control the laser with the ability to obtain a feedback signal suitable for lesion control,
- it reduced the laser power density on the subject's cornea,
- it reduced the laser power requirements for the same photocoagulation effect,
- it reduced the total lens count to three (plus a fourth optional lens which typically isn't needed),
- it eliminated the need for a synchronized chopping wheel,
- it reduced the space needed between the steering mirrors and the fundus camera by over 75%,
- it reduced the Fresnel losses in the system,
- and it reduced the scan distortion due to spherical aberration.

Diagrams of the overall optics design are presented in Section 3.7. Specialized aspects of the optical design are also discussed further in the chapter on laser pointing and control (Chapter 6) and the chapter on lesion control (Chapter 7).

Note that there are actually two optical designs for CALOSOS: one for digital-only retinal tracking, and one for hybrid retinal tracking. The latter optical design

was created in collaboration with R. Daniel Ferguson of Physical Sciences, Inc., and includes an additional pair of galvanometers and mirrors. More detail is given in Chapter 5, where the tracking system is discussed.

3.7 CALOSOS System Overview

As the overall system design is discussed, recall the primary goals of CALOSOS for this research. The system should be able to track the retina and compensate for any movement (for at least 10 deg/sec but preferably up to 50 deg/sec) during a retinal photocoagulation procedure, responding within 5 ms. The laser pointing, as updated by the retinal tracking, should be accurate to within 100 μm of the intended location on the retina. A real-time lesion reflectance signal should be obtained for typical clinical irradiations ($\simeq$100 ms) for use as a lesion control signal. And finally, the system should make the photocoagulation procedure not only safer but less tedious through capabilities such as automatically detecting and avoiding certain critical anatomy features on the retina and automatically generating lesion patterns as desired.

The overall design of CALOSOS, with the exception of the software, is best described graphically. The diagrams are presented in two parts, one depicting the computer and electronic hardware, and the other depicting the optics. Recall that there are two implementations of CALOSOS: one that uses digital tracking and one that uses hybrid tracking of the retina. Both are shown below.

3.7.1 Digital Tracking Implementation of CALOSOS

Electronic Hardware

The computer and electronic hardware for the digital tracking implementation of CALOSOS is shown in Figure 3.3. The VCR and monitor are optional. The fundus image is displayed in real time on the single computer monitor, along with various

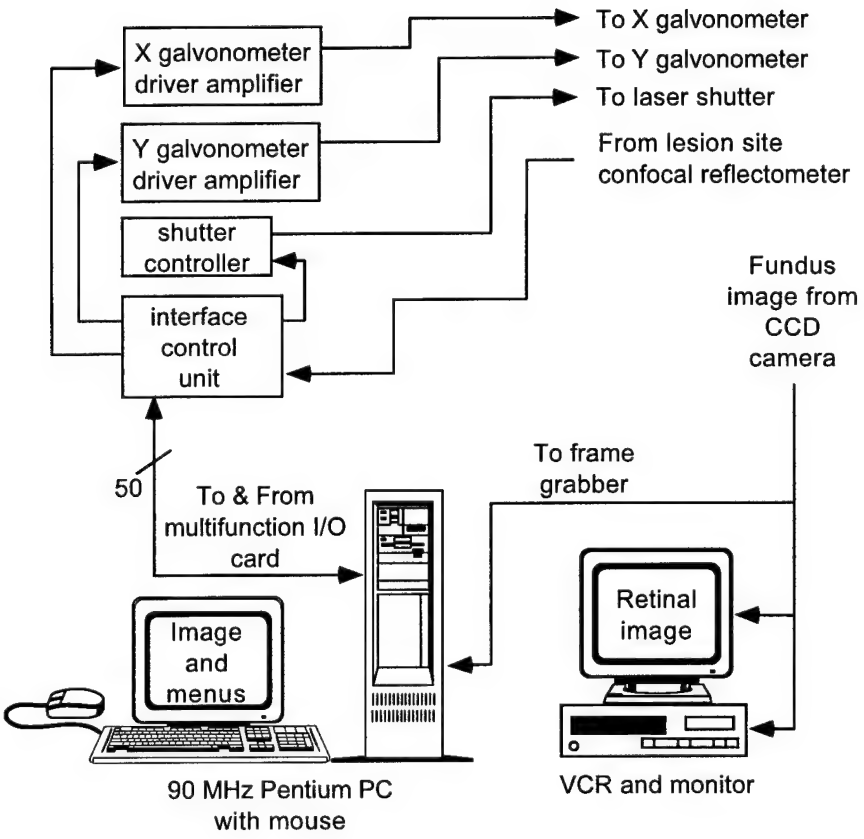

Figure 3.3: Computer and electronics hardware for the digital tracking version of CALOSOS.

Signal	Type	PC I/O
X galvo	analog	O
Y galvo	analog	O
shutter	digital	O
patient status	digital	I
lesion status	digital	I
clear status	digital	O
lesion control	analog	I

Table 3.2: Signals to/from the interface control unit.

menus and status messages. There is no need for the clinician to look anywhere else during a surgical procedure, as all information is presented in one place. The use of the mouse makes controlling the system particularly easy, especially the ability to add or erase designated lesion sites directly on the fundus image.

The interface control unit (ICU) is from a design by Barrett [15], with some modifications. Since all the signals to and from the PC-hosted multifunction data acquisition I/O card are supplied on a single 50-connector ribbon cable, the ICU separates and routes the signals to the appropriate place. These signals are listed in Table 3.2. The X and Y galvo signals are for steering the laser beam, and the shutter signal opens and closes the laser shutter. The patient status signal is a digital toggle connected to a simulated panic button that a human patient would have for situations such as an impending sneeze during photocoagulation, and the lesion status signal is a digital toggle to allow an externally generated lesion control signal to be used if desired. There are manual buttons for these on the ICU. The clear status signal forces a reset on the two status signal toggle states. The state of these toggles is displayed at all times on the computer monitor. The analog lesion control signal is routed from the confocal reflectometer and provides a real time lesion reflectance signal. The exact pin assignments can be found in Appendix B.

More detail regarding the CALOSOS hardware can be found in later chapters according to its particular function.

Optics

The optics design for for the digital tracking implementation of CALOSOS is shown in Figure 3.4. While a general description is given here, see Chapter 6 and Chapter 7 for more detail about functional specifics. The numerical specifications of the optical design can be found in Appendix B. Note that for the distances and focal lengths used in CALOSOS, Gaussian beam shaping through optical elements can be approximated with simple thin lens optics analysis [83, 84].

One significant change in the optical design compared to Barrett's work is in the beam shaping. A simplified comparison is shown in Figure 3.5 (beam size greatly exaggerated for clarity). Barrett used a variation of Method A (note that in place of the single lens L1 shown in Figure 3.5(a), Barrett actually used five lenses to expand and collimate the beam), where the beam is focused at the cornea and diverges at the retina. It's advantage is ease of alignment for the fundus camera, but it results in a high power density on the cornea (on the order of 500 W/cm^2) and can be greatly affected by small corneal imperfections.[4] Method A is also not suited to the use of a confocal reflectometer for a lesion control signal. The CALOSOS design uses Method B, where the beam enters the eye collimated and is focused by the optics of the eye to a minimum spot on the retina. This method makes alignment with the fundus camera more critical, but has four advantages. It lowers the power density on the cornea (to less than 2 W/cm^2), it is less affected by small corneal imperfections, it is well suited for confocal reflectometry, and it allows the use of lower laser input power to achieve the same photocoagulation effect on the retina.

For Method B in Figure 3.5 to work properly, L1 collimates the beam, and L2 brings the beam to a focus at the point which is also at the focal distance of L3. The orientation of L3 may seem opposite to conventional design rules, but the reason will be explained subsequently. The point in Figure 3.5 at the focal distance of both L2

[4]Ophthalmologists generally prefer to spread the laser power over as large an area of the cornea as is practical.

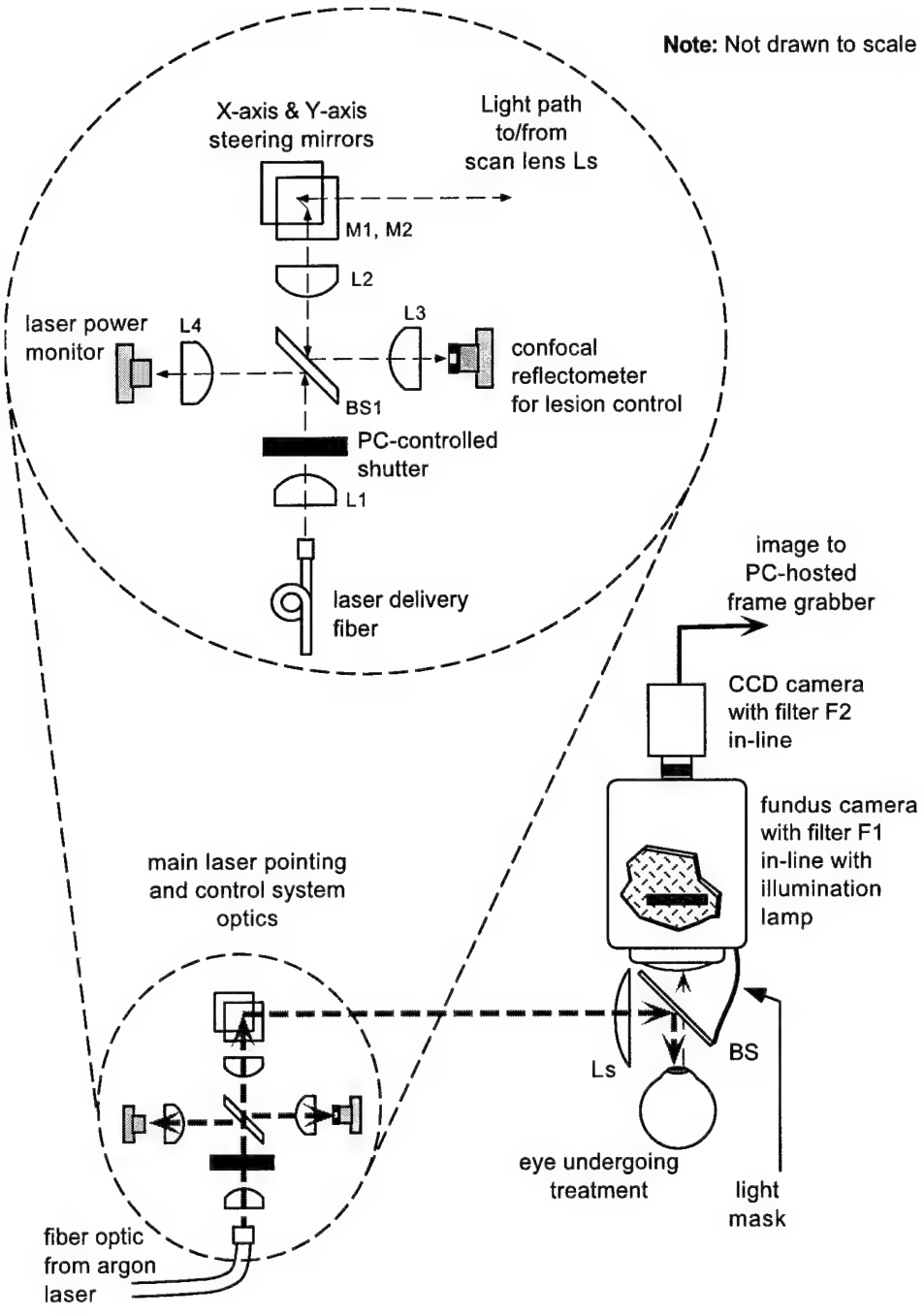

Figure 3.4: Optics design for the digital tracking version of CALOSOS.

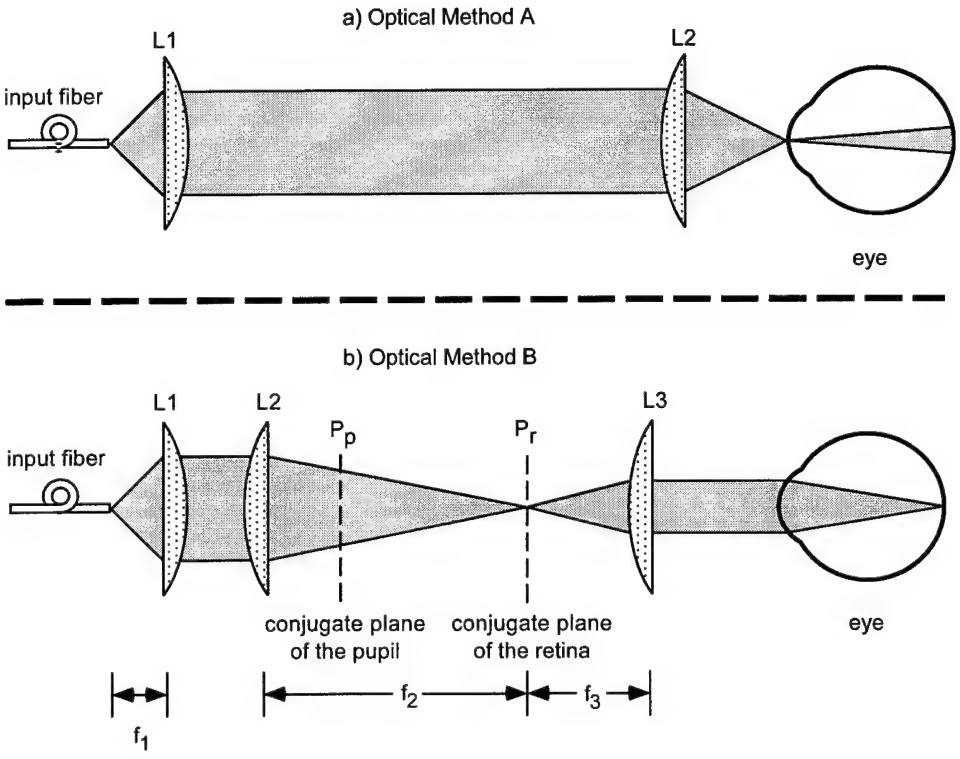

Figure 3.5: A comparison of laser beam shaping for use with CALOSOS.

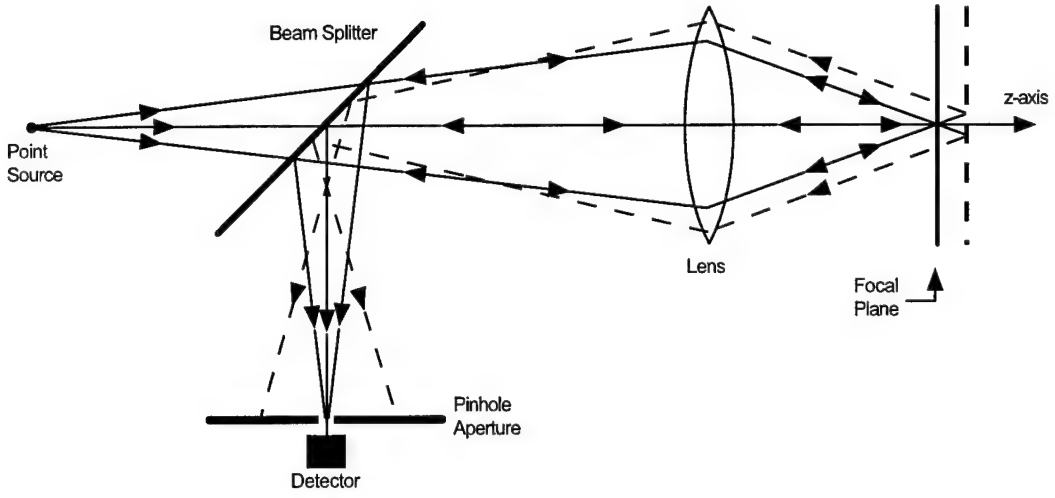

Figure 3.6: An example of confocal light detection.

and L3 is located at the conjugate plane of the retina designated P_r in the figure[5]. In Figure 3.5, the lenses L1, L2, and L3 equate to lenses L1, L2, and Ls in Figure 3.4. Note that the distance of the main optics assembly to the fundus camera is therefore crucial to proper optical performance.

One reason for bringing the beam to a focus at the retina is to allow the use of a confocal reflectometer to obtain a reflectance signal of the forming lesion [85]. Figure 3.6 shows how the use of a pinhole aperture allows an optical system to detect light only from the intended focal plane, rejecting light from other directions and distances. This high rejection of unwanted light allows the large amplification necessary to produce a useable signal from the low-level reflected laser energy which travels the return optical path. The specular reflection from the cornea is effectively eliminated. The incorporation of optics similar to Figure 3.6 can be seen in Figure 3.4, where L3 brings the returning light to a focus at the pinhole aperture of the confocal reflectometer. Note that since the laser power monitor is *not* a confocal device, lens L4 shown in Figure 3.4 is optional and typically is ommitted.

[5]Since the retina is a curved surface, the conjugate "plane" would also be curved.

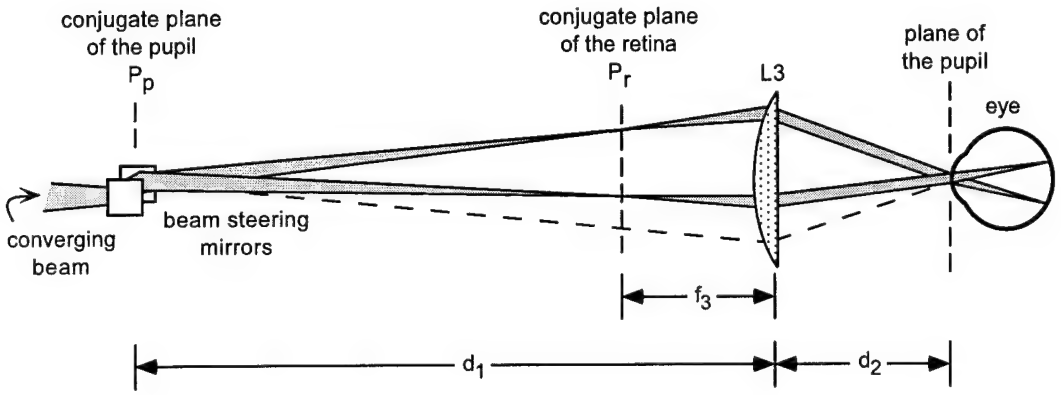

Figure 3.7: An example of laser beam coupling into the eye at two different steering angles.

Steering mirrors M1 and M2 in Figure 3.4 point the laser as needed, and the scan lens Ls (attached to the fundus camera) is used for angular magnification of the beam deflection. Beam splitter BS on the fundus camera directs the laser beam into the eye while allowing the fundus camera to image the retina. The design using a combination of M1, M2, and Ls to steer the beam appropriately on the retina is an adaptation of the design by Webb et al. [86–89] for the scanning laser ophthalmoscope (SLO) and the confocal scanning laser ophthalmoscope (CSLO).

A simplified beam steering diagram is shown in Figure 3.7, where L3 represents Ls. The main optical constraint is that the beam must pass through the pupil at all useable deflection angles. For this to be true, the steering deflection of the mirrors must occur at a conjugate plane of the pupil. Determination of the conjugate plane of the pupil follows from optics theory. From Figure 3.7,

$$\frac{1}{d_1} + \frac{1}{d_2} = \frac{1}{f_3} \tag{3.1}$$

where f_3 is the focal length of lens L3. If they can be placed close enough together, the x and y mirrors can "share" the same conjugate plane with acceptable performance. The CALOSOS optical design takes advantage of this. A secondary constraint on the design is the fixed distance of the eye to the fundus camera objec-

tive, which is 50 mm for the fundus camera used for CALOSOS. A tertiary constraint on the design is the desire to be able to steer across a 50 degree FOV across the retina. Appendix B lists the final design distances of Figure 3.4 under the tradeoffs of these constraints.

It is appropriate to expound on lens Ls at this point. The forward travelling laser beam enters Ls as a diverging beam and leaves collimated. In this situation of an infinite conjugate ratio, conventional design wisdom would indicate that spherical aberration with a plano-convex lens can be minimized if it is in the opposite orientation shown in Figure 3.4 [37]. But looking again at Figure 3.7, it can be seen that another congugate ratio is present, that of d_1/d_2 for the deflected beam. For CALOSOS, spherical aberration effects on the beam steering angles have a much greater impact on system performance than on the beam itself. The d_1/d_2 conjugate ratio dictates the orientation of Ls as shown. Residual spherical aberration effects on the beam steering would still prevent using the full 50 degree FOV with conventional optics. Therefore, Ls is specified to be an aspherical lens manufactured to display minimimal spherical aberration at large angles of incidence.

Another optical consideration of great interest to the ophthalmologist is the laser spot size on the retina. Refer to the simplified diagram of Figure 3.5(b). The fiber core from the argon laser is approximately 80 μm in diameter. This spot of light is magnified by the focal length ratio of L2/L1, which from Appendix B is found to be a factor of 10. Thus at the conjugate plane of the retina P_r, the spot is approximately 800 μm in diameter. This spot is then (de)magnified by the focal length ratio of Le/L3, where Le is the equivalent focal length of the human eye (17 mm, from [37,38]). From Appendix B, this ratio is roughly 1/3, and thus the laser spot on the retina is approximately 267 μm. This is a reasonable fixed size for a development system; a production system would allow a variable spot size.

3.7.2 Hybrid Tracking Implementation of CALOSOS

Electronic Hardware

The computer and electronic hardware for the hybrid tracking implementation of CALOSOS is shown in Figure 3.8. The setup is very similar to the digital implementation, with the addition of the analog tracking electronics and another pair of galvanometers and drivers. Since these additional items are used only for tracking, their discussion is postponed until Chapter 5.

Optics

The optics design for for the hybrid tracking implementation of CALOSOS is shown in Figure 3.9. Again, the setup is very similar to the digital implementation, with the addition of another pair of steering mirrors, and the necessary optics to support another confocal reflectometer. Since these additional items are also used only for tracking, their discussion is also postponed until Chapter 5.

For both the digital implementation and the hybrid implementation of CALOSOS, there are significant ramifications of the design approach that affect how much of the previous work can be directly applied.

3.8 Ramifications of Improved Design

The improved overall design for CALOSOS eliminates the major hardware, software, and optics limits of previous approaches. However, by changing the frame grabber, data acquisition card, and software environment all the software developed by previous researchers (over 3,000 lines of C code) was made unusable. Certain fundamental aspects of the previous software, such as Barrett's underlying algorithm for retinal tracking, were applied to the new environment with modest changes, but most other parts are totally new.

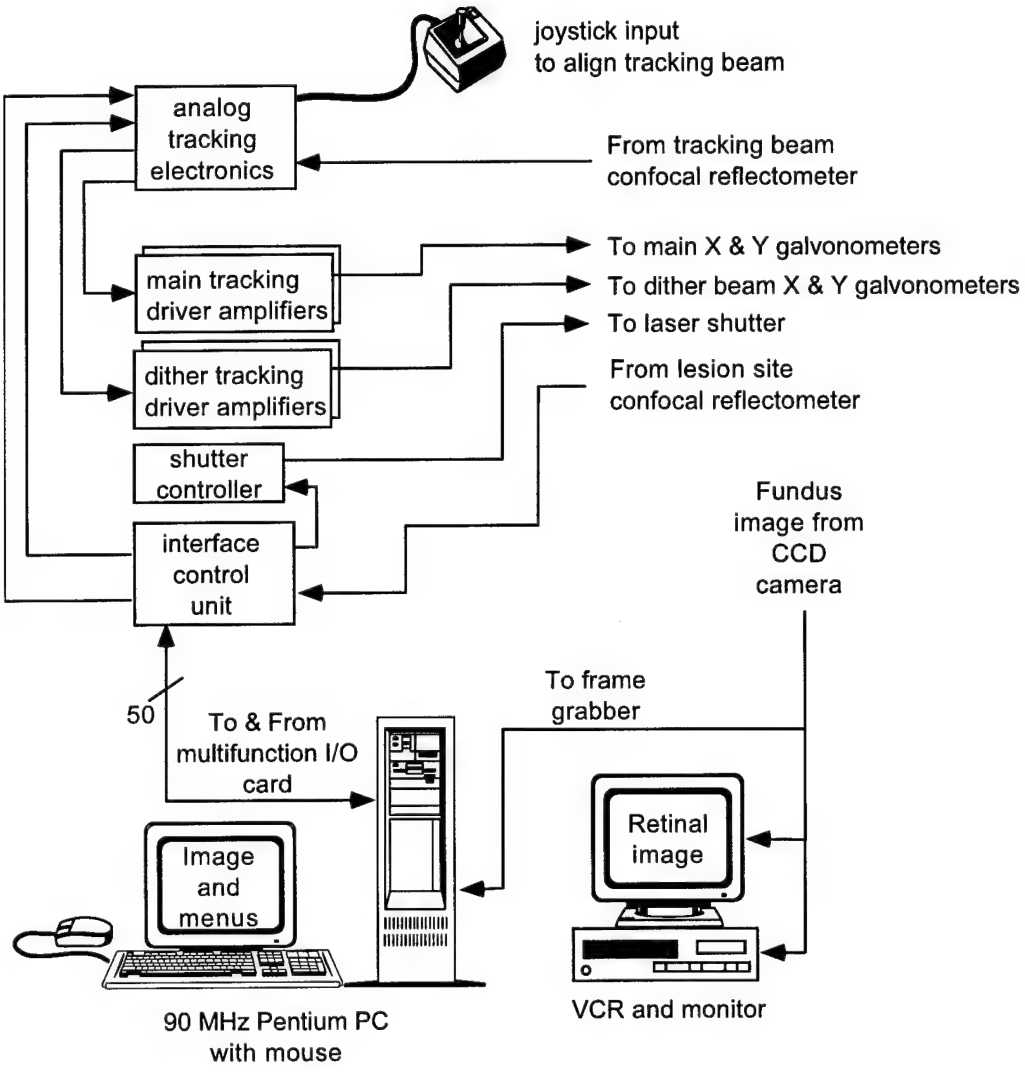

Figure 3.8: Computer and electronics hardware for the hybrid tracking version of CALOSOS.

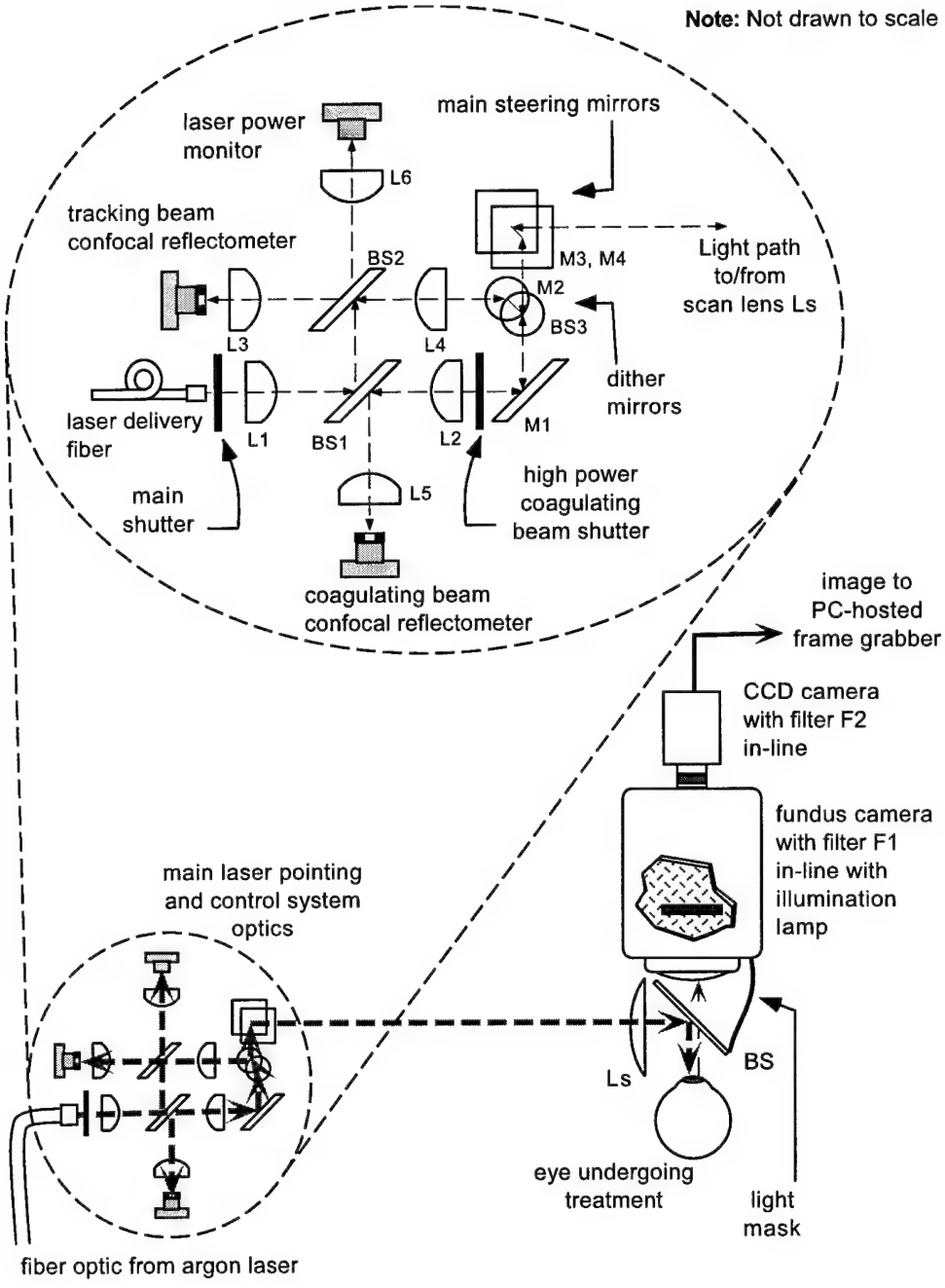

Figure 3.9: Optics design for the hybrid tracking version of CALOSOS.

The next four chapters detail my analysis and design regarding specific functional areas of CALOSOS: image processing, retinal tracking, controlling/pointing the laser, and controlling lesion formation.

Chapter 4

Retinal Image Formation and Image Processing

This chapter describes how the system design for CALOSOS is optimized to provide the best digitized retinal image within the constraints of system cost and performance trade-offs [90–95]. A simple method is described for estimating linear distances on the curved retina, followed by a discussion regarding the relevant characteristics and limitations of retinal image formation and image digitization from both an optical and electronic point of view. Interacting constraints, which are often overlooked by other authors, are given detailed consideration. This includes the relationship between optical resolution and spatial sampling, and the ramifications of finite video signal bandwidth on video resolution. Real-time techniques used to enhance the image are reviewed, and a new method to automatically detect critical vision anatomy in the image is introduced.

4.1 Estimating Retinal Distances

Before proceeding with the discussion on retinal image formation, a method of estimating spatial distances on the curved surface of the retina is needed. The static morphological features of the retina, such as the optic disk, blood vessels, and

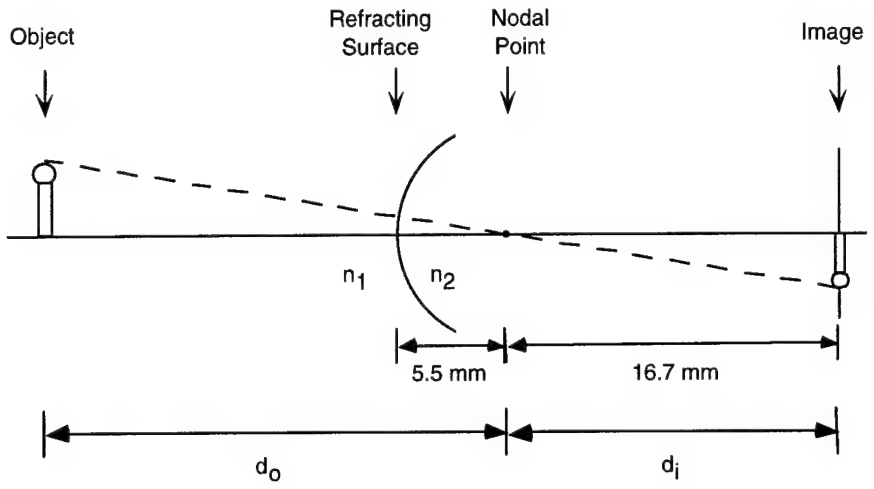

Figure 4.1: The reduced eye model for simplified calculations of human retinal distances.

the fovea, were discussed from an anatomical point of view in Chapter 2, where some spatial retinal distances were given. A straightforward technique to convert between angular span and spatial distance on the retina is given below. Based upon [31, 96], sufficient accuracy for finding distances on the human retina can be obtained from a simplified version of Hemholtz's schematic eye called the *reduced eye model* as shown in Figure 4.1. In the reduced eye model, there is a single refractive surface having a 5.5 mm radius of curvature, and a posterior nodal distance of 16.7 mm. Since a ray passing through the nodal point is by definition an undeviated ray, an angular span in degrees can be equated to a spatial distance on the retina by:

$$16.7 \text{ mm} \cdot \tan(1°) = 291.5 \ \mu\text{m/deg} \tag{4.1}$$

As an example, the optic disk is roughly circular and has a mean diameter of 1800 μm [26]. This value has been found to be nearly constant in all humans regardless of race, sex, or age and is often used as a "yardstick" in fundus photographs [25]. From Equation 4.1 above, the optic disk subtends an arc of roughly 6.2°. A 30° FOV of the fundus has a viewing circle with a diameter of 8.75 mm, while a 50°

FOV of the fundus has a viewing circle with a diameter of 14.6 mm. Equation 4.1 will be useful in finding the size of an image pixel in the retinal image.

Note that because the eye is not truly spherical, these distance calculations become less accurate as one moves away from the region of the fundus near the optic disk and fovea often referred to as the posterior pole [97]. However, these peripheral regions of the retina have no critical vision anatomy to avoid, so less accuracy is needed for laser surgery applications in these regions [3]. Therefore, the approximation of Equation 4.1 will suffice for the purposes of this discussion.

4.2 Analyzing Retinal Image Formation

Much of the operation of CALOSOS depends upon digitized retinal images. Barrett's earlier work [15] concentrated on choosing the best method to obtain the retinal image. While his selection of CCD camera technology for retinal imaging still appears the best design choice, what is missing is a detailed analysis of the limitations and information content of such an image. This analysis is necessary to ensure against losing or aliasing any high frequency (i.e. spatially small or sharp edged) features that CALOSOS needs, and also to identify how precisely location on the retina can be determined. Such an analysis requires an understanding of both spatial resolution (which determines the smallest detail available on the image), and of pixelation (which is the process of how the apparently smooth input image is partitioned into discrete pixels). Spatial resolution is a well-studied topic in optics [39, 98, 99], while pixelation (otherwise known as spatial sampling) is an important topic in image processing [90,100,101]. In assessing digital image quality, the two topics are interrelated and must be dealt with together; ideally, the spatial resolution and the pixelation are "matched" to each other [100, 102]. The subject is treated below in a systematic manner, with the total retinal image acquisition system consisting of four main components:

1. the optics of the eye,

2. the optics of the fundus camera,

3. the CCD camera,

4. and the computer's frame grabber.

The first two components optically determine the physical limits on the best possible spatial resolution of the retinal image, while the last two components perform the pixelation of the image, thereby determining the ultimate information content of the image. While a discussion of a final display device would also be appropriate if we were interested in human perception of the images, the operation of CALOSOS is based upon the digital representation of the image obtained by the frame grabber, which is independent of any display device.

A rigorous analysis of retinal image formation for CALOSOS would require complete knowledge of the optical and electronic properties of the total retinal image acquisition system. This depth of information is not available, but through the use of reasonable simplifying assumptions, a useful working analysis of retinal image formation can be made.

4.3 Optical Resolution of Retinal Images

An image can be no better than that allowed by the physical limitations of the optics which form the image. The discussion below regarding optical resolution is needed to evaluate spatial sampling with regard to the Nyquist limit of the Whittaker-Shannon sampling theorem, which requires at least two samples (in each dimension) for each minimum optically resolvable element in an image [100,103]. To account for non-ideal conditions, oversampling (2.3 samples per minimum optically resolvable element [100], for example) is often used if possible.

4.3.1 Image Evaluation

The topic of image evaluation and imaging system design is rather extensive; we synopsize the important points below, without derivation, as it pertains to spatial resolution for CALOSOS. See [39,83,98,104,105] for the formal theoretical foundations. Excellent treatments of practical evaluation and design of imaging systems can be found in [106–108].

In order to evaluate the spatial sampling requirements for pixelation discussed later in this chapter, the minimum optically resolvable element in an image, called a *resel* (see [100]), must be quantified. It is ultimately determined by the point spread function (PSF) of the optical system, which itself is determined by the diffraction of light and any optical aberrations [39,98], as well as the detectability threshold of the system. Two adjacent resels are some distance d apart. Definitions of terms such as numerical aperture (NA) and contrast (C), as well as a theoretical analysis of diffraction-limited and aberrated optics are given in Appendix A (see Section A.1).

CALOSOS Resel

What is an appropriate resolution metric for this design of CALOSOS? From [106, 107,109], it can be seen that for nearly all optical systems the "true" resel is minimum at the image center and is larger (typically by 25%) at the image edges. The aberration-free range for the resel-to-resel distance of $\lambda/2\text{NA} < d < 1.22\lambda/2\text{NA}$ derived in Section A.1 is thus valid only for the center of an image, and any additional aberrations would make the upper limit for d larger still. After examining the effects of various types of aberrations on the MTF given in [106], and the associated consequences for the PSF, an average increase in the upper limit of d across the image of 12.5% due to unavoidable center-to-edge distortions is assumed, and a further increase of 10% in the upper limit of d due to all other aberrations is assumed. From these assumptions, the possible range of a CALOSOS resel is $\lambda/2\text{NA} < d < 1.50\lambda/2\text{NA}$. The mean value of d in this range is $1.25\lambda/2\text{NA}$, which is very close to

the Rayleigh criterion of $1.22\lambda/2\text{NA}$. This may explain why the Rayleigh criterion is by far the most commonly used resolution metric for incoherent imaging, despite the objections of some authors [110,111]. For this reason, and to be consistent with most of the literature, a CALOSOS resel is defined as equivalent to the Rayleigh criterion. That is, an average value for CALOSOS under unknown (but minor) levels of aberration is defined as

$$1 \text{ linear resel} \equiv 1.22 \cdot \frac{\lambda}{2\text{NA}} \tag{4.2}$$

It is often convenient to use the angular form of the resel for ophthalmoscopic optics [96]. Given the reasonable assumption the small angle rule $\sin\theta \approx \theta$ holds, the definition becomes

$$1 \text{ angular resel} \equiv 1.22 \cdot \frac{\lambda}{D} \tag{4.3}$$

for a resel in radians, where D is the diameter of the limiting aperture [37,106].

Having established a resel for the system, the specific analysis of the optical portion of the retinal image acquisition system follows.

4.3.2 The Eye

At the risk of stating the obvious, the retinal image originates at the retina and therefore one cannot disregard the optics of the eye through which this image must pass. Note that this discussion is not concerned with the photoreceptors, or other aspects of the vision system. The goal here is to assess the optical quality of the retinal image obtained by the fundus camera. An often quoted resolution limit for the human eye (based only upon the diffraction-limited point spread function of the pupil) is 1 min of arc (equivalent to 4.9 μm at the posterior pole),[1] but this assumes

[1]Perhaps not coincidentally, the eye actually "sees" with this resolution. The minimum separation of individual photoreceptors in the fovea [31], and the sampling theorem requirement of at least two samples per resel, together yield a physiological resolution limit for the eye of just over 1 min of arc [111], closely matching optical resolution limit due to the diffraction-limited cutoff frequency of the typical 2 mm pupil in daylight.

a 2 mm pupil and illumination of 550 nm [37]. These conditions are *not* true for CALOSOS, so further investigation is needed.

Normal operating conditions of CALOSOS require a dilated pupil (typically 8 mm diameter), with the fundus camera illumination ring focusing on the cornea. Following the Gullstrand principle [24], the retinal image is formed by light emerging only from the inside of the illumination ring. Thus the limiting aperture for the optics of the eye under these conditions is the inner diameter of the illumination ring, which was measured to be 5 mm on the cornea. The illumination wavelength is assumed to be 568 nm (see Section A.4.1). If the eye had only the minor aberrations assumed when Equation 4.3 was defined, the resel would be 1.4×10^{-4} radians, or 0.48 min of arc. However, this is *not* the case. Extensive studies of the human eye by Campbell and Gubisch [112, 113] determined that considerable aberrations exist. In particular, the eye performs best at a pupil diameter of 2.4 mm; at smaller pupil sizes diffraction effects dominate, and at larger pupil sizes aberration effects dominate. The PSF of the eye when aberration dominates is still symmetrical, but differs from the Airy disk, having a Gaussian-shaped central lobe, with exponential tails [113]. At a pupil diameter of 5 mm, the optical performance is similar to a diffraction-limited eye with a 1 mm pupil [113]. Hence for CALOSOS, an estimate of the resel of the eye uses 1 mm instead of 5 mm in Equation 4.3; this yields approximately 6.9×10^{-4} radians, or 2.4 min of arc, keeping in mind the PSF is not an Airy disk. Using Equation 4.1, this equates to a linear resel of 11.6 μm on the posterior retina.

4.3.3 The Fundus Camera Optics

In CALOSOS, the retinal image is obtained by the fundus camera from reflected light gathered as it exits through the center of the illumination ring. Unfortunately, determining the resel of the fundus camera is not straightforward. Manufacturers do not reveal detailed information or specifications about their designs due to industrial

competition. Therefore, some detective work was needed. Partial disassembly of the Olympus Mydriatic Model GRC-W fundus camera used for CALOSOS, and information gleaned from many sources [24, 87, 89, 114] yielded enough information to understand the design.

A highly specialized optical instrument, the fundus camera utilizes an optimized optical design that creates an approximately 2× aerial image using an ophthalmoscopic aspheric objective lens which corrects for the curvature of the retina. This aerial image is then manipulated for various field of views (FOVs) by the secondary optics. There are two important ramifications of this design: first, changing the FOV (and thus the apparent magnification) will *not* change the resel of the fundus camera since the resel was determined by the initial aerial image; and second, the objective lens is the primary determinant of the fundus camera resel.

Examination revealed that the fundus camera objective lens has a 50 mm diameter, but is masked to an effective diameter of 35 mm. Assuming the illumination source is narrow-band and centered at 568 nm (as explained in Section A.4.1), the theoretical fundus camera resel is 2.0×10^{-5} radians. This is the resel as defined by Equation 4.3; it assumes only minor imperfections or aberrations of the fundus camera optics. Since the fundus camera is a high-quality medical instrument, and well-designed lens systems can approach the theoretical diffraction-limited behavior [40], this assumption is justified.

4.3.4 The Eye and Fundus Camera Combination

The resel for which the sampling theorem will be applied is that of the combined optics of the eye and the fundus camera. Since the two are considered separate components, multiplication of their OTFs to obtain a resultant OTF would be the next step. While the OTFs are unknown, enough information is known to estimate the PSFs, which are assumed to be symmetric. From the properties of the Fourier transform, multiplication of the OTFs is equal to convolution of the PSFs.

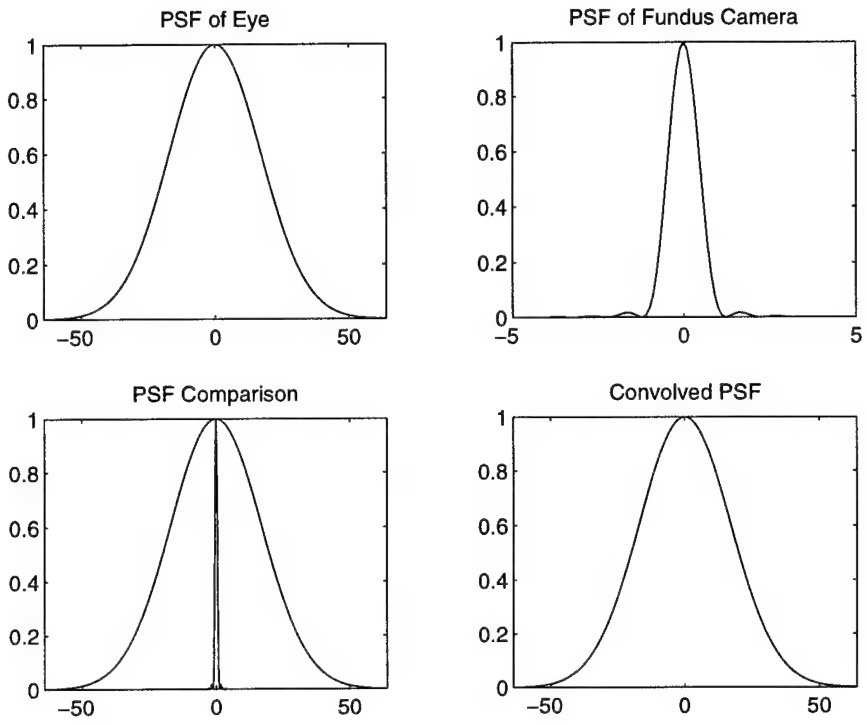

Figure 4.2: Convolution to obtain the combined PSF of the eye and fundus camera.

First note that the estimated Gaussian-shaped PSF of the eye has a resel over 33 times larger than the resel of the Airy disk PSF of the fundus camera. In the top two subplots of Figure 4.2, these two simulated PSFs are shown, using the Airy disk main lobe radius r_0 of the fundus camera as the relative base unit for both x-axes. The exponential tails of the eye PSF were not simulated, since they contribute little to the resel, but the equivalent r_0 point is scaled 33 times larger than the r_0 point for the fundus camera PSF. The lower left subplot of Figure 4.2 shows a comparison on the same axes of the two PSFs; note the fundus camera PSF nearly approximates an impulse function at this scale. The lower right subplot of Figure 4.2 shows the resultant convolution of the two PSFs. As expected, the result is nearly identical to the original PSF of the eye. An evaluation of the residuals between the original eye PSF and the convolved PSF showed a maximum deviation of 3% and an average

deviation of less than 1%. Therefore, assume that the resel determined from the PSF of the eye, 6.9×10^{-4} radians, is effectively the resel to be used with regard to the sampling theorem in the pixelation process.

Preliminary *in vivo* testing of CALOSOS involved rabbits and monkeys. From a purely optical point of view, the results with these nonhuman subjects should be similar. The measured total refractive power of the rabbit eye is 64 diopters compared to 60 diopters for humans, and a similar PSF dominates the combined eye and fundus camera optical system [14]. Primates, more so than rabbits, have nearly identical visual system characteristics compared to humans [115], with similar PSF implications.

4.4 Retinal Image Pixelation

The discussion now shifts from the image-creating optics to the electronics that form the final digitized retinal image. The primary concern here is related to the sampling of the optical image resels.

4.4.1 The CCD Camera

Spatial Sampling

Following the fundus camera, the retinal image is detected by the CCD camera. At this point the individual elements of the CCD array (768H×494V for the Panasonic GP-MF602 camera used for CALOSOS) impose spatial sampling that results in the first level of pixelation and places an absolute physical limit on the highest spatial frequency in the image that can be reconstructed without aliasing [92, 116]. An extended discussion of the CCD imaging array is beyond the scope of this chapter (see [105,116]), but clearly the small rectangular array elements cannot realize ideal Dirac delta functions for sampling the image. The finite size and shape of the individual elements result in a 2-D sinc function aperture effect [116]. Further non-

ideal effects result from the optically shielded spaces between horizontal elements required by the physical construction of the interline transfer type of CCD array used in this camera.[2] However, modern CCD arrays have a very high (0.6–0.75 typical) effective MTF all the way out to the Nyquist frequency [117, 118], which implies an associated narrow effective PSF. Hence for the purposes of this discussion, any non-ideal effects of spatial sampling by the CCD camera can be neglected [100, 102].

In order to compare the spatial sampling frequency to the image resel, the instantaneous field of view (IFOV) of a CCD array element in the x and y directions must be estimated. Measurements taken with the CCD camera attached to the fundus camera revealed that the centered image from the 50 degree fundus camera FOV filled 0.70 of the image frame horizontally and 0.94 of the image frame vertically. Thus the IFOV of a single CCD array element is $50/[(768)(0.70)] = 9.3 \times 10^{-2}$ deg/element horizontally, and $50/[(494)(0.94)] = 0.11$ deg/element vertically. In radians, the IFOV per element is 1.6×10^{-3} H by 1.9×10^{-3} V. Recall the Nyquist limit of the Whittaker-Shannon sampling theorem requires *at least* two samples (in each dimension) for each resel to avoid aliasing.

It follows then that in the optical setup used for CALOSOS, the CCD camera can sample resels no smaller than 3.2×10^{-3} radians horizontally by 3.8×10^{-3} radians vertically in order to avoid the possibility of aliasing. If circularly symmetric resels are assumed, the larger value of 3.8×10^{-3} radians would be the limit for a resel in both the x and y directions. From Equation 4.1, this equates to a minimum feature size of 63.5 μm on the retina which can be unambiguously imaged by the CCD camera.[3] Unfortunately, the retinal image resel determined above was 6.9×10^{-4} radians, which means the image is being potentially *under*sampled by a factor of 5.5!

[2]The interline transfer CCD array is the most commonly used sensor for solid state RS-170 cameras.

[3]Compare this to the fundus camera and eye combination alone, which can distinguish features as small as 11.6 μm on the posterior retina. The fundus camera can also record this feature size on film.

With the existing optics, a CCD camera having a 4224H×2717V sensor array would be needed to sample the retinal image resels at the Nyquist frequency. Even if such a camera were commercially available, it would be quite expensive and likely operate at much less than 30 frames/sec. Webb, one of the designers of the scanning laser ophthalmoscope (SLO) and it's confocal variant the CSLO, admits [100] that this undersampling situation is common in video ophthalmoscopy and microscopy, and offers some suggestions. One approach to consider (assuming the sampling frequency cannot be increased) is to increase the magnification of the image until a resel spans at least two sensor elements. But recall from Section 4.3.3 that the fundus camera design is such that changing the FOV (and thus the magnification) has *no effect* on the resel. An alternative would be to do what Webb calls "spoiling" the image resolution (by a slight defocusing, for example) until the resel grows large enough to span at least two sensor elements.

Yet the retinal images obtained by CALOSOS seem to be free of any obvious aliasing without resorting to "spoiling" the resolution. While the retinal image resel derived above is the smallest feature (and the reciprocal of the highest spatial frequency) that *could* appear in the image, that does not mean it *does* appear in the image. If, in fact, the smallest features that actually do appear in the image were large enough to span two or more CCD sensor elements, then no observable aliasing would occur. Ideally, the retinal image would be sampled with a 4224H×2717V (or larger) sensor array, and a 2-D Fourier transform would be performed to determine the spatial frequencies that actually are present in the image. Unfortunately, that is not an option. However, a 2-D Fourier transform can be performed on a retinal image sampled with a smaller array, with the knowledge that any spatial frequencies f_i present in the image that are higher than half the sampling frequency of f_s will be "folded" back and aliased at the lower frequency of $f_s - f_i$. If there is little or no energy in the image approaching the critical "folding frequency" of $0.5f_s$, then a cautious conclusion that aliasing is *probably* not a problem is warranted.

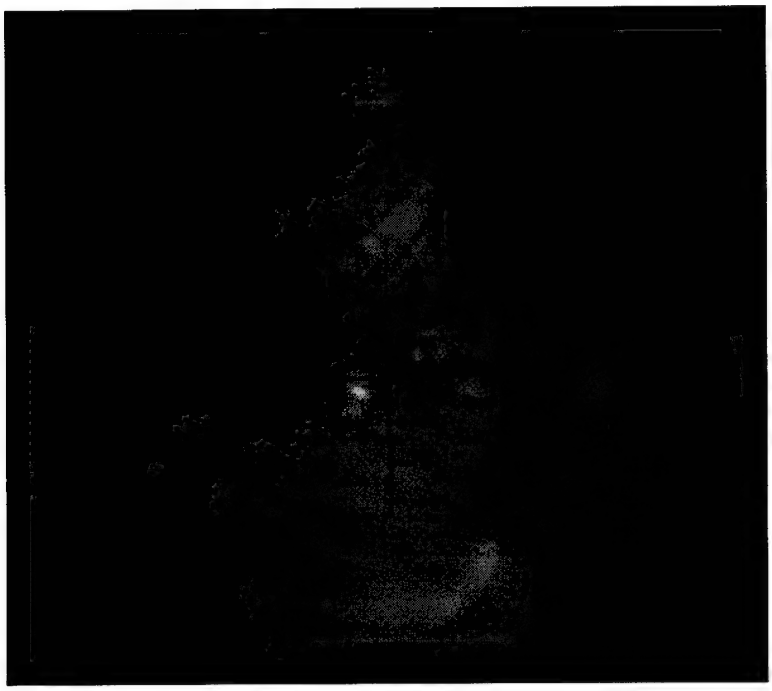

Figure 4.3: A rhesus monkey fundus image from CALOSOS.

In Figure 4.3, a fundus image of a rhesus monkey, taken during a CALOSOS experiment at Brooks AFB, TX, is shown. The illumination was narrowband diffuse light at 568 nm provided by the fundus camera, and the CCD array was 768H×494V. Major blood vessels, part of the optic disk (at the very top of the image), some recently created retinal lesions, and the cross hairs of the fundus camera can be seen. Thus this image contains features typical for CALOSOS. A 2-D Fourier transform of Figure 4.3 is shown in Figure 4.4, with the relatively large DC component eliminated to enhance the detail of the plot. Note that there is very little image energy at spatial frequencies approaching $0.5f_s$ (the highest spatial frequencies present are actually due to the cross hairs of the fundus camera). Recall from Chapter 2 that the blood vessels needed for tracking purposes are typically 150 μm wide or wider. Since it was determined above that the CCD camera used in the system could adequately

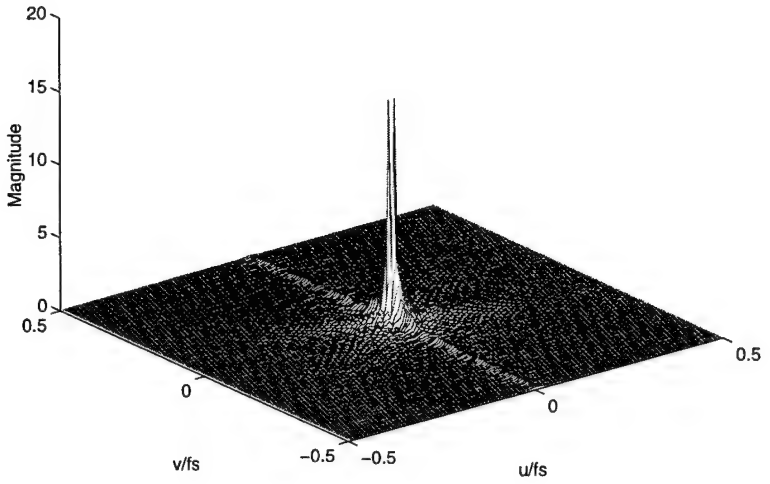

Figure 4.4: A 2-D Fourier transform of Figure 4.3 with the DC component eliminated for enhanced detail.

image a minimum feature size of 63.5 μm on the retina, it follows that the blood vessels will appear in the digitized retinal image with acceptable contrast.

This result, combined with the lack of aliasing apparent in visual inspection of displayed retinal images, leads to the conclusion that the spatial sampling provided by the CCD camera is sufficient for the frequencies actually present (and pertinent to CALOSOS) in the retinal images.

Video Signal Conversion

There are significant implications that are often overlooked when an optical image is converted to video [109]. Since an RS-170 camera is used, the image is converted to a standard analog signal prior to being sent to the computer.[4] This results in a situation where the horizontal resolution is limited by the video signal bandwidth (that is, by the information theory rules governing analog transmission in a continuous

[4]Analysis of the CCIR analog video standard used in Europe follows similarly.

channel [119]) and the vertical resolution is limited by the discrete number of lines used to make a video frame. From these values, the maximum effective resolution to be expected from this video signal can be calculated [109,117,120,121].

Before continuing, one specification given by camera manufacturers requires some explanation [117]. Horizontal resolution of video cameras is often specified in units of "TV lines" (TVL) which implies a black and white bar pattern target.[5] Note that in optics the phrase "line pairs" assumes counting each black and white alternation as a single line pair, but in the television and video industry each black or white line is counted separately. Thus 400 TV lines is the same as 200 line pairs. Also note that the TVL specification is *per picture height*, although this is seldom stated explicitly. For the 4:3 aspect ratio used throughout most of the world, this means that the horizontal resolution specification is for the lines resolved over the central 3/4 of a scan line. With that defined, the horizontal resolution of 570 TVL specified for the Panasonic GP-MF602 camera [122] used for CALOSOS can be interpreted correctly. Since 570 TVL is only for the central 3/4 of the horizontal scan line, close to 760 TVL would be expected for the full scan line (in reality, the resolution at the screen edge is less than at the center, so this is only approximate). It takes *two* TV lines for one complete spatial cycle of a black and white line pair, so the Nyquist frequency of an *ideal* camera, when specified in TV lines, would be equal to the number of CCD sensor elements in the appropriate direction. Given that there are 768 sensor elements horizontally in the Panasonic camera's CCD array, and the resolution (derived from the manufacturer's specification) across the full screen width approaches 760 TV lines, the camera MTF must be very high nearly to the Nyquist frequency, which as stated above is not unusual for modern CCD cameras [117,118].

Continuing with the calculations for horizontal resolution, the effects of converting the image to a time-varying analog voltage must be examined. Given a

[5]The unstated assumption for video cameras is the TVL specification is the point where the CTF response has dropped to 0.10.

bandwidth B, information theory dictates that the maximum number of independent values for a bandlimited analog signal is $2B$ per second [119]. The horizontal scan line period is T_h, but due to the required blanking interval T_b during the horizontal retrace, the active part of the scan line where information is written is $T_h - T_b$. Hence the total number of independent values possible in an entire scan line is

$$R_h = 2B(T_h - T_b) \tag{4.4}$$

The RS-170 standard specifies that one scan line period T_h is 63.556 μs and the blanking interval T_b will take up anywhere from approximately 10.4 μs to 11.5 μs of the scan line period, depending upon the video equipment manufacturer. Using a typical value of $T_b = 10.9$ μs, there remains 52.656 μs in which to pass information via a varying voltage level that cannot have more than $2B$ independent values per second. From Equation 4.4, the video bandwidth required to match the camera specification given above of 570 TV lines (TVL) per picture height is $(570 \cdot 4/3) \,/\, (2 \cdot 52.656 \times 10^{-6}) = 7.2$ MHz.

While the RS-170 standard specifies a video bandwidth of $B = 4.2$ MHz, this is intended for broadcast video which must adhere to strict FCC frequency allocations. When the video signal is locally generated and used, and not allowed to propagate freely in space, a related standard for closed-circuit television, RS-330, may be used. The RS-330 standard has horizontal and vertical timing requirements identical to the RS-170 standard, but relaxes the video bandwidth limitation. Note that while most CCD camera manufacturers specify a particular camera as RS-170, in reality it is likely RS-330 (this seems to be a little known fact, even among camera company representatives). This is because a 4.2 MHz video bandwidth would result in an R_h of 442, which means the camera would have to specified at 332 TVL rather than 570 TVL.

The CCD camera manufacturer was unwilling to reveal the actual video bandwidth of the GP-MF602 camera used for CALOSOS, so it was measured using a spectrum analyzer and found to exceed 7 MHz. Thus the 570 TVL specification

is likely valid. However, in most situations this resolution is wasted since many standard video devices have a channel bandwidth closer to 4.2 MHz.[6] In the design for CALOSOS, the frame grabber input stage limits the horizontal resolution.

Next, the vertical resolution is calculated. The RS-170 (and RS-330) standard specifies $N_f = 525$ scan lines per frame (interlaced 2:1 where each field contains 262.5 lines). However, a number of lines N_v are lost during the vertical retrace time; the RS-170 standard limits this to $N_v = 42$ lines per frame. An additional term called the *Kell factor* (K) was determined by visual trials in the early days of television to account for overlap in scanning spot systems and random spatial phase alignment. Thus the maximum vertical resolution is defined as

$$R_v = (N_f - N_v) \cdot K \tag{4.5}$$

Standard television systems typically use a Kell factor of 0.7, but for digital images and other images not derived from a scanning spot device a Kell factor of 1.0 is often recommended [109]. Following this recommendation for CALOSOS yields $R_v = 483$.

It can be seen from above that the maximum resolution expected from the CCD camera is 760H×483V. If more resolution is needed for a particular application, a higher cost alternative would be to select a different video format. Commonly available alternatives[7] include: Y-C (S-video), RGB, or digital (RS-422).

4.4.2 The Frame Grabber

The frame grabber in the computer imposes the next level of pixelation according to the input A/D converter and the dimensions of the frame buffer memory space. As far as image computations are concerned, the frame grabber is the final pixelation stage. When viewing an image, the dimensions of the display device add another pixelation stage, as does the human visual system itself; it is beyond the scope of this discussion to address these issues (see [31, 100]).

[6] Typical consumer TV sets seldom exceed 300H×338V resolution for this reason [120].

[7] The MuTech MV-1000 frame grabber used in CALOSOS has options to accept all of these video formats.

The MuTech MV-1000 frame grabber used for this research converts the RS-170 video signal into a standard size discrete array having the dimensions 640H×480V. These dimensions match the 4:3 aspect ratio of the RS-170 format, and therefore result in apparently square pixels. However, caution must be exercised when using the 640H×480V specification. From a signal processing point of view [103,123,124], the vertical resolution of 480 is a reliable number because the CCD camera started with 494 vertical samples, and the video converter then resampled this down to 483 before the frame grabber resampled again down to 480 vertical pixels. Since the numbers 494, 483, and 480 are nearly equal and monotonically decreasing, there is reasonable confidence that each of the 480 vertical pixels in the frame buffer represents a unique sample of the original image. The horizontal resolution of 640, however, is *not* as reliable a number.

While the CCD camera starts with 768 horizontal samples, the bandwidth limits of the camera video converter effectively reduces this to no more than 760 individual voltage variations in one scan line. The signal is then sent to the frame grabber, where the input bandlimiting lowpass filter has a cutoff of 5.5 MHz. This filter is required to ensure the Nyquist criterion is not violated at the frame grabber's analog-to-digital converter (ADC) stage. That is, in order to sample 640 pixels in a 52.656 μs active scan line, the sampling frequency f_s must be 12.15 MHz; bandlimiting the video signal to 5.5 MHz ensures there will be little or no signal energy at the foldover frequency of $0.5f_s$. Applying Equation 4.4 to a bandwidth of 5.5 MHz, this effectively limits the horizontal resolution to no more than 578 individual voltage variations in one scan line before the frame grabber resamples at 640 horizontal pixels. Just as there is a law of the conservation of energy, there is also a law of the conservation of information: one cannot create more output information than what is available as input. Thus each of the 640 horizontal pixels in the frame buffer *do not* represent a unique sample of the original image. This situation is governed by the rules of multirate digital signal processing for sampling rate conversion by

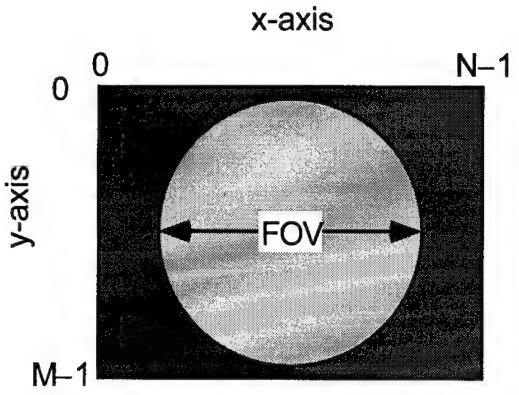

Figure 4.5: Representation of a circular image on a 4:3 rectangular video frame buffer.

an arbitrary factor [125]. The complexities of this subject are beyond the scope of this discussion, but the end result is that there can only be reasonable confidence of having the equivalent of 578 unique horizontal samples even though there are 640 horizontal pixels. This limits the *effective* horizontal spatial resolution of the retinal image.

4.5 Effective Spatial Resolution of the Retinal Image

From the analysis above, the actual spatial dimensions of the image pixels can now be determined. This is dependent upon the posterior nodal distance of the eye (see Figure 4.1 and Equation 4.1), the field of view (FOV) of the fundus camera, and the $N \times M$ dimensions of the image in the frame buffer. Due to the optics of the fundus camera, the actual retinal image is circular, while the frame buffer is rectangular with a 4:3 aspect ratio (see Figure 4.5). The relationship for either the vertical or horizontal pixel dimension is given as

$$\frac{\text{FOV (in deg)}}{P} \cdot 291.5\ \mu\text{m/deg} = \text{distance/pixel} \tag{4.6}$$

where P is the number of pixels in a vertical or horizontal diameter of the circular retinal image. Since P varies according to camera and mount, the easiest way to determine which frame buffer pixels are actually used for the retinal image is to snap a test frame and determine the boundaries of the image. Equation 4.6 can then be used to determine the spatial dimensions of the pixels. For CALOSOS, with a 50° FOV setting on the Olympus Mydriatic Model GRC-W fundus camera, and the Panasonic GP-MF602 CCD camera, the number of pixels was found to be 450 for both the vertical and horizontal diameters (due to the square pixels). Using Equation 4.6, the vertical and horizontal dimensions of the square pixels equate to approximately 32 μm on the retina. This number is a good value for general calculations regarding the retinal images. However, if more exactness is needed, recall that the *effective* horizontal resolution is less than 640 pixels, due to the limitations of the video bandwidth. Consider that the 450 frame buffer pixels measured for a horizontal diameter represented $450/640 = 0.7$ of the full line width. From Equation 4.4, only 578 unique values exist on an entire horizontal line, not 640. Then the *effective* number of pixels in a horizontal diameter of a 50° FOV fundus image would be $(578)(0.7) = 405$. Therefore the *effective* horizontal spatial distance on the retina between independent samples of the image is found by setting $P = 405$ in Equation 4.6, which yields approximately 36 μm. The vertical spatial distance remains at 32 μ m on the retina since it was based upon the actual number of active scan lines used in the video signal. The implications of the *effective* horizontal resolution primarily concern the laser pointing accuracy of the system.

Recall from Table 3.1 that CALOSOS requires 100 μm of pointing accuracy. To achieve this, one condition is that the image resolution provides at least two samples or pixels per 100 μm spatial distance in the horizontal and vertical directions [98, 100]. With the worst case analysis above yielding 36 μm horizontally and 32 μm vertically for the distance between independent samples, the 100 μm of pointing accuracy can be achieved. The theoretical pointing accuracy limit of the system

would be 72 μm horizontally and 64 μm vertically. This does not account for mechanical effects of the beam steering galvanometers (see Chapter 6). Note that for general image calculations where the true *effective* spatial sampling is not a critical factor, square pixels of 32 μm per side will be assumed.

If the accuracy limit of the system must be improved, the effective spatial resolution must be improved. The primary contributor to the spatial resolution limit is the CCD camera. It was previously stated that more resolution can be obtained for a given CCD array size by choosing a higher cost alternative camera which utilizes a different video format, such as Y-C (S-video), RGB, or digital (RS-422). Another method is to use a camera with a larger CCD array (having more pixels in each dimension). The fundus camera, while not as major a factor in spatial resolution as the CCD camera, should not be overlooked. As discussed in Section 4.3.3, the design of the Olympus Mydriatic Model GRC-W fundus camera makes the resolution invariant to changes in FOV, so a different model fundus camera might be required.

It is also important to note that a particular frame grabber pixel does not correspond exactly to a particular CCD camera pixel. If extremely precise location measurements need to be made of a digitized image, the recommended procedure [126] is to synchronize the camera with the frame grabber pixel clock (i.e. the sampling clock); a digital camera would yield the best results. CALOSOS does not require this level of precision to treat diabetic retinopathy and/or retinal breaks, and so the added complexity and cost are avoided. If CALOSOS were to treat macular degeneration, however, a synchronized digital camera (using a CCD sensor larger than 768H$\times$494V) would be recommended.

4.6 Retinal Image Quantization

Having determined the effective spatial resolution of the retinal images as acquired by this system, another aspect remains unaddressed. The intensity resolution of the image must also be analyzed.

4.6.1 Intensity Partitioning

Just as the optical image determined the size of a resel which was subsequently partitioned into pixels, the image/camera combination determines a "just detectable difference" (JDD) in intensity which is subsequently partitioned (or quantized) into gray levels by the frame grabber. The JDD for photodetectors is discussed in Appendix A (see Section A.2). In CALOSOS, the overall scene illumination, or light intensity, of the retinal image is controlled by adjusting the fundus camera illumination lamp setting. The resulting JDD and the overall dynamic range determine the number of gray levels needed to represent the image, and the number of gray levels determines the best possible quantization SNR.

4.6.2 Gray Levels

From the JDD discussion in Section A.2, it appears that given the dominant noise sources and the cost/performance trade-offs, a uniform-step quantizer is preferred for CALOSOS. For RS-170 video signals using standard CCD cameras and adequately illuminated scenes, an 8-bit (256 step) uniform quantizer is usually recommended [100, 109, 117].

4.6.3 Quantization SNR

As a check on this recommendation, the SNR due to quantization should equal or exceed the SNR of the CCD camera, which is specified as 56 dB [122]. For a uniform-step quantizer, the signal to quantizing noise ratio (SNR_Q) for converting a complex, arbitrary analog signal to a digital PCM signal is formally derived in [103], and the particular form of this for video signals given in [117] is shown below

$$\text{SNR}_Q = 6.02n + 10.8 + 10\log_{10}\frac{F_s}{2F_{v\ \max}} \tag{4.7}$$

where n is the number of bits, F_s is the sampling frequency, and $F_{v\ \max}$ is the effective video bandwidth. From [64], the values for an RS-170 video signal are

F_s = 12.15 MHz and $F_{v\ \max}$ = 5.5 MHz (determined by the video bandlimiting filter). For $n = 8$, $\text{SNR}_Q = 59.4$ dB, which exceeds the SNR of the camera. If $n = 7$, $\text{SNR}_Q = 53.4$ dB, less than the camera SNR. Thus the 8-bit uniform quantizer is an appropriate choice for CALOSOS.

4.7 Retinal Image Enhancement

The quality of the retinal image obtained by CALOSOS via the fundus camera and CCD camera may be degraded by several factors. The patient may have opacities in the eye due to various disorders such as cataracts [127]. The patient may have a low tolerance for fundus camera illumination levels, requiring the clinician to use suboptimal lighting. Clouding of the subject's cornea, while not usually a problem with human patients, is one of the most common problems plaguing extended *in vivo* experiments with laboratory animals. This is a result of drying of the corneal epithelium tissue since the normal irrigation with tears by blinking is suspended during the procedure. In any case, the image may need to be enhanced for the best performance of CALOSOS.

There are many ways to enhance an image [90–95], but most methods require significant computation by the CPU. When assessing enhancement methods for CALOSOS, the choice of appropriate techniques is driven by the real-time imaging requirement. Any time penalty imposed by the enhancement technique would reduce the tracking speed of the system; hence this discussion concentrates on those techniques which do not require the CPU.

4.7.1 Signal-to-Noise Ratio

Image enhancement is a large and active field of image processing. A large portion of the work has concentrated on noise removal [90, 91, 93, 94, 128–130], but it can be shown that noise contamination of the retinal images during acquisition is not a significant problem for CALOSOS. The specified signal-to-noise ratio (SNR) of the

CCD camera used (Panasonic GP-MF602) is 56 dB [122]; the specified SNR of the video circuitry in the frame grabber used (MuTech MV-1000) is 54 dB [64], and the SNR due to the quantization stage in the frame grabber was found from Equation 4.7 to be 59.4 dB. When cascading stages, the SNRs combine by the formula [131]:

$$\mathrm{SNR} = \frac{1}{\frac{1}{\mathrm{SNR}_1} + \frac{1}{\mathrm{SNR}_2} + \frac{1}{\mathrm{SNR}_3} + \cdots} \tag{4.8}$$

where the SNR values are in ratio form rather than decibel form. Using Equation 4.8, the combined SNR for the CCD camera, the framer grabber video circuitry, and the frame grabber analog-to-digital converter equals 51 dB. This is the theoretical SNR based only upon the specifications of the equipment used, and should be considered an upper bound. The actual SNR must be measured.

A straightforward method of measuring the noise in a digital imaging system is to determine the standard deviation σ, in gray levels, of a uniformly illuminated image [90, 109]. Then $\log_2 \sigma$ is the number of least significant bits that should be considered noise in the image. For example, if $\sigma = 4$, then $\log_2 4 = 2$ and we should consider the least significant 2 bits of the digital image to be noise. To convert this to a SNR value, an equation from Bendat and Piersol [132] for digitized data is shown below,

$$\mathrm{SNR} = 20 \log_{10} \left(\frac{2^n}{\sigma} \right) \tag{4.9}$$

where n is the number of bits per image pixel. For CALOSOS, images of uniform gray (using a standard Kodak photographic gray card and diffuse light) were taken with various levels of illumination and also with the lens port closed. The standard deviation of the 8-bit pixels was found to be $\sigma = 1.2$ gray levels; only the least significant bit is therefore noise. From Equation 4.9, $\sigma = 1.2$ and $n = 8$ yields an SNR of $\simeq$ 47 dB; this is the actual measured SNR of the entire image acquisition system for CALOSOS. As a point of comparison with human viewing of standard video, empirical tests show that an SNR of 36 dB appears grainy to a human observer, while an SNR of 42 dB looks very clean [109]. An SNR of 45 dB or better is

considered excellent for an RS-170 signal [117]. Thus the measured value of 47 dB is more than sufficient, and noise contamination is not a problem.

4.7.2 Tracking SNR

However, this classically defined SNR is of limited utility for CALOSOS. In the most general sense anything that isn't *signal* must be *noise*, and it would be helpful to have a more suitable figure of merit. One can establish a "customized" SNR if the signal of interest can be defined and if both the signal and noise can be quantified. In Chapter 5, a primary definition of "signal" for CALOSOS is the pattern of major retinal blood vessels used for the tracking algorithm; everything else in the image is therefore "noise." Due to hemoglobin absorption in the visible wavelengths, retinal blood vessels appear dark (i.e. toward the lower end of the gray scale) against a lighter fundus background [18]. A reasonable method to define the SNR in this case would be based upon the contrast between the blood vessels and the background of the fundus. If the average gray level of the fundus background is g_f, and the average gray level of the major blood vessels is g_{bv}, then the contrast would be $C_{bv} = (g_f - g_{bv})/(g_f + g_{bv})$. Mathematically, the contrast can range from 1 to -1 and is invariant to changes in illumination. Realistically, however, the actual contrast C_{bv} will range from 1 to 0 since the blood vessels will never be brighter than the background, as discussed above. This fact facilitates its use with logarithms. Furthermore, it is convenient to scale C_{bv} by the measured SNR of the image acquisition system determined from Equation 4.9. Then a "tracking SNR" called SNR_T can be defined such that

$$\mathrm{SNR}_T = 20 \log_{10} \left[\left(\frac{g_f - g_{bv}}{g_f + g_{bv}} \right) \left(\frac{2^n}{\sigma} \right) \right] \tag{4.10}$$

where n and σ are the same as used in Equation 4.9. The SNR_T allows a quantitative measure of the retinal image quality with regard to the tracking algorithm discussed in Chapter 5. See Figure 4.6. The best possible SNR_T is 47 dB, where $g_{bv} = 0$ and $g_f = 255$, which is the intrinsic measured SNR of the image acquisition system.

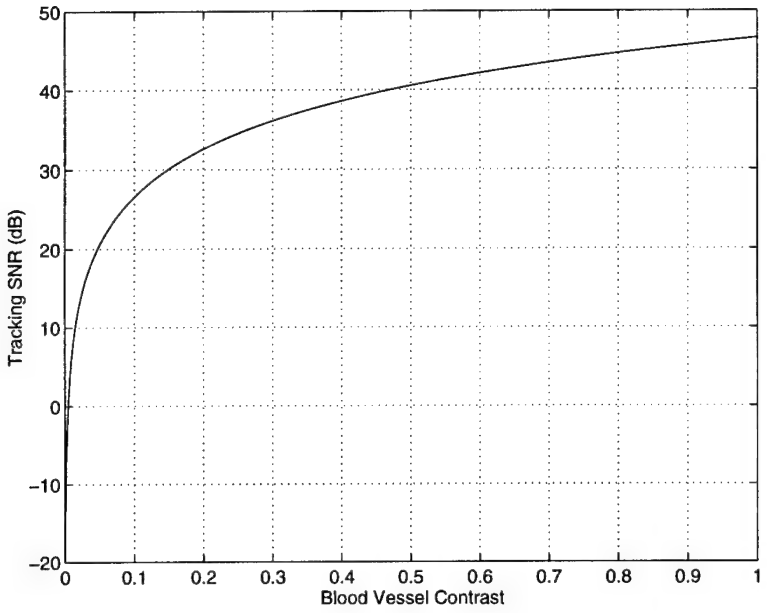

Figure 4.6: Tracking signal-to-noise ratio SNR_T versus blood vessel contrast.

As the blood vessels approach the same gray scale as the background (and would therefore be indistinguishable, with a contrast of zero), then SNR_T approaches the asymptotic value of $-\infty$ dB; this is the real-world worst case. As an example, if the major blood vessels had an average gray level of 60 and the fundus background had an average gray level of 120, then $\mathrm{SNR}_T = 37$ dB. Note that if the illumination is changed such that both gray levels are scaled equally, the SNR_T is unchanged, which (as noted in Chapter 5) matches the behavior of the digital tracking algorithm. By the definition of Equation 4.10, SNR_T is imaginary if the blood vessels are brighter than the background, which is appropriate.

4.7.3 Methods to Improve the Tracking SNR

Barrett identified two methods for improving the contrast of blood vessels in a fundus image without using the CPU [15]. He found that using narrowband illumination

of 568 nm rather than the typical broadband illumination made the blood vessels appear darker against a light fundus background. He further found that using a contrast stretching technique by reprogramming the frame grabber look-up table (LUT) could yield an improved image in some cases. Both methods are reviewed in Appendix A (see Sections A.4.1 and A.4.2), and are used in the design of CALOSOS.

While the illumination wavelength and LUT modification comprise the primary means to enhance the retinal image in real time, two other options were incorporated into the system design that also do not impose any time penalty. The frame grabber settings for high frequency boost and overall gain can be modified directly via the CALOSOS computer-user interface.

High Frequency Boost

The MV-1000 frame grabber's video bandlimiting filter is normally set for zero boost, which gives the flattest frequency response [64]. However, this can be adjusted to give up to 6 dB of high frequency boost, in which the gain of the filter is altered to peak near the original cutoff frequency. By increasing the high frequency boost of the filter, the actual -3 dB cutoff frequency is increased. While this can yield sharper details in the image (effectively increasing resolution), it also results in greater noise and the possibility of aliasing. At the maximum boost of 6 dB, gain at the original cutoff frequency increases from -3 dB to +3 dB, and the new -3 dB point is 2.33 times the original. This option should therefore be used with care, since at maximum boost the cutoff frequency for incoming RS-170 video signal changes from 5.5 MHz to 12.82 MHz. With a sampling frequency of 12.15 MHz (dictated by the pixel clock), this clearly violates the Nyquist criterion. The option is included to give the operator some flexibility in difficult imaging situations.

Overall Video Gain

The MV-1000 frame grabber's video amplifier follows the bandlimiting filter (and the clamping circuit for DC restoration), and is normally set to a gain of +2. For most video signals, this results in the optimal dynamic range for the 8-bit ADC. However, the CALOSOS computer-user interface allows the operator to modify the normal gain by a multiple from 0.5–2.0. This results in an actual video amplifier gain from 1–4. Because the normal gain level usually results in optimal video channel performance and minimum quantizer noise, this option should be used with care. As with the high frequency boost option, it is included to give the operator some flexibility in difficult imaging situations.

4.8 Computer Detection of Critical Vision Anatomy

While Barrett developed a method for detecting and avoiding certain critical vision structures in the eye [15], his implementation was exceedingly slow. During collaborative experiments with Dr. Barrett, it was agreed that as part of this research the function must be redesigned for faster execution.

4.8.1 Safety Considerations

Automated detection of critical vision anatomy is a specialized application of image processing for CALOSOS. It is used to help ensure that retinal lesions are not placed in locations that may cause harm to the patient. For example, the fovea must be avoided or the patient's visual acuity could be severely degraded. When operating near the posterior pole of the eye, the region defined by the convex boundary just containing the macula and optic disk is typically avoided for safety reasons [45]. Major blood vessels must also be avoided, or hemorrhaging could result. The small regions used by the tracking algorithm templates (see Chapter 5) also cannot be used as lesion sites, else digital tracking would suffer. For a more detailed discussion

of lesion placement, see Chapter 7.

Avoiding the region around the macula and optic disk is easily accomplished when the ophthalmologist designates (with the computer mouse) the area for automatic lesion pattern generation—the region containing the macula and optic disk is simply not included in the designated area. If for some reason lesion sites seem too close to this critical region, the clinician just uses the mouse cursor to erase those few lesion sites before photocoagulation begins. Since this is such a vital region, and because at most only a few lesion sites would have to be erased, the ophthalmologist's judgement is preferred rather than any attempt to automate the task [45].

Avoiding major blood vessels is quite different. The wide-spread pattern of blood vessels is random, and for a large lesion pattern there could be a great number of lesion sites that would be too close to a blood vessel. Visually inspecting each blood vessel path and manually erasing all the dangerous lesion sites would be time consuming, tedious, and prone to human error. As such, this task is an ideal candidate for automation.

4.8.2 A New Technique

In Barrett's implementation, automatic detection of retinal blood vessels (and supervised detection of the optic disk and macular region) was accomplished with a lengthy procedure consisting of 12 image processing steps, each performed on the entire image [15]. The overall procedure was based upon edge detection of the blood vessels, and the steps included median filtering, enhancing both horizontal and vertical edges, bar noise filtering, trimming the false edge at the limit of the FOV, local pixel connectivity scanning, and supervised spot noise removal. Accurate edge detection of a complex image is computationally expensive [133–135]. A more efficient method was developed by the author.

After considerable experimentation, a high-speed single pass algorithm was de-

vised which detects major blood vessels and automatically erases lesion sites which are too close. It also erases any lesion site close to a tracking template. Rather than processing the entire retinal image, the algorithm designates a small search area around each lesion site. In Chapter 5 it will be shown that the tracking templates have a maximum response when centered on a blood vessel; we use a variation on this technique to find if the response near the lesion site exceeds a threshold value. If it does, a blood vessel is assumed to be there and that lesion site is erased. The operator can adjust both the threshold value and the search size area to adjust for individual conditions, but the empirically determined default values (threshold: 80% of the best known 1-D tracking template response, search area radius: 4 pixels $\simeq 128$ μm) were found to perform well on a wide variety of simulated and real retinal images. See Figure 4.7 for a simulated retinal image with a large lesion pattern defined and no blood vessel masking, and Figure 4.8 for the same image with the result of automated blood vessel detection using the new high speed algorithm. The new technique also defines rectangular areas around each 1-D template member of the 2-D tracking template (see Chapter 5) and erases any lesion site which intersects with these areas.

A comparison between Barrett's method and the new technique using algorithm analysis indicates a speed up of over three orders of magnitude. Qualitative comparisons support this estimate. The new algorithm is also less susceptible to image intensity variations and noise.

One ramification of any procedure which removes lesion sites that are too close to blood vessels is a randomization of the previously regular lesion pattern, since the blood vessel distribution itself is random. This has implications for optimizing the laser pointing by minimizing galvanometer movements, a topic which will be discussed in Chapter 6.

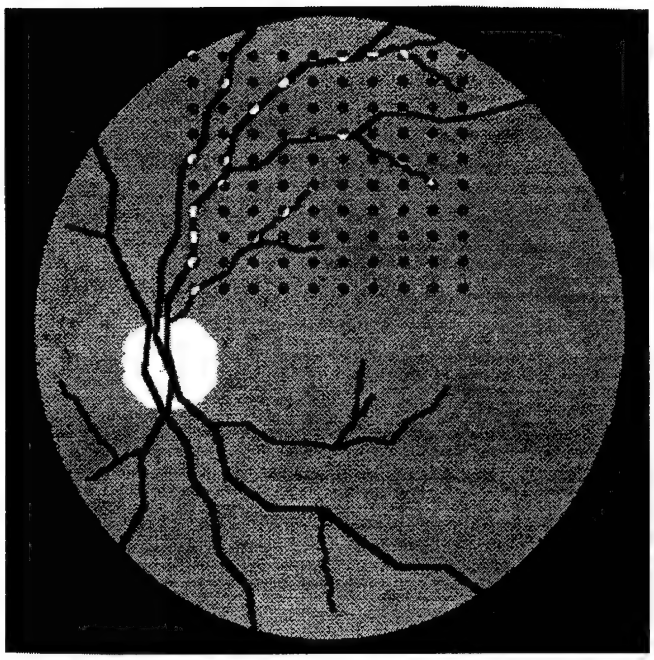

Figure 4.7: A simulated retinal image with a 10×10 lesion pattern and no blood vessel masking.

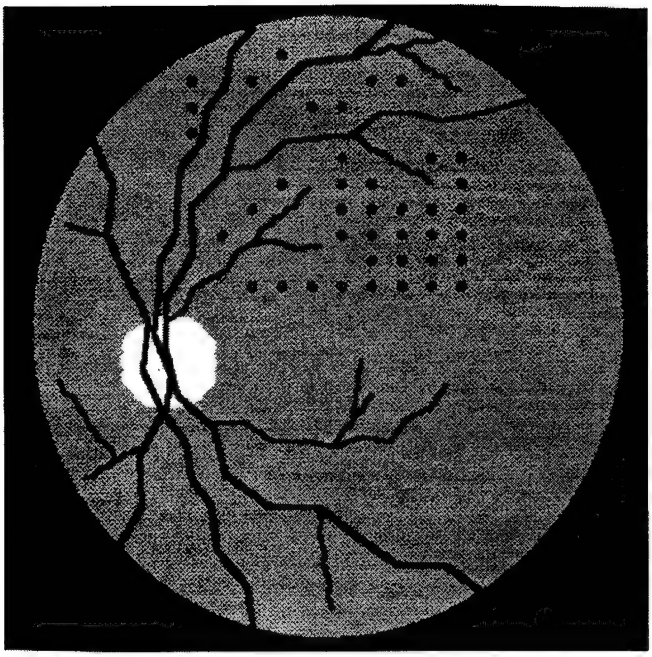

Figure 4.8: The same image as Figure 4.7 , with automated detection of blood vessels.

Chapter 5

Tracking the Moving Retina

This chapter concentrates on improvements made to Barrett's digital tracking technique, introduces the concept of analog tracking using a dithered tracking beam, and discusses the integration efforts to make the two systems work together in a hybrid design. A review of image registration and tracking techniques using digital images is given in Appendix A (see Section A.5).

5.1 The Need to Track the Retina

In Chapter 2 it was pointed out that the eye is always moving (even when fixated), and in Chapter 3 the requirement was discussed for CALOSOS to track the retina as it moves and to compensate for that movement. Many methods have been devised for eye tracking, but most are designed to monitor the anterior eye and cornea. Recall that the eye is a liquid-filled oblate spheroid of soft tissue; during an eye motion the movement of the cornea may not match exactly with the movement of the retina. In order to place retinal lesions with acceptable accuracy for laser surgery, a system must directly track the retina and compensate for any movement [136].

A few methods of tracking the retina directly have been devised in recent years [50, 53, 136, 137]. For CALOSOS, however, the choice of tracking methods is quite limited. When one accounts for the need to integrate (at the lowest reasonable cost)

a photocoagulator laser control and pointing subsystem, an automatic lesion pattern generation subsystem, a lesion growth monitoring and control subsystem, *and* the retinal tracking subsystem of choice, with response times of 5 ms—and have it all work together seamlessly—then the design alternatives narrow significantly.

Before discussing improvements made to Barrett's digital tracking implementation, the concept of retinal search area calculations must be established.

5.2 Search Area Calculations for the Retina

In order to maximize the speed of the retinal tracking algorithm, the area of search for the best 2-D template response must be limited. The required minimum search area is determined by the spatial resolution of the image pixels, the maximum anticipated eye velocity, and the image frame rate. For a simple one dimensional example, assume the pixel spatial resolution is 32 μm, the maximum eye velocity is 50 degrees/second, and the frame rate is 30 frames/second. Recall from Equation 4.1 that one degree is equivalent to approximately 291.5 μm on the human retina. Then for this example the tracking algorithm must search in each direction S pixels defined as:

$$S = \frac{(50 \text{ deg/sec})(291.5 \ \mu\text{m/deg})}{(30 \text{ fps})(32 \ \mu\text{m/pixel})} = 15.18 \simeq 15 \text{ pixels} \tag{5.1}$$

Since S is the distance the eye can travel in any direction, the search window would have to be at least $2S = 30$ pixels across. For a 2-D image the search window[1] is $2S \times 2S$, thus the required computation time varies with $4S^2$. Given Equation 5.1, if one can reduce the maximum velocity of the eye, or increase the frame rate and/or the pixel dimensions, then one can dramatically reduce the processing time of the tracking algorithm. This neglects the engineering trade-offs associated with higher frame rates or larger pixels.

[1]While the use of a square search window results in some "extra" pixels in each corner, the greater computational complexity of using a circular search window more than offsets its lower pixel total.

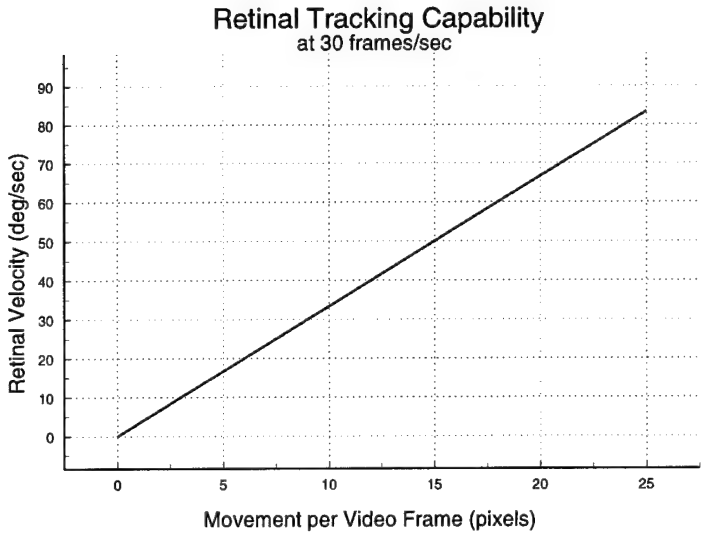

Figure 5.1: Maximum retinal tracking capability for a given image search distance.

From Equation 5.1, a plot of the minimum required S versus the maximum anticipated retinal velocity can be generated. Recall from Chapter 4 that the system design results in square pixels of 32 μm per side (on the retina), and a camera frame rate of 30 frames/second. This relationship of the required search distance (how far the eye would have moved) in one direction, compared to the retinal velocity, is shown in Figure 5.1. If the direction of movement is at some angle not parallel to either the x or y axis, then S would be slightly less according to the associated trigonometry; Figure 5.1 thus represents a worst case.

A useful insight provided by Figure 5.1 is that for a given execution speed, an algorithm will be able to search only some maximum window size of $2S \times 2S$. Therefore, at that value of S, Figure 5.1 yields the maximum velocity at which the algorithm can track. In the case of the design developed for CALOSOS, the execution time limit is dictated by the ability of the algorithm to "keep up" with the 30 frame/second rate of the CCD camera. This will be explored further below.

The 30 frame/second frame rate inherent in Figure 5.1 is achieved by the new design described in Chapter 3. Recall that Barrett's design was I/O limited to 7 frames/second. From Equation 5.1, that implies an S of 4.29 times that indicated in Figure 5.1, and a total search area 73.5 times larger (from the $4S^2$ relationship) for a given retinal velocity. Thus the achievement of a sustained 30 frame/second rate for CALOSOS results in a major improvement in system performance.

While the design improvements described in Chapter 3 for CALOSOS eliminated the video I/O bottleneck, Barrett's digital tracking algorithm itself also must be optimized for best performance.

5.3 Improvements to Barrett's Retinal Tracking Implementation

Barrett devised a highly efficient template method for tracking the retina [15], but his software implementation of the algorithm needed greater optimization. An increase in speed by a factor of almost 2 resulted naturally due to the change from 16-bit DOS to the 32-bit extended DOS environment, but other changes were required for the algorithm to be able to search a sufficiently large window while keeping up with the 30 frame/second CCD camera. A review of Barrett's implementation is given in Appendix A (see Section A.6).

5.3.1 Overall Improvements

From a general perspective, Barrett used nested function calls in C for various parts of the algorithm. This resulted in overhead associated with pushing the current CPU registers on the stack, passing any parameters from memory to the stack and then from the stack to the CPU, and then popping CPU register data from the stack to the CPU when the function call returned to the previous level. For CALOSOS, this was changed to in-line C code and macros, which eliminates the overhead just

described. Additionally, the complier optimizations were set such that if a function call was needed, the function parameters would be passed directly to the internal CPU registers rather than the stack, an option which also significantly reduces overhead.

5.3.2 Improvements to Template Response Calculations

Barrett determined the template response directly as defined by Equation A.16, using CPU-intensive floating point calculations throughout, converted the result to an integer, and normalized to a 0–100 range. For CALOSOS, this was totally reimplemented using integer calculations only, which are performed much faster by the CPU. Observe that the denominator of Equation A.16 cannot exceed 1020 since each pixel has a maximum value of 255. Taking advantage of this, Barrett's template response given in Equation A.16 was modified to be

$$R = \frac{(P1 - P2 - P3 + P4) \cdot 1020}{P1 + P2 + P3 + P4} \tag{5.2}$$

which, by using integer math, executes much faster. Since Equation 5.2 must be executed six times (for each of the six 1-D templates) during each pass through the image search loop, the affect on algorithm execution speed is significant. Measurements showed this change alone resulted in a 20% speed improvement. Another advantage of the integer technique used here is a finer granularity of the tracking response. Barrett's technique has a granularity of 100 steps; the new system has a granularity of 1020 steps over the same range of pixel values.

5.3.3 Improvements to Template Response Figure of Merit

Further improvement to Barrett's technique was made by modifying the figure of merit used to ascertain the "best" template response and its associated location on the image. To reduce the possibility of false positives, the individual and overall template responses for the current image must be compared to the expected responses

from the reference image. Some uncertainty in template response is to be expected due to photometric variations at different positions of the template since the fundus illumination is not completely uniform across the FOV. Barrett used the ratio technique to compare the expected response to the actual response of the current image: a floating point divide obtained the ratio of (current response)/(expected response). If the ratio was significantly larger or smaller than 1.0, then that template location was considered to represent a potential false positive and rejected. For this new design, the figure of merit was changed to the absolute value of the difference (AVD).[2] That is,

$$\text{AVD} = |(\text{current response}) - (\text{expected response})| \tag{5.3}$$

where the template location was considered to represent a potential false positive and rejected if the AVD exceeded a threshold value (30% of the expected response). Thus an integer subtraction and absolute value call was used rather than a floating point divide. Since both the current response and the expected response are integer values, the integer version of the C math function "abs(x)" could be used rather than the much slower floating point version "fabs(x)." Equation 5.3 is calculated seven times (once for each of the six 1-D templates and once for the total response) during each pass through the image search loop; the measured speed improvement of the search loop was 17%.

5.3.4 Improvements to Tracking Relock Technique

Barrett's tracking implementation wisely used a small S for the normal search window since it could be searched quickly, but if a loss of lock condition was detected it closed the laser shutter and jumped to a large 100×100 pixel search window and attempted to find[3] the "lost" template location. If the template was "found," the

[2]Barrett independently arrived at a similar technique at about the same time as the author, albeit still using floating point math.

[3]Using one horizontal and one vertical template.

program tried to switch back to the small search window again. If the small window then achieved lock, the laser shutter was reopened. The problem with this approach is that considerable time elapses while scanning the large search window, such that excessive eye movement (greater than the size of the small search window) can occur before the program switches back to the small search window. The result is that for even moderate eye movement, the small window may not be able to regain tracking lock, with the potential for oscillating between small and large windows ad infinitum. For example, during experiments in collaboration with Dr. Barrett at Armstrong Laboratory (Brooks AFB, TX) when Barrett's software was used for tracking, it was impossible to relock on a slowly moving rhesus monkey retina.[4]

Despite the considerable speedup in the tracking algorithm realized by the changes discussed above, the possibility of such relock oscillation would still exist (albeit at higher retinal velocities) if a simple two-stage relock method were used. To maximize the chances of relock, a multistage "zoom out, zoom in" algorithm was designed and implemented. That is, if a loss of lock condition is detected, the laser shutter is closed and the normally small search window is enlarged by a moderate amount, which can be quickly searched. If the template is "found" the program returns to the small search window, checks for a template lock and, if found again, reopens the laser shutter and continues. If the template was *not* "found" when using the moderate search window, a somewhat larger window is used. The search window is thus incrementally increased in size until the template is "found" or until a certain number of unsuccessful attempts causes the tracking operation to abort. Once "found," the window size is incrementally decreased in size (with the searching getting faster and faster with each smaller window size), checking at each window size for the presence of the template, until finally normal operation can resume with the small search window. A flowchart of how this relock technique is used with the improved digital tracking algorithm is shown in Figure 5.2.

[4]The difficulty in locking was made worse by a cloudy cornea and a subtle software bug discovered after the experiments.

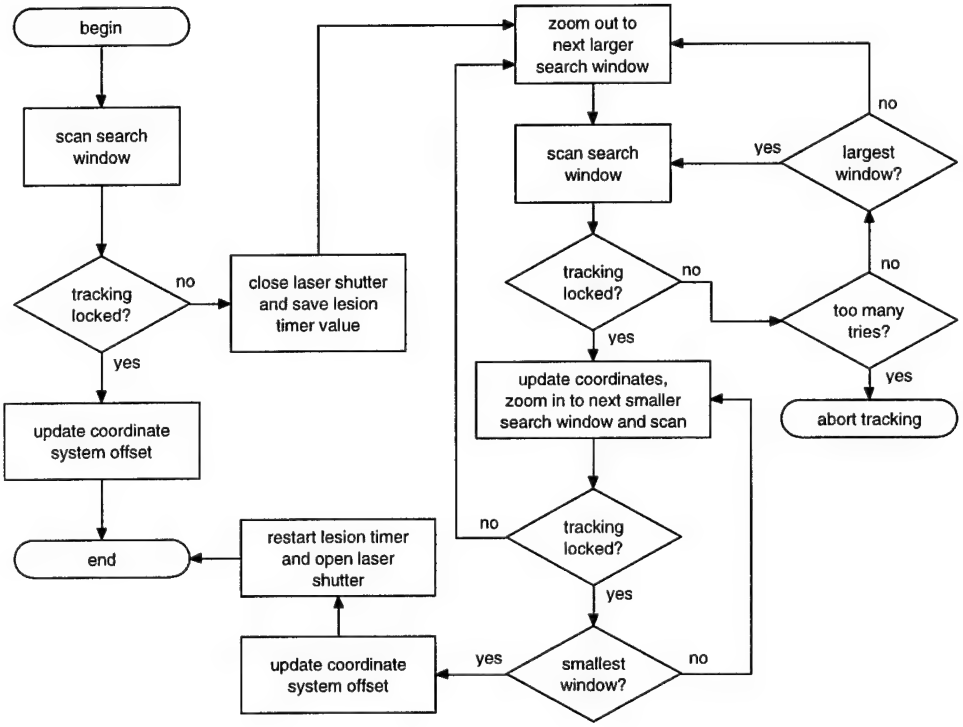

Figure 5.2: Flowchart of improved digital tracking with the "zoom-out, zoom-in" relock technique.

Tests showed this "zoom out, zoom in" technique to be superior to Barrett's two-stage relock method. An initial implementation using the two stage relock method limited the otherwise improved tracking algorithm such that it could only achieve relock at a maximum equivalent retinal velocity of 9 deg/sec using a simulated retinal image. For the same image conditions, the "zoom out, zoom in" technique was able to achieve relock at up to the maximum tracking capability of the system (approximately 40 deg/sec equivalent retinal velocity for the conditions of the test cited). As the retinal velocity increases toward the maximum capability of the system for the given image conditions, the "zoom out, zoom in" technique takes longer to relock due to the need for larger search windows. The longest time for relock was measured to be 6 seconds, and the shortest time typically took three video frames ($\simeq$100 ms).

5.4 System Optimizations for Digital Tracking

In addition to the incremental improvements upon Barrett's technique discussed above, several fundamental design challenges had to be overcome to create an optimized digital tracking capability that took best advantage of the new system. The complete change in the hardware and software environment compared to Barrett's system necessitated a different approach to the overall digital tracking implementation.

5.4.1 The Master Mode Dilemma

To take greatest advantage of the PCI bus for image data transfers, the frame grabber should be operated in master mode. As discussed in Chapter 3, PCI bus master mode is a special type of direct memory access (DMA), where the frame grabber becomes bus master and transfers data directly into main system memory without CPU intervention, thus freeing the CPU for template calculations. Since master mode is of little use without some efficient means to signal the CPU when

new data is ready, the tracking implementation must also support interrupt-driven operation. Both capabilities are necessary for optimized retinal tracking.

Yet when CALOSOS was being developed, the PCI bus was still relatively new, PCI chip sets were still evolving, and no frame grabber company had yet been able to reliably perform sustained master mode transfers to memory using interrupts, without crashing the system. The engineers at MuTech were diligently working on the problem, but progress was slow. To overcome this challenge, the author assembled, via Internet e-mail, a team of experts to help. Engineers and programmers from Massachusetts, Texas, California, and Australia freely contributed their time and suggestions[5] while the author and MuTech engineers attempted various solutions. After six weeks of intensive effort and hundreds of email messages, a solution was found that allowed sustained master mode transfers to memory using interrupts without any system crashes. The details of the solution are now proprietary to MuTech and are seamlessly incorporated into the latest version of the MV-1000 software support library. For the CALOSOS system design, an interrupt-driven master mode tracking implementation was created.

5.4.2 The Image Data Validity Dilemma

With the master mode dilemma solved, image data could be transferred directly to system memory at the full 30 frames/second speed of the camera. But another potential problem still had to be overcome. If the time required for the CPU to perform the tracking calculations was greater than 1/30 of a second, then new image data would be overwritten in memory before the calculations were complete. Conversely, if the time required for the CPU to perform the tracking calculations was less than 1/30 of a second, then the CPU would finish and then begin to recalculate using "old" image data. Either situation is undesirable.

While interrupts are used to signal the end of a frame transfer to memory, the

[5]See the Acknowledgments section at the beginnning of this document.

complete solution to this dilemma also requires a double buffering technique. That is, two image data buffers are created. While one buffer is being written into by the frame grabber, the other buffer is used for calculations by the CPU. Software flags are set and reset as needed to ensure that the buffer assignments are only swapped at the appropriate time for the CPU and only after an entire frame has been completely written into memory. This allows full speed image data acquisition while ensuring validity of the image data used for tracking calculations.

5.4.3 Digital Tracking Analysis of the New Design

Given the various improvements to the digital tracking implementation, combined with the improvements to the hardware and software environment, the new design is able to track at much greater retinal velocities than previous systems. While the video I/O bottleneck of Barrett's system limited its capabilities to roughly 2 degrees/second, this new implementation has no significant I/O limitation using standard frame rate cameras. Thus for CALOSOS, the real limitation is the speed at which the CPU can calculate the template response and update the coordinate system. The primary determining factor is the size of the search window: if a window is so large that it cannot be searched in less than 1/30 second, then the double image buffers will not swap at the full frame rate of the camera. To test the capabilities of the software, various search windows were specified while measuring (using a microsecond resolution timer) the frame rate utilization. Figure 5.3 shows the measured values of CALOSOS for search window size and the associated *effective* frame rate. Note that for search window sizes up to 44×44 pixels (that is, where $S = 22$ pixels),[6] the 90 MHz Pentium used for the system could maintain a full 30 frame/second rate. Referring back to Figure 5.1, this equates to a theoretical tracking speed of 70 degrees/second on the retina; this is 35 times faster than Barrett's original system. The actual achievable tracking speed is somewhat less (on

[6] In practice, it's easier to implement the window such that its dimensions are $(2S+1)\times(2S+1)$.

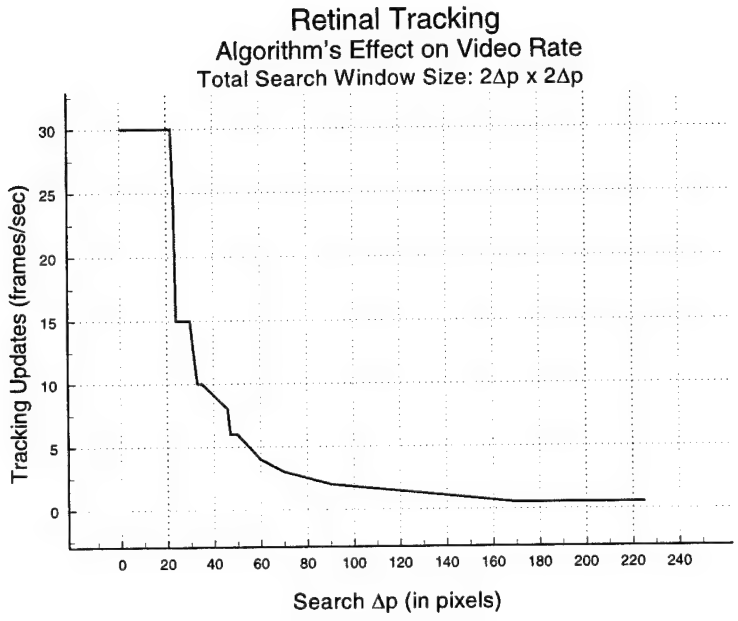

Figure 5.3: CALOSOS effective frame rate for a given search window size.

the order of 50 degrees/second), due mainly to imperfect image conditions. Test results of actual tracking speeds are given in Chapter 8.

This tracking capability of the new system, while considerably faster than previous systems, still has significant limitations.

5.4.4 Limitations of Digital Tracking

The digital tracking method just described has many advantages. For example, once the 2-D template has established its origin on the image, a Cartesian coordinate system is defined globally for the fundus image, which greatly facilitates the integration of lesion pattern creation and laser pointing. The digital method is also very flexible due to its software implementation.

Yet a key disadvantage of this method is its limited data acquisition speed. For lowest system cost a standard RS-170 camera should be used, but as previously stated this 30 frame/second device forces the minimum possible response time to 33 ms (plus overhead). Recall from Table 3.1 that the system response time must be 5 ms or less, and the pointing accuracy must be 100 μm or less.

To meet the response time requirement of 5 ms using digital tracking, a camera with a frame rate of more than 200 frame/second must be used. There are also frame rate implications for the interplay between maximum tracking speed and pointing accuracy. Note that the 22 pixel search capability discussed above, which yielded a 70 degrees/sec tracking velocity, also means that the laser spot could move up to 704 μm off target between video frames. To meet the pointing accuracy requirement of 100 μm, the allowed error in the irradiation site is only $\simeq$ 3 pixels in any direction. Maintaining this error limit at 30 frame/second means the eye velocity limit would be approximately 10 degrees/second. While this is the minimum tracking requirement from Table 3.1, a 200 frame/second camera would improve this to approximately 70 degrees/second while simultaneously meeting the response time requirement.

Surprisingly, the system would *not* require a faster CPU in this instance to

keep up with the faster 200 frame/second data rate. While the image data would be acquired 6.67 times faster, the smaller search window of only 3×3 pixels could be searched 53.79 times faster than the 22×22 window that is the current system maximum for a 30 frame/second rate. In practice, a search window of 7×7 pixels would be recommended: it would provide an even lower probability of losing lock, and yet still have a reasonable design margin for the window search time to keep up with a 200 frame/second data acquisition rate.

Unfortunately, such a high speed camera is not a good engineering solution, at least at the time of this writing. Not only are the few available models of 200 frame/second cameras prohibitively expensive, they have insufficient resolution, and cannot be used with standard monitors or VCRs. An additional disadvantage is the short integration time of light energy on the CCD array, which would adversely affect fundus image quality. As technology improves and prices fall, this option should be revisited, but for the current design of CALOSOS a 200 frame/second camera is not a good trade-off. Hence some alternative was sought to overcome the limitations of digital tracking.

5.5 System Integration for Hybrid Tracking

To overcome the frame rate problems of the digital tracking method, the use of an analog tracking technique was investigated. This analog technique was developed by R. Daniel Ferguson of Physical Sciences, Inc. (Andover, MA) as a stand-alone method to eliminate retinal motion-induced artifacts from confocal reflectometer signals obtained during laser photocoagulation. These artifacts are discussed in more detail in Chapter 7. Ferguson and the author collaborated to perfect the analog technique as applied to the needs of CALOSOS [138–140], and the integration efforts are discussed below. A general overview of Ferguson's analog tracking technique is given in Appendix A (see Section A.7).

5.5.1 Digital and Analog Tracking

While extremely fast compared to the digital tracking method, the analog tracker has some significant disadvantages if used without the additional capabilities of the digital system. Used alone, no coordinate system data is provided by the analog tracker, making the implementation of lesion pattern creation and laser pointing subsystems much more difficult. Even more importantly, the analog tracker is a purely local device—once the dither beam has "fallen off" the reference lesion and lost lock, the system has no idea where the tracking beam is pointing relative to the reference lesion and no way to relock the tracking beam. With this in mind, a combination of the digital and analog techniques into a single hybrid implementation was investigated.

Both the digital tracking system developed by the author and the analog tracking system developed by Ferguson were originally conceived and built as stand-alone devices. This made the integration task extremely difficult, but the potential advantages of a truly hybrid system made it worthwhile to pursue a proof-of-concept effort. Both the digital and analog tracking methods each have advantages and disadvantages when considered separately for use with CALOSOS. In a combined hybrid digital/analog system, however, a synergistic design can be achieved which capitalizes on each tracking technique's individual strengths while overcoming their particular weaknesses.

As implied above, the video-based digital tracking and reflectometry-based analog tracking are highly complementary. The former is a global tracking approach which makes lesion pattern generation particularly easy, but its response time is too slow. The latter is a local tracking approach which is very fast but has no knowledge of the total image or any absolute coordinate system. The fusion of these two approaches into a fully integrated hybrid design promises an easy to use, flexible system that can generate and place lesions on the retina in any definable pattern while compensating for eye movements with the required speed and resolution. The

only disadvantage of a hybrid design is an increase in the complexity of the system; the parts count is larger, the optical alignment is a bit more involved, and the overall cost is slightly higher. Yet at the time of this writing, it appears to be the most cost-effective solution to meet all the system design requirements.

5.5.2 Aspects of an Ideal Hybrid System

If the digital and analog systems had been designed and built from the start as parts of an integrated system, there would be little or no conflict between the two. This is the situation envisioned for the next generation of hybrid implementation. A brief description of the main aspects of such an ideal hybrid system will serve as a point of comparison for the remaining discussion.

In an ideal hybrid system:

- both digital and analog subsystems could control the main steering and dither tracking galvanometers without conflict,
- the computer would control the coagulating beam shutter without affecting the tracking beam or the aiming beam,
- the computer mouse could be used to designate the reference lesion, and direct the tracking beam to lock on,
- both the analog and digital subsystems would provide an unambiguous loss of lock signal to the computer,
- the galvanometer driver amplifiers would be fully adjustable for zero and gain to aid in beam pointing alignment,
- the analog system would be the primary tracker during photocoagulation, with the digital tracker working in the background as a slower complement and to detect possible rotation,

- the digital tracker would be invoked if the analog system loses lock, whereupon it steers the tracking beam back on to the reference lesion,
- the computer checks the location of the aiming beam prior to each irradiation.

Such an ideal hybrid system is a practical goal, but the first generation implementation resulting from this research was intended only as a proof-of-concept for the hybrid approach.

5.5.3 Specific Integration Obstacles

The stand-alone analog tracking system was built by Ferguson as a hardwired "black box" with outputs for the dither tracking galvanometers, the main steering galvanometers, and the coagulating beam confocal reflectometer. The input was a joystick for steering the tracking beam on to a reference lesion, and manually directing the coagulating beam once the tracking beam was locked. This design was fully consistent with original intended use of obtaining motion-stabilized reflectance signals during photocoagulation. Unfortunately, it presented formidable obstacles to integration with the digital computer-based system developed by the author. The most serious obstacles, and how they were overcome for proof-of-concept experiments, are listed below.

Tracking Conflicts

The only means available to incorporate beam steering inputs from the digital system into the analog system was to wire it into the analog electronics such that the digital and analog galvanometer steering voltages were summed prior to being sent to the galvanometer driver amplifiers. This is not the ideal method, and has several negative ramifications. For example, this dictates that only one tracking method can be employed at any given time. If both tracking methods were active, they would try to cancel each other. Consider that when an eye movement occurs, the

analog system very quickly adjusts the main steering galvanometers to move with the eye motion. The digital tracking system would also detect the original eye motion (albeit not as quickly) and, having no way of knowing the situation had already been rectified, would also send a corrective voltage to the main steering galvanometers. This would cause the steering mirrors to begin to move twice as far as actually needed, whereupon the analog system would interpret this as additional eye movement and generate an opposite correction voltage. This battle between the two systems would render the hybrid tracking system useless. Given a choice between the two, the analog tracker, with its faster response time of 5 ms, provides a superior motion-stabilized confocal reflectometer signal and less tracking update lag time error, and is thus the preferred method. A special software routine was written which allows the digital system to supply lesion pattern offset voltages to the galvanometers without invoking the digital tracking algorithm.

Shutter Control Conflicts

The digital system uses a computer controlled shutter to turn the laser beam on and off as needed for photocoagulation. However, the design of the analog system incorporates an arrangement of beamsplitters to use 4% of the main beam power as the tracking beam. Closing the shutter on the laser would therefore interrupt the tracking beam with a resultant loss of lock. The analog system optics are extremely compact to allow the four galvanometer mirrors (x and y for tracking and for main steering) to "share" the conjugate plane of the pupil, which leaves little room for a shutter. By rearranging the beamsplitters at the laser delivery fiber site, sufficient room was made to allow the computer to turn the coagulating beam on and off without disrupting the tracking beam, but the arrangement is far from ideal.

Lack of Analog Loss of Lock Signal

While a low DC level at the tracking beam confocal reflectometer indicates a loss of lock (see Section A.7), there was no way to signal this condition to the computer. As a result, system operation had to proceed on the assumption that the analog tracker was locked and maintained lock. As a partial workaround for this, the software routine that would normally check for the actual laser position during digital tracking (and supply a closed loop correction) was modified to sense when the coagulating beam deviated more than 10 pixels from the expected location (indicating an analog loss of lock or a serious beam pointing malfunction). If this occurred, the routine would abort any lesion pattern in progress and close the shutter. This capability was demonstrated during an *in vivo* test described in Chapter 8.

Beam Pointing Alignment Conflicts

When the laser pointing system is aligned with the digital system's template-based coordinate system, the tracking signal integrators are shorted to zero volts and the tracking beam is adjusted to the exact center of the digital image. The coagulating beam is then steered along the alignment pattern generated by the digital system, and the beam is made to match the same pattern as displayed on the computer screen. Unfortunately, the "black box" electronics of the analog system had no option to adjust the zero and gain of the driver amplifiers as is available for the digital system. As a workaround, an external voltage divider was placed in series with the main steering galvanometer inputs, which simulated a gain control. The zero adjustment had to be made by manually adjusting the steering mirrors on the galvanometer shafts. This is far from the ideal situation, but it effectively provided a short-term fix to the alignment dilemma.

Another alignment-related problem was that for a typical reference lesion not located in the exact center of the digital image, an offset error would be introduced into the lesion pattern placement that was directed by the digital system. A software

routine was written that allowed the user to click the mouse on the designated reference lesion after the analog system had established lock, which provided the offset from the image center to the rest of the digital system software. Special versions of the beam pointing macros were written which took the reference lesion offset into account, with the result being the lesion pattern created by the digital system was placed in the correct location on the retina.

With these workarounds in place, the partially integrated hybrid system could be operated to provide a proof-of-concept. A general description follows.

5.5.4 First Generation Hybrid Operation

In the hybrid approach for CALOSOS, the digital tracking system establishes the 2-D template on the retinal image which defines the Cartesian coordinate system for the retinal image. This allows easy specification and generation of a lesion pattern using the computer monitor and mouse. The analog tracking system's dither beam is locked to a reference lesion using a joystick. The tracking vector $\vec{t}$ is generated from the analog system's error signals to compensate for eye movements. A lesion pattern offset vector $\vec{q}$ is generated from the digital system based upon the lesion site locations with respect to the template-based coordinate system origin and the reference lesion offset from center. The signal that is sent to the main steering mirrors is the sum $\vec{t} + \vec{q}$. This results in a motion stabilized lesion pattern being produced on the retina. Note that in this first version of the hybrid design, the digital tracking algorithm does not perform during photocoagulation. The computer attends only to the creation of the lesion pattern. If the analog system loses lock, the coagulating beam moves from its expected location which in turn is detected by the digital system. The laser shutter is then closed and photocoagulation is suspended until tracking lock is reestablished. The current implementation, being a first generation of the hybrid approach, doesn't meet the description of an ideal hybrid system described in Section 5.5.2, but there is no technical barrier preventing

the next version of CALOSOS from having this level of integration. See the Chapter 9 discussion about future work.

This first generation of an integrated system demonstrated that a hybrid digital/analog design is a viable approach with significant advantages over purely digital or analog methods. While a fully integrated system remains to be built, the long-term advantages of the digital/analog synergy which will be realized in future versions of CALOSOS make this a worthwhile effort.

5.6 Summary of Retinal Tracking

It has been shown how digital tracking and analog tracking can both be implemented to compensate for movements of the retina during photocoagulation. If the two approaches are combined into a hybrid design, it becomes possible for the first time to meet all the CALOSOS performance requirements in a cost-effective manner.

Chapter 6

Controlling and Pointing the Laser

This chapter examines the Laser Positioning and Control System (LPCS). For CALOSOS to perform retinal photocoagulation, it must be able to turn the laser beam on and off, and also direct the laser beam to the appropriate location on the retina. First the various components of the laser pointing and control system are analyzed, then the technique for system alignment prior to photocoagulation is outlined, followed by a description of how the pattern of lesion sites is generated to which the laser beam will be pointed. The chapter concludes with a discussion of how the actual pointing of the laser beam to each of the lesion sites is optimized for best overall performance.

6.1 Laser Pointing and Control System Analysis

The CALOSOS Laser Pointing and Control System (LPCS) applies techniques used in the scanning laser ophthalmoscope [86], and is a derivative of the system developed by Barrett [15], with improvements to enhance overall performance. The subject is treated in a systematic manner, where the ensemble LPCS consists of seven main components:

1. the data acquisition I/O card,

2. the interface control unit,

3. the laser shutter,

4. the beam shaping optics,

5. the scan coupling lens/beam splitter combination,

6. the x and y galvanometer driver modules,

7. and the x and y galvanometer/mirror combinations.

The beam shaping optics are also used for optimizing the confocal reflectometer signals discussed in Chapter 7; therefore, that aspect of the optical design is covered there. Note that the LPCS design is effectively the same for the digital tracking implementation and the hybrid tracking implementation; any differences that affect performance will be noted below. The reader may want to review the figures in Chapter 3 that depict the arrangement of the various components.

6.1.1 Data Acquisition I/O Card

The data acquisition I/O card used for CALOSOS is a National Instruments AT-MIO-16, capable of multichannel analog input, multichannel digital I/O, and two channel analog output. This component's purpose is to translate the various signals (for the laser shutter, beam steering galvanometers, patient status, lesion status, status reset, and lesion reflectance) between the host computer and the rest of CALOSOS.

With regard to the LPCS performance, the most critical signals are the two analog output voltages which are used to steer the galvanometers. Each analog voltage has a resolution of 4095 discrete steps due to the 12-bit DAC of the data acquisition I/O card, with an accuracy of ± 0.25 LSB. Disregarding the rest of the LPCS for the moment, this would translate into a resolution of 0.012 (with an accuracy of ± 0.003) degrees per step over the entire 50 degree FOV, which translates

into just over 3.6 ± 0.9 μm/step on the retina. Recall, however, that in Chapter 4 the dimensions of an image pixel were found to be approximately equivalent to a 32 μm square on the retina. When the two coordinate systems are coaligned (see below) this larger resolution, dictated by the CCD camera, prevails.

The analog output circuitry of the AT-MIO-16 can be updated at up to 250 kHz, and is rated with a settling time (to within 0.024% of the full step response) of 4 μs for a 20 V step, and a slew rate of 30 V/μs, with typical output loading impedances [69]. The slew rate (which is also the maximum slope of the transient response) can be interpreted to mean that a full -10 V to $+10$ V swing can occur in $(20\text{ V})/(30\text{ V}/\mu\text{s}) = 667$ ns. Adding settling time yields 4.667 μs. Since the LPCS is designed such that the full -10 V to $+10$ V swing will scan the galvanometers across the entire 50 degree FOV of the fundus camera,[1] then the signal could theoretically (neglecting for the moment the physical constraints of the galvanometer/mirror combination) direct the laser to move 50 degrees across the retina and settle in 4.667 μs. This translates to 10.7×10^6 degrees/second! This far exceeds the ability of the galvanometer/mirror combination, and so contributes negligible beam steering error. For all practical purposes, the signal from the AT-MIO-16 can be considered ideal.

6.1.2 Interface Control Unit

The custom-built Interface Control Unit (ICU) serves two purposes. It's primary purpose is to route various signals to and from the data acquisition I/O card's 50-pin ribbon cable and the individual components of the LPCS. Table B.1 in Appendix B contains details regarding individual connector pin assignments.

The secondary purpose of the ICU is to enable the CALOSOS development system to simulate the patient status switch and a lesion control signal. A commercial system would provide a status switch (in a "deadman" configuration) for the patient

[1] Actually, less than the full voltage swing is required to scan the entire FOV, so this is a conservative estimate.

to signal if he or she needed to interrupt the procedure, for example to sneeze. The lesion control signal is present to simulate an external device signalling that a lesion is complete. This would be in addition to the integrated lesion reflectance signal, and provides extra flexibility in the testing of CALOSOS. These switches are toggled by appropriate logic gates and can only be reset via the host computer. If either switch is depressed, the computer senses the fact and closes the laser shutter. In the case of the patient status switch, the progression through the lesion pattern is stopped unless clinician manually restarts it. In the case of the lesion control signal, the system moves on to the next lesion site (if any) in the pattern and continues. The action of these switches was tested and verified during system operation. The maximum response time is just over 33 ms when used with digital tracking, since the check for these status switches is polled between video frames. This response time could be improved in a commercial system if the switches were wired directly to interrupt lines and appropriate interrupt servicing routines were written. When used with analog tracking during hybrid operation, the response time is on the order of a few microseconds, since the CPU continually polls the status lines without invoking the digital tracking algorithm.

6.1.3 Laser Shutter

The laser shutter assembly is a Uniblitz model LS6Z with a Uniblitz D122 controller. The laser shutter signal comes from the computer via the data acquisition I/O card and the ICU to the shutter controller, which is configured so that unexpected conditions such as power failure will always close the shutter. It will stay closed even after restoration of power until an active signal from the user resets it. The shutter aperture is 6 mm in diameter, with blades coated to withstand a CW laser power density up to 5 W/mm^2 in the visible wavelengths; this is more than adequate for CALOSOS. The shutter can open within 1.8 ms and close within 0.8 ms of the appropriate signal from the computer. The speed with which the shutter can close

is an important aspect of patient safety; recall the design specifications require a response time of 5 ms. Thus CALOSOS should detect and signal an anomalous condition in no more than 4.2 ms to allow time for the shutter to close.

6.1.4 Beam Shaping Optics

The beam shaping optics were discussed in Chapter 3. While they are in the optical path of the Laser Positioning and Control System (LPCS), they contribute nothing to the actual pointing of the laser. The primary purpose of the beam shaping optics is to enable the use of confocal reflectometers, and to ensure the appropriate spot size results on the patient's retina.

6.1.5 Scan Coupling Lens and Beam Splitter Combination

The scan coupling lens and beam splitter physically attach to the fundus camera. The primary purpose of the scan coupling lens is to provide the angular magnification for steering the laser beam to the appropriate point on the retina. Given the LPCS lens specifications and distances listed in Appendix B, the scan coupling lens provides an angular magnification of approximately 3:1 to the retina. Hence for a -25 degree to $+25$ degree coverage of a 50 degree retinal FOV, the galvanometers must provide a -8.33 degree to $+8.33$ degree steering range.[2]

As noted above, this represents approximately one third the maximum range of the G124 galvanometers used for the digital tracking version, ensuring the active steering range is well within the most linear central region. For the hybrid tracking version, larger G310 galvanometers were used to accommodate larger mirrors for the combined coagulating beam and the dither tracing beam. The required beam steering range is approximately 83% of the maximum steering range of the G310 galvanometers used for CALOSOS. While this makes it more difficult to ensure linear scan response, the next size galvanometer (the G320) has a much lower resonant

[2]All angles are specified as optical angles, which are twice the mechanical angle, unless otherwise stated.

frequency due to its greater armature mass. An engineering trade-off analysis indicated the G310 galvanometers should be used. Note that it may be possible for future hybrid designs to use G100 series galvanometers.

As mentioned in Chapter 3, a significant potential source of steering error is spherical aberration of the laser beam scan, especially at extreme steering angles. CALOSOS minimizes this in two ways. First, the physical orientation of the plano-convex scan lens was chosen to give lower spherical aberration of the scan pattern (not the beam itself) as dictated by the beam steering conjugate ratio. Second, an aspherical lens was chosen for the scan coupling lens, which is designed to minimize spherical aberration at large angles of incidence. It does not, however, perform field flattening of the curved retina. That would require a specialized ophthalmoscopic aspherical lens, which is much more costly.

The scan coupling lens also provides additional beam shaping for laser delivery to the retina, but this is not directly related to the Laser Positioning and Control System (LPCS).

The beam splitter is used to allow the laser light to be coupled into and out of the eye while simultaneously allowing the fundus camera to obtain an image of the retina. For an optimal trade-off between laser power delivery efficiency and fundus camera image quality, an AR-coated dichroic beam splitter was used which passes 95% of light above 550 nm in transmission, yet reflects 97% of the argon wavelengths ($\lambda = 488$ nm and 514 nm).

6.1.6 Galvanometer Driver Modules

The galvanometer driver modules transform a -1 V to $+1$ V position signal into an appropriate current for the galvanometers. In the digital tracking version, two General Scanning AX-200 driver modules (x and y) are used. In the hybrid tracking version, four General Scanning A-102 driver modules (an x and y for both the main steering and for the tracking beam) are used. The performance of the AX-200

and A-102 modules is identical; only the housing and power supply differ. Since the tracking beam control was already discussed in Chapter 5, this section addresses only the pointing of the main steering mirrors. In that context, there is no functional difference between the digital tracking version and the hybrid tracking version. In the digital tracking version the position signal is sent from the computer's data acquisition card, whereas in the hybrid tracking version the position signal is a sum of the signal from the computer's data acquisition card (primarily providing the lesion pattern vectors) and the appropriate tracking beam lock-in amplifier (for tracking the retinal movements).

The driver modules are variable impedance amplifiers which dynamically adjust their response to step changes in the input, thereby minimizing distortion of the output [141]. The driver modules are designed to be used with G100 and G300 series galvanometers, and are rated at a frequency response of 0–20 kHz. The AX-200 or A-102 modules can drive the G100 and G300 series galvanometers full scale sinusoidally at up to 85% of the loaded resonant frequency; triangular or square wave inputs can be used full scale at up to 5% of the loaded resonant frequency (see the discussion in Section A.8 regarding resonant frequency calculations). The transient response is improved using the AX-200 or A102 modules since the back-EMF of the galvanometer coils are used to partially damp unwanted oscillations. Because these driver modules use a current (rather than voltage) output stage, the electrical time constant L/R of the connected galvanometer does not affect performance within the voltage headroom of the output stage [142].

6.1.7 Galvanometer and Mirror Combination

The actual steering of the laser beam is accomplished with the commonly used configuration of two orthogonal (x and y) galvanometers and mirrors. See Figure 6.1 for a simplified example. The digital tracking version uses model G124 galvanometers and the hybrid tracking version uses G310 galvanometers to position the main

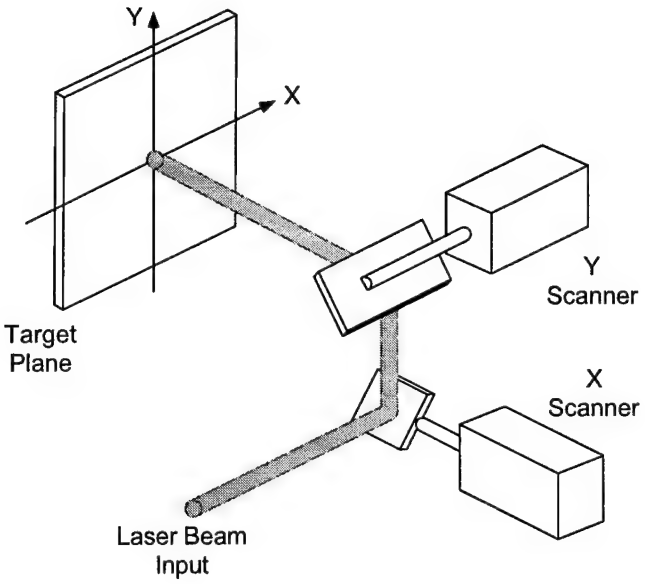

Figure 6.1: Laser beam steering via two orthogonal galvanometers and mirrors.

steering mirrors of the Laser Positioning and Control System (LPCS).

While Barrett used a similar beam steering configuration [15] as shown in Figure 6.1, he used different galvanometers (G108s) and did not provide a quantitative analysis of the associated design limitations. Since the design analysis is rather lengthy and would interrupt the flow of this discussion, it can be found in Appendix A (see Section A.8).

A summary of the design analysis in Section A.8 indicates that both the G124 and G310 have sufficient speed to track the maximum anticipated retinal velocity. The overshoot and settling time effects are neutralized by inserting a 50 ms software delay after large steering movements. The stated linearity and hysteresis worst case specifications appear to exceed the 100 μm pointing accuracy requirement, but only a change to more expensive closed loop galvanometers would alleviate this. System tests indicate that in actual use these effects less than specified, and are overshadowed at the edge of the FOV by spherical aberration of the scan pattern

due to scan lens Ls. The recommendation is given that for the current development system the existing galvanometers (and scan lens) are acceptable, but for a system intended for clinical trials they should be replaced with closed loop galvanometers and the scan lens should be replaced with an ophthalmoscopic aspheric lens.

6.1.8 Timing Accuracy

While not a physical component of the Laser Positioning and Control System (LPCS), an important function is the timing accuracy for laser irradiation. Assuming the lesion control signal does not prematurely end the irradiation, the maximum irradiation time specified by the clinician must not be exceeded. The architecture of PC-compatible computers includes a standard programmable timer chip, which is always set by the operating system to "tick" with an interrupt interval of 18.2 times per second [54]. This is how often the system date and time are updated, which translates into a time resolution of 54.95 ms. Time-related functions typically available to the programmer via languages such as FORTRAN, C, or assembly language draw upon the system date and time, so they too are limited to this resolution.

Yet the design for CALOSOS requires a system response time of 5 ms or less, primarily due to the typical clinical irradiation times of 100 ms. It would do little good to design the rest of CALOSOS to a 5 ms response time if the irradiation time could only be measured to a resolution of 54.95 ms! One cannot just blindly reprogram the timer chip, since many computer operations, such as diskette access, depend upon the timer period. Luckily, an assembly language procedure written by Michael Abrash (and graciously placed in the public domain) temporarily reprograms the hardware timer chip, performs a limited period timing measurement function with a resolution of approximately 1 μs, then resets the timer chip back to its original value.[3] The software written for CALOSOS incorporates the Abrash timer procedure for monitoring laser irradiation duration with a resolution that is

[3]During the time period being measured, any mouse, keyboard, or diskette drive activity should be avoided.

better than the system requirement.

6.1.9 Summary of LPCS Analysis

From the above discussion it is apparent that of all the design issues, the parameters related to the galvanometers and the scan coupling lens contribute the most to the performance of the Laser Positioning and Control System (LPCS). Note that the LPCS uses inexpensive components appropriate for a proof-of-concept development system. Before the start of clinical trials, some system components would be upgraded as needed. In particular, closed loop galvanometers with position sensors and the associated driver modules, while much more expensive than the open loop models described above, would greatly improve the dynamic laser pointing ability. An ophthalmoscopic aspheric lens for Ls would reduce the spherical aberration at the edge of the FOV.

6.2 Laser Pointing and Control System Alignment

For accurate placement of laser-induced lesions on the retina, precise alignment is required between the coordinate systems of the Laser Positioning and Control System (LPCS) and that of the digital imaging system. This coalignment is performed each time CALOSOS is to be used. The single monitor design and the ability to both draw figures and use the mouse cursor directly on the real-time retinal image make this procedure much easier than any previous approach.

For the digital tracking version of CALOSOS, the user simply selects the alignment menu, and chooses an alignment pattern to be displayed on the same screen with the live video retinal image. Choices include a centered spot, a slow ramp, a fast ramp, and a user defined shape. The LPCS then directs the laser (at a safe low power) to the coordinates that correspond to the alignment pattern. The user then adjusts the zero offset and gain controls of the galvanometer driver modules, and possibly may adjust the optics slightly, until the laser pattern on the retina

matches the alignment pattern being superimposed on the live video. When this is true, coalignment exists between the 4095×4095 LPCS coordinate system and the 451×451 coordinate system of the digital image. This procedure typically can be performed in five minutes or less.

If the hybrid tracking version is being used, one additional step is required. The error signal integrators are cleared to zero (there is a pushbutton on the joystick to accomplish this), and the tracking and coagulating beams are both aligned to the center of the image.

Note that the ability to align the coordinate systems is somewhat dependent upon the size of the laser beam spot on the retina. If the beam as shown in the computer image were one pixel in size, then exact alignment would be theoretically possible, but for the larger spot sizes encountered in actual use, accuracy relies upon the operator's ability to visually determine the center of the spot and direct it to the correct pixel coordinate. It may be possible to create an automated alignment procedure that improves on this limitation.

6.3 Automated Generation of Lesion Patterns

One of the advantages of a robotic photocoagulator is the ability to relieve the clinician of the tedious task of manually creating a pattern of lesions. As noted in earlier chapters, panretinal photocoagulation (PRP) treatments for diabetic retinopathy can require a pattern of up to 3000 lesions per eye. Treatments for retinal tears or breaks do not require as many lesions, but the need to create a double ring of lesions around the tear can be time consuming and prone to error.

Barrett's earlier work [15] included a method to automatically generate various lesion patterns, but it was an inefficient implementation that did not lend itself well to the new software environment or to optimizing the galvanometer movements. Thus this function was redesigned and implemented for the new system software.

Once the tracking template (discussed in Chapter 5) is established on the retinal

image, a Cartesian coordinate system exists which can be used as a reference for placing lesions. Choice of treatment (diabetic retinopathy or retinal tear) is easily selected from the CALOSOS user interface using the mouse or keyboard. The clinician then uses the mouse to indicate on the retinal image the outer boundaries of where the lesion pattern is to be placed. A click of the mouse tells the computer to automatically generate the requested pattern (PRP rectangular matrix, PRP radial matrix, or retinal tear double ring) within the boundary specified. An example of a computer generated PRP rectangular matrix was shown in Figure 4.7. The clinician further has the option to add or erase individual lesion sites to this pattern by using the mouse at any time prior to photocoagulation.

6.4 Optimizing Galvanometer Movements

The laser pointing movements required to create a lesion pattern should be optimized for best performance of CALOSOS. As discussed above, the predominant limitation to laser pointing accuracy and speed are the mechanical characteristics of each galvanometer and its attached mirror. For a given galvanometer and steering mirror combination, any design strategy which minimizes the required galvanometer movements will tend to maximize the system performance.

6.4.1 Optimizing a Uniformly-Spaced Lesion Pattern

For a uniformly spaced lesion pattern, minimizing the galvanometers movements can be accomplished with a sorting algorithm [72,75]. For example, if a rectangular pattern is generated using two nested **for** loops, the resulting order of the lesion sites as stored in the pattern array results in a path through the pattern as shown in Figure 6.2(a).Note that this causes large "jumps" of the galvanometer (the y galvanometer in this example) when traversing to the next column. A simple resorting of the array results in the path shown in Figure 6.2(b). After this optimization, the largest step size is reduced (averaged across a representative sample of lesion

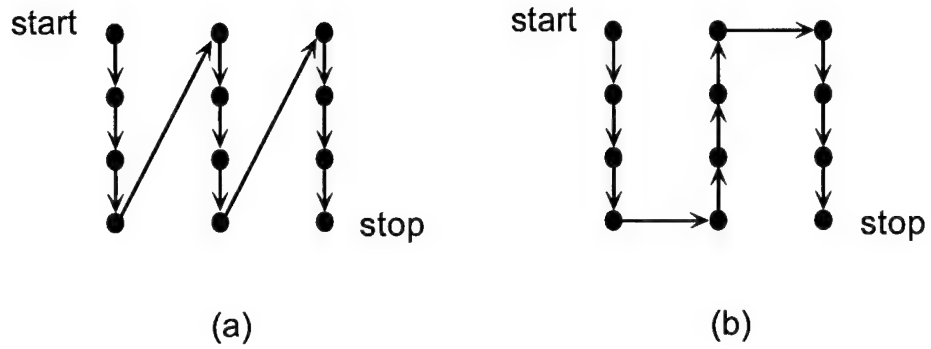

Figure 6.2: Comparison of paths through a uniformly-spaced lesion pattern: nonoptimized (a), and optimized (b).

patterns) by a factor roughly equivalent to the square root of the total number of lesions in the pattern. A 10×10 pattern would have its largest step size, on average, reduced by a factor of 10. This technique is implemented in the CALOSOS software for all routines that generate uniform lesion arrays.

6.4.2 Randomization of the Lesion Pattern

As discussed in Chapter 4, when a uniformly-spaced lesion pattern has lesion sites eliminated that lie on or near major blood vessels, the resulting pattern is random (recall Figure 4.8). This is due to the inherently random distribution of the major blood vessels. Note that while the general location of major blood vessels is anatomically predictable, the exact path of a blood vessel is not. The overall blood vessel pattern is unique to each person, a fact which forms the basis for retinal pattern identification programs.

A uniformly-spaced lesion pattern can also be randomized to some degree when the operator chooses to manually erase or add to some of the lesion sites in the pattern using the mouse.

6.4.3 Finding an Optimized Path Through a Random Pattern

Problem Definition

While optimization of the path through a uniformly-spaced lesion pattern can be solved with a straightforward sorting algorithm, randomization of the path transforms the task into a much more difficult graph theory problem of combinatorial minimization. The challenge is to find the shortest path through each of the lesion sites without revisiting any one site; this is in essence a form the famous "travelling salesman" problem [75]. The travelling salesman must find the shortest itinerary to N cities without retracing his path. It can be shown that there are $N!$ different paths that can be taken; this class of problem is known as *NP-complete*, one of the most difficult types of problems to solve [73]. For an *exact* solution to an NP-complete problem, the computation time increases with N as $\exp(\alpha N)$, where α is some positive constant; the time quickly becomes prohibitive as N increases [143]. Other examples of the travelling salesman problem in electrical engineering include finding the optimum path for robotic equipment to drill predefined holes in printed circuit cards, and finding the optimum layout of numerous circuit elements in a high density integrated circuit to minimize interference between connections.

Solution: Simulated Annealing

A practical algorithm to solve the travelling salesman problem was finally found using the method of *simulated annealing.* This technique is a stochastic optimization method derived from the use of Monte Carlo methods in statistical mechanics [144]. The definition of annealing is the slow cooling of a liquid into a solid, allowing time for redistribution of atoms as they lose motility an thus ensuring that a low energy state (crystallization) will be achieved [143]. It was this thermodynamic model that was the object of the original algorithm proposed by Metropolis et al. [145]; it effectively found optimally low energy states with a computational complexity as a small power of N [143]. Hence the name "simulated annealing." In practice,

simulated annealing may not always return the absolute lowest energy state, but its results are usually very close to the exact solution.

It was observed [146,147] that the effective search for a low energy state could be applied to combinatorial minimization problems such as the traveling salesman if the energy state is likened to the cost of a solution. The technique of simulated annealing has since been successfully applied to a variety of problems in electrical engineering as diverse as robotic printed circuit card drilling, integrated circuit design, wire routing, coding theory, speech recognition, image processing, logic optimization, and magnetic materials [135,148–153]. CALOSOS adds robotic laser surgery of the retina to that list.

While it is beyond the scope of this discussion to completely analyze the Metropolis algorithm of simulated annealing, a brief description is in order (see [143] for a concise overview and [135, Chap. 4] for an excellent detailed treatment). The algorithm is based on stationary Markov chains (see [154] for a discussion of stochastic processes). Let $\mathbf{S} = \{S_1, S_2, \ldots, S_N\}$ be the finite set of all possible states of the simulated thermodynamic system. Each state S_i has a corresponding energy E_i. For a system in thermal equilibrium at temperature T, a sample of the states would be expected to exhibit a probability density of

$$p(S_i) = \frac{\exp\left(\frac{-E_i}{kT}\right)}{Z_T} \qquad \text{for } 1 \leq i \leq N \tag{6.1}$$

where k is Boltzmann's constant and

$$Z_T = \sum_{S_i \in \mathbf{S}} \exp\left(\frac{-E_i}{kT}\right) \tag{6.2}$$

is the normalization factor which ensures that $\sum_{S_i \in \mathbf{S}} p(S_i) = 1$. For many systems, Z_T is unknown because the number of states, while finite, is very large and thus not conducive to computing the solution to Equation 6.2 for all necessary values of T. This implies that while E_i is known, the probability $p(S_i)$ given by Equation 6.1 cannot be determined directly. The method used by the Metropolis algorithm is to

construct a finite Markov chain having an invariant distribution identical to that of Equation 6.1 (see the proof in [135]). The result is a system which is assumed to change energy states from E_i to E_j with a probability

$$p_{ij} = \begin{cases} \exp\left(\frac{-(E_j - E_i)}{kT}\right) & \text{for } E_j \geq E_i \\ 1 & \text{for } E_j < E_i \end{cases} \tag{6.3}$$

Note that the ramification of Equation 6.3 is that the simulation *always* takes a step to a lower energy state and *sometimes* takes a step to a higher energy state. This mirrors annealing in nature, where there is a chance for the thermodynamic system to get out of a local energy minimum in favor of finding a better, more global, minimum. Note that by the simple substitution of the energy state E_i with the cost C_i of a solution, the Metropolis algorithm for simulated annealing can be applied to any combinatorial minimization task for which a cost metric can be defined for the set of solutions.

For practical use of this technique using Monte Carlo methods, the required ingredients are: a description of the system configuration, a random number generator to change the configuration, a cost function C which must be minimized, a control parameter T (the "temperature" of the system), and an *annealing schedule* which determines both the number of repetitions to be completed before assuming an invariant distribution of p_{ij} and the decrement step size for T. To apply simulated annealing for optimizing the path taken by the Laser Pointing and Control System (LPCS) through a randomized pattern of lesion sites, the total path length is equated to C. The remaining implementation choices were adapted directly from [143].

As a simple example with a very small value of N, recall the lesion pattern of Figure 6.2. In Figure 6.3, that same pattern has had three lesion sites removed either due to proximity to a major blood vessel or manual erasure by the clinician.

In Figure 6.3(a), the path as optimized previously for the uniform pattern now results in larger galvanometer movements than necessary for the "randomized" pattern. The path found by the simulated annealing algorithm is shown in Figure

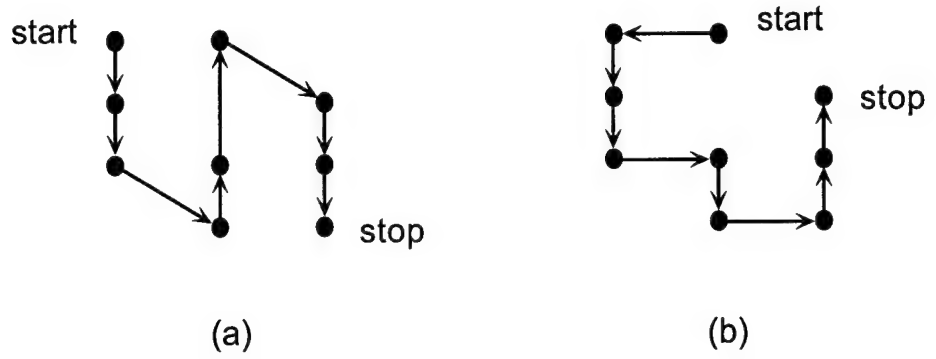

Figure 6.3: Comparison of paths through a "randomized" lesion pattern: nonoptimized (a), and optimized (b).

6.3(b). Note in this simple case this is also the exact solution. The reduction in the largest step size due to this form of optimization is difficult to quantify due to the random nature of the lesion patterns. The improvement is at least as significant as the sorting technique used for uniform patterns, but is more generally applicable.

A routine which implements the simulated annealing procedure described above was written and incorporated into the CALOSOS system software. The user simply selects "optimization" from the lesion pattern menu, and within a few seconds the optimized path through the pattern, with minimal galvanometer movements, is computed and assigned to the pattern. Since the step by step progress through a large, complex lesion pattern would require many images to demonstrate visually to the reader, the small pattern of Figure 6.3 is used as a generalized example.

6.5 Summary of Laser Pointing and Control

From the above discussion it was shown how the laser is directed to the appropriate location on the retina for the specified irradiation time. The components used in this development version of the Laser Positioning and Control System (LPCS) are

marginal in certain aspects (such as galvanometer linearity and hysteresis) with regard to meeting the 100 μm pointing accuracy requirement. Yet for development work, they are deemed acceptable with the caveat that a system intended for clinical trials would upgrade the galvanometers and the scan lens. The optimization of the path taken by the LPCS through the lesion pattern is a new capability never before available, and the application of simulated annealing to randomized lesion patterns efficiently allows optimization in any situation.

Chapter 7

Controlling Retinal Lesion Formation

In this chapter, the need for feedback control of lesion formation is reviewed, and the potential viability of using lesion reflectance for that purpose is outlined. The first known method for obtaining a motion-compensated real-time reflectance-based signal for irradiations as short as 100 ms is then described. Some reflectance predictions based upon Monte Carlo simulations of lesion formation are discussed, along with some anomalies not predicted by the model. A summary is then given regarding the current limitations of reflectance-based lesion control. Note that some anatomically-related background was previously given in Chapter 2; see [41,42,155,156] for more theoretical background on laser-tissue interactions.

7.1 The Need for Feedback Control

Recall from Section 2.4 that the absorption coefficient μ_a of the retinal pigment epithelium (RPE) determines the rate of lesion formation for a given laser power. Since μ_a of the RPE varies significantly across the fundus, lesion formation is difficult to predict [4]. The result is that for identical laser power and irradiation time, the diameter and depth of retinal lesions will vary considerably at different locations on the retina. Unfortunately, the human visual response time ($\simeq$180 ms) is too slow for an ophthalmologist to react and compensate in real time to a dynamically

forming lesion (assuming a typical irradiation of 100 ms) [14]. Thus some method of automated lesion control is highly desirable for both increased safety and enhanced therapeutic effect.

While both diameter and depth are measures of a retinal lesion's size, depth is the more critical from a patient safety standpoint. If the lesion grows too much in depth, it could induce hemorrhage through the choroid or cause non-local vision impairment from damage to the nerve fiber layer (recall Figure 2.3).

7.2 Obtaining a Lesion Reflectance Signal

7.2.1 Reflectance as an Indicator of Lesion Morphology

Researchers such as Weinberg [16], Birngruber [4], Markow [8], Yang [13,17], Jerath [10, 14, 20, 51, 52], and others [18–20], have demonstrated that lesion diameter and depth can be inferred noninvasively from the reflectance of the lesion. This indicates that lesion reflectance could be used as a feedback signal to dynamically control lesion formation.

The photocoagulation process causes the scattering coefficient μ_s to increase, which increases the reflectance[1] of the area where the lesion is forming, shown in Figure 7.1 [21]. A laser-induced lesion typically appears as a round bright spot on the retina, with the center brighter than the edges. An axial cross-section of the reflected light from a growing lesion in an albumen eye phantom is shown in Figure 7.2 for several instants during irradiation. Lesion diameter can be measured directly from the reflectance image boundaries of the lesion, but lesion depth appears to be more strongly correlated with the reflectance of the central area of the lesion. See Figure 7.3 for an empirically derived correlation from Yang [13]. Jerath demonstrated these concepts using both albumen eye phantoms and *in vivo* using pigmented rabbits [14].

[1] To be more precise, the signal consists of backscattered light—but the term reflectance is used throughout the literature.

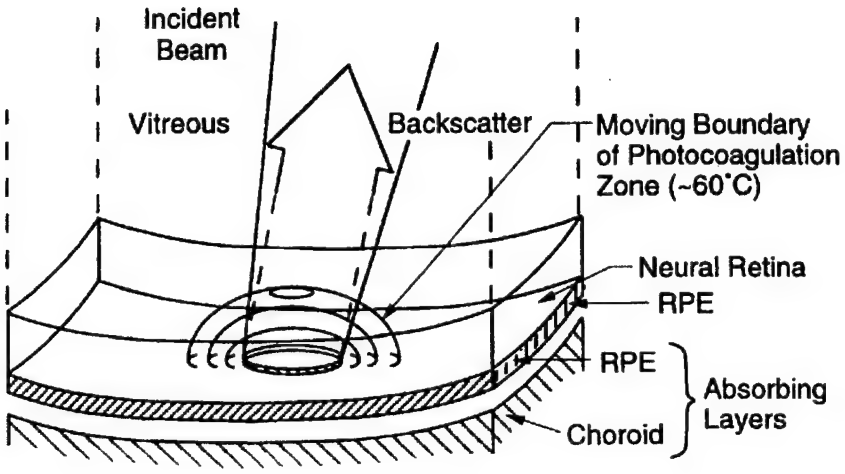

Figure 7.1: The higher scattering coefficient of a retinal lesion increases its reflectance.

7.2.2 Lesion Reflectance from a Confocal Reflectometer

While Jerath used a CCD camera to obtain reflectance data (for very long irradiation times), it was pointed out in Chapter 3 that there were several drawbacks to this approach. The most important drawback is the camera frame rate; for a typical 100 ms irradiation time only three data samples would be available.

Confocal reflectometry has been shown to be an alternative technique to obtain a real-time lesion reflectance signal for irradiations on the order of 100 ms or shorter [21]. Inderfurth et al. gathered data from rabbits and from the clinical photocoagulation treatments of 68 patients (corresponding to $\simeq$12,000 retinal lesions) at the New England Eye Center (Tufts University School of Medicine) by attaching a confocal reflectometer to a standard slit lamp microscope. Their preliminary results on rabbits led them to believe that the latency time and initial slope of the reflectance signal may provide information that can be used to create repeatable lesions on the retina, as originally predicted by Weinberg [16]. In Figure 7.4, two

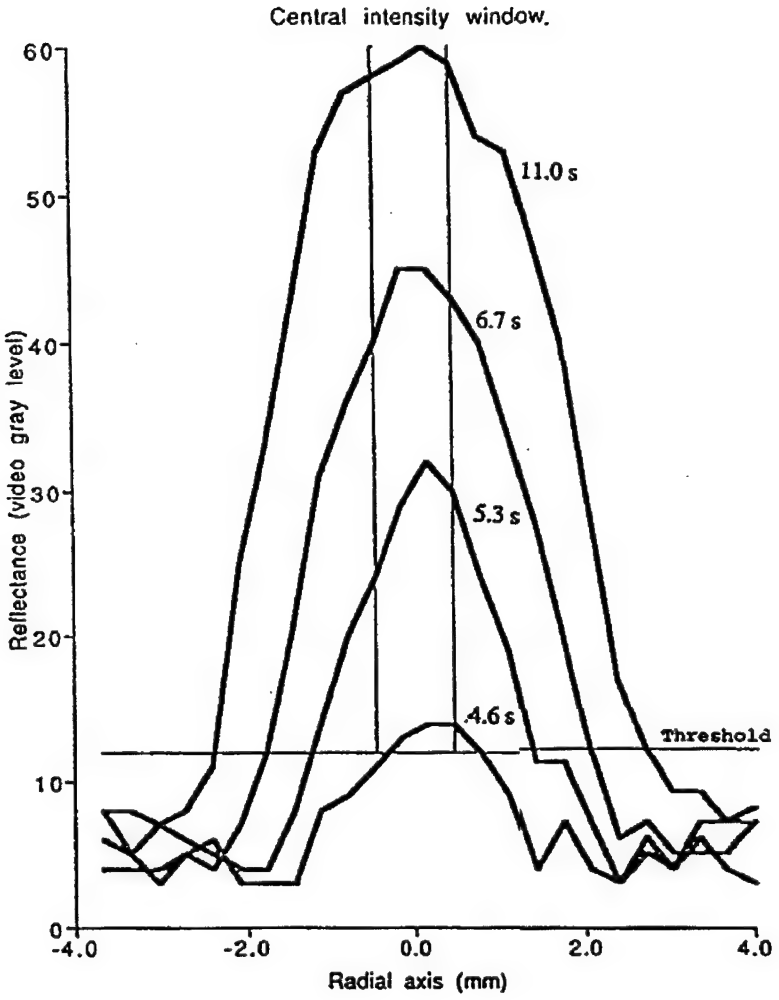

Figure 7.2: Reflectance profile of an albumen eye phantom, obtained with a CCD camera, showing the formation of a laser-induced lesion at several instants during irradiation.

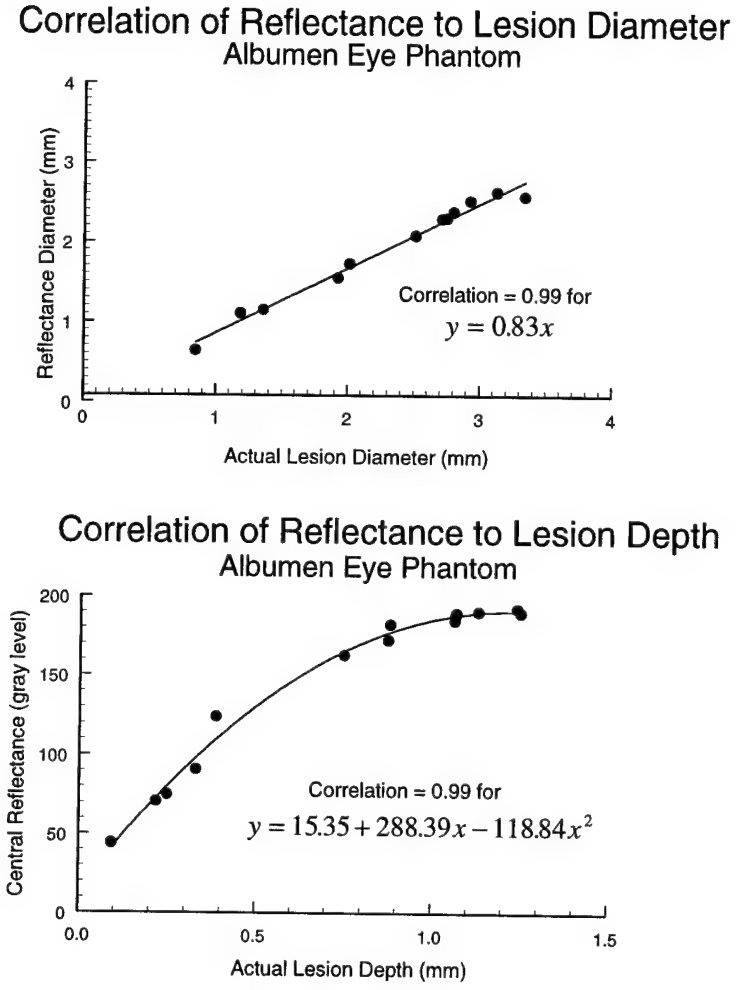

Figure 7.3: Correlation of reflectance to diameter and depth of normal argon laser-induced lesions [1]. Reflectance diameter calculated from above-threshold pixel dimensions.

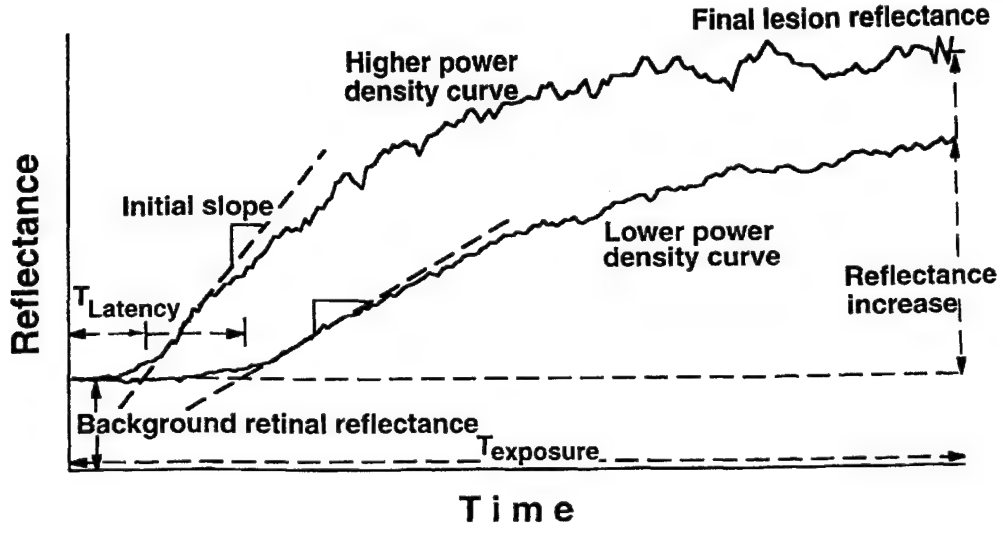

Figure 7.4: Typical signals obtained from a confocal reflectometer during photocoagulation of a rabbit retina.

typical reflectance signals (as obtained by a confocal reflectometer) are shown for two different laser power levels, with the latency and initial slope identified [21].

Since the confocal optics have limited lateral spatial acceptance, the characteristics of the signal obtained depends partly upon the imaged size of the confocal pinhole compared to the size of the retinal lesion. If the confocal spot size is significantly smaller than the anticipated lesion size, then the signal will resemble the central reflectance measurement used by Jerath. If the confocal spot size is the same size or larger than the anticipated lesion size (as was the case for Inderfurth's setup), then the signal measures total reflectance such as used by Weinberg and Birngruber. In general, total reflection is the easier signal to obtain.

7.2.3 Lesion Consistency versus Calibrated Lesion Depth

The time-varying reflectance of a retinal lesion conveys information about its growth during the photocoagulation process. If the ultimate goal of using this signal is to

enable the clinician to produce consistent lesions across the retina independent of RPE variations, then it appears that information derived from total reflectance (such as initial slope and perhaps latency time) has the potential to allow this [16]. On the other hand, if the ultimate goal is the considerably more difficult one of enabling the clinician to produce calibrated-depth lesions (that is, lesions with a specific depth), also independent of RPE variations, then it appears a central reflectance signal would be needed [51]. Calibrated lesion depth is more difficult to implement because no two patients have the same calibration baseline, and this information is not easily obtained. One tool that may assist in this endeavor is optical coherence tomography (OCT); see future work recommendations in Chapter 9.

It is not the purpose of this discussion to decide which lesion control goal is more appropriate, only to point out that the choice of confocal aperture and the information derived from the signal obtained should be made with the appropriate goal in mind.

7.2.4 Motion-Induced Reflectometer Signal Corruption

Inderfurth et al. were not able to derive a control algorithm from their database on human lesion formation. They found that the data were too corrupted by motion artifacts. Since the confocal reflectometer only detects light from the small spot on the object plane that corresponds to the detector's pinhole at the image plane, any movement of the retina caused large variations in the reflectance signal.[2] When the retina was motionless, as with a heavily sedated rabbit, the signal was like that shown in Figure 7.4, but the human subjects exhibited too much movement. These motion artifacts made the real-time extraction of initial slope or latency time impossible. This highlighted the fact that precise eye tracking with a fast response time was a prerequisite to obtaining useful lesion data from a confocal reflectometer on human patients. Chapter 5 discusses retinal tracking.

[2]This phenomenon inspired Ferguson to use this effect for analog tracking (see Chapter 5).

From the work of Inderfurth et al. it is not clear whether latency time and/or initial slope of the reflectance signal provide the necessary information for controlling lesion formation. Jerath's work using central reflectance must also be considered. The technique of applying a reflectance signal to lesion control needs further study.

7.2.5 Lesion Reflectance Acquisition for CALOSOS

As noted in Chapter 3, the author's optical design of CALOSOS incorporates a confocal reflectometer which images the coagulating beam spot on the retina while other parts of the system track the retina and compensate for motion. This allows a usable reflectance signal to be obtained in real-time from the lesion site. A sampling frequency of 1 kHz for the reflectance signal provides sufficient temporal resolution for short irradiations, and the retinal tracking capabilities of CALOSOS mitigate the motion artifacts experienced by Inderfurth. This minimizes the problems which plagued previous attempts to obtain a real-time reflectance signal.

The optical design developed for CALOSOS uses 100 μm confocal pinholes. This aperture size, when propagated through the beam shaping lenses (listed in Appendix B) and the optics of the eye, results in a confocal spot of approximately 320 μm diameter on the retina. Since typical retinal lesions are 300–400 μm diameter, this signal measures the total reflectance of the lesion.

Some initial reflectance data using CALOSOS was obtained by Maharajh [157]. In collaboration with the author, Maharajh used the optical setup designed and built for CALOSOS (shown in Figure 3.4) to obtain real-time dynamic reflectance signals of 100 ms argon laser irradiations of stationary albumen eye phantoms. Maharajh's study investigated latency time, slope, and inflection point of the reflectance signal. He found the strongest correlation between lesion depth and initial slope, indicating this may be the best metric to extract from the reflectance signal to control the depth of a lesion.

If slope is the primary measure, some means must be used to determine its value

in real-time despite the statistical fluctuations obvious in Figure 7.4. A similar problem is discussed by Engelken [158], when determining saccadic eye velocity from the slope of an eye position vector. His recommended approach is to use a median filter followed by differentiation, rather than a totally linear approach. Further investigation is needed.

CALOSOS was also used by the author to obtain real-time reflectance signals of lesion formation during motion, on both albumen eye phantoms and *in vivo* using rabbits. This represents the first time motion-compensated lesion reflectance data has been obtained in real-time for irradiation times as short as 100 ms. See Chapter 8 for test results.

If lesion reflectance is to be used as a control signal, the characteristics of the signal must be understood. What should an ideal lesion reflectance signal look like? A theoretical model of lesion reflectance is helpful as a complement to the empirical studies; this is most easily implemented by using a Monte Carlo simulation.

7.3 Monte Carlo Simulations of Lesion Reflectance

See Appendix A (Section A.10) for a brief introduction to the Monte Carlo technique for modeling laser tissue interactions.

7.3.1 Improving the Simulation Fidelity

Until recently, Monte Carlo simulations have generally relied upon the "infinite slab" approach. Assume the collimated laser beam propagates along the z-axis, and is normal to the tissue surface. A typical model assumes each tissue boundary has a constant z value, and is infinite in the xy plane. This makes the geometry calculations straightforward when moving the simulated photon along its path.

However, actual lesions formed in the retina are not infinite slabs; they have a finite radius. Since we are interested in the reflectance of a lesion as a possible

signal to control its depth as it is being formed, the lesion must be modelled more accurately than by using an infinite slab approach.

The choice of what shape to use for the buried lesion was studied by the author. Almost any finite radius shape should provide an improved simulation of a retinal lesion than provided by an infinite slab geometry, but some shapes will be better than others. A simple cylindrical shape with a finite radius and depth is the easiest to implement, but the sharp edges are not realistic. Weinberg hypothesized that actual retinal lesions grow in the shape of an oblate spheroid, shown conceptually in Figure 2.7. The Monte Carlo simulation is affected only by the shape of the lesion "above" the layer representing the highly absorbing RPE, so only the top half of the shape must be modelled. While a true oblate spheroid geometry would be arduous to implement, a hemisphere with its radial center at the top boundary of RPE layer is easier to implement and provides nearly the same shape. The hemisphere shape should provide a more realistic reflectance response than a "top hat" cylindrical shape. To test this hypothesis, both shapes were implemented.

7.3.2 Implementing a Buried Lesion Model

The programming required to implement the full three dimensional geometry of a photon scattering through such a model is considerably more complex than the infinite slab model, yet as discussed above such fidelity is needed for lesion control signal investigations.

The hemispherical model for the buried lesion, with its radial center located at the top boundary of the RPE layer, is shown in Figure 7.5. Layer 1 represents the low-absorption, non-scattering neural retina; layer 2 represents the low-absorption, highly scattering lesion; and layer 3 represents the highly absorbing RPE. A cylindrical "top hat" model can be envisioned similarly.

Based upon earlier work by Jerath [14], the first (top) layer is given the optical properties of uncoagulated egg white, the second layer (the lesion) is given the

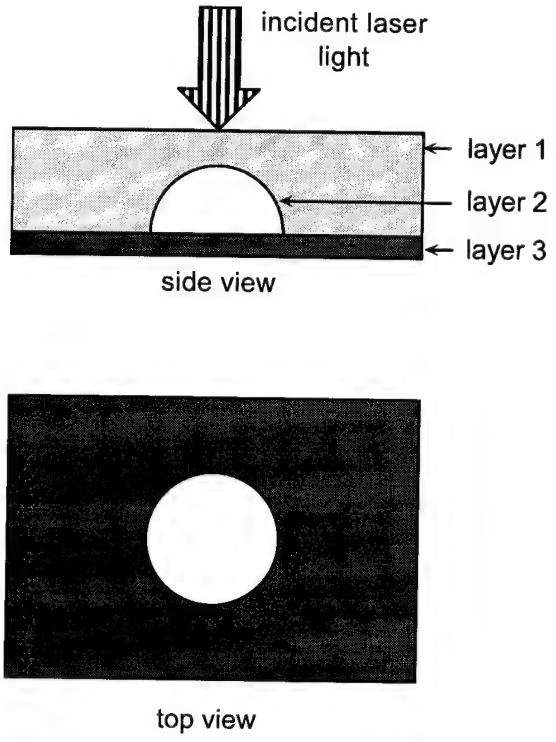

Figure 7.5: The three layer model of an eye phantom with a buried lesion.

Layer	μ_a	μ_s	g
1	0.03	0	0
2	0.03	26.7	0.85
3	50	0	0

Table 7.1: Optical properties of an eye phantom when using an argon laser. Units for absorption and scattering coefficients are mm^{-1}.

optical properties of coagulated egg white, and the third (bottom) layer is given the optical properties of the black paint (all at the wavelengths of an argon laser). These values mimic the behavior of the human eye, and can be easily assembled for empirical verification with an albumen eye phantom (see Appendix A). The numeric values are shown in Table 7.1. Since lesions forming in an eye do so in an index-matched environment, the model assumes no change in n between layers. Even with a relatively simple shape as a half sphere, the many possible photon paths are difficult to handle properly in the presence of the buried lesion.

For example, Figure 7.6 shows some possible paths, with a starting and ending point for a given photon, in a two dimensional top view of the phantom. The most difficult case to handle is when the photon passes completely through the lesion, since a simple check of the beginning and ending points would not reveal the complete story. This condition must be detected, and the photon must be moved back to the first boundary crossing, the optical properties updated, and the path recomputed.

There is a direct analytic solution to determine if the photon *could* have passed through the lesion. For simplicity, we assume the two dimensional case in the xy plane; hence the lesion boundary appears as a circle. If an infinite line coincident with the photon path intersects the circle, where the circle is defined by $x^2+y^2 = R^2$ and the line by $y = ax + b$, then the photon *may* have passed through the lesion.[3] The beginning and ending positions of the photon are x_1, y_1 and x_2, y_2. Thus:

$$a = \frac{y_2 - y_1}{x_2 - x_1}$$

[3]Note that for the hemispherical model of a buried lesion, the radius R is also equivalent to the thickness of the lesion.

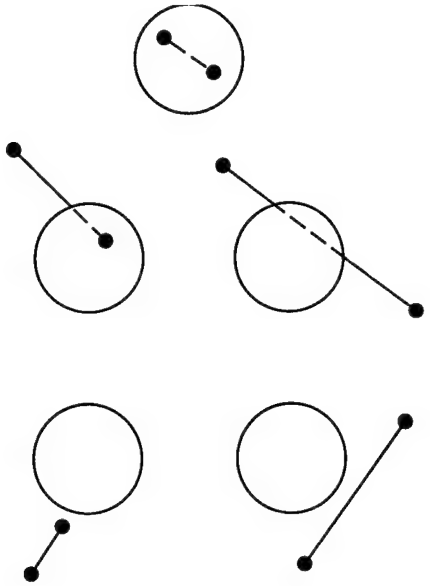

Figure 7.6: A few possible photon paths in the eye phantom (top view). The dashed line indicates where the photon would pass through the buried lesion.

$$b = y_2 - ax_2$$

$$\begin{aligned} x^2 + (ax + b)^2 &= R^2 \\ x^2 + (ax)^2 + 2abx + b^2 &= R^2 \\ (1 + a^2)x^2 + 2abx + (b^2 - R^2) &= 0 \end{aligned}$$

Then let $A = 1 + a^2$, $B = 2ab$, and $C = b^2 - R^2$. Solve for

$$x = \frac{-B \pm \sqrt{B^2 - 4AC}}{2A}$$

to see if an intersection exits. If the radical is negative, no intersection is possible; if the radical is zero, the line is tangent to the circle; if the radical is positive, there are two possible intersection points. In the last case, the points must be evaluated to see if they are on the actual photon path (between the beginning and ending points), checked for the appropriate z value, and the photon path adjusted as needed. The overall operation of the software is shown graphically in Appendix A (Figure A.19).

7.3.3 Model Results

The results of the Monte Carlo simulation with a buried lesion should yield a prediction of the actual signal. Since an albumen eye phantom is most easily used as a first order verification of the model, the parameters listed in Table 7.1 were used for an evaluation of the Monte Carlo model. Other controlling parameters specified were 5000 photons,[4] a Gaussian laser beam (power is normalized) having a diameter of 750 μm, the "top" layer (uncoagulated egg white) had a thickness of 2 mm, the "bottom" layer (black paint) had a thickness of 0.01 mm, and the lesion thickness ranged from 0–1.8 mm. Note that for the hemisphere model, radius and thickness of the lesion refer to the same value. For 100 data points, the thickness increment (or radius increment for the hemisphere) was 18 μm. A cylindrical model and a hemispherical model of a buried lesion were simulated. The cylindrical model results, for four different lesion radii, are shown in Figure 7.7. The hemispherical model results are shown in Figure 7.8, where the radius is equivalent to the thickness.

Note the greater similarity in shape between the response of the hemispherical model of Figure 7.8, and the actual data of Figure 7.4, compared to the response of the cylindrical model of Figure 7.7. It appears that the sharp edges of the cylindrical model result in a less realistic response curve than the more biologically accurate hemispherical model. The actual reflectance signal response in an albumen eye phantom found by Maharajh [157] and the author using the confocal reflectometer of CALOSOS also more closely matched the hemispherical model of Figure 7.8. Thus the hypothesis is supported that the hemispherical model is the more accurate method to simulate a dynamic confocal reflectance signal for laser-induced lesions.

This model will be especially useful for future studies that explore variations on the confocal aperture and its effect on the reflectance signal. Assuming the model has sufficient fidelity, much of that work could be accomplished via simulation. In the

[4]Since only reflectance was desired, only 5000 photons were needed [41]. Larger numbers of photons (up to 10^5) were tested, but did not change the outcome of the simulation.

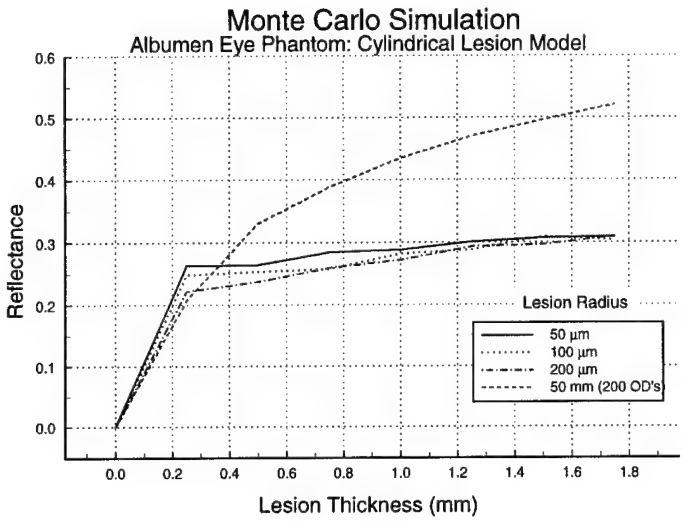

Figure 7.7: Monte Carlo simulation of buried cylindrical lesion in an albumen eye phantom. Gaussian laser beam (power is normalized) having a diameter of 750 μm and $\lambda = 488$ nm and 514 nm; 5000 photons simulated.

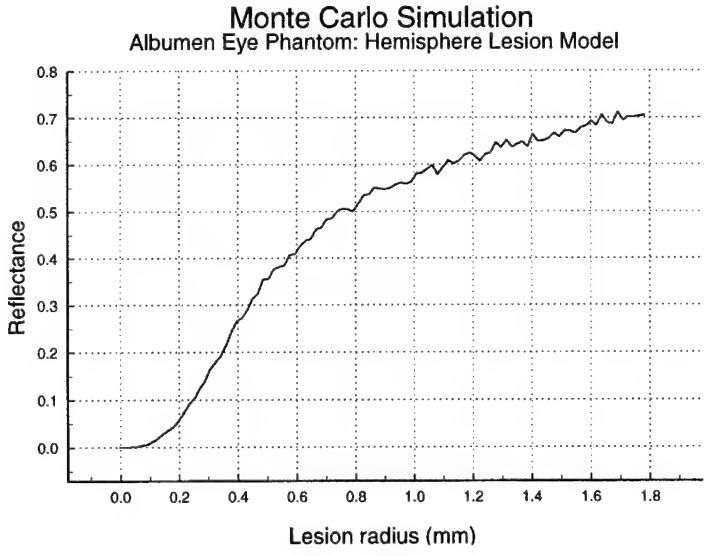

Figure 7.8: Monte Carlo simulation of buried hemispherical lesion in an albumen eye phantom. Gaussian laser beam (power is normalized) having a diameter of 750 μm and $\lambda = 488$ nm and 514 nm; 5000 photons simulated.

course of comparing this model to real world lesion formation, however, the author discovered that in certain laser power regimes, the resulting lesions formation did not conform to this or any other known model.

7.4 Lesion Reflectance Anomalies

The expected monotonic increase (on average) in reflectance with irradiation time—and the associated correspondence with lesion diameter and depth—is not always valid. Lesions have been observed by the author, and confirmed by others, that exhibit an annular reflectance pattern (a bright ring surrounding a dark center), which cannot be explained by current models. This annular shaped reflectance has been measured even though the laser irradiance profile had a Gaussian shape.

7.4.1 Investigative Methods

To ascertain whether these anomalous lesions were reproducible, the author and Barton [159] set out to intentionally create anomalous lesions. An albumen eye phantom (fresh clear egg white at 22 °C covering a highly absorbing black surface) was irradiated with an argon laser (a Coherent Model 900 Photocoagulator, $\lambda = 488$ and 514.5 nm) having a Gaussian beam profile and a 750 μm diameter spot on the phantom, to create a total of 320 lesions. The first 20 lesions were used to test the absorption uniformity of the eye phantoms. After verifying that any spatial variation of the phantom absorption was negligible, 300 data lesions were created. A lesion at each of 100 different power settings (75 mW to 200 mW, with increments of approximately 1.25 mW between settings) was created at a constant irradiation time of 0.5 seconds per lesion. This procedure was repeated two more times for the total of 300 data lesions. The eye phantoms were illuminated with a uniform diffuse white light source, and imaged using a standard RS-170 CCD camera (Sony XC-75 with 768×484 pixels) with a F/5.6 macro lens, such that the spatial dimensions of each camera pixel was approximately 300 μm square. After all the lesions were

created and imaged, the actual depth of each lesion was then physically measured using a confocal microscope (Zeiss Laser Scan Model 10), and the actual diameter was measured using a standard microscope with calibrated reticule.

No in vivo tests were conducted, but archival fundus camera images were used to compare with *in vitro* results from the albumen eye phantom.

7.4.2 Results

Normal lesions were formed at power levels up to approximately 180 mW. At power levels greater than 180 mW, anomalous lesions were formed with a roughly annular reflectance pattern. At the highest power levels, an occasional popping sound could also be detected. Close visual inspection revealed the dark lesion center was often not homogeneous, but consisted of several small dark regions surrounded by a thin bright membrane giving the appearance of multiple bubble formation at the center of the lesion. An anomalous lesion with a dark center is shown in Figure 7.9. Some of the dark regions did not have intact membranes; they resembled craters in the central surface of the lesion.

When the reflectance from the lesion image was compared with the actual measured values, the diameter correlated to reflectance for both normal and anomalous lesions. However, this correlation was not true for lesion depth. In Figure 7.10, the average lesion central reflectance versus actual average measured depth for the lesions formed at all 100 power settings is shown. Note how the central reflectance of the anomalous lesions shows little or no correlation to lesion depth whereas the normally formed lesions show the typical strong correlation.

Observations indicated that under certain conditions during irradiation, the reflectance of the lesion center first began to rise normally, then actually *decreased* for these anomalous lesions. Under other conditions the central reflectance of the anomalous lesions simply lagged behind the lesion periphery. The specific conditions are still being investigated.

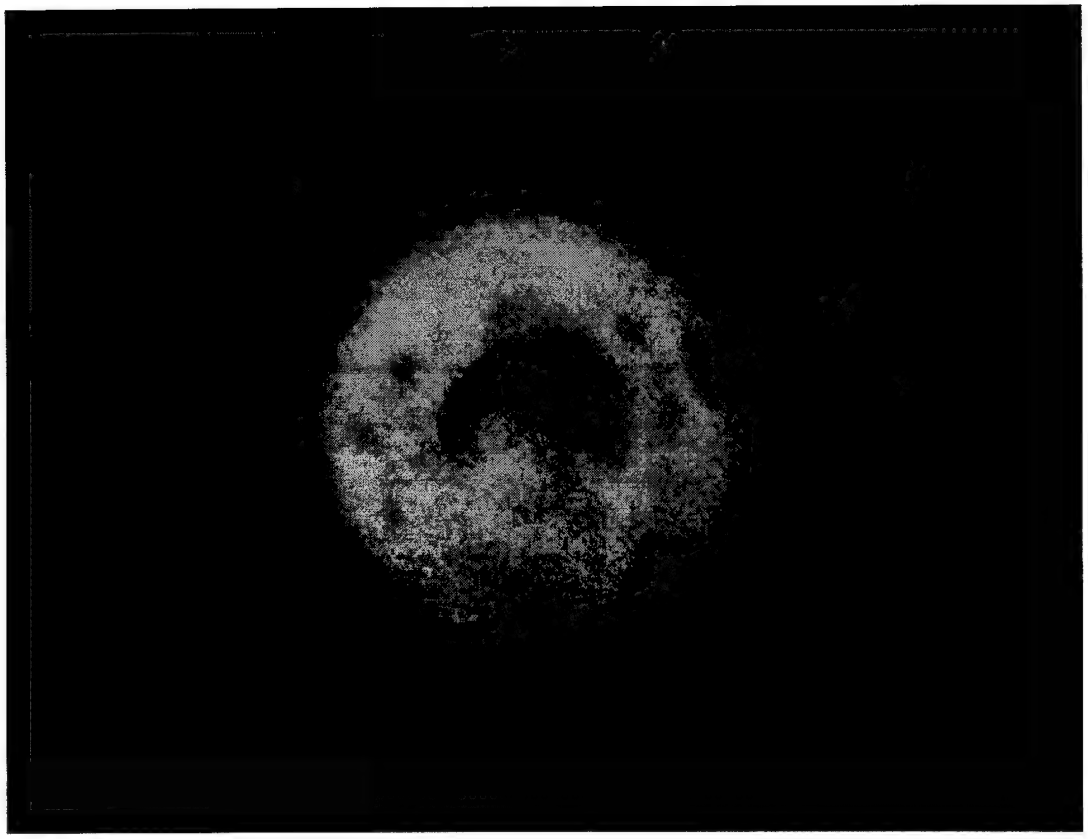

Figure 7.9: Anomalous lesion (900 μm diameter) formed in an albumen eye phantom. Bubbles at the center of the lesion result in a lower reflectance and hence an overall annular reflectance pattern. Gaussian beam profile, $\lambda = 488$ and 514 nm, 750 μm spot, irradiation time of 0.5 s at 195 mW.

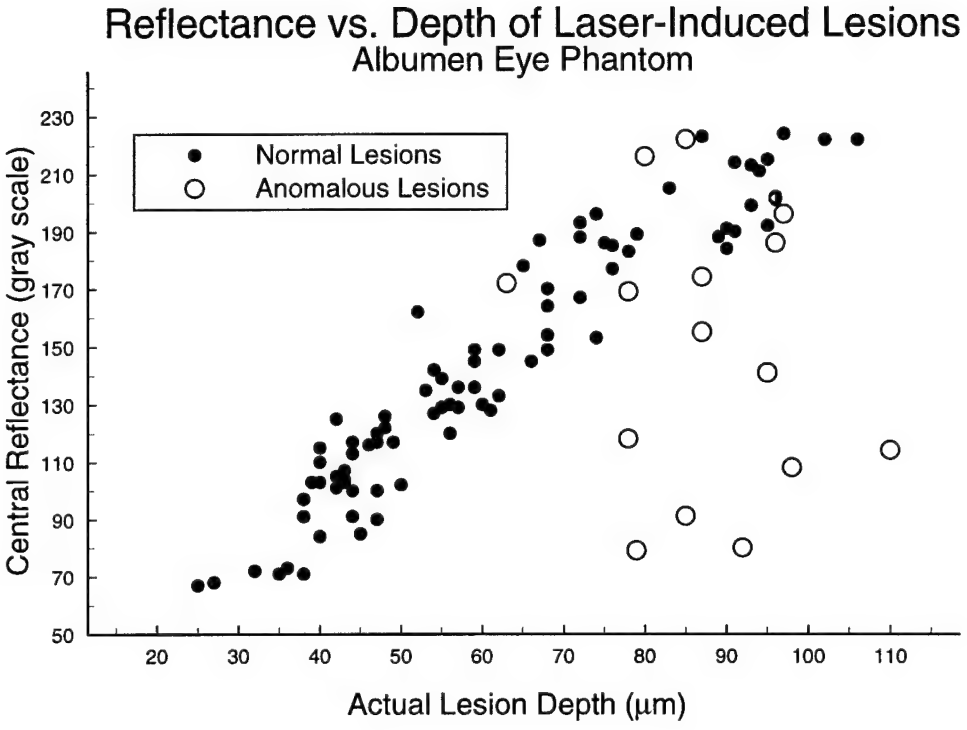

Figure 7.10: Reflectance vs. depth of normal and anomalous lesions. Anomalous lesions were those exhibiting an annular reflectance pattern. Central reflectance was determined as the average of the central 300 μm of each lesion. Total size of each lesion ranged from 400–1500 μm in diameter.

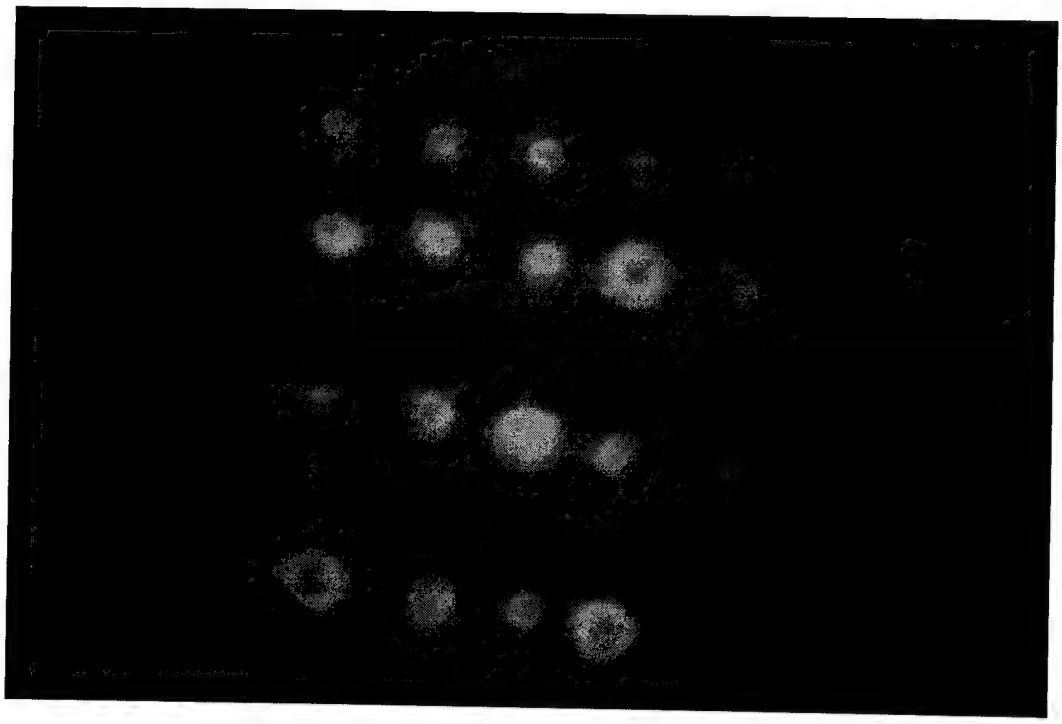

Figure 7.11: A fundus camera 20° FOV showing anomalous lesions (having an annular reflectance pattern) in a rhesus monkey retina following argon laser photocoagulation. Gaussian beam profile, $\lambda = 514$ nm, 500 μm spot, irradiation time of 7 ms at 287 mW/cm^2. Used with permission from Walter Reed Army Institute of Research, U.S. Army Medical Research Department, Brooks AFB, TX.

The phenomenon is not confined to albumen eye phantoms, but is also found *in vivo*. Figure 7.11 shows anomalous lesions having an annular reflectance pattern on the retina of a rhesus monkey following argon laser photocoagulation.

7.4.3 A Possible Explanation

Since anomalous lesions were created only at the higher power levels, the critical factor is likely associated with a photothermal effect related to the laser power. Continuous wave lasers such as argon photocoagulators seldom induce photomechanical effects [160], but vaporization bubbles may occur when temperatures exceed 100

°C. Optically speaking, photocoagulation of the retina is due to light absorbed in the retinal pigment epithelium (RPE); scattering is insignificant [161]. In this case, the maximum rate of heat deposition per unit area is directly proportional to the output power of the laser and the absorption coefficient of the tissue, and inversely proportional to the laser beam spot size. In this experiment, the absorption coefficient and laser spot size were held constant; only the laser power was varied. As power was increased the rate of heat deposition increased, and therefore the tissue temperature increased.

The visual observation of the appearance of bubbles or craters in the center of an anomalous lesion and the detection of an occasional popping sound were associated with the annular reflectance pattern. A similar phenomenon, dubbed the "popcorn effect," was found from pathologic analysis of soft tissue described by Thomsen in [162]. Thomsen postulates that when tissue temperatures exceed the vaporization temperature of water (100 °C), one of the effects is the formation of subsurface pockets of superheated steam and tissue constituents which affect the progression and rate of further photothermal injury. These bubbles, seen microscopically by Thomsen to be extracellular vacuoles formed between subsurface layers of coagulated tissue, enlarge with further irradiation and can rupture explosively, resulting in a popping sound. Thomsen's observations are further supported by the work of others [160, 163–166]. While the laser thermal ablation experiments of Thomsen and others cited did not test photocoagulation of retina or retinal phantoms, it seems reasonable to infer that the anomalous lesion formation was due to a similar phenomenon, *if* the tissue temperature exceeded the threshold of 100 °C.

To ascertain whether the tissue temperature exceeded 100 °C, the temperature was computed using a simplified thermal model of transient heat flow in an infinite composite solid with constant heat flux [167, Chap. 2]. In this model, the flow of heat is linear, with the lines of flow parallel to the x axis, and the isothermal surfaces are planes perpendicular to the x axis. The two dissimilar materials meet

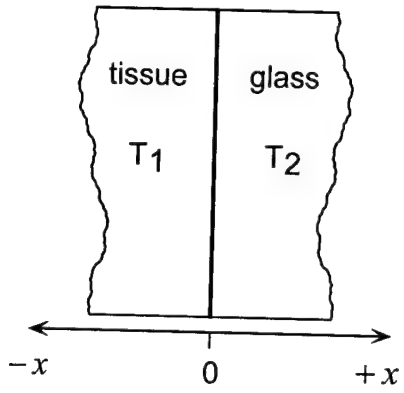

Figure 7.12: Schematic for thermal model of an infinite composite solid.

at the plane of separation defined by $x = 0$. To model the albumen eye phantom, an infinitesimally thin absorbing layer at $x = 0$ was assumed with tissue on one side and pyrex glass on the other side (see Figure 7.12). Absorption of the laser light at $x = 0$ produced a constant heat source that created a constant heat flux q_0/A which conducted into the tissue (where $x < 0$) and into the glass (where $x > 0$). This one dimensional model provided an estimate of temperature at the center of the laser spot. Note that albumen eye phantoms, despite the absence of choroidal blood flow, still provide a good thermal analog to the eye since perfusion is not a significant factor in the thermal response of retinal photocoagulation [168].

The tissue was assumed to begin at an initial temperature $T_i = 22$ °C. The computed temperature of the solid is a function of position and time where $T_1(x,t)$ is the temperature in the tissue (for $x < 0$), and $T_2(x,t)$ is the temperature in the glass (for $x > 0$). Note: the subscripts 1 and 2 are used below to denote properties for tissue and glass respectively. The boundary conditions at the plane of separation were

$$T_1 = T_2 \quad \text{for } x = 0,\ t > 0 \tag{7.1}$$

$$k_1 \frac{\partial T_1}{\partial x} = k_2 \frac{\partial T_2}{\partial x} \quad \text{for } x = 0,\ t > 0 \tag{7.2}$$

where k is the thermal conductivity. From [167], the solution in this case to Equations 7.1 and 7.2 for the tissue temperature T_1 is

$$T_1 - T_i = \frac{2q_0}{A} \cdot \frac{\sqrt{\alpha_1 \alpha_2 t}}{k_1\sqrt{\alpha_2} + k_2\sqrt{\alpha_1}} \cdot \text{ierfc}\frac{|x|}{2\sqrt{\alpha_1 t}} \tag{7.3}$$

where α is the thermal diffusivity and ierfc is the integral of the complementary Gaussian error function [167, Appendix II]. Since the primary interest is in the temperature of the tissue in contact with the surface of the absorbing layer, only the temperature T_1 for $x = 0$ must be calculated. Thus for a given time t, the surface temperature from Equation 7.3 is

$$T_1 = \frac{2q_0}{A} \cdot \frac{\sqrt{\alpha_1 \alpha_2 t}}{k_1\sqrt{\alpha_2} + k_2\sqrt{\alpha_1}} + T_i \tag{7.4}$$

Using the thermal properties for tissue and pyrex glass from [169, Table 15.5], set $k_1 = 0.50$ W/(m $\cdot$ °C), $\alpha_1 = 130 \times 10^{-9}$ m^2/s, $k_2 = 1.4$ W/(m $\cdot$ °C), and $\alpha_2 = 754 \times 10^{-9}$ m^2/s. Note that similar values can also be found in [170, Table A.3]. The 750 μm laser spot diameter results in $A = 442 \times 10^{-9}$ m^2 and q_0 (assuming negligible absorption except in the absorbing layer) is simply the laser beam power in W, first multiplied by 0.865 to account for the fraction of power within the $1/e^2$ Gaussian beam radius.

Equation 7.4 was evaluated for the range of laser power used (75–200 mW) versus time (0–0.5 s). The result is shown graphically in Figure 7.13. This graph does not take into account the phase change of water and the required pressure-dependent heat of vaporization [163]. Figure 7.13 clearly shows that the tissue of the retina or eye phantom at the center of the laser beam can reach the temperature regime of laser thermal ablation as described by Thomsen and others.

For a finite Gaussian laser beam, the maximum irradiance occurs at the center of the beam. Thus, vaporization would be initiated at nucleation sites in close proximity to the center of the irradiance. The hypothesis is therefore reasonable that the annular reflectance pattern of the anomalous lesions is due to some form

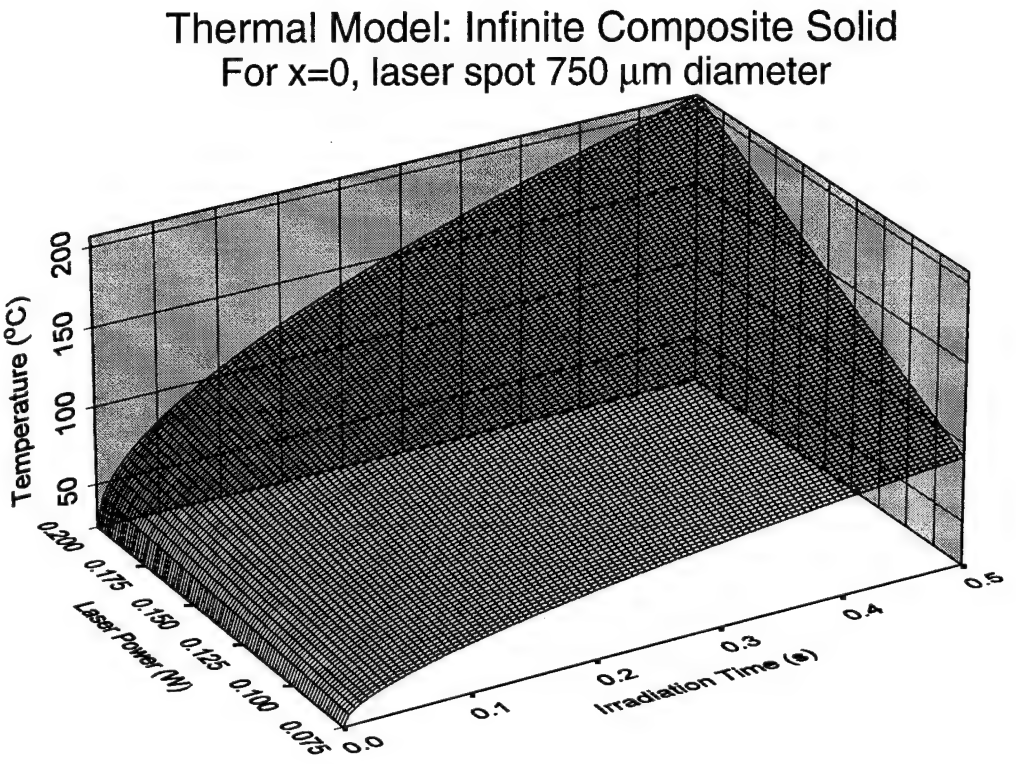

Figure 7.13: Theoretical tissue temperature using the simplified thermal model of an infinite composite solid, consisting of tissue and glass. Note that the phase change of water and the pressure-dependent heat of vaporization is not reflected in this graph.

of laser thermal ablation similar to the "popcorn effect." Further experiments are needed which seek to quantify the threshold of anomalous lesion formation.

7.4.4 Conclusions Regarding Anomalous Lesions

In the past, occurrences of annular lesions in clinical patients have often been assumed to be due to hemorrhage, but the author's investigations of dynamic lesion formation in albumen eye phantoms and archival fundus photo examination of human photocoagulation patients show that a dark center can form independent of any hemorrhage.

The lack of correlation of actual lesion depth to the reflectance of anomalous lesions has several ramifications. Postoperative examination of fundus images may not provide reliable information about lesion depth. More disturbing, however, is the implication that retinal lesion formation is not well understood when tissue temperature exceeds 100 °C. More research is needed on dynamic lesion formation and lesion reflectance, especially for short duration pulses where bubble formation and collapse produce strong acoustic transients [165,171,172]. Until more is understood about the exact mechanisms involved which can result in these anomalous lesions, use of reflectance to infer lesion morphology must be used with caution. The possible occurrence of microscopic vaporization bubbles owing to excessive heat must be considered in efforts to quantify and standardize photocoagulation dosimetry [20]. Most importantly for this research, any effort to use reflectance as a feedback control signal for automated photocoagulators [52] must consider the effect of retinal tissue vaporization on the reflectance image.

7.5 Summary of Reflectance as a Lesion Control Signal

From an engineering development point of view, reflectance-based lesion control is far from perfected. The decision of whether to use a large confocal spot yielding total reflectance, or a small confocal spot yielding central reflectance, must be re-

solved in the context of the "consistent lesion versus calibrated-depth lesion" issue. There are still more questions that must be answered about lesion reflectance, in particular with regard to anomalous lesion formation. However, the technique still has significant potential for bringing a measure of real-time control to the lesion formation process of clinical retinal photocoagulation. With the design of CALOSOS, there now exists the capability to acquire a lesion reflectance signal in a clinically realistic scenario.

Chapter 8

CALOSOS System Operation and Test Results

This chapter outlines a typical operational scenario for CALOSOS, then describes the various system tests conducted as part of this research. The test results involving simulated retinas, eye phantoms, and *in vivo* using laboratory animals[1] are presented. This is followed by some observations gleaned during the tests, which will lead naturally into the next and final chapter of this dissertation.

8.1 System Operation

The user of this system typically follows the following order of tasks:

1. Get the patient situated and comfortable.

2. Align the laser and the computer coordinate systems. This involves using the various alignment patterns with the low power aiming beam; the patterns can be seen on the computer display as they are projected on the patient's retina.

[1] All animals involved in this study were procured and cared-for in accordance with the Animal Welfare Act and the "Guide for the Care and Use of Laboratory Animals" prepared by the Institute of Laboratory Resources of the National Research Council (NRC). Both the Animal Resource Center (at the University of Texas) and the Armstrong Laboratory (at Brooks AFB, TX) are fully accredited by the American Association for Accreditation of Laboratory Animal Care (AAALAC).

3. Build a template on appropriate blood vessels for digital tracking and establishing an image coordinate system. The computer finds the best selections from the area designated by the user.

4. Irradiate once (in a safe area of the retina) to create a reference lesion if one is not already present (for hybrid operation only).

5. Click the mouse on the reference lesion to tell the computer what the reference offset is (for hybrid operation only).

6. Specify a pattern of lesions as desired.

7. Begin photocoagulation.

The user can then repeat this procedure for additional lesion patterns without need for realignment, unless the patient has moved significantly.

During the actual photocoagulation, the software operation can be seen graphically in Figure 8.1. The box labelled "digital tracking: update offsets" was previously defined in Figure 5.2. Earlier chapters have given detailed descriptions of the various operations depicted in Figure 8.1. Note that in hybrid operation, the analog tracking signal is continuously updating the voltage to the main steering galvanometers directly, without intervention by the computer.

Recall that at the current level of integration, digital tracking and analog tracking cannot be used simultaneously (see Chapter 5). In hybrid operation, the digital computer provides beam steering information for the desired lesion pattern, timing and control of the laser shutter, and monitors patient and lesion status lines, but only the analog tracker compensates for eye movement. It is anticipated that future versions will allow both types of tracking at once.

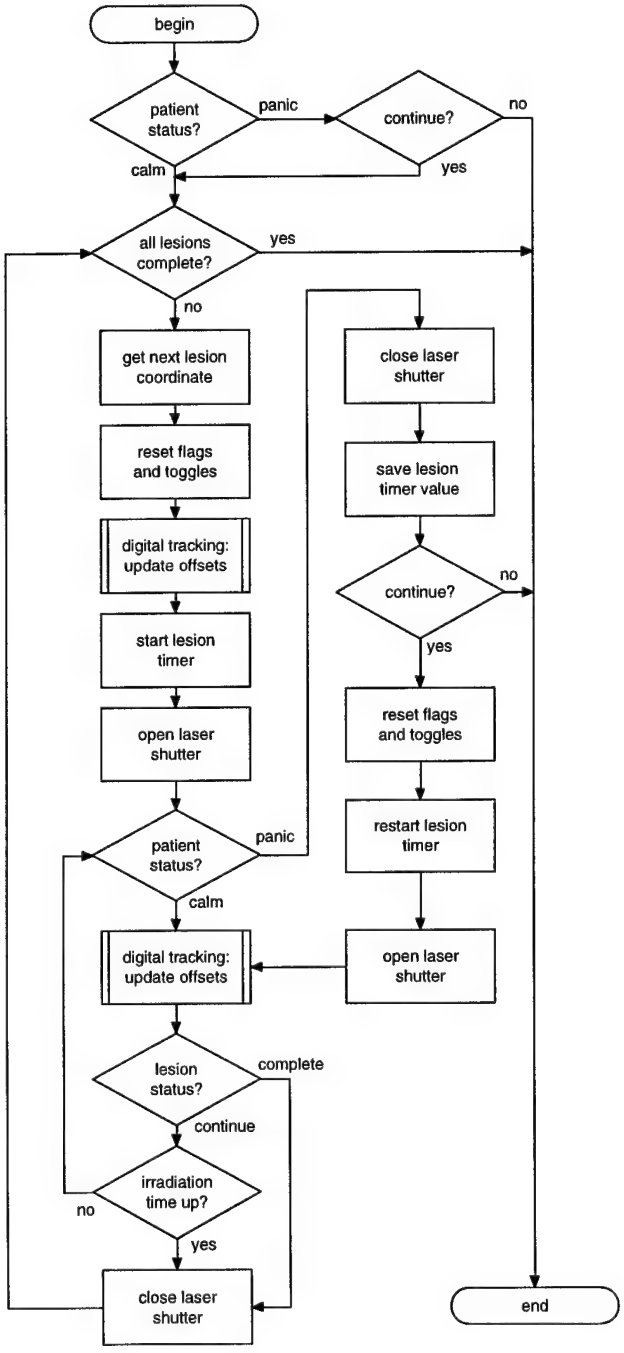

Figure 8.1: Flowchart of CALOSOS software during photocoagulation.

8.2 System Test

To test and evaluate the operation of the current design as a system for photocoagulation, experiments were performed on a simulated picture of a human retina, *in vitro* using an albumen eye phantom, and *in vivo* using rabbits and monkeys. The reader may wish to review the electronics and optical setup described in Chapter 3 and shown in Figures 3.3, 3.8, 3.4 and 3.9. If a test was specific to the all digital or to the hybrid implementation of CALOSOS, the distinction is made below as needed. In the following discussion, the term "forward optical path" is used to indicate the direction of photons from the argon laser delivery fiber to the target, and the term "reverse optical path" is used to indicate the direction of photons from the target back through the reciprocal optical path. For all tests, the argon laser delivered power primarily at two wavelengths: $\lambda = 488$ nm and 514 nm.

There were many incremental tests performed during development of CALOSOS. The tests listed below are the most representative of the overall system operation, and were chosen to provide the reader with the best insight into the strengths and weaknesses of the current design.

8.2.1 Tests Using a Simulated Retina

These tests were performed to evaluate the ability of the system to track a moving "retina" at various tracking signal to noise ratios (SNR_T), update the laser pointing as needed, direct the beam through the pupil of the eye at various scan angles, and obtain a reflectance signal from a confocal reflectometer through all the optical elements in the light path.

Test Setup 1

This test was performed for digital tracking only, and did not use the laser. The equivalent of this test was performed on the analog tracker using an eye phantom as described later in this chapter. The optical setup shown in Chapter 3 (see Figure 3.4)

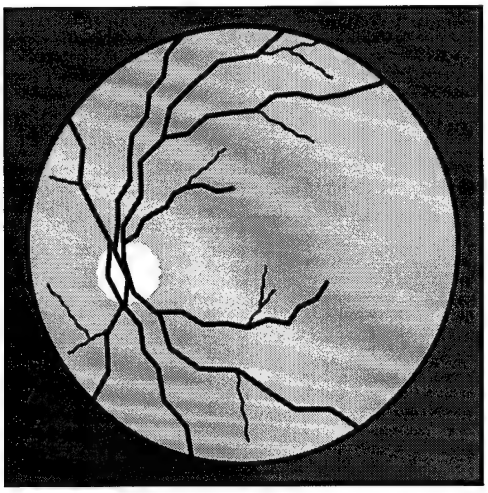

Figure 8.2: A simulated retina used for testing CALOSOS. Blood vessels were simulated using a fractal algorithm to enhance realism.

was used without the fundus camera, the attached scanning lens (Ls) or beamsplitter (BS). The fundus camera was not used for this test because its field flattening ophthalmoscopic objective lens would distort the planar simulated retina. An $f = 50$ mm F/1.4–F/32 (adjustable in half-stops) lens was used for the CCD camera in place of the fundus camera optics. The illumination was provided by normal overhead lights in the laboratory. The simulated retina, shown in Figure 8.2, was placed 800 mm from the CCD camera focal plane (to allow the camera lens to come to focus).

Figure 8.2 was printed at a size such that the image filled the CALOSOS computer screen as an actual retina would if the fundus camera were used; the physical diameter of the simulated "fundus" was 90 mm. The computer screen diameter was 450 pixels, measured along either of the Cartesian axes.

The simulated retina was attached to the pen holder carriage of an upright XY plotter (Hewlett-Packard model H14-7005B), to allow controlled movement of the target during the test. The signal voltages to drive the XY plotter were generated in one of two ways: using an external signal generator (BK Precision model 3011B)

for periodic movement (sine and triangle wave), or using the analog outputs of a data acquisition card (Data Translation DT2801 installed in a 66 MHz 486DX2 PC) for random movement (zero mean Gaussian distribution).

The tracking signal-to-noise ratio SNR_T (recall Equation 4.10 and Figure 4.6) was controlled by printing multiple versions of Figure 8.2 with different brightness backgrounds. Fine tuning the SNR_T was possible by adjusting the lens aperture at the CCD camera. While the tracking SNR is defined to be invariant to uniform changes in illumination, the "blood vessels" were very dark (having a low valued gray scale) at all lighting levels, so that adjusting the lens aperture affected the brightness of the simulated fundus background's gray scale value more than the blood vessel gray scale value, thereby changing the SNR_T.

Test Procedure

The XY plotter was driven with signals of various frequencies and amplitudes to simulate a variety of retinal velocities. The maximum physical deviation was approximately 50 mm (peak) due to FOV limitations. A given velocity was tested at both a large deviation and a small deviation to test for sensitivity to excursion magnitude. For example, 50 mm at 1 Hz and 5 mm at 10 Hz result in equivalent velocities. While the XY plotter could not respond faster than 9 Hz, this was more than adequate.

The usable SNR_T depends upon the contrast of the actual "blood vessels" used to form the template. Therefore, the SNR_T was determined from the total template response (which is a scaled measure of the blood vessel contrast) provided by the system software and Equation 4.10. Specifically,

$$\mathrm{SNR}_T = 20 \log_{10} \left(\frac{T_R}{6 \cdot 1020} \cdot 213.3 \right) \tag{8.1}$$

where T_R is the total template response, the factor of 6 averages the value for the six 1-D templates that make up the 2-D template, the factor of 1020 divides out the

scaling factor used in the template response, and 213.3 is the maximum image SNR value of $2^n/\sigma$ determined in Chapter 4.

Since the input voltage to the XY plotter is a position signal, the instantaneous velocity is the derivative with respect to time. The maximum velocity of the simulated retina can be determined for periodic motion by measuring the physical displacement, multiplying by the input frequency, and adjusting for the waveform shape. For a triangular wave, the maximum velocity equals the average velocity. The maximum velocity of a sine wave is at the zero crossing (assuming a zero average value). At this point the derivative is a cosine, and the maximum velocity is thus equal to 2π times the amplitude of the sine wave. Measurements for random signals are more indirect. For random motion at a known rate of voltage changes per second, the signals sent to the XY plotter were stored, and the volts/mm sensitivity of the XY plotter was measured with a known signal. The actual displacement, and thereby the actual velocity, could then be calculated.

The actual velocity is not a very useful figure, however; the equivalent retinal velocity is a more meaningful number with which to evaluate CALOSOS. The equivalent retinal velocity was determined by utilizing the fact that under normal operating conditions with the fundus camera in the setup, the retinal image diameter would equate to a 50 degree FOV. Since the retinal image fills a 450 pixel diameter circle on the computer screen, there are 9 pixels/degree. Maximum excursion was determined from frame by frame analysis of video tape, and the maximum velocity was determined as described in the paragraph above. For example, if the simulated retina moved 90 pixels in 0.5 seconds this would equate to 20 deg/sec equivalent retinal velocity.

Loss of lock for various velocities was forced by temporarily obscuring the CCD camera lens. This allowed the relock routine to be tested.

An important criterion of tracking in addition to its velocity capabilities is the potential for false positives, which would result in a tracking position error. This

is difficult to quantify in a meaningful manner since the susceptibility to false positives is highly dependent upon the choice of template locations. The closer the template pattern is to a unique pattern (in both the x and y directions), the lower the probability of encountering a false positive. See Chapter 5 for how false positives are minimized. The various tracking tests used the best template that still allowed the necessary image excursion. By recording the tracking correction signal and comparing it to the XY plotter signal, a false positive could be identified.

An additional verification of the digital tracking ability was obtained by using a video tape of a rhesus monkey retina, obtained during tests at Armstrong Laboratory (Brooks AFB, TX) in collaboration with Dr. Steven Barrett. The retina was moving at less than 10 deg/sec.

Test Results

Note that these results measure the tracking system only; the laser pointing and control system was not involved. The overall results of the digital tracking test are summarized in Figure 8.3, where the values indicate the maximum tracking speed before losing lock.

For one of the random signals with velocities below the maximum for the SNR_T, the recorded values are normalized and plotted in Figure 8.4 for visualization of the path taken by the XY plotter and to demonstrate the fidelity of the tracking correction signal determined by CALOSOS.

The system had different sensitivities to amplitude (i.e. displacement of the XY plotter) and frequency. While a displacement of 10 mm at 1 Hz stresses the system with the same velocity as a displacement of 1 mm at 10 Hz, the system response was not the same. Typically, the maximum velocity before losing lock was invariant to this interplay between amplitude and frequency (assuming the displacement did not move the templates out of the FOV), but the fidelity of the tracking signal was much more sensitive to frequency than amplitude. This effect can be seen in Figure

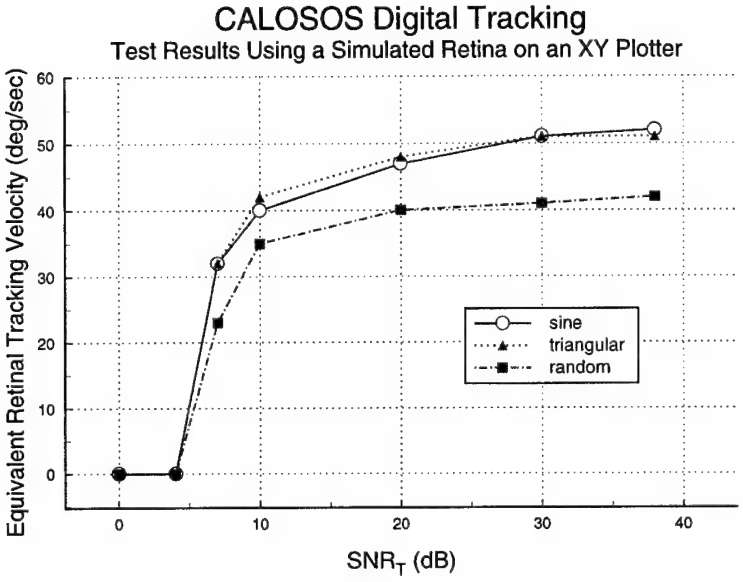

Figure 8.3: Results of the digital tracking tests for CALOSOS. Note: typical *in vivo* SNR_T seldom exceeds 20 dB.

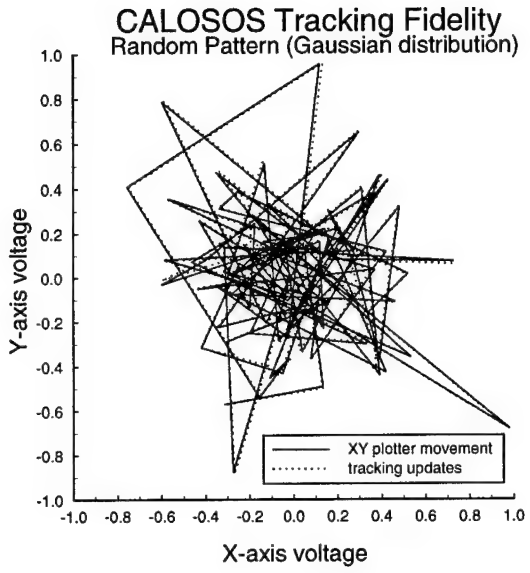

Figure 8.4: Example of random movement for the digital tracking test.

8.5, where the tracking fidelity deteriorates with increasing frequency due to the 30 frame/second update rate of the digital tracker.

When the system lost lock, the zoom-out, zoom-in relock routine was able to relock within six seconds or less (this operation is primarily CPU-limited) if the velocity was below the maximum tracking capability for the given SNR_T. If velocity was above the maximum, the system lost lock unintentionally, and it was not able to relock unless the velocity was reduced. After 50 unsuccessful tries to relock, the tracking routine automatically aborts to avoid an endless loop.

False positives were very rare in all the tests. For the sine and triangular movements, a false positive of one or two pixels occurred on average once every 500 cycles of the displacement signal only near the maximum velocity for a given SNR_T. At lower velocities for a given SNR_T, no false positives were observed during 1000 cycles. For random movements, false positives occurred more often, occurring on average once every 225 displacements only near the maximum velocity for a given

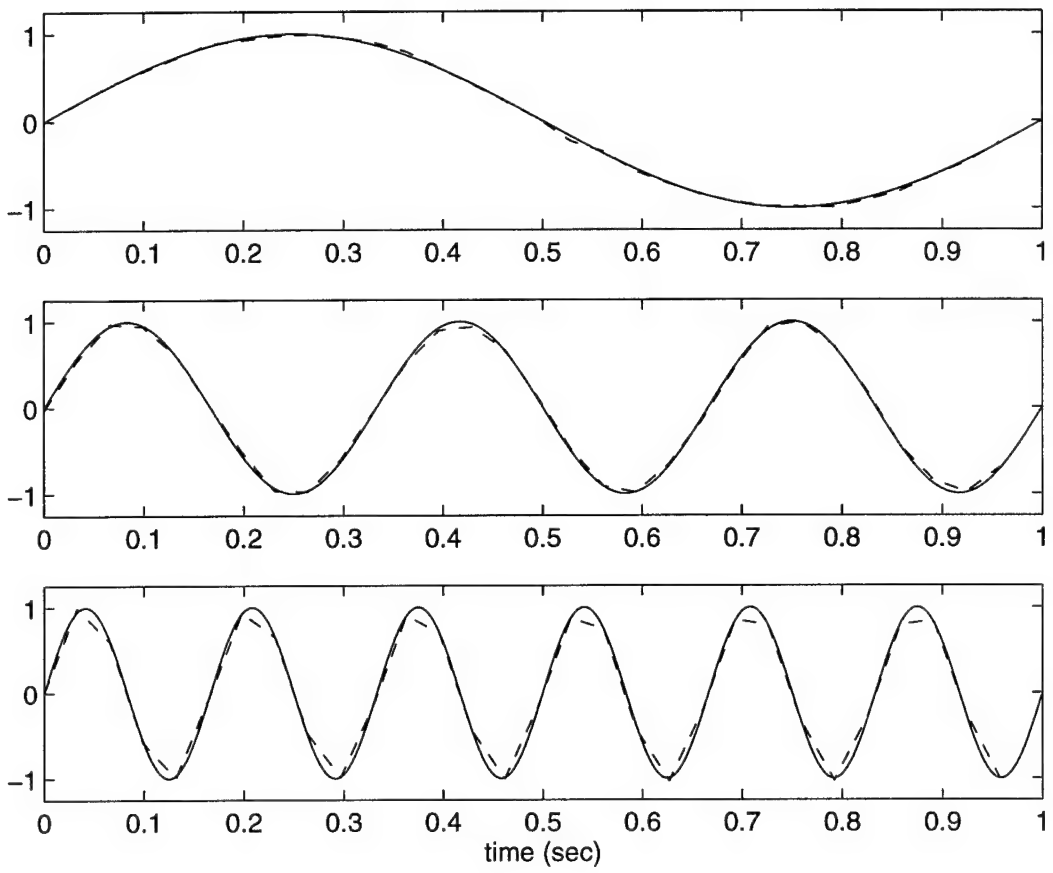

Figure 8.5: Normalized target displacements (solid line) and tracking updates (dashed line) for a 1 Hz, 3 Hz, and 6 Hz sinusoid. Displacement amplitude was held constant. Only the x axis signal is shown.

SNR_T. At lower velocities for a given SNR_T, no false positives were observed during 1000 displacements.

The standard VHS video tape of the monkey retina had a poor SNR and fluctuating dynamic range, and the SNR_T was never higher than 6 dB and often lower. For moderate retinal movements, however, the system was able to track. As the retinal movement approached 10 deg/sec, loss of lock occurred.

Discussion

The tracking ability, as expected, is dependent upon the SNR_T, which in turn is dependent upon the contrast between the blood vessels and the fundus background. While the theoretical maximum tracking velocity is approximately 70 deg/sec (see Chapter 5), the observed maximum tracking velocity was just over 50 deg/sec for periodic movements, and just over 40 deg/sec for random movements. This is partly due to the fact that the maximum SNR_T with the simulated retina was 38 dB, as opposed to the theoretical maximum of almost 47 dB. Better lighting may have improved this, but the image lighting was already better than would be encountered *in vivo*, for which the SNR_T seldom exceeds 20 dB. The poorer performance with random movement is attributed to the fact that the excursions sometimes were large enough for one or more of the tracking templates to move out of the FOV.

The results shown in Figure 8.5 highlight the time lag problem of digital tracking with a data rate of 30 frame/second. During the test the tracking system, operating in PCI master mode, was keeping up with the CCD camera at 30 frames/sec; therefore tracking updates occurred 30 times each second. Note all tracking systems which use "past" data must always "catch up" to the moving target. At a 50 deg/sec target velocity and 30 tracking updates per second, the target can move 1.67 degrees before the next tracking update occurs. This would equate to an almost 486 μm tracking error on the posterior pole of the retina, even though the tracking system exhibited no false positives and remained locked. This fact is a serious limitation to

digital tracking at 30 frames/second.

The ability to relock quickly is a new capability, and demonstrates the utility of the zoom-out, zoom-in relock routine. For low velocities, the system can relock and continue so quickly it is imperceptible to the user (except in normal operation the laser shutter would be closed during the relock sequence).

The poor overall performance with the video taped monkey retina is attributed to the poor signal quality of the tape itself. The monkey had a cloudy retina, and standard VHS also lacks sufficient video bandwidth and resolution. A better image recorded on S-video would be preferred.

Test Setup 2

A setup similar to Test Setup 1 was used, except the laser was coaligned with the CCD optical axis with a beamsplitter. In place of the simulated retina, gridded heat sensitive paper was attached to the XY plotter pen holder carriage. A black marker was used to draw simulated blood vessels on the paper.

Test Procedure

An alignment pattern was used to coalign the CCD image and laser pointing coordinate systems. Signals similar to that used for Test Setup 1 were applied to the XY plotter. The digital tracking templates were chosen from an area outside the area where the beam splitter appeared in the image, and XY plotter excursion was limited to keep the templates from passing into the beamsplitter area, and to keep the laser from pointing outside the beamsplitter. This eliminated the large change in template response which would otherwise occur, and kept the laser directed to the target, but restricted the allowable pointing angle of the laser to approximately ± 5 degrees. Recall that in normal use, the laser beam is steered to a maximum deviation of ± 8.3 degrees for a full 50 degrees on the retina. Lesion sites were selected on specified points of the gridded heat sensitive paper. Photocoagulation was

simulated by burning a mark on the paper. Laser parameters were $\lambda = 488$ nm and 514 nm, 1.25 W at the target, and 400 ms irradiations. A shorter irradiation time was desired, but the laser was set to maximum and this irradiation time was required to produce visible marks on the paper.

Test Results

With the XY plotter motionless, no error could be measured regarding the location of the burn mark and the designated lesion location. This was partly due to the relatively large size of the burn marks and the limited allowable angles. As the target velocity was slowly increased, the burn marks began to slightly "smear" in the direction of motion, partly due to the system trying to "catch up" to the movement and partly due to the 400 ms irradiation time. Tracking was similar to Test Setup 1 in all other respects. A scanned image of a burned target which was moving 10 mm p-p at 5 Hz is shown in Figure 8.6.

Discussion

This test verified that the laser can be pointed to the desired location by the computer, based upon the digital tracking templates. The slight smearing was an expected side effect of the tracking lag time dictated by the 30 frames/second update rate and the longer than desired irradiation time. This test was not intended for high accuracy; it was used as a first order check on the Laser Pointing and Control System. More accurate measurements, taken from video frames, are described later in this chapter.

Test Setup 3

The optical setup shown in Chapter 3 was used, including the fundus camera, the attached scanning lens (Ls) and beamsplitter (BS). At 50 mm from the fundus camera objective, at the point where the "eye undergoing treatment" is shown in

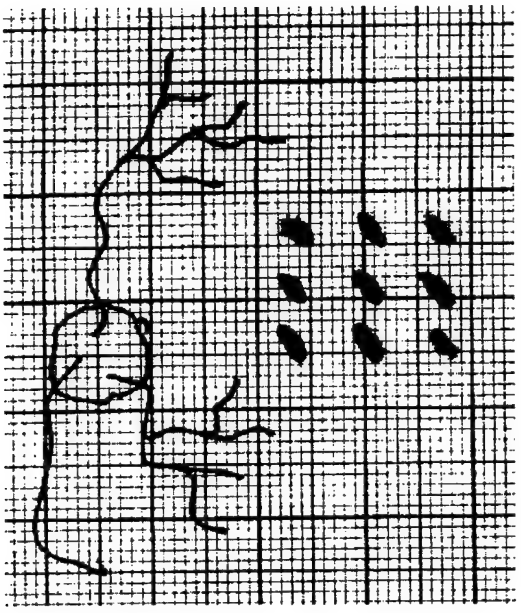

Figure 8.6: Heat sensitive paper target irradiated at $\lambda = 488$ nm and 514 nm, 1.25 W, 400 ms at each location. The motion was 10 mm p-p at 5 Hz.

Figures 3.4 and 3.9, one of two items was placed: a variable aperture or an $f = 17$ mm 0.5 inch diameter biconvex lens with no antireflection coating.

The variable aperture simulated both the pupil of the eye and inner diameter of the fundus camera illumination ring. The 17 mm lens simulated the gross optics of a human eye. Note that the human eye averages 60 diopters, which equates to a 16.7 mm focal length (assuming two optical surfaces surrounded by air). Since there is an index of refraction mismatch between air and the cornea of a biological eye, a lens without an antireflection coating was used to approximate the anticipated specular reflections from the cornea.

When the aperture was in place, a beam stop was placed at a noncritical distance behind it (that is, on the side opposite the fundus camera). When the 17 mm lens was in place, a target was placed behind the lens at its focal point. This target consisted of a black-painted metal plate with a low density random pattern of white

dots (formed by "flipping" the applicator brush for a bottle of *White-Out* correction fluid); the dots ranged in size from approximately 500 μm to 4 mm with most of them being at the smaller end of the range.

Test Procedure

With the variable aperture in place, the laser alignment menu of the CALOSOS user interface was used to select a linear ramp alignment pattern across the "retinal" FOV displayed on the computer screen. In normal operation the patient's dilated pupil is larger than the 5 mm inner diameter of the fundus camera illumination ring. Thus 5 mm is the limiting aperture size. The variable aperture was adjusted to 5 mm while the laser was directed in the alignment pattern. The laser was observed to see if it passed through the aperture without occlusion.

With the 17 mm lens and dotted target plate in place, the target was slowly moved such that one of the white dots moved in and out of the laser spot. The confocal reflectometer signal was observed for a rise in voltage when the highly reflective white dot was under the laser beam. For the hybrid implementation, this was performed for both the coagulating beam and the tracking beam. Also for the hybrid implementation, the target was moved while the tracking beam was locked on to one of the white dots. The equivalent retinal velocity of the target was determined post test from the video tape of the CCD camera image.

Test Results

The laser pattern passed through the 5 mm aperture with no occlusion. Since the collimated laser beam meets the aperture at the back focal point of the scanning pattern, the pattern appears almost as a point and easily passed through opening. The point for the coagulating and tracking beams (in the hybrid implementation) were not quite coincident, but were approximately 1.5 mm apart. However, they both passed through the aperture. Little spherical aberration of the pattern was

Figure 8.7: Response of the coagulating beam confocal reflectometer when small white dots on a black background target were passed slowly through the beam. The target was at the intended retinal plane.

evident on the planar target.

The reflectometer signals showed a clearly detectable response to the change in reflectance caused by the white dots, as shown in Figure 8.7. When the target plane was moved approximately 10 mm closer or further along the forward optical path, however, the response dropped to nearly zero, as shown in Figure 8.8. When at the proper distance, the tracking beam was able to hold lock at an equivalent of more than 60 deg/sec. Moving the target plane the same ± 10 mm caused the tracking beam to lose lock at less than 2 deg/sec; the maximum speed varied linearly with this distance.

Discussion

The pattern does not quite appear as a point through the aperture because the x and y steering mirrors "share" the conjugate plane of the pupil; thus a small amount of error is present. This blurring is more pronounced in the hybrid implementation because there are four mirrors, rather than two, "sharing" the conjugate plane of the pupil. However, there is still more than adequate clearance through the 5 mm aperture.

Figure 8.8: Response of the coagulating beam confocal reflectometer when small white dots on a black background target were passed slowly through the beam. The target was 10 mm further away than the intended retinal plane.

The confocal reflectometer response was validated with the same number of optical surfaces in the optical path that would be present *in vivo*. The reflectometer signal can be controlled by adjusting the gain on the associated transimpedance amplifier. Since lesions are less reflective than the white dots, the gain would be set higher for *in vivo* operation. The change in reflectometer response due to axial translation is an expected effect of the confocal optical design. While it can have detrimental side effects if the axial movement is too large, the confocal design is necessary to selectively admit the lesion reflectance and block other light such as specular reflections from the cornea.

Test Setup 4

To ascertain the level of galvanometer overshoot and settling time, a stationary white target was placed 1 m from the steering mirrors.

Test Procedure

With the shutter under computer control, the beam was directed by the G124 galvanometers (used for digital-only tracking) to move diagonally from −8.33 degrees

delay (ms)	G124 x	G124 y	G310 x	G310 y
0	11	18	2	2
5	8.5	14	1	1
10	6.5	10.5	<1	<1
15	5	7.5		
20	3.5	6		
25	2.5	4.5		
30	2	3.5		
35	1.5	2.5		
40	1	2		
45	<1	1.5		

Table 8.1: Maximum overshoot of galvanometer steered laser beam, measured in mm at a target distance of 1 m, versus a given software delay inserted before opening the shutter. All measurements ±0.5 mm. Distances of less than 1 mm were not measured.

to +8.33 degrees (the full operational range of motion) in one step and open the shutter. The maximum overshoot was measured on the white target. Through an iterative process, an increasing amount of time delay was added before the shutter opened until the overshoot was negligible. On another date, the test was duplicated with the G310 galvanometers, which are used for hybrid operation.

Test Results

Maximum overshoot of the G124 galvanometers with zero shutter delay was measured to be approximately 11 mm in the x direction and 18 mm in the y direction on the white target. At a delay of 45 ms the overshoot appeared negligible. The G310 galvanometers worst case overshoot under the same conditions was approximately 2 mm in both x and y directions. A 10 ms delay was needed to allow the G310 galvanometers to settle. Measurements of maximum overshoot taken for various settling time delays are shown in Table 8.1.

Discussion

The maximum overshoot is unequal for the G124 galvanometers due to the difference in the mass of the two UT fabricated mirrors (refer to Appendix A). At a 1 m target distance, 18 mm deviation is roughly 1 degree. Due to the 3:1 angular magnification of the system design, this would equate to 3 degrees on the retina. If left unchecked, this could result in a transient beam pointing error of 874.5 μm on the retina if the full FOV were traversed in one step. While this worst case step size is an unlikely occurrence, a delay of 50 ms (padded from 45 ms for safety) was incorporated into the system software for laser movements between lesion sites and for recovery after loss of lock. The user finds this delay imperceptible. To meet the 100 μm pointing accuracy on the retina, the deviation should not exceed 2 mm. A 2 mm deviation at a 1 m target distance corresponds to 114×10^{-3} degrees; the 3:1 angular magnification transforms this into 343×10^{-3} degrees on the retina, which is equivalent to approximately 100 μm.

The G310 mirrors were custom designed by the manufacturer for the G300 series, and were well balanced, leading to the better overshoot behavior. Rather than have separate laser pointing routines, the 50 ms delay is also used when the G310 galvanometers are employed in hybrid operation.

8.2.2 Tests Using an Eye Phantom

One additional factor was added here compared to the tests with the simulated retina: photocoagulation of the albumen eye phantom. As such, the eye phantom tests evaluated the system's ability to simultaneously track a moving "retina," update the laser pointing as needed, perform photocoagulation, and obtain a reflectance signal from a confocal reflectometer.

Test Setup 1

This test was performed in collaboration with R. Daniel Ferguson of Physical Sciences, Incorporated (PSI). It represented the first attempt by the author to integrate the digital system designed and built by the author and the analog system designed and built by PSI. Since the digital tracking updates would try to cancel the analog tracking updates, and vice versa, the digital tracking was disabled for this test. At this level of hybrid operation, the digital computer provided beam steering information for the desired lesion pattern, but the analog tracker compensated for eye phantom movement [138–140, 173]. The laser shutter was operated manually.

For these tests, a setup almost identical to that described in Section 8.2.1 as Test Setup 2 was used, with the albumen eye phantom target placed at the retinal conjugate plane (250 mm along the forward optical path from lens L2, approximately 165 mm along the forward optical path from the main steering mirrors). A beamsplitter was used to coalign the optical axis of the CCD camera and the laser pointing system (in the same manner as the fundus camera is coaligned with the laser under normal operation). The CCD camera looked through the beamsplitter in transmission and the laser beam was directed on to the eye phantom by reflecting from the beamsplitter. Since the eye phantom for this test was mounted vertically on the upright XY plotter, and needed to exhibit dark "blood vessels" against a lighter background for the digital tracking template, the standard black-painted petri dish phantom was modified as discussed below.

A thin Kapton® film[2] immersed in a cuvette of ordinary egg white provides an excellent simulation of the fundus for photocoagulation. The film absorbs 70% to 95% of the incident argon laser radiation depending on thickness and the resulting "lesions" which form are highly reproducible, exhibiting dynamics and appearance remarkably similar to those on the human retina. The small thermal mass of the Kapton film, its thermal stability and its absorption characteristics are responsible

[2]Constructed of polyimide, Kapton is a registered trademark of the 3M Corporation.

for the fidelity of the simulation, and rival the more common black-painted petri dish.

The eye phantom tests used a setup which consisted of a petri dish where the Kapton film (marked with dark indelible ink lines to represent blood vessels) was suspended, filled with eggwhite and sealed with plastic wrap. The dish was mounted vertically on the pen holder carriage of the XY plotter and driven with both sinusoidal and ramping (triangle wave) displacements of known frequency and amplitude from the external signal generator. The motion occurred along a path rotated 45 degrees from the x and y axes of CALOSOS, thus stressing both x and y tracking and steering assemblies. The random signal was not available. Illumination for the CCD camera image was provided by an articulating desk lamp with a 100 W light bulb. Signals from the confocal reflectometers for both the tracking beam and the coagulating beam were recorded using a Clevite Brush Mark 220 strip chart recorder.

Test Procedure

A digital template was established using the hand drawn "blood vessels" and used for the coordinate system reference. Lesion patterns were then defined as needed according to this coordinate system. In order to disable the digital tracking for test purposes, a video tape was made of the stationary eye phantom. This tape was then used as video input to the computer frame grabber to "fool" the system into thinking the target was not moving. Otherwise the digital tracking signals would tend to cancel the analog tracking signals.

A reference lesion was created while the target was still stationary, and the tracking beam was manually directed (using the joystick) to the reference lesion where it established lock. The displacement signals were than sent to the XY plotter and velocity was increased until tracking lost lock. Various lesions (individual and patterns) were created, and tracking was intentionally broken during some photo-

coagulations to observe the effect. The laser parameters were: argon laser ($\lambda = 488$ nm, 514 nm), 250 mW, 400 μm spot on the eye phantom surface.

Test Results

The maximum tracking velocities before losing lock are shown in Table 8.2. Recall that the optical design for the hybrid implementation results in a 3:1 optical demagnification between the retinal conjugate plane and the retinal plane. An example

Waveform	Tracking Limit	Retinal Equivalent
Sine	1 Hz, 2 cm p-p, 6 cm/sec	68.6 deg/sec
Sine	9 Hz, 2 mm p-p, 6 cm/sec	68.6 deg/sec
Triangle	1 Hz, 2.5 cm p-p, 5 cm/sec	57.2 deg/sec
Triangle	9 Hz, 2 mm p-p, 6 cm/sec	68.6 deg/sec

Table 8.2: Results of the hybrid tracking subsystem with an eye phantom located on an XY plotter at the conjugate retinal plane. Note: 9 Hz was the maximum XY plotter response. Retinal demagnification of 3:1 assumed.

of calculating the equivalent retinal velocity would be: given 6 cm/sec, the velocity is divided by 3 to account for the optical demagnification, then divided by 291.5 μm/deg spatial equivalence at the posterior pole of the eye, yielding 68.6 deg/sec. This yields the retinal equivalent velocities shown in Table 8.2. In general, the results seem to depend on velocity only and are not particularly sensitive to different amplitude versus frequency combinations for the same velocity.

The eye phantom is shown in Figure 8.9 following photocoagulation of a 3×4 lesion pattern during a 5 mm p-p, 1 Hz triangular motion, and several individual lesions formed during a 1 cm p-p, 1 Hz triangle motion. This is equivalent to 11–23 deg/sec on the retina. The single lesion furthest to the left and below the 3×4 pattern was the reference lesion, and was formed when the target was stationary.

A closer view of the lesions is shown in Figure 8.10, where an additional 3×4 pattern (at the bottom of the image) was created with a 5 mm p-p, 1 Hz triangle motion, equivalent to 11 deg/sec on the retina.

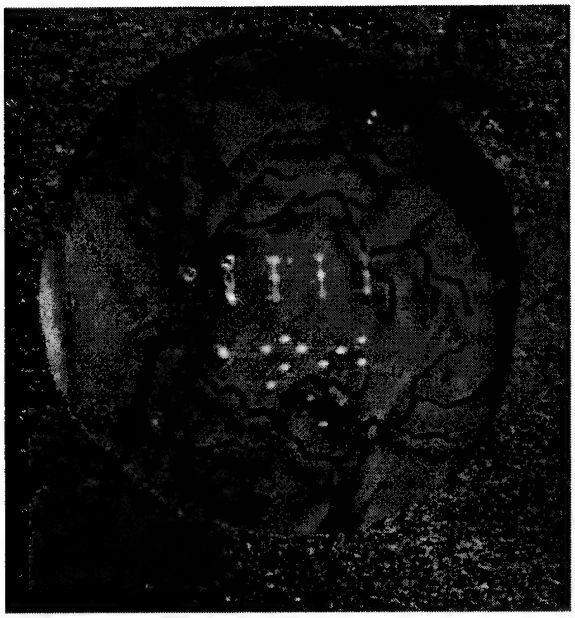

Figure 8.9: Lesions created in an eye phantom during motion. Displacement: 0.5–1 cm p-p, 1 Hz triangle waveform, equivalent to 11–23 deg/sec on the retina. Argon laser ($\lambda = 488$ nm, 514 nm), 250 mW, 400 μm spot. Streaks between lesions due to manual shutter operation.

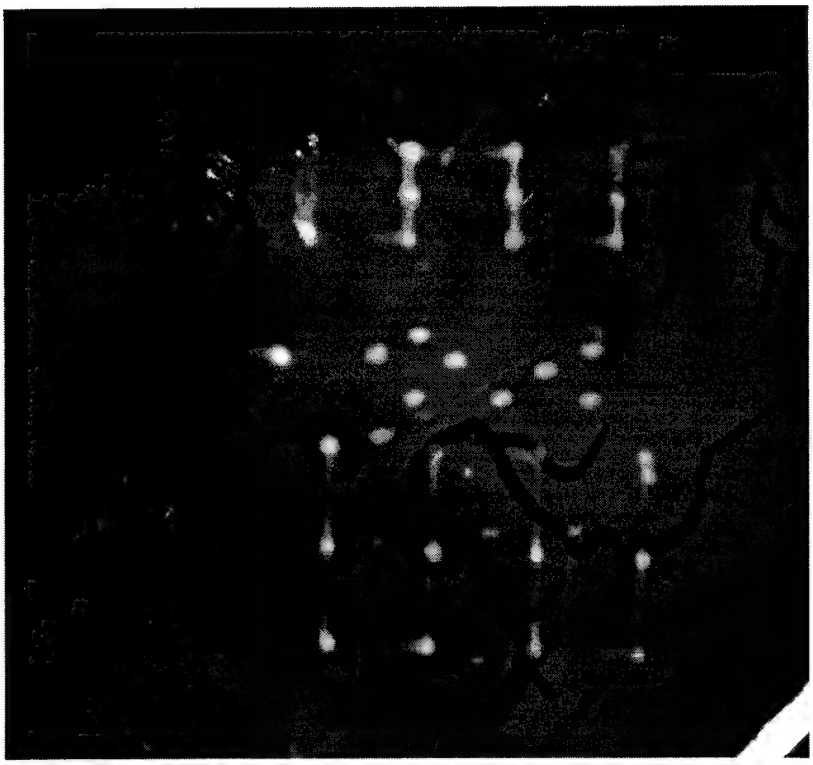

Figure 8.10: Closer view of lesions created in an eye phantom during motion. Displacement: 0.5–1 cm p-p, 1 Hz triangle waveform, equivalent to 11–23 deg/sec on the retina. Argon laser (λ = 488 nm, 514 nm), 250 mW, 400 μm spot. Streaks between lesions due to manual shutter operation.

Signals obtained from the coagulating beam confocal reflectometer for a stationary target, and a moving target with and without tracking are shown in Figure 8.11 where the x axes are marked in seconds.

A comparison of the confocal reflectometer signals from the coagulating beam and the tracking beam (with the time axes aligned) is shown in Figure 8.12 where the x axes are marked in seconds.

Signals obtained from the coagulating beam reflectometer when the target was stationary, then began to move, then when tracking lock was intentionally broken, and finally with tracking lock restored is shown in Figure 8.13 where the x axes are marked in seconds.

Discussion

The tracking performance of the analog system appeared robust. Experimentation with the dither circle diameter demonstrated that optimum performance was achieved when the dither radius was approximately equal to the reference lesion radius. Increasing the dither signal feedback gain too much caused the tracking beam to throw itself off the reference lesion even when the target was stationary. The system thus needed to be "tuned" to the specific operating conditions for optimum performance.

In Figures 8.9 and 8.10, lesions formed during motion are shown. The slight "smearing" between sites of the rectangular patterns was due to the lack of a computer controlled shutter during the pattern creation. There was no physical room for one in this early test. Because the digital tracking system was not active, the location of the lesion patterns was relative to the offset of the analog system's reference lesion. From the digital system's point of view, the reference lesion was always located in the exact center of the image. The digital system provided lesion pattern coordinates relative to this assumption.

This test was the first attempt at integrated hybrid operation of the digital

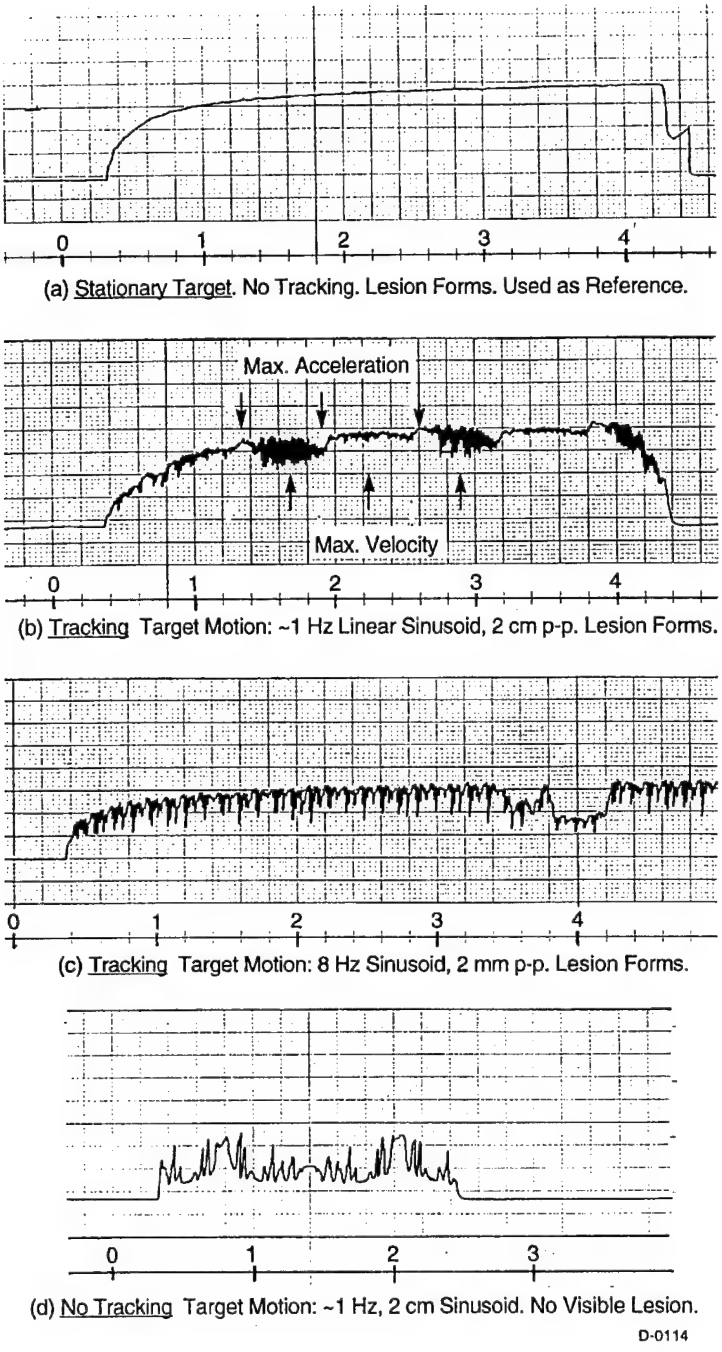

Figure 8.11: Dynamic confocal reflectometer signals of the coagulating beam.

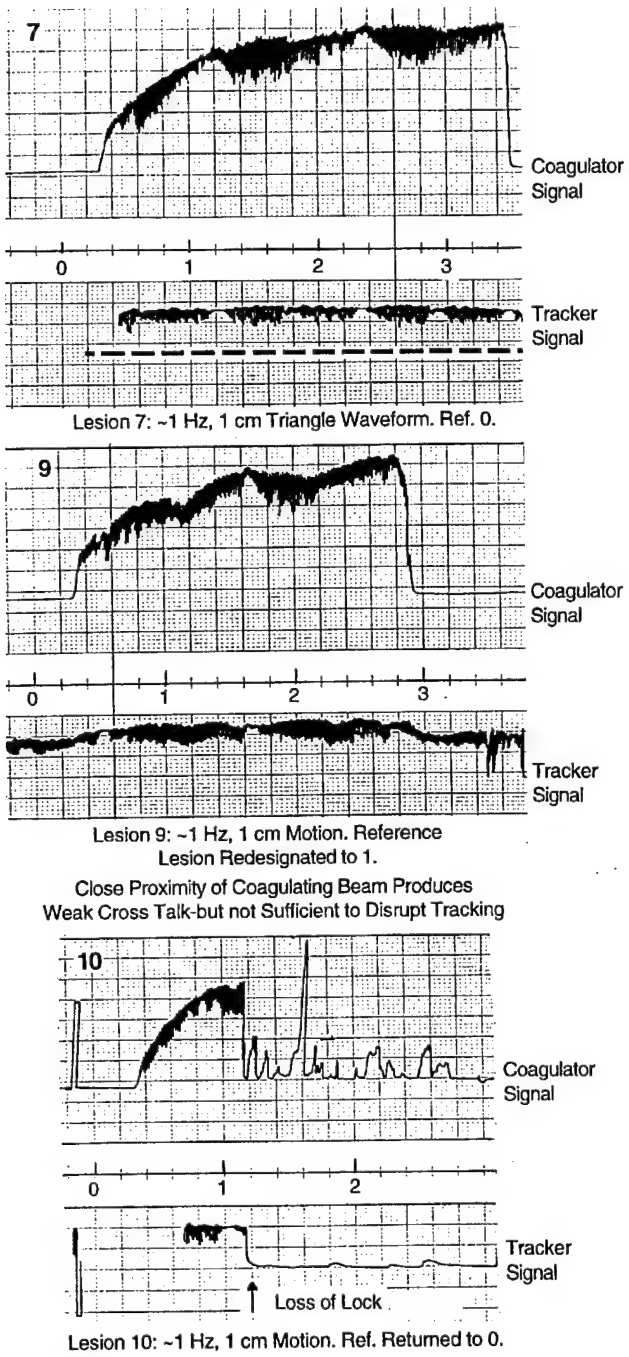

Figure 8.12: Comaprison of coagulating and tracking beam reflectometers.

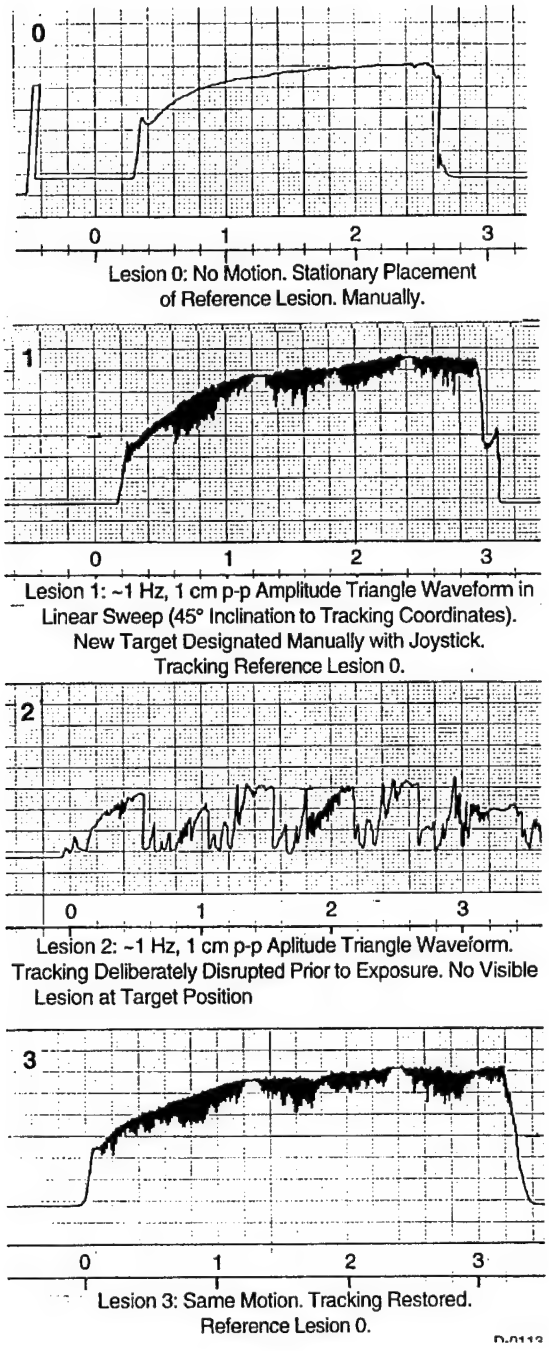

Figure 8.13: Coagulating beam reflectometer signals when target is stationary, moving and locked, unlocked, and relocked.

and analog systems. The lesion pattern optimization routines did not yet exist, and the large spatial jumps from the bottom of one column of the pattern to the top of the next column of the pattern frequently caused the analog system to lose lock. The analog system circuitry was not properly balanced to counteract these movements with regard to the tracking beam. As a temporary workaround, a low pass filter was placed in series with the galvanometer driver inputs to moderate the transient jumps in position. While this allowed the test to continue, the maximum equivalent retinal velocity while creating lesion patterns was approximately half the single lesion maximum velocity. Subsequent alterations in the analog circuitry and the creation of the lesion pattern optimization routines eliminated this problem in the *in vivo* tests.

The confocal reflectometer signals clearly demonstrated the effect of tracking a moving target. During motion, lesions formed easily and in a fixed place on the eye phantom as long as tracking was locked. If lock was broken, the relative movement of the coagulating beam with respect to the eye phantom did not allow sufficient heat deposition for a lesion to form. This is clearly shown in Figures 8.11, 8.12, and 8.13. Not only does this demonstrate the value of tracking during photocoagulation, but the coagulating reflectance signals may be used in the future to ensure consistent lesion formation independent of absorption coefficient variations on the retina. Reflectance as a control signal requires more study.

Test Setup 2

The purpose of this test was to compare the motion artifact on the confocal reflectometer signal using improved digital tracking versus analog tracking. Recall that digital tracking can update no faster than the 30 frame/second rate of the CCD camera, whereas the analog tracker updates approximately every 5 ms. This test used an identical setup to that above, except for the use of both tracking systems (individually).

Test Procedure

The analog tracker was operated manually, without assistance from the computer. Only individual lesions were created, without regard to location on the eye phantom. No patterns were created. With the XY plotter stationary, the coagulating beam was directed (using the joystick) to an arbitrary location on the eye phantom and a reference lesion was created. A sinusoidal signal was sent to the XY plotter at 6 Hz, 2 mm p-p for approximately 40 deg/sec maximum retinal equivalent velocity. Multiple individual lesions were created while the confocal reflectometer signal was sampled (at 100 Hz) and stored. Irradiations were manually controlled at approximately 1 second duration.

The digital tracker was used normally. With the XY plotter stationary, a digital tracking template was created from the hand drawn "blood vessels" on the Kapton. A sinusoidal signal was sent to the XY plotter at 6 Hz, with displacement adjusted for approximately 20 pixels p-p, equivalent to 40 deg/sec maximum retinal velocity. Multiple individual lesions were created, each with 1 second irradiation, while the confocal reflectometer signal was sampled (at 100 Hz) and stored.

The laser parameters were: argon laser (λ = 488 nm, 514 nm), 250 mW, 400 μm spot on the eye phantom surface.

Test Results

Reflectometer signals using the two tracking systems are shown in Figure 8.14, where the motion artifact in the digitally tracked signal is evident.

Discussion

As expected, the slower update rate of the digital tracking resulted in greater motion artifact on the reflectometer signal. For the best reflectometer data, the analog tracking system should be employed.

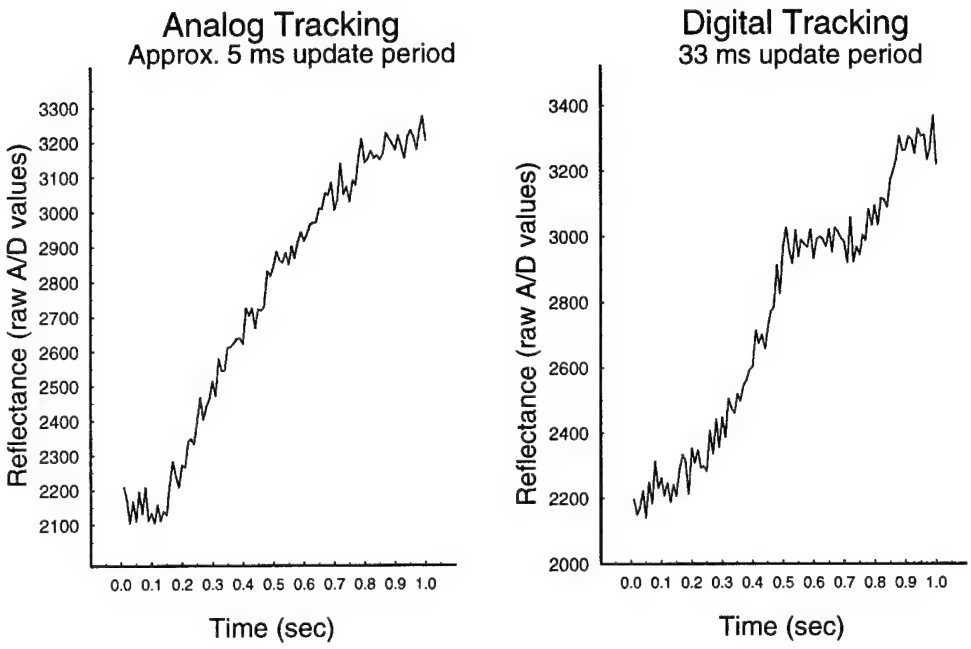

Figure 8.14: Comparision of confocal reflectometer signals with analog tracking and digital tracking. Motion of target was 2 mm p-p, 6 Hz, for an equivalent retinal velocity of 40 deg/sec.

8.2.3 Tests Using Animals

These *in vivo* tests were the most demanding scenario for the system. When living biological tissue is involved, the ability to control variables is reduced greatly, yet operation *in vivo* is the ultimate and absolutely necessary test for any biomedical engineering design.

Test Setup 1

In collaboration with Dr. Steven Barrett, a single cross-bred Californian/New Zealand pigmented rabbit was used for an early *in vivo* test of the digital tracking system. This test used the first optics design by the author to improve the beam pointing system that was used originally by Barrett. Compared to the final optics design shown in Figure 3.4, the confocal reflectometer and its beamsplitter were not present, nor was the converging lens L2. The scan lens Ls was a 63 mm plano-convex. The new G124 galvanometers, each with their dual coils rewired in series by the author for greater sensitivity, were used. The controlling software was from Barrett's original system, but rehosted by the author on a 66 MHz 486DX2 computer (twice as fast as that which Barrett had originally used).

The rabbit was kept sedated during the procedure, and survived without harm. Full adherence to UT Animal Resources Center (ARC) approved protocol #06951603, in compliance with the National Institute of Health (NIH) Assurance #1496, was observed at all times. The anesthesia was a mixture of Ketamine (ketamine hydrochloride at 35 mg per kg bodyweight) and Rompun (xylazine hydrochloride at 5.9 mg per kg bodyweight) applied intramuscularly with a 22 gauge needle and syringe. The eye under treatment was dilated with one drop of Mydriacyl (tropicamide) 1% solution applied topically, and was held open with a small 10-1000 barraquer wire speculum. The cornea was periodically moistened with sterile saline solution. The rabbit's body was secured on the animal platform in front of the fundus camera by a safety strap.

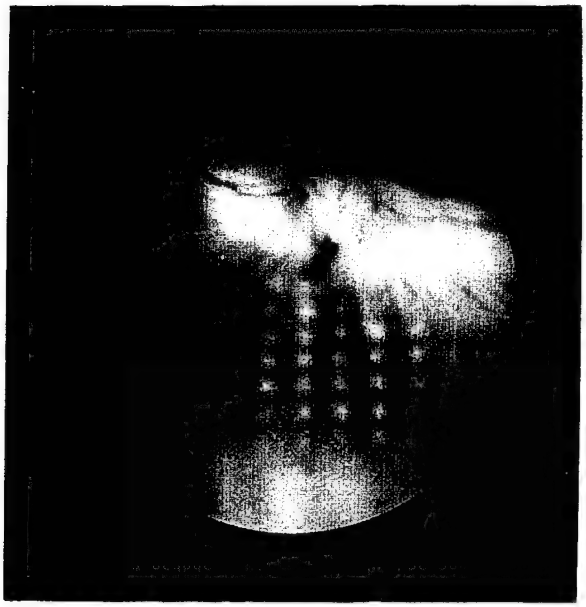

Figure 8.15: Fundus image of photocoagulation on rabbit fundus. Argon laser ($\lambda = 488$ nm, 514 nm), 100 mW at the cornea, 291 ms average irradiation time.

Test Procedure

The test procedure followed the steps 1–3, 6, and 7 described in Section 8.1 for a typical clinical operating scenario. A rectangular 7×5 lesion pattern was designated. The laser parameters were: argon laser ($\lambda = 488$ nm, 514 nm), 100 mW at the cornea, 291 ms average irradiation time.

Test Results

A fundus photograph of the resulting retinal lesion pattern can be seen in Figure 8.15, where the 7×5 lesion pattern is evident.

Discussion

The improved optics were able to produce a large rectangular pattern on the rabbit fundus with less geometric distortion than previously experienced by Barrett. A

comparison of the specified lesion pattern coordinates and the frame grabber image of the lesion pattern indicated that the laser positioning accuracy was within ±2 pixels (±64 μm on the retina) near the top of the pattern, which is near the image center. The laser positioning accuracy deteriorated to within ±15 pixels (±480 μm on the retina) near the bottom of the pattern, which is near the edge of the image FOV; this was likely due to spherical aberration from the scan lens. Therefore lesion sites should only be placed at the edge of the FOV if the positioning tolerance can be relaxed.

Test Setup 2

At Armstrong Laboratory (Brooks AFB, TX), in collaboration with Drs. Steven Barrett, Clarence Cain, and Ben Rockwell, a single rhesus monkey was used for an *in vivo* test of the digital tracking system. The purpose of the test was to see if the system could also control an ultrashort pulse laser and direct it to the desired position on the retina. The optics were the same as for Test Setup 1 described above; Barrett's digital tracking software was hosted on a 100 MHz 486DX4.

The monkey was kept sedated during the procedure, and survived without harm. Care of the animal was provided by professional animal handlers assigned to Brooks AFB, TX. Strict adherence to the approved protocol was observed at all times. Although sedated, there was still considerable eye movement (less than 10 deg/sec) along with a cloudy cornea, which challenged the tracking and relocking of Barrett's tracking algorithm. After additional anesthesia was administered, the eye movement slowed enough to allow Barrett's tracking algorithm to lock satisfactorily.

Test Procedure

The monkey was irradiated with two different lasers: a standard CW argon laser, and the ultrashort pulsed laser. For each type of laser, the test procedure followed steps 1–3, 6, and 7 described in Section 8.1 for a typical clinical operating scenario.

A rectangular 3×4 lesion pattern was designated each time. The laser parameters were: argon laser ($\lambda = 488$ nm, 514 nm), 150 mW at the cornea, various irradiation times; ultrashort laser ($\lambda = 580$ nm), 120 femtosecond pulses at a 10 Hz repetition, 3–4 μJ/pulse rate at the cornea, irradiation of approximately 3 seconds per lesion site.

The first 3×4 lesion pattern with the argon laser used an irradiation time of 125 ms with no immediate visible result. A second attempt, on the same coordinates, used an irradiation time of 250 ms with no immediate visible result. A third attempt, on the same coordinates, was then made using an irradiation time of 375 ms, with visible lesions observed.

The first attempt with the ultrashort laser, directed to a different set of lesion coordinates, produced visible lesions.

Test Results

A fundus photograph of the resulting retinal lesion patterns can be seen in Figure 8.16. An annotated version of this photograph is shown in Figure 8.17, where the lesion patterns due to the argon and ultrashort lasers are identified.

Discussion

This test presented many challenges. The scan lens Ls and beamsplitter mounted on the fundus camera conflicted with the monkey's nose. A new low-profile scan lens holder was designed on the spot by the author and a smaller beamsplitter was used, allowing sufficient clearance for the monkey. The initial levels of anesthesia were insufficient on the first day. On the second day the monkey was sedated appropriately. The fact that Barrett's software had trouble locking during moderate eye movement on the first day pointed out the need for more digital tracking improvements as described in this dissertation and verified experimentally in Section 8.2.1 above.

Figure 8.16: Fundus image of lesions on the retina of a rhesus monkey due to a CW argon laser and an ultrashort pulsed laser. Argon (inferior nasal location): λ = 488 nm and 514 nm, 150 mW, 750 ms irradiation per lesion. Ultrashort (superior temporal location): λ = 580 nm, 120 fs pulse at a 10 Hz repetition rate, 3–4 μJ/pulse, 3 sec irradiation per lesion.

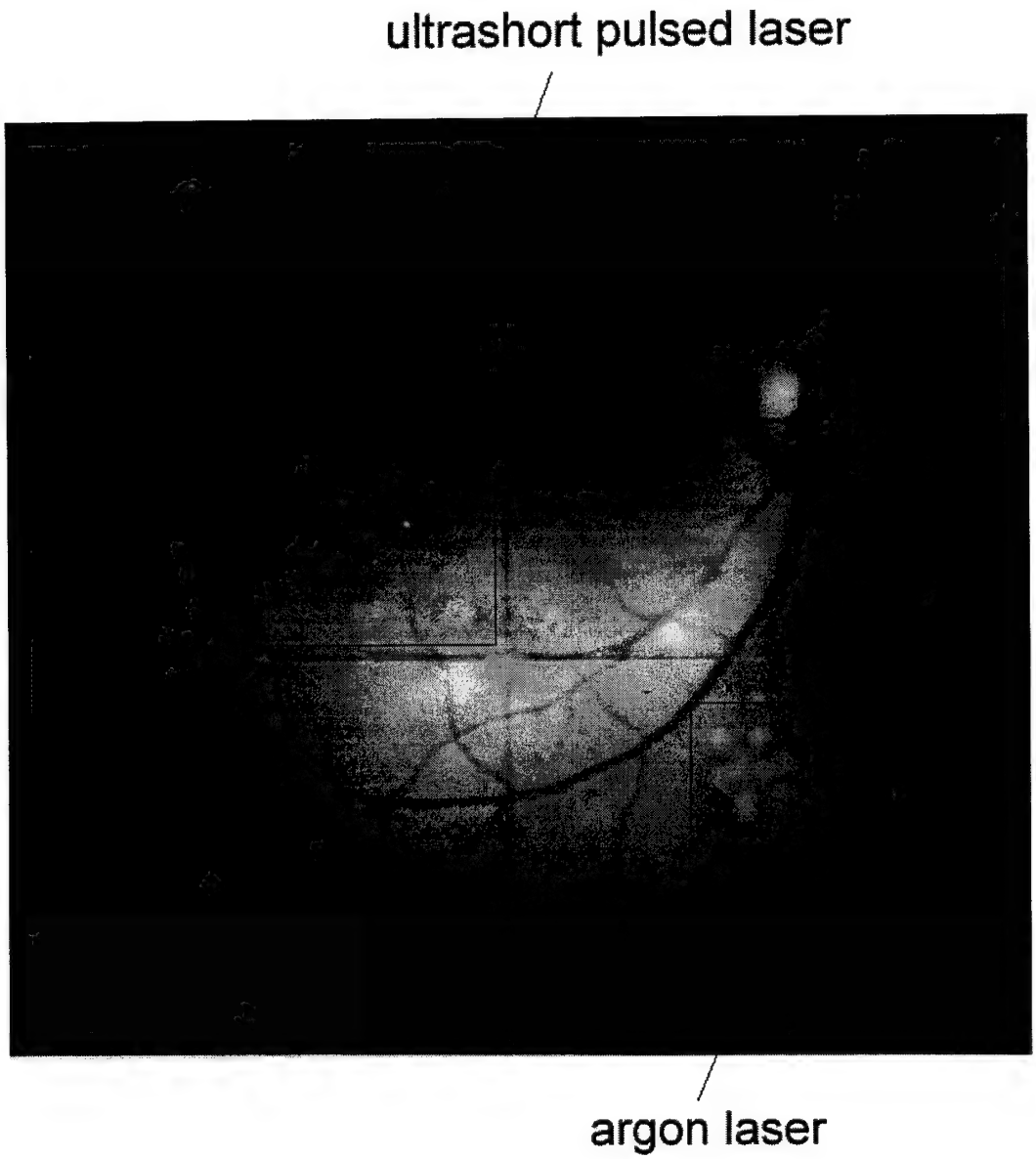

Figure 8.17: Annotated fundus image of rhesus monkey following photocoagulation. Argon: $\lambda = 488$ nm and 514 nm, 150 mW, 750 ms irradiation per lesion. Ultrashort: $\lambda = 580$ nm, 120 fs pulse at a 10 Hz repetition rate, 3–4 μJ/pulse, 3 sec irradiation per lesion.

In Figure 8.17, the lesion pattern produced from the argon laser is seen in the lower right part of the image. The 3×4 pattern was placed three times in the same place because lesions did not appear immediately. After a few minutes, all three sets of irradiations produced lesions. Because the pattern-to-pattern placement had position variations of up to ±5 pixels, the resulting pattern looks partially smeared.

A more spread out 3×4 pattern using the ultrashort laser is shown in the upper left quadrant of Figure 8.17. The lesion pattern is bounded on the right and bottom by the fundus camera crosshair. While difficult to see given the contrast of the image, the lesions are present and could be seen more easily by eye through the fundus camera. This proved the system could effectively point and control other types of lasers.

Test Setup 3

In collaboration with R. Daniel Ferguson, two Dutch Belted rabbits were used for an *in vivo* test for the hybrid operation of the system. This breed of rabbit is preferred by ophthalmological researchers as its corneal curvature resembles a human cornea more than other breeds. The new system design described in this dissertation was used in the hybrid operation mode; refer to Figures 3.8 and 3.9. The digital computer and new software manipulated and displayed the CCD camera image from the fundus camera, provided beam steering information for the alignment pattern and the desired lesion pattern, controlled the laser shutter, and monitored the patient status and lesion status inputs. The analog tracker compensated for eye movement. The motion-compensated confocal reflectometer signal of the coagulating laser beam was sampled at 1 kHz and stored. Note that the new software provided the ability to use the digital templates while suspending digital tracking updates to avoid the conflict between the analog and digital tracking signals (as discussed in Chapter 5). This allowed full use of the mouse-driven computer interface with the real-time fundus video image, and eliminated the need to use a video tape of a static image.

Since the confocal reflectometer signal was to be obtained during movement, analog tracking was selected since its tracking update rate is 6 times faster than the digital tracking update rate. This faster update rate results in a significant reduction of possible motion artifact on the confocal reflectometer signal, as shown in Figure 8.14.

The same animal protocol as for Test Setup 1 above was used for the rabbits, although they were only lightly sedated to allow reflexive eye movements that would stress the tracking system. Both animals survived without harm. The rabbit's body was secured on the animal platform in front of the fundus camera in a holder built at Armstrong Laboratory (Brooks AFB, TX) and designed specifically for ophthalmic research with rabbits. The rabbit's nose rested in a padded annular holder which elevated the animal's chin. This not only ensured against breathing problems due to possible pressure on the trachea while in the holder, but also positioned the eye at the optimum location for the test.

This setup is similar to that described in Section 8.2.1 as Test Setup 3, except the rabbit eye took the place of the aperture or 17 mm lens. A potentiometer was attached to the animal platform such that the voltage across it varied as the platform was rotated about the axis of the rabbit eye.

Test Procedure

The basic test procedure followed the steps 1–7 described in Section 8.1 for a typical clinical operating scenario using the hybrid mode of operation.

A digital template was established using the retinal blood vessels of the rabbit; the template was then used as the retinal coordinate system reference. Lesion patterns were then defined as needed according to this coordinate system. The software routine was used which was written specifically for hybrid operation, which suspended digital tracking updates and relied upon the analog tracker.

A single photocoagulation was performed to create the reference lesion. The

tracking beam was then manually directed (using the joystick) to the reference lesion where it established lock. Various lesions (individual and patterns) were created in the rabbit fundus. The laser parameters were: argon laser (λ = 488 nm, 514 nm), 175 mW at the cornea, approximately 275 μm diameter spot on the retina. All irradiations were 100 ms. The confocal reflectometer signal was sampled (at 1 kHz) and stored. Movement of the animal platform was severely restricted due to the lack of space between the animal and the system optics.

The ability of the computer to find the laser spot and check it's position was also tested.

Test Results

The template response for both rabbits was approximately 450, indicating a useful SNR_T of roughly 24 dB.

Fundus photographs of the rabbits are shown in Figures 8.18 and 8.20. Annotated scans of these photographs are shown in Figures 8.19 and 8.21.

In Figure 8.19, several individual lesions can be seen in the lower center, and a 3×4 lesion pattern can be seen near the center of the image. The rabbit eye exhibited rotation during creation of this 3×4 pattern, and as a result the center column is somewhat tilted. This pattern, when compared to the computer coordinates specified for the pattern and adjusted for image registration between frames, was located no more than ±2 pixels (±64 μm on the retina) of the intended location if rotation is factored out. With rotation, the maximum error was 17 pixels (±544 μm on the retina) at the top of the center column. A second 3×4 pattern was attempted right of center in the image of Figure 8.19, while the computer performed closed loop verification of the laser position. Rapid movement of the eye (including 30 deg/sec impulsive jerks) during this pattern caused the reference lesion to almost lose lock during the first two columns of the pattern. As the third column began, the tracker did lose lock, and the computer did not find the laser beam within the allowable

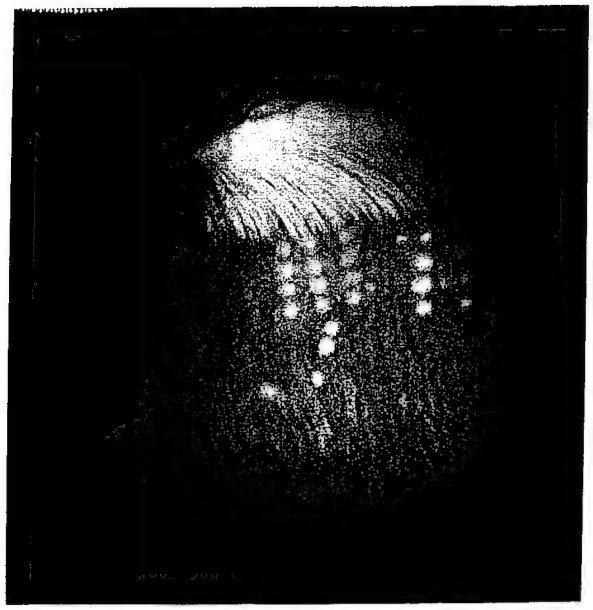

Figure 8.18: Photocoagulation on a rabbit fundus using hybrid operation. Argon laser ($\lambda = 488$ nm, 514 nm), 175 mW at the cornea, approximately 275 μm diameter spot on the retina.

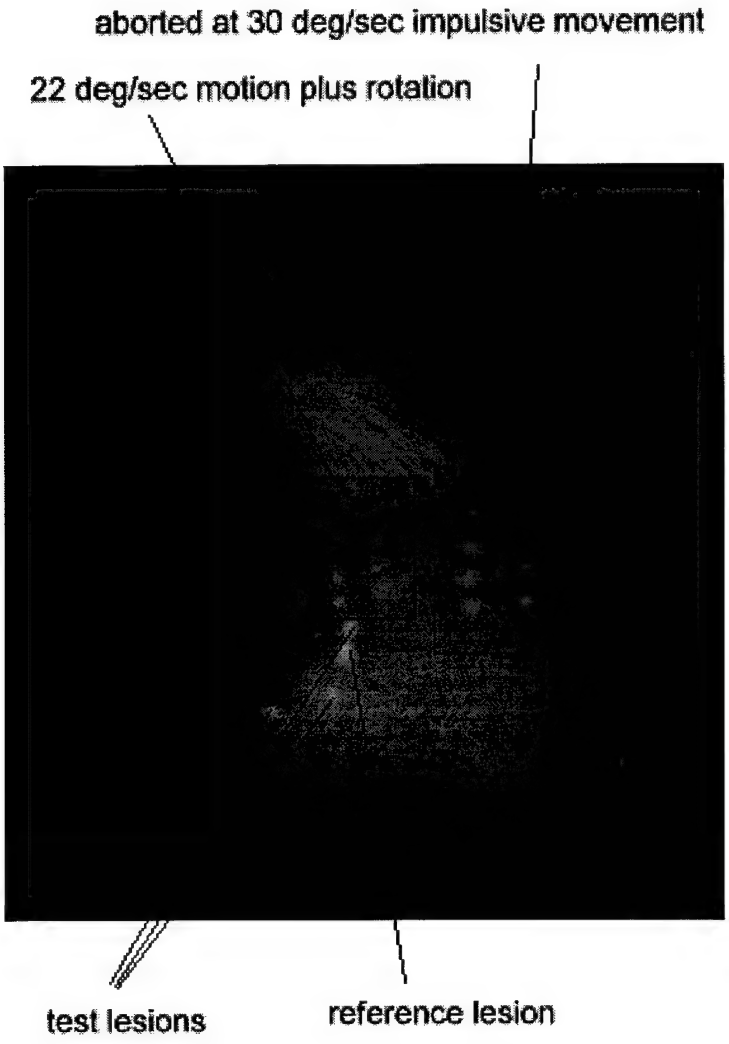

Figure 8.19: Annotated version of Figure 8.18.

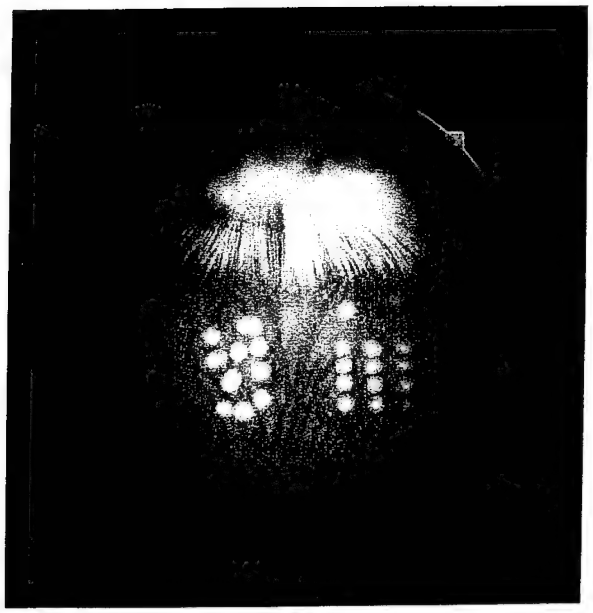

Figure 8.20: Unlocked and locked photocoagulation on a rabbit fundus using hybrid operation. Eye motion was up to 32 deg/sec. Argon laser ($\lambda = 488$ nm, 514 nm), 175 mW at the cornea, approximately 275 μm diameter spot on the retina.

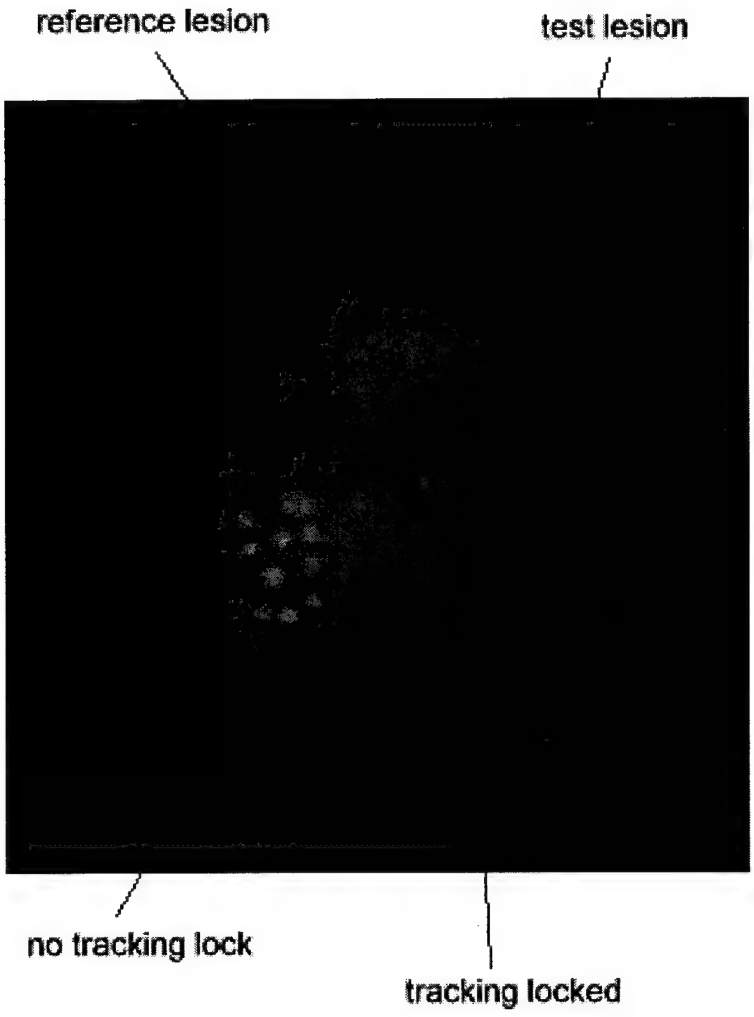

Figure 8.21: Annotated version of Figure 8.20.

region, and immediately aborted the rest of the pattern.

In Figure 8.21, two individual lesions can be seen right of center, and two 3×4 patterns were created during eye motion of up to 32 deg/sec. The pattern on the left of the image was created when the system had intentionally lost lock; this pattern illustrates the relative movement of the fundus during irradiation. The pattern on the right of the image was created when the tracking system was locked; this shows motion compensation of the tracking updates during irradiation. This pattern, when compared to the computer coordinates specified for the pattern and adjusted for image registration between frames, was no more than ±2 pixels (±64 μm on the retina) of the intended location. The maximum error was in the lower right corner, where the error was 4 pixels (±128 μm on the retina).

No motion signal was obtained from the potentiometer due to the restricted movement. In a frame-by-frame analysis of the video tape, velocities of the rabbits' reflexive eye movements were determined. The maximum velocity the system could track without losing lock varied according to the optical condition of the cornea, and the location of the reference lesion. A clearer cornea permitted faster velocities, as did a reference lesion near the center of the FOV. The lowest velocity at which tracking lock was broken was 30 deg/sec, during a short, highly impulsive movement. The highest velocity at which tracking lock was broken was 38 deg/sec, during a relatively smooth movement.

A confocal reflectometer signal obtained from one of the lesions in Figure 8.20 is shown in Figure 8.22. During this irradiation, the rabbit's eye exhibited motion at up to 14 deg/sec.

Discussion

Figure 8.18 clearly shows that a single dither beam for tracking is susceptible to rotation. When a more fully integrated version of the system allows simultaneous digital tracking, this rotation would be detected since the digital template will not

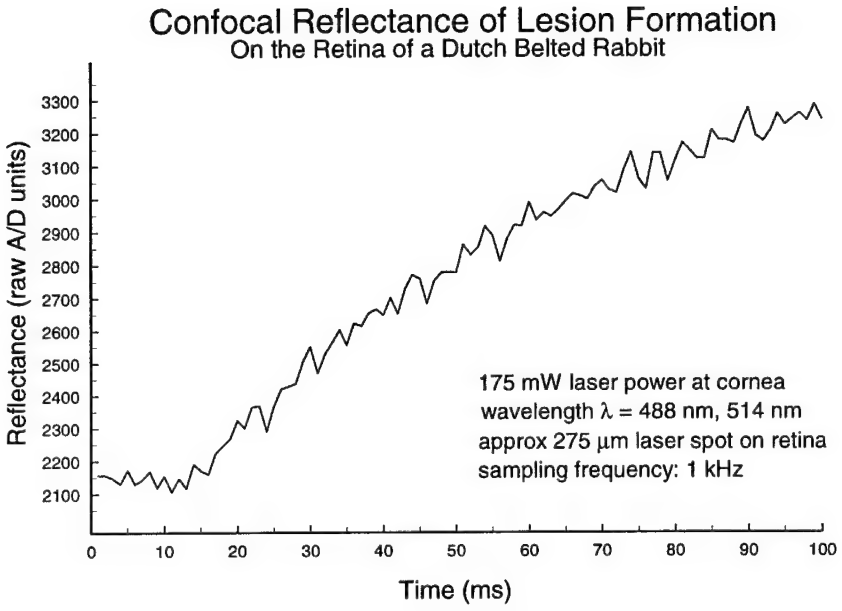

Figure 8.22: Confocal reflectometer signal for a 100 ms irradiation on a rabbit fundus during tracked motion of up to 14 deg/sec.

lock in the presence of rotation. Figure 8.18 also demonstrates the fail-safe value of having the computer check for the laser beam location on the image. The computer aborted the errant lesion pattern when the analog tracker lost lock. A more fully integrated system would have access to a loss of lock signal from the analog electronics, but the laser checking feature still would provide important closed loop control. This feature would be better suited to checking the location of an aiming beam prior to opening the shutter, both for added safety and to reduce pixel saturation problems encountered with the full power laser.

Figure 8.20 is a good comparison of photocoagulation with and without tracking. The relative accuracy of the lesion placement does not meet the requirement at the very edge of the FOV, but is within specification in the more central area of the image. Closed loop galvanometers may improve this, as would an ophthalmoscopic aspheric lens (which performs field flattening for the retinal image). The aspheric lens used in this test is better than a standard lens, but spherical aberration is still a problem.

The maximum tracking velocity was lower than that found with an eye phantom, but still an order of magnitude faster than Barrett's original system. The reduced tracking performance is attributed to the poorer characteristics of the total optical path. While the results with the eye phantom seemed to depend only upon retinal velocity, loss of lock *in vivo* was observed for impulsive movements that otherwise were within the normal tracking velocity limits. It is hypothesized that this acceleration sensitivity is due to some residual imbalances between the tracking and steering control in the analog system which are only manifested in the poorer optical conditions found *in vivo*. This effect requires further investigation.

The confocal reflectometer signal shown in Figure 8.22 is relatively free from motion artifact. The random noise seen in the plot is not motion-induced (confirmed by motionless tests which also had this level of noise). Figure 8.22 represents the first time a motion stabilized reflectance signal has been obtained *in vivo*.

8.3 Observations

The improved digital tracking system was shown to be able to track at velocities of up to 25 times that of Barrett's original system, with a robust relock technique. The analog tracking system is equally as fast, but provides tracking correction updates 6 times more often. This has a significant effect on the ability of the system to mitigate motion artifact from the reflectance signals and to reduce the lag time tracking error.

The analog and digital systems must be more closely integrated for more flexible, robust performance. This first generation hybrid design consists of a digital system designed and built by the author at UT (in Austin, TX) and an analog system designed and built by R. Daniel Ferguson at PSI (in Andover, MA). Both systems were originally intended as stand-alone devices, and the integrated hybrid operation of the two systems is difficult. The next logical phase would be to rebuild both systems as one, with full hybrid operation intended from the start. Neither system alone can perform as well as a true hybrid system.

One integration issue that came to light is the need to reference digital beam position vectors to the analog reference lesion offset from the image center. Because of this, the digital system must scale the analog output voltage such that it could, in the worst case (given the reference lesion is at an extreme edge of the image), provide twice the normal full-scale voltage to the galvanometers. This can be accomplished by appropriate scaling in the software.

In marginal optical situations often found *in vivo*, the reference lesion should be selected as close to the image center as safely possible for best performance. Also for safety, the laser beam location check should be performed by the computer, but preferably on an aiming beam rather than a coagulating beam.

The use of both G310 and G108 galvanometers in the analog optical design resulted in some imbalance between the tracking beam and the coagulating beam. The different mirror masses, armature inertias, and torque constants between the

two resulted in dynamic interaction between the two sets of galvanometers that was impossible to eliminate. The next version of the system should use matched galvanometers for tracking and main steering.

Overall, the tests demonstrated that significant progress has been made toward developing a practical robotic photocoagulation instrument for an ophthalmologist. There is still more work ahead before the device is ready for clinical trials, however.

Chapter 9

Summary and Conclusions

The hybrid combination of the digital and analog systems described in this dissertation appears to be the best approach for meeting the specifications of CALOSOS.

9.1 Major Accomplishments

As a recap for the benefit of the reader, the major accomplishments of this research are listed below.

9.1.1 CALOSOS System Design

- A flexible, "window and mouse" user interface was created that greatly simplifies system operation.
- Digital tracking was improved by a factor of 25, to approximately 50 deg/sec equivalent retinal velocity.
- Analog tracking was partially integrated with the digital system; this allowed first generation hybrid operation.
- Hybrid operation at 68 deg/sec *in vitro* and 38 deg/sec *in vivo* was demonstrated.

- Real-time, motion-stabilized dynamic reflectance signals were obtained for the first time; irradiations on the order of 100 ms were recorded by the system.

9.1.2 Publications and Presentations

Various aspects of CALOSOS, including its design evolution and experimental results, have been reported in journals and at conferences. The reader is directed to the Reference section, items [6, 49, 57, 58, 138–140, 159, 173–177], for complete bibliographical listings.

9.2 Recommendations and Future Research

There is still considerable work to be done before a viable biomedical instrument can be fielded which would be both commercially and clinically successful.

The digital and analog systems must be more completely integrated; this will most likely require the systems to be rebuilt with the integration goal in mind.

A potential improvement to the optical design would have the CCD image formed through the beam steering optics, with an integrated illumination ring source focused on the cornea. This would eliminate the need for a separate fundus camera, allow more working room for the patient, and result in a motion stabilized digital image that would always have the coagulating beam at the center of the image. This concept requires investigation.

Another potential improvement would be to employ a separate tracking beam source, possibly at a wavelength of $\lambda \simeq 900$ nm where the silicon response has a high quantum efficiency. This would allow greater sensitivity, and also improve the laser safety margin since longer wavelengths have greater exposure limits [30]. Another significant benefit would be the partial decoupling of the coagulating beam and tracking beam, which would eliminate many of the integration problems encountered in this research.

The next generation hybrid system should use identical, closed-loop galvanometers for beam steering. This would improve the pointing accuracy and mechanical dynamics.

More research is needed regarding the use of reflectance as a lesion control signal. The anomalous lesions discovered in the course of this dissertation need to be understood. The wavelength dependence of the reflectance signal is also an important topic, as is understanding the effects of different confocal apertures.

The laser shutter placement should be modified to allow an aiming beam to be used with the system for easier operation. The computer-based check of the laser spot position would also be more effective if used with an aiming beam.

The potential for a fully digital system using a 200 frame/second or faster camera should be revisited. If this becomes practical, a much more simplified system would be possible than the hybrid design.

Strobed lighting for the digital image should be investigated. This would reduce image blurring, and provide a higher SNR_T.

Finally, the possible application of optical coherence tomography (OCT) should be investigated as a means of dynamic lesion control. It's characteristics offer potential for actual calibrated depth control of a lesion.

9.3 Conclusion

This research made significant progress toward the goals outlined for CALOSOS: a reliable, safe, cost-effective system which can control laser photocoagulators of the type found in an ophthalmologist's office. The system as envisioned will safely create therapeutic retinal lesions of a specified number and location in minimal time with little or no human intervention.

While integration and lesion control questions require further study and development, the system described in this dissertation represents the most capable design currently available for robotic photocoagulation.

Appendix A

Supporting Topics

A.1 Determining Optical Resolution

This section describes the factors which detemine optical resolution. Ideal optics are discussed first, followed by some ramifications of aberrations.

A.1.1 Definitions and Assumptions

Some definitions and assumptions are helpful before proceeding. Assume that the retinal image is formed by narrowband incoherent light (see Section A.4.1). All optical lenses, apertures, entrance/exit pupils, etc., are assumed to be circular. Furthermore, as Castleman states [101], a safe assumption is that high quality optical components (lenses, cameras, etc.) such as those used for CALOSOS have the characteristics of linearity, shift-invariance, and phaselessness within their normal operating range; any significant deviation from this due to aberrations will be discussed. This discussion will refer below to the numerical aperture, or NA, of an optical system, which can be defined in terms of lens parameters (NA $= D/2f$ for lens diameter D and focal length f) or in terms of the imaging geometry (NA $= n \sin \alpha$ for index of refraction n of the medium, and the half angle α of the imaging light cone). The standard definition of contrast in an image is used: $C = (I_{\max} - I_{\min})/(I_{\max} + I_{\min})$, where I is the measured brightness of a point in the image.

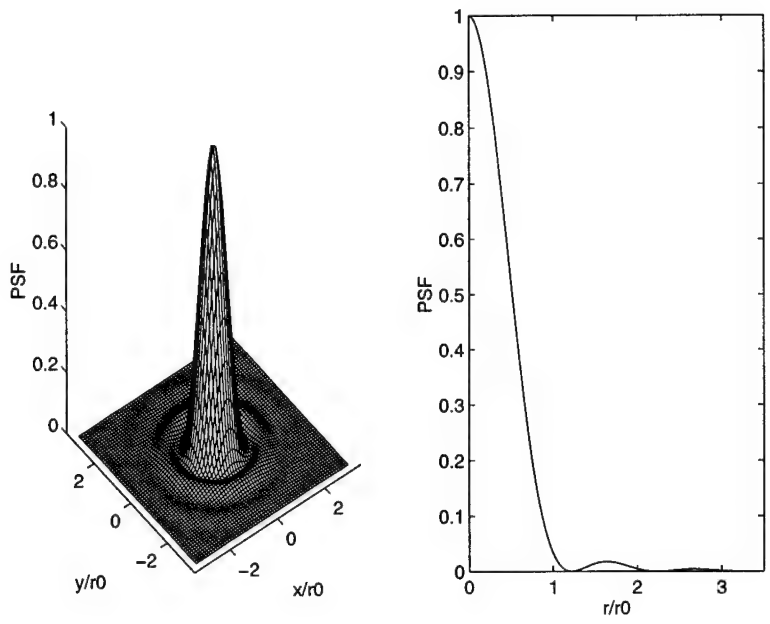

Figure A.1: The point spread function (PSF) of an ideal circular lens.

A.1.2 Diffraction-Limited Optics

Disregarding aberrations for now, begin by assuming ideal (i.e. diffraction-limited) lenses and perfect detectors. One useful formulation [92,101] for the PSF of an ideal circular lens is given by

$$h(r) = \left[2 \cdot \frac{J_1\left(\pi \cdot \frac{r}{r_0}\right)}{\pi \cdot \frac{r}{r_0}} \right]^2 \tag{A.1}$$

where $J_1(x)$ is a first order Bessel function of the first kind, r is the radius equal to $\sqrt{x^2+y^2}$ in the focal plane, and r_0 is a constant scaling factor equal to $\lambda/2\text{NA}$. Equation A.1, shown graphically in Figure A.1, describes the familiar Airy disk pattern, where the first zero occurs at $1.22r_0$. This forms the basis of the Rayleigh criterion for specifying optical resolution. It states that two equal intensity, mutually incoherent point sources on a sourceless background can be resolved if they are separated by a distance d equal to or greater than the first zero of the PSF. By this

definition

$$d = 1.22 \cdot \frac{\lambda}{2\text{NA}} \tag{A.2}$$

is the minimum separation between resolvable objects. If we choose to use this criterion, d would be the size of a resel. However, the Rayleigh criterion is not a physical law, it is simply a rule of thumb [110]. Other resolution measures, such as the Sparrow criterion (defined as the distance between two point sources where the second spatial derivative of intensity evaluated at the midpoint between the two sources equals zero), have also been put forth [104, 106, 110]. For incoherent light,[1] the Sparrow criterion evaluates to approximately

$$d = \frac{\lambda}{2\text{NA}} \tag{A.3}$$

which is equivalent to stating that d equals r_0 from Equation A.1. Authors such as Guenther [110] and Ronchi [111], however, warn that the somewhat arbitrary criteria of either Rayleigh or Sparrow may be too restrictive for general imagery; Guenther goes on to recommend utilizing Fourier optics [98, 178] to examine the spatial frequency domain before deciding on a resolution criterion for a particular application.

The two-dimensional Fourier transform of the PSF is the optical transfer function (OTF), which in general is a complex-valued function of two orthogonal spatial frequency variables. The modulus (i.e. magnitude) of the OTF is the modulation transfer function (MTF).[2] The MTF is one of the most widely quoted optical and imaging system specifications. At a particular spatial frequency, the MTF is the factor by which the contrast of sinusoidal features in the object are scaled in the image. As the MTF decreases, so does contrast and hence visibility of features in the image—this implies another way to specify resolution. It should be noted that resolution only partly describes image quality; contrast at various spatial frequencies

[1] The Rayleigh criterion is inappropriate for coherent light, but the Sparrow criterion can be used for either [110]. The Sparrow criterion evaluates to $\simeq 1.5\lambda/2\text{NA}$ for coherent sources.

[2] A minority of authors such as Smith [106] define the MTF as just the real part of the complex OTF.

making up the image is also important. However, because an appropriate resel is sought in order to evaluate the spatial sampling of the image, this discussion concentrates on resolution.

Still disregarding aberrations, assume the OTF is real and therefore equivalent to the MTF for two reasons [101]. One is the assumption above of a phaseless system, and the other is that the PSF defined by Equation A.1 is an even function—the Fourier transform of an even function is a real-valued, even function. From [101,106], a particularly useful formulation for the OTF of an ideal circular lens can be derived, given by

$$H(q) = \begin{cases} \frac{2}{\pi} \cdot \left[\cos^{-1}\left(\frac{q}{f_c}\right) - \frac{q}{f_c} \sin\left(\cos^{-1}\left(\frac{q}{f_c}\right)\right) \right] & \text{for } 0 \leq q \leq f_c \\ 0 & \text{for } q > f_c \end{cases} \tag{A.4}$$

where q is the radial spatial frequency variable equal to $\sqrt{u^2 + v^2}$ given that u and v are spatial frequency variables related to the x and y directions of the focal plane (respectively), and f_c is called the cutoff frequency and is equal to $2\text{NA}/\lambda$. Note that f_c of Equation A.4 is the inverse of r_0 from Equation A.1. Figure A.2 graphically depicts Equation A.4, where it can be seen that the OTF (and thus the MTF) decreases with increasing spatial frequency until at f_c the MTF is zero. Sinusoidal features with spatial frequencies above f_c will not appear in the image, implying a resolution limit related to f_c. *If* the retinal image consisted entirely of purely sinusoidal objects, and *if* objects could be detected all the way down to where the contrast C equalled zero, then an appropriate resolution metric would be $1/f_c = r_0$. In that case

$$d = \frac{\lambda}{2\text{NA}} \tag{A.5}$$

would be the minimum separation between resolvable objects, which is the same as the Sparrow criterion of Equation A.3. However, neither of these two conditions typically exist in a generalized imaging system and in particular don't exist in the retinal image formation of CALOSOS.

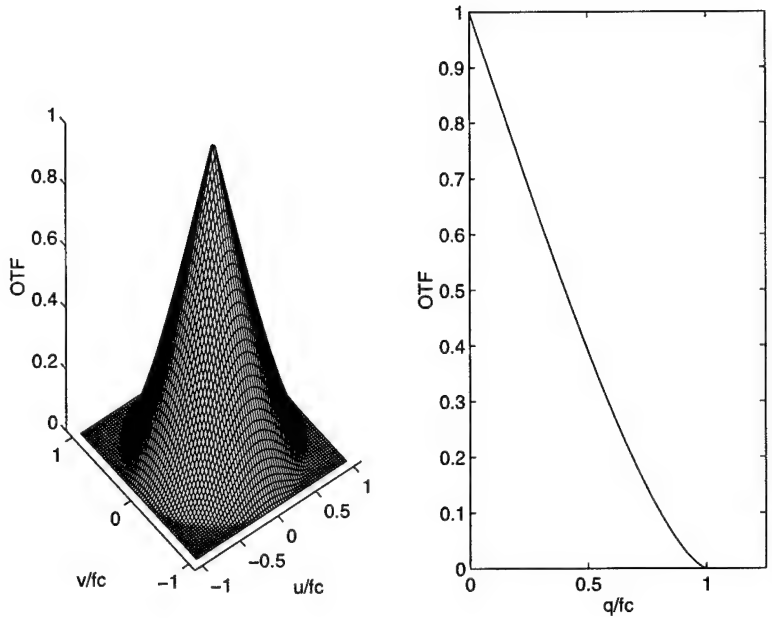

Figure A.2: The optical transfer function (OTF) of an ideal circular lens.

First, the retinal image does not consist of purely sinusoidal, single frequency objects. For example, a sharp-edged blood vessel object in the space domain would consist in the spatial frequency domain of many frequencies. Any of those frequencies greater than f_c would not appear in the image, and frequencies less than f_c would appear with their contrast scaled down by the MTF. The end result is the blood vessel would appear in the image, albeit with reduced contrast and blurred edges.[3] Second, the minimum detectable contrast using non-ideal equipment is greater than zero; the human eye can detect contrast down to 0.02 but typical video equipment can rarely detect contrast less than 0.1 under the best conditions [106, 117]. Taken together, this means an appropriate resolution metric specific to CALOSOS is not as simple as that implied by Equation A.5.

While the MTF is often specified for lenses and some cameras, the television,

[3]This low-pass blurring effect is also equivalent to convolution (in the space domain) of the object and the PSF.

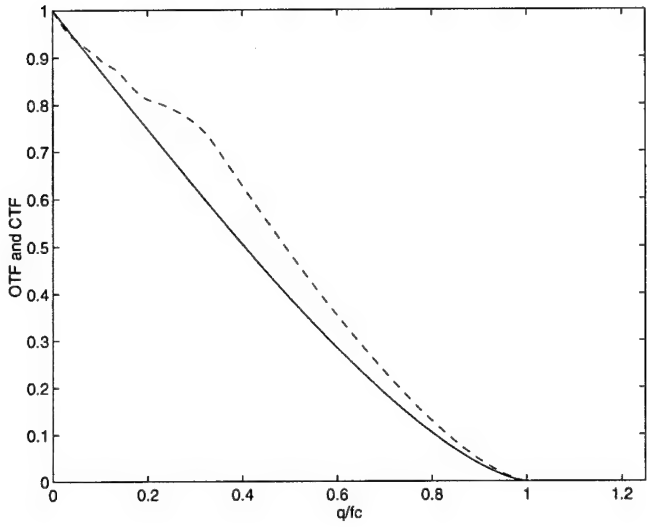

Figure A.3: A comparison of the MTF (solid line) and CTF (dashed line) of an ideal circular lens.

video, and imaging industries more often use the contrast transfer function (CTF), which is much easier to generate [105, 117]. The CTF is the factor by which the contrast of square wave features (i.e. a bar pattern), rather than sinusoidal features, in the object are scaled in the image. From the Fourier series that describes a unit square wave, we can find the conversion to get the MTF if the CTF is specified, as shown below [109, 117].[4]

$$\mathrm{MTF}(f) = \frac{\pi}{4}\left[\mathrm{CTF}(f) + \frac{\mathrm{CTF}(3f)}{3} - \frac{\mathrm{CTF}(5f)}{5} + \frac{\mathrm{CTF}(7f)}{7} - \cdots\right] \tag{A.6}$$

A comparison of the MTF and CTF of a diffraction-limited circular lens is shown in Figure A.3. For typical commercial video systems, the CTF is nearly the same as the MTF at all but the lowest spatial frequencies, and the two are sometimes used interchangeably [109].

It might be expected from the foregoing discussion that the "true" diffraction-limited resel would be $\lambda/2\mathrm{NA} < d < 1.22\lambda/2\mathrm{NA}$. Indeed, a large number of careful

[4] Conversely, $\mathrm{CTF}(f) = \frac{4}{\pi}\left[\mathrm{MTF}(f) - \frac{\mathrm{MTF}(3f)}{3} + \frac{\mathrm{MTF}(5f)}{5} - \frac{\mathrm{MTF}(7f)}{7} + \cdots\right]$.

observations by the astronomer Dawes [106] found d to be in this range between the Sparrow and Rayleigh criteria, and Inoué notes the same for contrast-enhanced video microscopy [109]. But it should be pointed out that these were the results of concentrated efforts to maximize resolution using diffraction-limited optics, which is *not* the case for CALOSOS. In particular, the effects of aberrations must be considered.

A.1.3 Aberration Effects

When the optics include significant aberrations, the PSF and OTF can be complex-valued and asymmetrical. In general, aberrations will broaden the PSF and consequently narrow the OTF. An excellent treatment of these effects can be found in [106]. Aberrations can reduce the cutoff frequency, cause contrast reversals, cause zero contrast "bands" to appear below the cutoff frequency, and generally reduce image quality. A proposed quantitative measure of aberrated image quality is the *Strehl ratio* [106], which is the ratio of the volume integral of the aberrated MTF to the volume integral of the diffraction-limited MTF. When discussing aberrations, it is important to note that optical components not separated by a diffuser of some sort may compensate for the aberrations of each other—hence the term "corrected" optics. Otherwise the MTFs of system components are cascaded by multiplication. The concept of aberration tolerance should be considered: how much aberration can be considered acceptable within the system requirements? From [106], most imaging systems can withstand aberration resulting in up to one-quarter wavelength of optical path difference (OPD) from a "perfect" spherical reference wavefront without a noticeable effect on image quality. High quality optics, such as those used for CALOSOS, typically achieve this [107].

A.2 Just Detectable Difference for Photodetectors

Photodetectors in the UV to near IR spectrum are typically photoemissive, photovoltaic, or photoconductive; the primary parameters are quantum efficiency and the limiting noise mechanism [102, 116, 179]. For CALOSOS, the retinal image is obtained by the photoconductive CCD array, and this discussion will concentrate on that. The primary noise mechanisms for a CCD imaging detector include radiation (also called photon) noise (due to statistical fluctuations in photon arrivals), thermal (or Johnson) noise, generation-recombination (or GR) noise (due to variations in the semiconductor charge carrier generation and recombination), trapping noise, and reset noise [105]. A complete treatment of detector noise would include parameters often found in specifications such as noise equivalent power (NEP), responsivity ($\mathcal{R}$), and detectivity (D^*), but that is beyond the scope of this discussion. See [107] for more detail. An excellent thoretical treatment of detector noise source processes can be found in [179]. For electronic noise reduction techniques, see [180].

A perfect "noiseless" detector must still contend with radiation noise. The JDD is thus dependent upon the number of photons received, and requires the use of Poisson statistics [100]. A perfect detector receiving n photons produces a signal that just detectably larger (on average) than when it receives $n-\sqrt{n}$ photons and just detectably smaller (on average) than when it receives $n+\sqrt{n}$ photons; thus the JDD is $\sqrt{n}$. The implication of this is that the JDD of an ideal detector is not constant across all intensity levels—it varies with the square root of the number of photons received. For the most efficient operation with an ideal detector, the quantizer of the frame grabber ADC would have nonuniform gray level steps,[5] which is much more expensive and complicated than a standard uniform-step quantizer. In practical use, most designs incorporate the relatively inexpensive uniform-step quantizer with a step size equal to the smallest JDD and the number of steps sufficient for the dynamic

[5] Or a compander coupled to a uniform quantizer—see [90] for a discussion of optimal quantization.

range (see [100] for an excellent treatment). This design choice is further supported by the fact that noise sources of nonideal detectors reduce the dependence of the JDD on the image intensity.

The noise of a nonideal photodetector includes those additional noise mechanisms listed above, which are usually considered as an equivalent number of "dark current photons" designated n_{dark}, with the nonideal JDD being $\sqrt{n + n_{\text{dark}}}$. Note that the thermal and reset noise components of n_{dark} are not affected by the actual number of photons received. If the dominant detector noise source is thermal, which is usually the case for CCD arrays operated at room temperature [107], then the JDD of the detector is not as dependent on the intensity level of the image as is an ideal detector. The image from the CCD camera is also affected by the (primarily thermal) noise from the detector preamplifier [105], which is also independent of the image intensity level. Modern non-intensified CCD cameras operated at room temperature and with appropriate illumination levels (as is CALOSOS), are predominantly limited by this preamplifier noise.

A.3 Chromatic Characteristics of Retinal Images

It is helpful to briefly outline how retinal images are dependent upon the wavelength of the illumination light source. One of the best treatments of monochromatic illumination in regular fundus photography can be found in [181]. Figure A.4, adapted from results presented there, clearly shows how the choice of illumination wavelength affects the contrast (and thus the visibility) of various structures on the retina. Thus the desired features of the fundus can be emphasized and/or deemphasized simply by the choice of illumination wavelength.

Note that if the fundus is imaged with a scanning laser ophthalmoscope (SLO) [86] or a confocal scanning laser ophthalmoscope (CSLO) [89], then the optimum wavelengths may differ somewhat from Figure A.4 because of differences in scattering events experienced by the returning image-forming light [182, 183]. The design

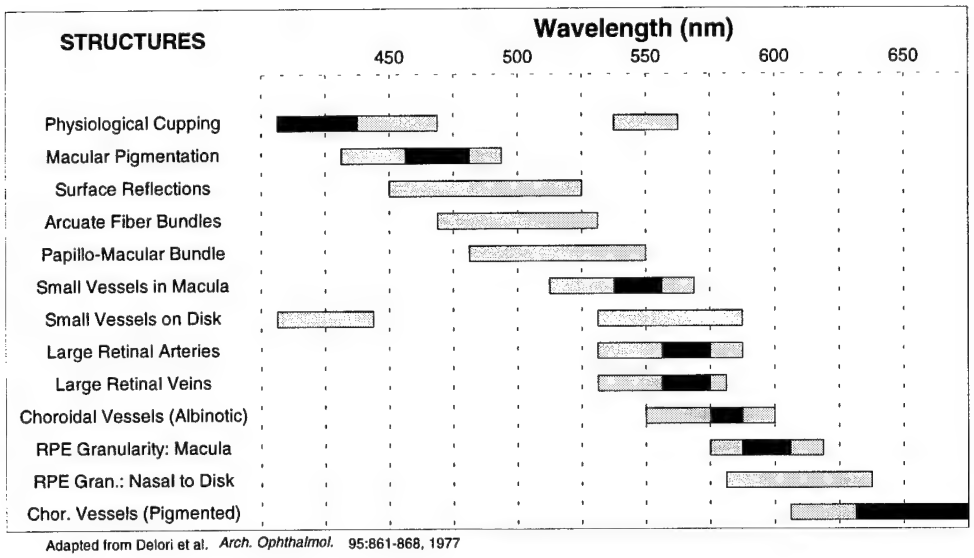

Figure A.4: Spectral ranges of optimal visibility for various structures in the human retina. Shaded bands: good contrast; dark bands: best contrast.

of CALOSOS is such that Figure A.4 applies.

While not shown in Figure A.4, a retinal lesion formed as a result of photocoagulation has a higher reflectance than surrounding tissue at all the visible wavelengths. Hence it appears as a bright spot in fundus photographs.

A.4 Barrett's Methods of Image Enhancement

This section reviews the methods Barrett devised for improving the contrast of blood vessels in retinal images. See [15] for more detail.

A.4.1 Using Optics to Improve the Tracking SNR

Based upon Equation 4.10, anything that makes the blood vessels darker and/or the background lighter would improve the SNR_T. The methods must be chosen with care, however, as the real-time demands of CALOSOS prohibit computationally

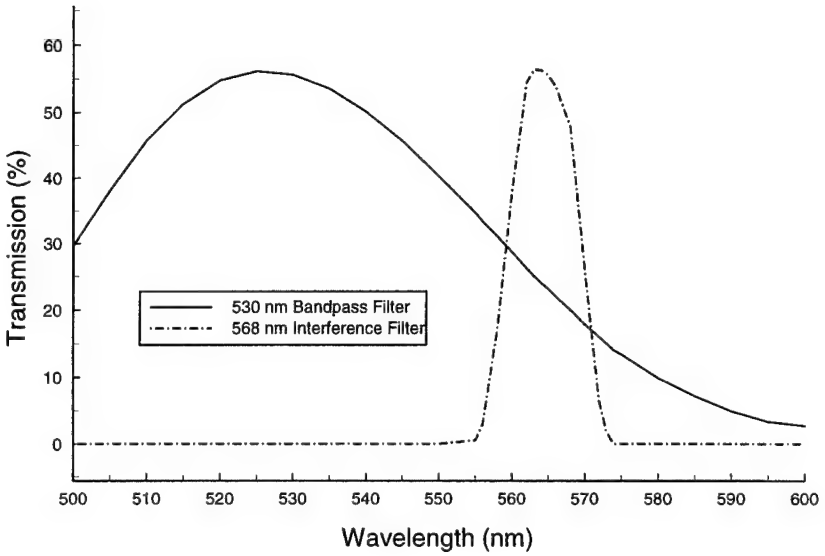

Figure A.5: A comparison of illumination lamp filters for fundus camera imaging. Data taken with a Varian 2300 spectrophotometer [15].

complex solutions. Recall from above that careful choice of illumination wavelength can emphasize desired fundus structures. To emphasize major retinal blood vessels (arteries and veins), it can be seen from Figure A.4 that illumination somewhere in the spectral range of 560–575 nm would yield the best contrast, and hence the highest SNR_T and most robust tracking. As a general purpose device, a typical fundus camera generally incorporates a fairly broad-spectrum filter for the illumination lamp in order to make the greatest number of retinal structures visible. For example, the standard filter for the Olympus model GRC-W Mydriatic fundus camera used in this research is a broad bandpass filter centered about 530 nm. To emphasize the retinal blood vessels, this filter is replaced with a narrow-band 568 nm interference filter (see Figure A.5). Use of the 568 nm filter is an ideal form of image enhancement, as it greatly increases the contrast of the retinal blood ves-

sels optically without imposing any time penalty. Barrett proved this in [15], and effectively employed the technique in his system.

The only disadvantage to this form of enhancement is that less total energy from the fundus camera illumination lamp reaches the retina, but the marked increase in blood vessel contrast makes this a good trade-off. The filter is easily removable to allow color photographs through the fundus camera; otherwise the photos would look unusually green.

A.4.2 Using LUTs to Improve the Tracking SNR

Another method that can be employed to enhance the image without any time penalty is to reprogram the frame grabber look-up tables (LUTs) to alter the gray level of the pixels [64, 109, 184]. Normally the LUTs simply pass the original gray scale value of each pixel unchanged to the main computer memory. That is, 0 is mapped to 0, 1 is mapped to 1, ..., and 255 is mapped to 255. But the LUTs can be programmed such that any given gray scale value of the image can be mapped to any output gray scale value, as shown in Figure A.6. Once programmed, the LUTs impose no additional time delay on the image throughput.

A technique called *contrast stretching*, based on the histogram of the image, can be implemented quite easily using LUTs [91, 184] to globally improve the overall contrast of the retinal image and thereby improve the SNR_T. A software subroutine was written for CALOSOS which scans a user-selected portion of the reference image for G_L, the minimum gray scale value, and G_H, the maximum gray scale value, then programs the LUTs to stretch the contrast such that the new (typically lower) minimum gray scale value is $\hat{G}_L$ and the new (typically higher) maximum gray scale value is $\hat{G}_H$. This transformation is described by the relationship shown

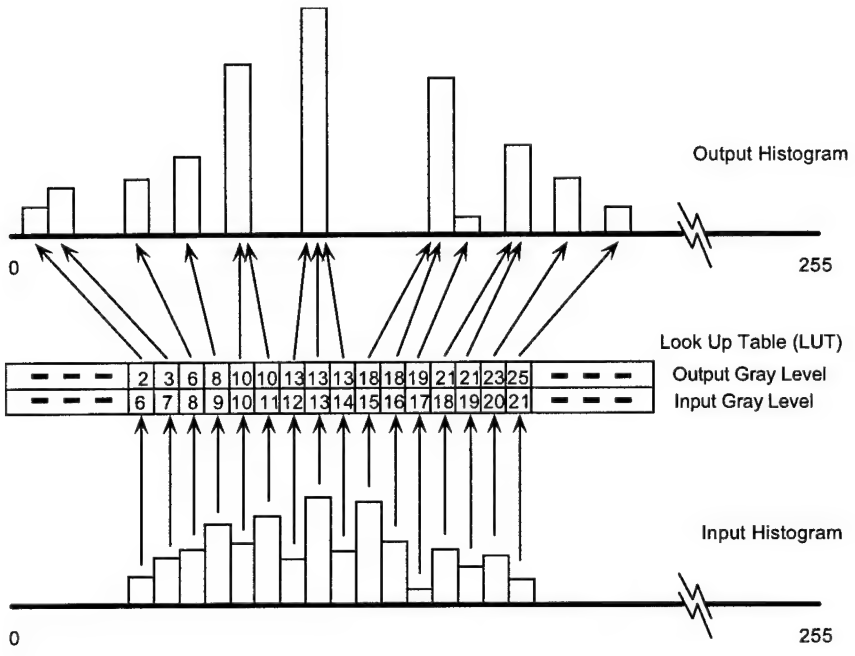

Figure A.6: An arbitrary remapping of the frame grabber look up table (LUT) to modify the image.

below,

$$\hat{g} = \begin{cases} \hat{G}_L & \text{for } g \leq G_L \\ \hat{G}_L + \dfrac{(g - G_L)(\hat{G}_H - \hat{G}_L)}{G_H - G_L} & \text{for } G_L < g < G_H \\ \hat{G}_H & \text{for } g \geq G_H \end{cases} \tag{A.7}$$

where g is the input gray scale value of the source image, and $\hat{g}$ is the output gray scale value actually sent to the main computer memory. The use of contrast stretching by reprogramming the LUTs is another ideal form of image enhancement, as it can greatly increase the contrast of the retinal blood vessels without imposing any time penalty. Barrett also proved this in [15], and effectively employed the technique in his system.

A disadvantage to this form of enhancement is that is can also increase the noise in an image, since the variance of the noise process is "stretched" along with the image. Therefore, this option is under complete operator control through the CALOSOS computer-user interface.

A.5 Overview of Digital Tracking

The tracking task requires the system to determine when an eye movement has occurred, ascertain the direction and magnitude of the movement, and generate an appropriate correction signal. Assuming that the system is acquiring digitized images of the scene of interest (for CALOSOS, this would be the retina), then movement has occurred if two subsequent images don't "line up" feature by feature. Typically one of the images is designated the *reference image*, and the task is to determine what would be necessary to get the second image to line up with the reference. This is activity is called image registration, and has been studied at length [90, 91, 93, 94, 185]. Note that unless the system implements some sort of predictive algorithm, tracking systems based on past data are always "playing catch-up." However, reliable predictive tracking algorithms for even specialized cases are not yet proven. The discussion here concentrates on the classical past data

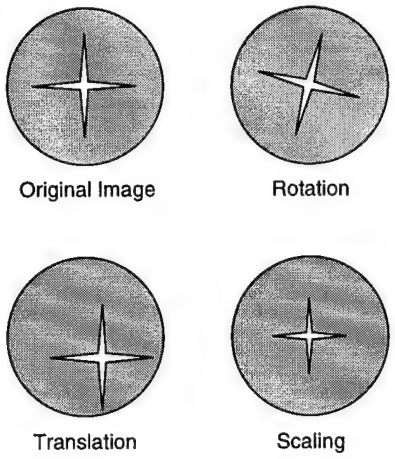

Figure A.7: A generic image shown with examples of rigid transformations.

techniques.

A.5.1 Image Transformations

When the current image has changed compared to the reference image, there has been a *transformation* of the image. Following the discussion in [185], the most common categories of general transformations are: rigid, affine, projective, perspective, and global polynomial. Rigid transformations, the least general category, take place when there is relative movement between the image and the sensor, yet objects in the image retain their relative shape and size. Since the main concern here is with movement of the retinal image with respect to the CCD camera sensor, the discussion[6] is restricted to rigid transformations. See [185] for more detail on other types of transformations. Rigid transformations are composed of some combination of rotation, translation, and change of scale. See Figure A.7.

The rigid transformation is linear and can be described mathematically with four parameters: t_x, t_y, s, and θ, where t_x and t_y are the elements of the translation

[6]Photometric variations, such as image illumination, are ignored for the moment. They will be discussed later.

vector, s is the scale factor, and θ is the rotation angle. This transformation maps a point (x_1, y_1) in the reference image to a point (x_2, y_2) in the current image via the following relationship:

$$\begin{pmatrix} x_2 \\ y_2 \end{pmatrix} = \begin{pmatrix} t_x \\ t_y \end{pmatrix} + s \begin{pmatrix} \cos\theta & -\sin\theta \\ \sin\theta & \cos\theta \end{pmatrix} \begin{pmatrix} x_1 \\ y_1 \end{pmatrix} \tag{A.8}$$

See [91, 126] for more formal 4×4 matrix representations of image formation geometry; the notation above is adequate to this discussion. Equation A.8 can be rewritten more compactly using the notation:

$$\vec{p}_2 = \vec{t} + s\mathbf{R}\vec{p}_1 \tag{A.9}$$

where $\vec{p}_2$ and $\vec{p}_1$ are the coordinate vectors of the two images, $\vec{t}$ is the translation vector, s is the scaling factor (a scalar quantity), and $\mathbf{R}$ is the rotation matrix.

Brown [185] categorized types of image variations, and selected appropriate registration methods for each category. Given the rigid, frequency-independent variations for which CALOSOS must compensate, Brown recommends either correlation-based or sequential methods. The next section will examine the appropriateness of these techniques to CALOSOS.

A.5.2 Correlation-Based and Sequential Registration Methods

In image registration, the task is to assess the closeness of the match between the reference image and the current image, and generate sufficient information to allow an inverse transformation. There are several figures of merit that can used for quantifying the match, such as maximum error, absolute error, and mean squared error (MSE). One classic technique which leads to correlation-based methods is to use MSE [91]. For a reference image f and a subset g of the current image, and R defining the area boundary of g, the MSE of g compared to f is defined as

$$\text{MSE} = \sum_{x,y \in R} \sum (f - g)^2 \tag{A.10}$$

In the literature, the subset g of the current image is often referred to as a *template*, and is significantly smaller than f. We can decompose Equation A.10 into its constituent parts:

$$\text{MSE} = \underbrace{\sum_{x,y\in R}\sum f^2}_{\substack{\text{reference image} \\ \text{energy over } R}} + \underbrace{\sum_{x,y\in R}\sum g^2}_{\substack{\text{template} \\ \text{energy over } R}} - \underbrace{2\sum_{x,y\in R}\sum f\cdot g}_{\text{cross correlation } C_{fg}} \tag{A.11}$$

The first term varies only with R and is independent of g, and the second term is constant; the third term is (minus two times) the cross correlation between f and g. Thus we see that to minimize the MSE (which we must do to obtain the best match) we need to maximize the cross correlation of the reference image and the template. The template is scanned around the reference image, and the (x, y) coordinates where the correlation is maximum gives the location of the best match. Using the notation of Equation A.8, the change from the original template origin on the reference image (x_1, y_1) and the new template origin on the current image (x_2, y_2) yields the components of the translation vector $\vec{t}$, where $t_x = \Delta x$ and $t_y = \Delta y$. To normalize C_{fg}, the Schwartz inequality given as

$$C_{fg} \leq \sqrt{\sum_{x,y\in R}\sum f^2 \cdot \sum_{x,y\in R}\sum g^2} \tag{A.12}$$

can be applied to define the normalized correlation

$$C'_{fg} = \frac{C_{fg}}{\sqrt{\sum_{x,y\in R}\sum f^2 \cdot \sum_{x,y\in R}\sum g^2}} \tag{A.13}$$

where $0 \leq C'_{fg} \leq 1$.

Note that traditional image correlation yields a reasonable answer for transformation, but does not perform well in the presence of rotation or scale change. A related, more powerful (albeit more complex) technique was developed by Cideciyan [186] which yields the values needed for a complete inverse transformation to overcome rotation, translation, and scale change. The steps involved in Cide-

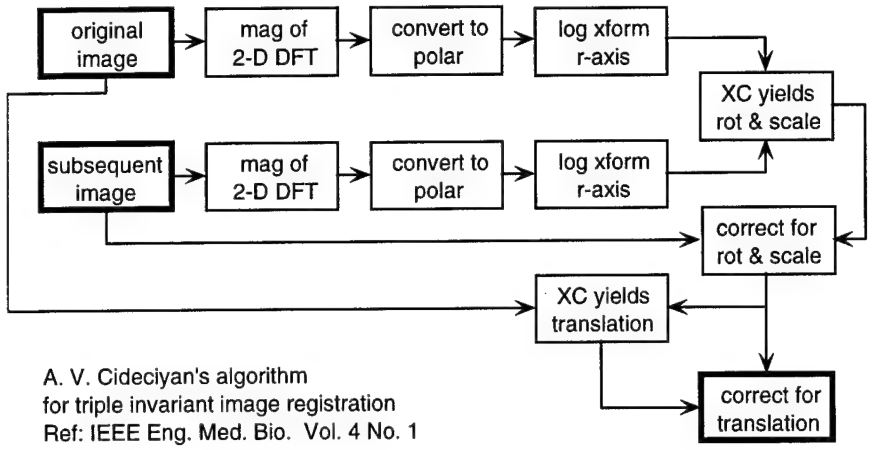

Figure A.8: Schematic flow chart of Cideciyan's technique for image registration.

ciyan's algorithm are shown graphically in Figure A.8; this technique is a blend of correlation-based and Fourier-based methods.

At this point the question arises concerning the actual types of image movement for which CALOSOS must compensate. Barrett showed [15] that for a human patient motionless in a chin rest with the conjugate eye fixated, the fundus camera image exhibited negligible rotation or change of scale. He determined that for the development of a robotic retinal photocoagulator, translation was the only significant tracking challenge. Therefore, CALOSOS needs only to determine the translation vector $\vec{t}$ from Equation A.9 to adequately track the retina, since we can assume $s = 1$ and $\mathbf{R}$ is equal to the identity matrix $\mathbf{I}$. In the unlikely event of the image properties deviating from this, it will be sufficient to detect the anomalous condition and temporarily suspend irradiation until the image returns to normal.

All correlation-based methods of image registration are computationally intensive; as such they are unsuitable[7] for the real-time retinal tracking necessary for CALOSOS. Sequential methods such as sequential similarity detection (SSD) first proposed by Barnea and Silverman [187] substitute a computationally simpler figure

[7]Using inexpensive general purpose computers.

of merit for the MSE described above. SSD typically uses the sum of the absolute value of the difference (SAVD) between pixels:

$$E(u,v) = \sum_{x,y \in R} \sum |f(x,y) - g(x-u, y-v)| \tag{A.14}$$

To further speed the registration process, the SSD technique often employs an error threshold which, when exceeded, terminates examination of the current template location early and moves the template to the next location. See [187, Fig. 2].

Non-normalized SAVD results in unacceptable numbers of erroneous registrations (i.e. false positives) due to its sensitivity to image illumination variations [188]. At the cost of added computational complexity, the SAVD measure can be normalized by subtracting the average intensity of the reference image and the template:

$$E'(u,v) = \sum_{x,y \in R} \sum \left| \left[f(x,y) - \overline{f} \right] - \left[g(x-u, y-v) - \overline{g} \right] \right| \tag{A.15}$$

By using the normalized SAVD for the figure of merit, acceptable image registration can be performed up to two orders of magnitude faster than the correlation-based techniques [93]. But even greater savings can be realized. By using the *a priori* knowledge of fundus image feature sets, the registration technique can be optimized for retinal tracking. Peli et al. [189] initially improved upon the standard normalized SSD technique with particular application to retinal images by restricting the template regions to those containing blood vessels. However, the reference image had to be manually evaluated for gray level thresholds to determine appropriate template regions. The modified SSD technique resulted in only a modest increase in speed, but significantly reduced false positives compared to the standard SSD. While other techniques have been proposed for real-time fundus image registration (for example [12, 136, 137]), they require expensive, specialized equipment or are suitable only for fundus images which include the optic disk. It appears that some form of normalized SSD is best suited for the real-time retinal tracking required for CALOSOS. This agrees with the recommendations of Brown [185] and supports the work of Markow [53] and Barrett [50].

A.6 Barrett's Digital Retinal Tracking Technique

Barrett (following Markow's earlier work [8], which evolved independently of Peli et al. [189]) devised a variation [15] of the SSD technique which was uniquely optimized for retinal tracking.

A.6.1 Blood Vessel Templates

The basis of Barrett's technique is to use a variable width (called *elastic* in the literature) one-dimensional template using only four pixels each, which has a maximum response when centered over a blood vessel. This is illustrated in Figure A.9 for an ideal image and a single width template. Note that the template response,

$$R = \frac{P1 - P2 - P3 + P4}{P1 + P2 + P3 + P4} \tag{A.16}$$

is normalized and is therefore robust in the presence of uniform image illumination variations. The image region between pixel $P2$ and $P3$ is the elastic region which is adjusted according to the width of the blood vessel. The width of the template is thus defined as the distance, in pixels, between $P2$ and $P3$ inclusive. When the template width equals the blood vessel width and is centered over the blood vessel, the highest response occurs.

Henceforth any reference to 1-D templates will refer to these four pixel templates developed by Barrett. When referring to the orientation of a template, some ambiguity is possible. This is because a 1-D template where all four pixels lie in the same *horizontal* row of the image will yield its highest response for a *vertical* blood vessel, as illustrated in Figure A.9. To remove ambiguity from the discussion, we will always refer to a 1-D template's orientation as defined by the template's pixels, not by the direction of the blood vessel it "prefers." Hence, a *horizontal template* is one consisting of pixels in the same horizontal row (and tending to select a vertical blood vessel); a *vertical template* is one consisting of pixels in the same vertical column (and tending to select a horizontal blood vessel).

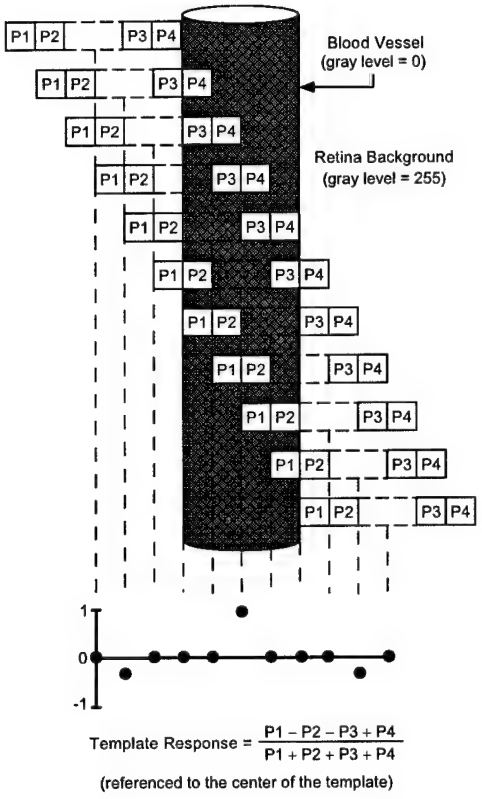

Figure A.9: Template response in the vicinity of a retinal blood vessel.

A.6.2 The Two Dimensional Tracking Template

In order to register and thus track retinal images, a two dimensional template is needed. Barrett combined multiple 1-D templates into a 2-D tracking template by locking in the relative offsets of each 1-D template on the reference image from a given template origin, where the 2-D template response was the sum of the 1-D template responses. He then scanned the 2-D template over the current image, and the location of maximum 2-D template response yielded the updated location of the template origin. He experimented with various configurations, and found that six 1-D templates (three horizontal, three vertical) yielded the best compromise between computational complexity and tracking accuracy. Using only horizontal and vertical templates also reduced the computational requirements of the algorithm. To select appropriate templates, the computer scanned the reference image over some user designated region looking for the highest responding horizontal and vertical templates, and used the first horizontal template as the 2-D template origin. By splitting the template selection search region into three equal areas and confining a horizontal/vertical template pair to each region, the software ensured that the selected templates were spatially distributed across the search region. This reduced the possibility of false positives. A conceptualized view of Barrett's templates on an image of the fundus is shown in Figure A.10.

The six 1-D templates together form a single 2-D template which can be used to determine eye movement between video frames. The technique is highly efficient as it requires examination of only 24 pixel values for the entire 2-D template. The best that Peli *et al.* [189] managed with their modified SSD technique was a threshold search on an 8×8 template and a full 8×8 normalization step. The increase in efficiency using Barrett's templates is obvious. Furthermore, because of the small number of pixel values to be examined, the added complexity of a threshold search is not needed.

For tracking, Barrett found that earlier proposals to use a coarse/fine search

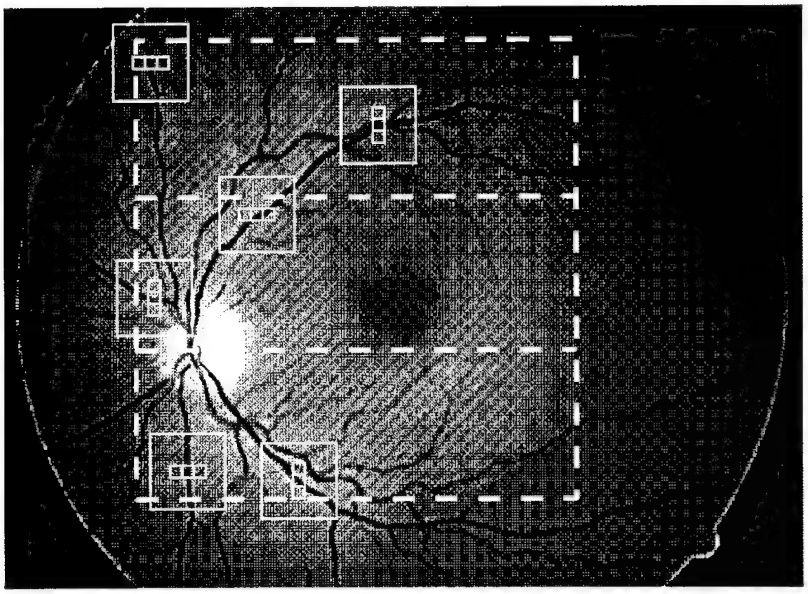

Figure A.10: A conceptualized view of the tracking templates on a fundus image.

strategy for speed resulted in an unacceptable number of false positives [15]. Instead, he implemented a "limited exhaustive search" routine using the 2-D template, achieving better than 99% correct registration (within a 100 μm error radius on the retina) at moderate retinal velocities ($<$ 2 deg/sec). The search was "limited" because he searched only within the pixel radius of anticipated maximum eye movement between frames.

Furthermore, as discussed in Chapter 6, the laser pointing and control system uses inexpensive open loop galvanometers to steer the laser beam; there is no position feedback from the galvanometers. To achieve some level of closed loop control, a desirable addition to the tracking algorithm searches for and locates the laser spot on the retina and compares this to the intended location. If the error is small, a correction signal can be generated. If the error is large, irradiation is aborted. See Chapter 6 for more details about laser pointing and control.

A.7 Ferguson's Analog Retinal Tracking Technique

Recall that a laser-induced retinal lesion is more highly reflective than normal retinal tissue: it looks bright compared to the darker surrounding tissue in fundus images. Ferguson uses that feature to advantage by moving a low-power [30] secondary laser beam in a small circle ("dithering" the beam) around a designated reference lesion, and detecting the returning light with a confocal reflectometer [21,85]. Recall basic confocal reflectometry was explained in Section 3.7.1; the reader may also wish to review the optical layout that incorporates Ferguson's analog tracking optics with the appropriate CALOSOS optics as shown in Figure 3.9.

A.7.1 Generating Analog Tracking Signals

At any given instant, when this "dithered" beam is pointed on the reference lesion the reflectometer signal is high; when it is pointed off the lesion the reflectometer signal is low. Thus the reflectometer output signal varies synchronously (when corrected for phase shifts) with the periodic dither signal which drives the dithering mirrors, as shown in Figure A.11 and discussed more completely below. This output is processed to yield Δx and Δy error signals from the confocal reflectometer, which initially increase as the dithered tracking beam moves farther from the center of the reference lesion. The error signals contain all the information needed to redirect the tracking beam back to the center of the reference lesion, thereby minimizing the error signal. By integrating these error signals over time, so that cumulative errors produce net displacements and using them to drive the main steering mirrors in the tracking beam path, arbitrary motions of the reference lesion relative to the tracking beam can be followed. Since the reference lesion is fixed with respect to the retina, this results in retinal tracking. Such a control system is a variation on the servo loop concept, and is similar to the "auto-lock" method commonly used in satellite tracking [190].

Figure A.11(a–c) depicts some representative dither circle signals, and the re-

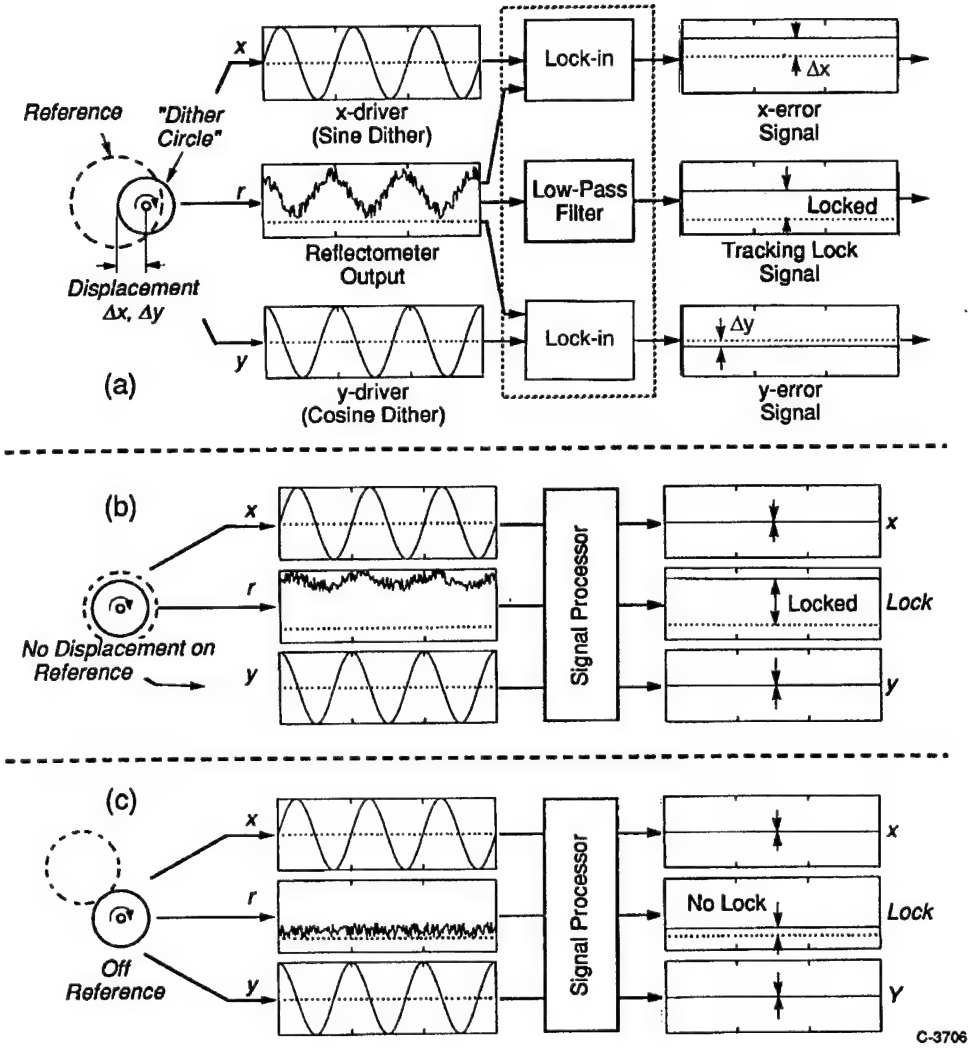

Figure A.11: Analog method of obtaining Δx and Δy tracking signals from a confocal reflectometer.

sulting reflectometer signals. Phase-sensitive detection is accomplished with lock-in amplifiers, which are simply analog multipliers (mixers) followed by low-pass filters [191], which in turn produce DC offset voltages proportional to the amplitude of the components of the reflectometer signal which are in phase with the associated dither signal. The resulting pair of error voltages constitute a tracking correction vector (equivalent to $\vec{t}$ from Equation A.9) which is relayed to the main steering mirrors. Figure A.11(a) shows a case in which the dither circle is displaced along the x-axis (but not the y-axis) relative to the reference lesion. There is a Δx error signal proportional to the displacement, and a zero Δy error signal. Note the average value, or DC level, of the confocal reflectometer is significantly greater than zero. Figure A.11(b) represents a case in which the dither circle is centered and locked on the reference lesion (the eye may or may not be stationary at this instant) so that null error signals are produced. Again the DC level of the confocal reflectometer is significantly greater than zero. In Figure A.11(c), the dither circle as "fallen off" the reference lesion completely and the error signals are meaningless. But note that the DC level of the confocal reflectometer signal is now very low. This low DC value condition indicates a loss of analog tracking lock.

A.7.2 Analog Tracking Performance Metrics

Ferguson and the author have attempted to quantify the analog tracking performance. The maximum tracking speed on the retina is related to the dither frequency and reference lesion size. The basic relationship is

$$v_{\max} = kDf_d \tag{A.17}$$

where $v_{\max}$ is the maximum eye velocity that can be tracked, k is a system dependant dimensionless constant related to the error signal gain (which affects its detectability) and the transient response[8] of the associated circuitry (which determines how

[8]This is limited primarily by the low-pass filter at the output of the lock-in amplifier. But increasing the cutoff frequency of this filter would decrease the selectivity of the lock-in amplifier.

quickly the error signal can change values), f_d is the dither frequency, and D is the diameter of the relatively circular reference lesion. For example, at a retinal velocity of 50 degrees/second, the retina moves at $\simeq$14.6 mm/sec. With a 2 kHz dither frequency, this corresponds to a retinal displacement of approximately 7.3 μm per dither cycle. Assuming a typical reference lesion diameter of 400 μm, and a tracking beam initially centered on the reference lesion, over 54 dither cycles would occur before the tracking beam "fell off" the reference lesion by a distance of D, assuming no tracking correction. This relatively large number of cycles per reference lesion diameter affords sufficient opportunity to generate a detectable tracking signal and correct for the motion before tracking lock is lost. The value of k can be determined empirically by adjusting the integration time for the tracking error signal until the system operates satisfactorily. This integration time equals some number of cycles of the dither frequency, and the inverse of the number of cycles equals k. For the analog electronics used with CALOSOS, the value of k was empirically determined in this way to be approximately 0.1, yielding a theoretical maximum retinal tracking velocity of over 274 degrees/second with a 400 μm reference lesion. As was described in Chapter 8, the real-world achievable tracking velocity is much less ($\simeq$ 70 deg/sec with an eye phantom, $\simeq$ 38 deg/sec *in vivo*).

The response time τ of the analog tracking system is inversely proportional to k from Equation A.17, since k is in part a measure of how many dither cycles are needed to generate a detectable error signal, and in part how quickly the error signal can change values. Taking the inverse of the empirically determined k for CALOSOS yields 10 cycles of the 2 kHz dither signal, which equals a response time of $\tau = 5$ ms. Thus τ can be determined using the relationship

$$\tau = \frac{1}{k \cdot f_d} \tag{A.18}$$

Increasing the dither frequency f_d would make the system faster, but the galvanometers driving the dither mirrors are operating in superresonant mode, and further increases in frequency would be difficult with the inexpensive galvanometers used

for the prototype.

The theoretical resolution of the analog tracking system is a complex relationship of several factors. It is proportional to the overall detectability of the reflected tracking beam, the ratio of the tracking beam spot diameter to the reference lesion diameter, the ratio of the dither circle diameter to the reference lesion diameter, the tracking beam cross-sectional profile, and perhaps other factors. Quantitative analysis of this figure of merit is still being investigated. The bounding value of tracking resolution is determined by the retinal velocity and the response time, just as was calculated above for digital tracking. For the specified resolution requirement of 100 μm, and the analog tracking response time of 5 ms determined above, then the retinal velocity must be such that the eye moves less than or equal to 100 μm in 5 ms. This yields a maximum retinal velocity of 20 mm/sec, which is equivalent to 68.6 deg/sec eye velocity.

The optimal sizing of the reference lesion, tracking beam spot, and dither circle can be derived mathematically by convolving the two light intensity profiles (the lesion reflectance profile and the tracking beam profile) and solving for the dither circle that yields the greatest rate of change in the overlap. If one assumes a typical case of a Gaussian reflectance profile of the reference lesion and a Gaussian profile of the tracking beam, the convolution of two Gaussians is another Gaussian, and is separable into x and y components. When the reference lesion and the tracking beam spot are the same size Gaussian, for example, such that the variance σ^2 is equal for both, then the optimal dither circle radius is σ. This also makes intuitive sense since this is the point where the slope of the Gaussian curve has the greatest magnitude; thus the derived error signal will have the greatest amplitude. The designer should not expend too much effort on these calculations, however, since the actual properties of the reference lesion will vary widely from case to case in clinical use. The user can easily adjust the dither signal amplitude for the best tracking lock.

A.7.3 Analog Tracking Implementation

The analog tracking system creates the dither signal in a simple, symmetrical fashion. By driving the x and y dithering mirrors 90 degrees out of phase at identical amplitudes, a "dither circle" is produced. The mirrors are attached to a pair of orthogonally-mounted General Scanning model G108 galvanometers and driven at 2 kHz. This driving frequency is well above the loaded resonance frequency for these scanners ($\simeq$500 Hz), but because only small amplitudes were required for the dithering motion this super-resonant driving did not present a problem (see Chapter 6 for a discussion about galvanometer resonance). The G108 galvanometers have the smallest available armature inertia and therefore the most rapid response (if size of the mirrors is limited). The first dither mirror is 15 mm diameter by 1 mm thick. The second dither mirror is actually a beamsplitter instead of a mirror. In reflection, it serves as the second dither axis "mirror." In transmission, however, it serves as a non-deflecting window through which the high-power coagulating beam passes on the way to the main steering mirrors (see Figure 3.9). This design innovation minimizes (and equalizes) the optical path lengths between the optical surfaces in both the tracking and coagulating beam legs of the optical system, reduces the number of required components, and allows all four steering mirrors to "share" the conjugate plane of the retina as required for coupling into the eye (recall Figure 3.7).

The confocal reflectometers were custom fabricated using Hamamatsu SK-2863 photodiodes, 100 μm pinholes and hand-wired, low-noise transimpedance amplifier cards. For convenience in alignment, these were designed to mount directly in standard optical mounts.

The main steering mirrors are further down the optical train than the dither mirrors. In order to be certain to accommodate the range of angular motions of the dither mirrors, much larger mirrors were selected for the main steering galvanometers. The design ramification of this is that the main steering galvanometers for analog tracking need to drive larger inertial loads than they do in the digital

tracking implementation. As a result, larger G310 galvanometers were selected. See Section A.8 for an engineering analysis of the galvanometers.

The signal processing and control circuitry for the analog tracking system is implemented in hardware using inexpensive, standard devices such as low-noise quad TL074 op-amps, AD633 multiplier/divider chips, analog switches, and numerous passive components. These are variously configured as buffers, filters, dividers for reflectance normalization, multipliers for the phase-sensitive lock-in amplifiers (for extracting error signals), integrators with reset for driving the main steering galvanometers—all the circuits which comprise the servo loop. The detailed schematics are too complex to be instructive in this discussion. Four standard galvanometer driver module plug-in cards (A-102) are used to steer the dither and main tracking mirrors; see Chapter 6. Two vector cards were hand-wired: one for each axis, x and y, each with two of the plug-in galvanometer driver cards. A rack-mounted panel arrangement was used to assemble the overall electronics module, including two $\pm$15V, 1.5 amp power supplies. Reflectometers and galvanometers were connected via shielded cables and D-shell connectors. Twenty-turn trim potentiometers were used for dither phase adjust, drive phase adjust, and feedback gain adjust; all offset and trim adjustments were accessible from the rear of the enclosure. Selectable gain switches were brought to the front panel to adjust reflectometer gain and power normalization. A 180 degree drive phase switch was also brought to the front panel to allow tracking on dark spots (like blood vessel branches) if needed. Panel BNC connectors were included for external targeting inputs and the external dither oscillator. Output BNC connectors were added for monitoring reflectometer signals and galvanometer drive signals. A joystick was modified to reset the integrator and steer the beam to manually acquire the reference lesion with the tracking beam.

A.8 Galvanometer Beam Steering Analysis

Galvanometers and mirrors, configured as in Figure 6.1, are a cost effective method to steer laser beams to specific locations. An analysis of a particular design is prudent to ensure that the desired performance, such as scanning speed or pointing accuracy, can be met.

A.8.1 Sources of Error

Galvanometers are electro-mechanical devices, and typically are the limiting component when designing a beam steering system [192, 193]. For analyzing performance and possible sources of pointing error, specifications of interest include resonant frequency, temperature sensitivity, cross-axis motion, linearity, repeatability, and hysteresis. Other potential sources of error that are related to galvanometer beam steering systems are mirror flatness and cosine error. Note that the galvanometers used for the CALOSOS prototype are inexpensive open loop models, with no position feedback. See Chapter 5 for how the detection of the laser spot on the retinal image can provide some degree of closed loop control.

A.8.2 Design Implications of Resonant Frequency

The most critical design parameter affecting performance of galvanometers is the *mechanical resonant frequency*, which is a function of both the armature inertia and the mirror inertia. It determines the upper bound on the speed of the galvanometer. The unloaded (no mirror) resonant frequency of a galvanometer, and the armature inertia from which it is derived, is given as a standard specification. The loaded (with mirror) resonant frequency is determined by applying the ratio of the mirror inertia to the armature inertia to a derating curve supplied by the galvanometer manufacturer. The derating curve for the G100 and G300 series galvanometers is shown in Figure A.12.

The recommended design range for the ratio of the mirror inertia to the armature

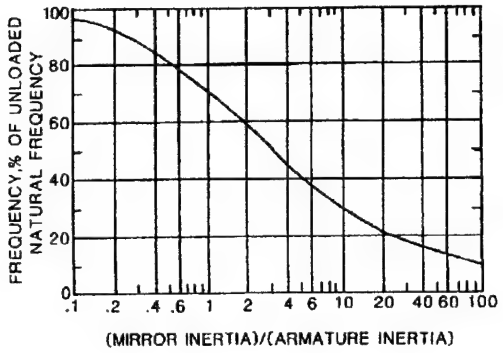

Figure A.12: Resonant frequency derating curve.

Dimension	X Galvo	YGalvo
thickness	1 mm	1.5 mm
width	12 mm	9 mm
length	12 mm	19 mm

Table A.1: Dimensions of mirrors used on G124 galvanometers.

inertia (I_m/I_a) is roughly from 1:1 to 10:1 [192,193]. Calculations of unknown mirror inertia must include both the mirror and the mirror holder used to secure the mirror to the armature shaft. Typically, the mirror and mirror holder can be divided into a number of basic shapes for which equations of inertia are well known [194, 195]. See Figure A.13.

While the G310 galvanometers used factory supplied mirrors with the inertia specified, the inertia of the UT-fabricated mirrors and mirror holders must be calculated. The mirrors had the dimensions shown in Table A.1, where the length is the dimension parallel to the axis of rotation, and width is the dimension perpendicular to the axis of rotation. The mirror holders were constructed according to the mechanical drawing shown in Figure A.14 and fabricated from aluminum. The equations from Figure A.13 were applied.

The digital tracking version uses G124 and the hybrid tracking version uses G310 galvanometers, which have different armature inertias. The design calculation

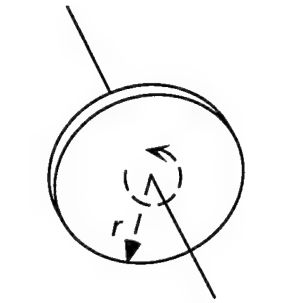

Thin disk of radius r rotating about axis through center:

$$I = \frac{1}{2}mr^2$$

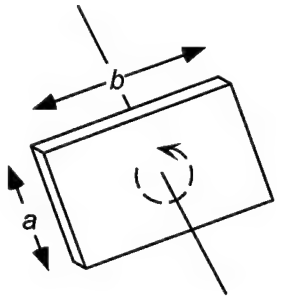

Thin rectangular object rotating about axis through center:

$$I = \frac{1}{12}m(a^2 + b^2)$$

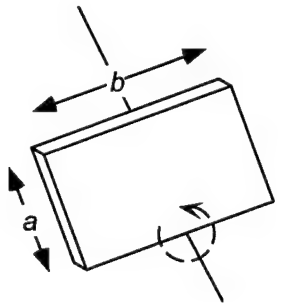

Thin rectangular object rotating about axis on edge:

$$I = \frac{1}{3}m(a^2 + b^2)$$

Figure A.13: Moment of inertia calculations for some basic shapes.

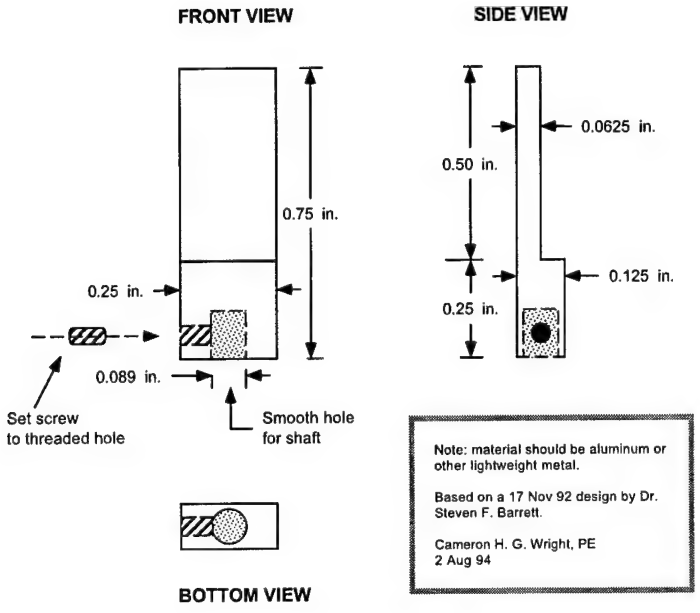

Figure A.14: Mechanical drawing for mirror holders used on G124 galvanometers.

results for both galvanometers are summarized in Table A.2, where the mirror inertia given is the greater of the x or y axis. The mirrors and mirror holders for the G124 were custom fabricated for CALOSOS, and were as low in inertia as possible within the constraints of mirror size. The mirror and mirror holder assembly for the G310 were purchased from the galvanometer manufacturer and were a better match as evidenced by the I_m/I_a ratio.

Note that the sinusoidal, triangular, and square wave ratings in Table A.2 are for full scale deflections. A tracking correction signal to the galvanometer would most resemble a square wave input (for worst case analysis). If the galvanometer was driven full scale across the entire 50 degree FOV of the retina at the frequency shown for a square wave in Table A.2, this would equate to a retinal velocity of 550 deg/sec for the G124, and 400 deg/sec for the G310. However, this is an unrealistic scenario. More likely is the galvanometer steadily scanning in small steps across the FOV in response to the tracking system compensating for eye movement. In this

Parameter	G124	G310
unloaded f	700 Hz	230 Hz
mirror inertia I_m	0.176 g·cm^2	4.554 g·cm^2
armature inertia I_a	0.017 g·cm^2	4.0 g·cm^2
I_m/I_a	10.4	1.14
derating factor	$\simeq$0.3	$\simeq$0.7
loaded f	210 Hz	161 Hz
sinusoidal max	179 Hz	137 Hz
triangular, square max	11 Hz	8 Hz
avg. torque T	70 dyne·cm	950 dyne·cm
avg. $\alpha = T/(I_m + I_a)$	363 rad/s^2	111 rad/s^2

Table A.2: Design factors determining galvanometer scanning performance.

case the upper frequency bound is the loaded resonant frequency.

Within the usable bandwidth defined by the loaded resonant frequency, important design parameters are angular acceleration, overshoot, and settling time [142]. It is reasonable to assume [192, 193] that the galvanometer dynamics can be represented as a second order system which is critically damped or moderately underdamped.[9] The transient response is given [196] by

$$v(t) = A - B\frac{\exp(-\zeta\omega_n t)}{\sqrt{1-\zeta^2}}\sin\left(\omega_n\sqrt{1-\zeta^2}\,t + \cos^{-1}\zeta\right) \qquad \text{(A.19)}$$

where A is the new angular position, B is the step size from the old position to the new position (hence the old position equals $A - B$), ζ is the damping coefficient (sometimes called the damping ratio), ω_n is the undamped natural frequency, t is time, and the step change occurs at $t = 0$. The peak magnitude of the transient component at any time is equal to or less than $\exp(-\zeta\omega_n t)$, so the settling time to a 5% peak-to-peak error band takes 4 time constants and settling time to a 2% peak-to-peak error band takes almost 5 time constants of the transient response term [196] where one time constant is $1/(\zeta\omega_n)$. These parameters determine how quickly the galvanometer can point to a new location and settle on the intended location with acceptable accuracy. Equation A.19 is graphed in Figure A.15, where

[9]Overdamped systems have no overshoot and hence settling time is meaningless.

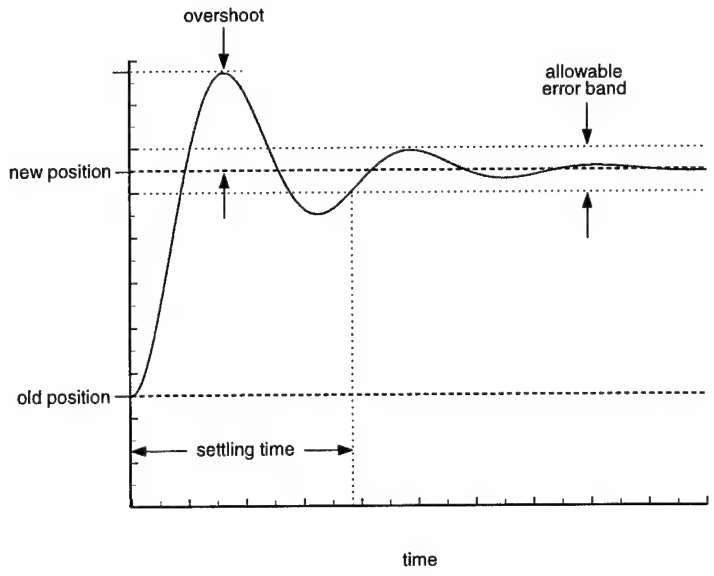

Figure A.15: Transient response of an underdamped galvanometer and mirror combination to a step change in the position signal.

an arbitrary step change in the position signal and a moderately underdamped system is assumed. Note that the step size affects the magnitude of overshoot and the settling time.

Most practical galvanometer-based systems are intentionally operated underdamped for speed [197]. Traditional linear control systems theory would dictate further analysis of Equation A.19, where ζ describes the loss mechanisms [196]. Unfortunately, at the micro-radian and millisecond regime, typical galvanometer losses (bearing, drag, mechanical hysteresis, and aerodynamic losses) do *not* fit the linear model [142], so a quantitative analysis is somewhat abbreviated. Instead, experimental verification of the initial design parameters is used, with adjustments made as necessary.

There is sufficient information for a quantitative analysis of angular acceleration (see Table A.2), which (combined with the loaded resonant frequency) is useful

for initial design sizing and for comparisons between galvanometer choices. The maximum angular acceleration is derived from the well known torque equation

$$T = \alpha I \tag{A.20}$$

where T is torque (in N·m or dyne·cm), α is the angular acceleration (in radians/sec^2), and I is total inertia (in kg·m^2 or g·cm^2) of the armature and mirror assembly [196]. For obvious reasons, the angular acceleration of a galvanometer is often described in the literature as its *torque to inertia ratio* [142]. Caution must be exercised using specified torque values as it is not constant over angle, and only approximately linear with current [142]. Overshoot is typically specified as a percentage of the step size, and the settling time of the system is a measure of how long it takes for oscillations to die down (to an acceptable error band) after the galvanometer and mirror are pointed to a new location. Both overshoot and settling time are primarily dependent on the I_m/I_a ratio, the $T/(I_m + I_a)$ ratio of the loaded galvanometer, and the angle traversed between points.

From Table A.2, the higher values of I_m/I_a and $T/(I_m+I_a)$ for the G124 should result in greater overshoot and longer settling time compared to the G310. As explained above, the overshoot and settling time must be empirically determined for the Laser Pointing and Control System (LPCS). System testing revealed that for small steps in the position signal such as smooth tracking, overshoot and settling time were too small to accurately measure for either type of galvanometer. But for large steps in the position signal, the G124 exhibited pronounced overshoot that exceeded the 100 μm pointing accuracy requirement, and had a settling time of up to 45 ms. For the same large steps, the G310 was within the 100 μm pointing accuracy requirement, and had a settling time of up to 10 ms. See Chapter 8 for more details on the test results. These large steps would typically only occur during a movement between lesion sites in a pattern, or when a fast eye motion has caused the digital tracking algorithm to temporarily lose lock. In either case, the laser shutter would be closed during the actual movement. To compensate for the

settling time of the LPCS after a large pointing signal step, the control software incorporates a 50 ms delay before the laser shutter is allowed to open after a beam movement to a new lesion location or after tracking lock is reestablished. Further improvement is achieved by minimizing the necessary galvanometer movements for a particular lesion pattern; see Section 6.4.

A.8.3 Other Performance Factors

While resonant frequency is the most important design criterion, other performance factors must be taken into account. *Temperature sensitivity* is a change in pointing angle due to a change in temperature. *Cross-axis motion* is unwanted movement of the galvanometer shaft orthogonal to its normal axis of rotation. For example, cross-axis motion of the x galvanometer would result in laser beam displacement along the y axis. *Linearity*, as its name implies, is simply the linearity of the change in pointing angle to the change in input current. *Repeatability* is a measure of the galvanometer's ability to point to the same angle when given the same input current. *Hysteresis* determines how closely the pointing angle matches at the same input current value when it is preceded by an increasing input current compared to when it is preceded by a decreasing input current. When calculating the potential pointing error on the retina due to these factors, the angular magnification of approximately 3:1 on to the retina must be considered. The designer should note that most of these specifications are typically given as a percentage of the maximum utilized peak to peak scanning angle. Recall the optical scanning angle used for the LPCS galvanometers (both digital and hybrid implementations) is -8.33 degree to $+8.33$ degree, hence the peak to peak deviation is 16.66 degrees.

As an example calculation, the repeatability is specified as $\leq 0.05\%$ p-p. For the maximum peak to peak swing of 16.66 degrees used for the design of CALOSOS, this equates to ≤ 0.00833 degrees. The 3:1 angular magnification of the CALOSOS optical design modifies this into a retinal angle of ≤ 0.025 degrees. From Equation

Factor	Rating	Angle	Error on Retina
Temp. Sens.	0.06%/°C	0.01 deg/°C	0.03 deg/°C $\simeq$ 8.7 μm/°C
Cross-axis motion	10 μrad	10 μrad	30 μrad $\simeq$ 0.5 μm
Linearity	$\leq$ 1% p-p	$\leq$ 0.17 deg	$\leq$ 0.5 deg $\simeq$ 146 μm
Repeatability	$\leq$ 0.05% p-p	$\leq$ 0.008 deg	$\leq$ 0.025 deg $\simeq$ 7.3 μm
Hysteresis	$\leq$ 0.7% p-p	$\leq$ 0.12 deg	$\leq$ 0.35 deg $\simeq$ 102 μm

Table A.3: Calculated maximum pointing error on the retina due to the galvanometers. Values have been rounded for clarity.

4.1 this is equivalent to $\simeq$7.3 μm on the retina. Other calculations follow similarly.

Table A.3 is a summary of the engineering design analysis relating these factors to the potential pointing error on the retina. Recall that the design specification is a pointing accuracy of 100 μm on the retina. The specifications that exceed the design criteria are the linearity and hysteresis ratings. The manufacturer documentation implies that typical performance is much better than this worst case rating. Since the only alternative for improving these factors would be to use much more expensive galvanometers, the actual performance was tested. The typical pointing accuracy in actual use was $\pm$2 pixels ($\pm$64 μm) near the image center, but up to $\pm$5 pixels ($\pm$160 μm) near the edge of the FOV. This effect near the edge of the FOV was likely dominated by spherical aberration of the scan angles by scan lens Ls, and would not be affected by changing galvanometers. Details can be found in Chapter 8. A design suitable for clinical trials should incorporate closed loop galvanometers and an ophthalmoscopic aspherical scan lens to minimize these poining errors.

Two other performance factors that can introduce errors are *mirror flatness* and *cosine error*. If the galvanometer mirrors are not perfectly planar, small pointing errors can be introduced. No measurable effect from this was observed during testing. Cosine error is a distortion of the laser spot when pointing the beam at large angles of incidence to the target plane; the result is that a normally round spot would appear elliptical. CALOSOS directs the laser to the retina, which is nearly round rather than planar, and therefore cosine error is relatively small even at large angles of incidence.

A.9 Eye Phantoms

Research using eye phantoms is much easier than using an eye of a living subject. However, for the results to be meaningful, the eye phantom must closely mimic the parameters that determine any effect being studied. In the case of studying retinal photocoagulation, the critical parameters are the optical properties and the response to heat.

As luck would have it, there is a very convenient, easily obtainable material which has nearly the same optical properties as the human neural retina: albumen (egg white). Since the measured optical properties are so close, it is expected that light to behaves similarly; empirical evidence supports this. But for a phantom to be useful it must also exhibit a response to heat similar to the retina.

In Chapter 2, it was described how the denatured tissue of a retinal lesion appeared white due to an increase in the scattering coefficient. Anyone who has ever fried an egg has observed exactly the same effect in egg white as the albumen coagulates. Empirical measurements have shown the degree of change in μ_s to be close enough between neural retinal tissue and albumen to make a reasonable phantom. Hence the use of egg white as a substitute for the retina has been widely accepted.

Various techniques have been employed to build an appropriate eye phantom using egg white. Since an ophthalmologist is most concerned with the lesion formation in the neural retina rather than the choroid, the model does not need to include the choroid. However, there is a need to simulate the retinal pigment epithelium (RPE).

A particularly simple yet effective eye phantom is shown in Figure A.16. A glass petri dish, with its inside bottom painted with high-temperature resistant flat black paint, is filled with egg white. The raw egg white exhibits optical properties close to the neural retina, and the black paint is highly absorbing as is the RPE. When the laser irradiates the phantom, light passes through the egg white and is absorbed by the black paint. This causes significant heat generation, which in turn

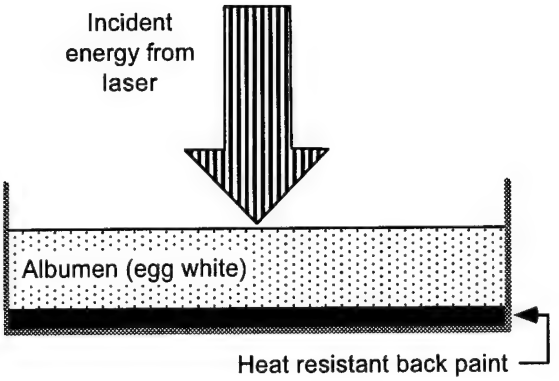

Figure A.16: An eye phantom using a petri dish filled with egg white. The bottom of the petri dish has been painted black to simulate the RPE.

will locally coagulate the egg white. As the egg white coagulates, the scattering coefficient increases and a white "lesion" appears. Since the thickness of the black paint varies across the surface of the petri dish, there is a variation in μ_a similar to that in the RPE.

A.10 The Monte Carlo Method

When developing a technique for lesion control based upon reflectance, some method of predicting the assocoated dymanics of laser-tissue interaction is needed. The exact analytical solution to light propagation in tissue, relying on Maxwell's equations, is exceedingly cumbersome [41]. Furthermore, the uncertainty of known tissue optical properties makes the effort toward an exact solution less motivating. There has been considerable research done to create analytical approximations to the solution, such as the Kubelka-Monk model and the Diffusion Approximation. While more tractable than the exact solution, they are still quite difficult to implement and solve in closed form on a general purpose computer. See [156].

A different approach relies on the Monte Carlo technique [144] to create a probabilistic model of the light propagation [155]. This method simulates the "random

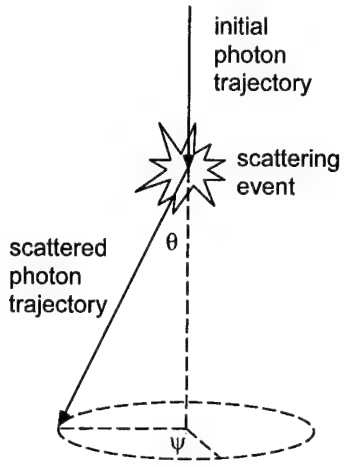

Figure A.17: A photon encountering a scattering event.

walk" of photons in a medium that contains absorption and scattering sites, using the known rules that govern photon movement in tissue. For example, Figure A.17 depicts a photon encountering a scattering event. Controlling parameters such as the mean free path s of the photon, whether or not a scattering event or absorbing event occurs, and the scattering angle can all be determined probabilistically using the known optical properties and the probability distribution of the event. The Monte Carlo method maps the probablilty of the various photon events to uniform probability distributions easily generated by computer. This mapping is shown graphically in Figure A.18, where $p(x)$ represents the known probability density function of a photon event, and $p(\zeta)$ is the uniform probability density function generated by the simulating computer. At a boundary (where one or more of the optical properties changes), the photon is either reflected or moves across the boundary. The computer makes various decisons as to the photon path as shown in Figure A.19. See [41] for an excellent treatment of all the implementation issues. The Monte Carlo technique is rigorous yet statistical in nature, and therefore provides a useful simulation only for a large sample size of photons. For example, 3000 photons can

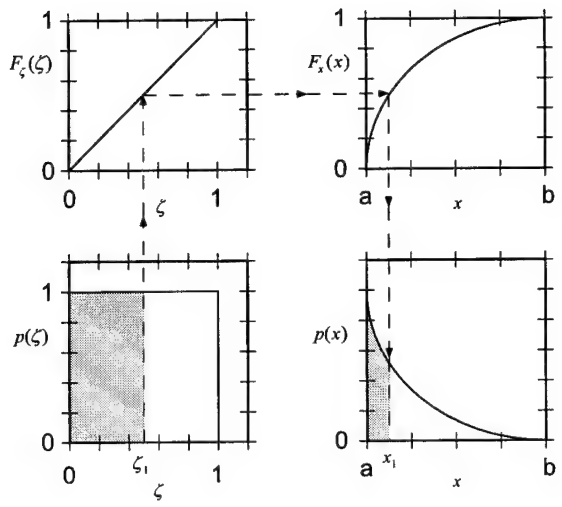

Figure A.18: Monte Carlo method of mapping probability distributions for simulation.

yield an acceptable result when seeking only reflection from tissue, but to map three dimensional spatial distributions inside tissue can require 10,000–100,000 photons or more [41]. Some researchers regularly use up to 1,000,000 photons per simulation for particularly complex sensor geometries and fiber delivery systems. Given the power of today's desktop computers, this is not a problem.

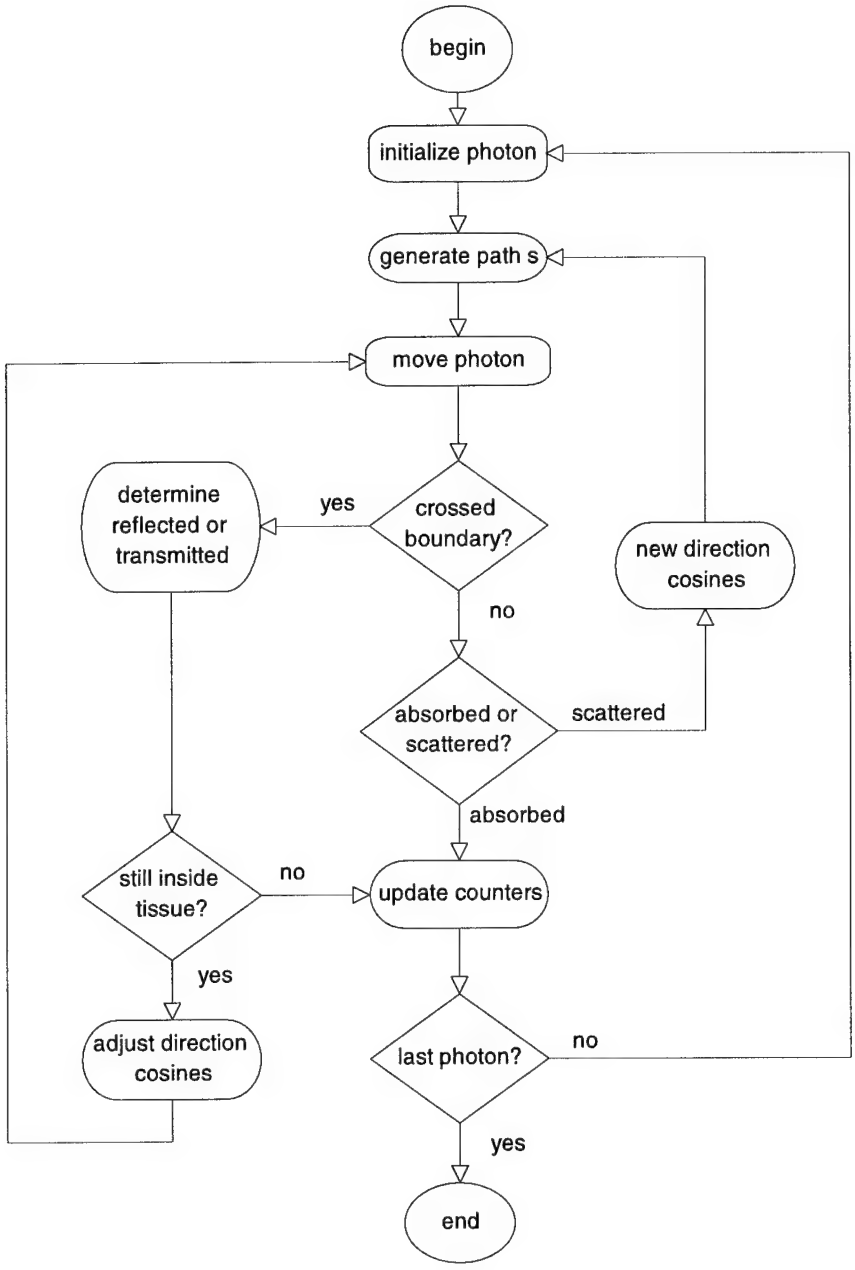

Figure A.19: Flow chart of computer-based decisions for a Monte Carlo simulation of light-tissue interaction.

Appendix B

CALOSOS Equipment and Setup

The CALOSOS system was designed to use standard off-the-shelf components wherever possible. This not only keeps cost down, but allows flexibility in assembling the design. The equipment used for the results described in this document is described below.

B.1 Computer and Electronics Hardware

The following computer and electronics hardware is used for CALOSOS:

- Computer: Gateway 2000 P5-90 (a 90 MHz Pentium with 16 MB RAM, utilizing a Neptune PCI bus chip set).
  - Frame grabber: MuTech MV-1000.
  - Data acquisition/control: National Instruments AT-MIO-16.
- CCD camera: Panasonic GP-MF602.
- Galvanometers: General Scanning Corp.
  - Digital tracking: (2) Model G124, (2) Model AX200 driver/amplifiers.

Signal	I/O Type	ICU pins	Adapter pins
X galvo	analog out	22	20
Y galvo	analog out	24	21
AO GND	analog out	23,25	23
Laser shutter	digital out	35	25
Status reset	digital out	36	27
Patient status	digital in	38	26
Lesion status	digital in	39	28
DIO GND	digital in/out	26,27,32,37,42,47,48	24,33
Lesion reflectance	analog in	*	NA
AI GND	analog in	*	NA

Table B.1: Interface Control Unit (ICU) pin assignments for connector and adapter. Pins marked with a * were separately wired.

  - Hybrid tracking: (2) Model 310 (for main steering), (2) Model G108 for dither beam, (4) Model A102 driver/amplifiers.

- Custom electronics:

  - Interface control unit for shutter, galvonometer, patient status, lesion status, and lesion reflectance signals. See Table B.1 for connector pin assignments.
  - Dither tracking and signal conditioning module for generating the dither beam deflection signals and processing the confocal reflectometer signals.

Note that the interface control unit (ICU) was modified from a previous design by Barrett. Since the original design was intended for use with the older DT2801 I/O card, an adapter cable was constructed which adjusted the pin assignments to match the newer NI AT-MIO-16 I/O card used by CALOSOS. Thus there are two columns of pin assignments shown in Table B.1: the actual ICU connector pins (which match a DT2801), and the corresponding adapter pins (which match an AT-MIO-16). Note that for much of the testing, the lesion reflectance signal was actually acquired by a separate computer (a Gateway 66 MHz 486 with a DT2801 I/O card). See [15] for more information on the internal ICU wiring.

The separate routing of the individual signals from ICU is straightforward. The X & Y galvo signals are connected to the signal inputs of the appropriate AX200 driver/amplifier. The shutter control signal is routed to the Uniblitz D122 controller's 5-pin connector (pin 2 for signal, pin 3 for ground). The lesion reflectance signal comes from the appropriate confocal reflectometer. For the hybrid tracking version, the galanometer driver/amplifiers are encased inside the custom enclosure, so the X & Y galvo signals from the ICU are routed to the appropriate BNC conectors on the enclosure.

B.2 Optics

The following electro-optical components are used for CALOSOS:

- Fundus camera: Olympus Mydriatic Model GRC-W.
- Argon Laser: Coherent System 900 Photocoagulator.
- Laser shutter: Uniblitz LS6Z shutter with a Uniblitz D122 controller.
- Miscellaneous Optics: commercially available AR-coated lenses and beam splitters as specified in Tables B.2 and B.4. The beam splitter used for the confocal reflectometer was custom-order dichroic designed specifically for the argon wavelengths. The confocal pinholes are 100 μm. Critical distances are shown in Tables B.3 and B.5; some minor adjustment may be necessary to accomodate variations in optical elements.

Note there are two designs for the main optics assembly: one for digital tracking and one for hybrid tracking.

To adjust the size of the confocal spot imaged on the retina, change the focal length (and associated distance) of the 25 mm lens. As specified here, the spot on the retina equals 3.2 times the physical size of the confocal pinhole. A longer lens would reduce the size of the imaged spot on the retina.

Optical Element	Description
L1, L3, L4 (optional)	PCX, $f = 25$ mm, 1 in. diam., AR coated
L2	PCX, $f = 250$ mm, 1 in. diam., AR coated
Ls	Aspheric PCX, $f = 53$ mm, F/# 0.82, AR coated
BS1	80/20 beamsplitter, dichroic (488 & 514 nm)
BS	50/50 beamsplitter, 50 mm diam., AR coated
M1, M2	minimum size first-surface mirrors

Table B.2: Optical elements for digital tracking version.

From	To	Distance
Fiber tip	L1	25 mm
L1	L2	not critical
L2	M1, M2 (midpoint)	85 mm
M1, M2 (midpoint)	Ls	218 mm
L3	reflectometer	25 mm
L4 (if used)	power monitor	approx. 25 mm

Table B.3: Optical distances for digital tracking version.

Optical Element	Description
L1, L3, L5, L6 (optional)	PCX, $f = 25$ mm, 1 in. diam., AR coated
L2, L4	PCX, $f = 250$ mm, 1 in. diam., AR coated
Ls	Aspheric PCX, $f = 53$ mm, F/# 0.82, AR coated
BS1, BS2	80/20 beamsplitter, dichroic (488 & 514 nm)
BS3	50/50, minimum size, AR coated
BS	50/50 beamsplitter, 50 mm diam., AR coated
M1, M2, M3, M4	minimum size first-surface mirrors

Table B.4: Optical elements for hybrid tracking version.

From	To	Distance
Fiber tip	L1	25 mm
L1	L2	not critical
L2	M1 (turning mirror only)	not critical
L2	BS3, M2, M3, M4 (midpoint)	85 mm
BS3, M2, M3, M4 (midpoint)	Ls	218 mm
L3, L5	associated reflectometer	25 mm
L6 (if used)	power monitor	approx. 25 mm

Table B.5: Optical distances for hybrid tracking version.

Appendix C

CALOSOS Software Organization

C.1 Compiler

The software for CALOSOS was written in ANSI C using the Watcom C/C++ compiler (version 10.0, patch level B). It was compiled as a DOS4G/W execuatable, running in 32-bit protected mode extended DOS, with a 4 Gbyte flat address space. See Chapter 3 for details about this environment.

C.2 Support Libraries

In addition to the standard libraries bundled with the compiler, the following object-code libraries were used.

```
support software for the MuTech frame grabber:
   \mv-1000\lib\mv1.lib
SciTech Software's Mega Graphics Library (MGL):
   \scitech\lib\dos32\wc\mgldos.lib
a protected mode library for MGL and DOS4G/W:
   \scitech\lib\dos32\wc\dos4gw\pmode.lib
protected mode version of the precision timer:
   \scitech\lib\dos32\wc\ztimer.lib
```

Note that the data acquisition library is not used, as a custom one for 32-bit protected mode was written and debugged as part of this research. No 32-bit

extended DOS library is available from the vendor.

C.3 Include Files

Each source file includes the master header file `calosos.h`, which in turn loads all the needed header files in the appropriate order. The include files loaded are:

```
// ANSI C standard library headers
#include <stdio.h>
#include <string.h>
#include <malloc.h>
#include <conio.h>
#include <stdlib.h>
#include <stddef.h>
#include <stdarg.h>
#include <ctype.h>
#include <i86.h>
#include <math.h>

// MuTech header files for frame grabber
#include ''mv1.h''

// header files for SciTech Software utilities
#include ''ztimer.h'' // precision timer routines
#include ''mgraph.h'' // for MGL graphics library
#include ''pmode.h'' // for protected mode compatibility

// CALOSOS-specific header files. Don't change the order!
#include ''defines.h''
#include ''typedef.h''
#include ''vars.h''
#include ''prototyp.h''
```

The above is an easy-to-read version of the contents of `calosos.h`.

C.4 Source Code Files

The source code files are separated by function, as will be obvious from the list below. In most cases the purpose of each function is self-evident from its name. If

in doubt, check the heavily commented source code.

```
// in calosos.c
void main(void);

// in alaser.c
void laserAlign(void);
void laserCenter(void);
void laserRamp(int side, int delayFactor);
void laserCheckOpenShutter(void);

// in template.c
void templateFunctions(void);
void defineTemplateArea(int *ax1, int *ay1, int *ax2, int *ay2);
void findBestTemplates(int ax1,int ay1,int ax2,int ay2,
                       int aya,int ayb);
void displayTemplate(void);
void displayOffsetTemplate(int relX, int relY, int tMatch);
void make2DTemplate(void);
void xorTemplate(void);

// in lesnpatt.c
int lesionPatterns(void);
void rectPattern(int wide, int high);
void radialPattern(int wide, int high);
void packPattern(void);
void setIrradiationTime(void);
void testPattern(void);
void xorPattern(void);
void addLesion(void);
void eraseLesion(void);
void deconflictPattern(void);
int look4BloodVessel(int x, int y);
void minLesionPath(void);

// in tracking.c
void testTrackMenu(void);
void testTrackSim(void);
void testTrack(void);
int trackRelockSM(void);
int trackRelockMM(void);

// in retsurg.c
```

```
void photocoagulation(void);
int lastWarning(void);
void askLaserCheck(void);
void digitalSurg(void);
void hybridSurg(void);
int patientPanicOK(void);
int checkLaserPositionSM(int px, int py);
int checkLaserPositionMM(int px, int py);

// in testutil.c void
testUtilities(void);

// in cwmv1.c
void startMV1(void);
void grabSingleFrame(void);
void startMasterMode(void);
void stopMasterMode(void);
void irqCallback(short status);
void adjustMV1(void);

// in cwnidaq.c
void ni_init_all(void);
void ni_init9513(void);
void ni_ao_mode(int);
void ni_ao_set(int,int);
void ni_dio_config(int,int);
int ni_dio_rbit(int);
void ni_dio_wbit(int,int);
int ni_dio_rall(void);
void ni_dio_wall(int);
void laserShutter(int state);
void resetStatus(void);

// in cwmgl.c
void setbwpalette_mgl(MGLDC *dc);
int waitEvent(void);
int ggetchar(void);
void gputchar(char ch);
int gprintf(char *format, ...);
int gscanf(char *format, ...);
bool pause(void);
void initFatalError(void);
```

```
void nonFatal_MGL_Error(void);
void defaultAttributes(MGLDC *dc);
MGLDC *startMGL(void);
void imageClear(void);
int getMouseX(event_t evt);
int getMouseY(event_t evt);
void putMouse(int x, int y);
void gPrompt(char *msg);
void gnewLine(int lines);
void saveEntireScreen(void);

// in guimenus.c
void initTitle(void);
void imageTitle(char *title);
void sideTitle(char *title);
void bottomTitle(char *title);
void sideClear(void);
void bottomClear(void);
int putSideText(char *menuItems[]);
int putBottomText(char *menuItems[]);
int waitMenuItem(void);
bool exitPause(void);
void badChoice(void);
void notAvailable(void);
void nonFatalError(char errmsg[]);
void welcomeBackToMainMenu(void);
void makeAnotherSelection(void);
void updateStatus(void);

// in cwanneal.c
void anneal(float x[], float y[], int iorder[], int ncity);
int irbit1(unsigned long *iseed);
int metrop(float de, float t);
float ran3(long *idum);
float revcst(float x[], float y[], int iorder[], int ncity, int n[]);
void reverse(int iorder[], int ncity, int n[]);
float trncst(float x[], float y[], int iorder[], int ncity, int n[]);
void trnspt(int iorder[], int ncity, int n[]);
float *vector(long nl, long nh);
int *ivector(long nl, long nh);
void free_vector(float *v, long nl, long nh);
void free_ivector(int *v, long nl, long nh);
```

Note that the software is written assuming the MV-1000 and AT-MIO-16 are installed. At start-up, the hardware is queried, and if these are not found, the program exits. Also note the program assumes the graphics card adheres to the VESA VBE 2.0 specification, which permits linear framebuffer access and high speed graphics. Since most graphics cards don't fully support VBE 2.0, the computer `autoexec.bat` file should load in the `univbe.exe` driver to add such support.

Finally, for actions which are time-critical such as closing the laser shutter, there are high speed macro definitions in the header file `define.h`.

The full source code program listings are contained in an Addendum to this dissertation. Contact the author or Dr. A. J. Welch to request access to the Addendum.

References

[1] Y. Yang, M. S. Markow, H. G. Rylander III, W. S. Weinberg, and A. J. Welch, "Reflectance as an indirect measurement of the extent of laser-induced coagulation," *IEEE Trans. Biomed. Eng.*, vol. 37, pp. 466–473, May 1990.

[2] J. M. Krauss and C. A. Puliafito, "Lasers in ophthalmology," *Lasers Surg. Med.*, vol. 17, no. 2, pp. 102–159, 1995.

[3] G. L. Spaeth, ed., *Ophthalmic Surgery: Principles and Practice.* W. B. Saunders, 1982.

[4] R. Birngruber, V. P. Gabel, and F. Hillenkamp, "Fundusreflectometry: A step towards optimization of retina photocoagulation," *Mod. Prob. Ophthalmol.*, vol. 18, pp. 383–390, 1979.

[5] M. S. Markow, A. J. Welch, H. G. Rylander III, and W. S. Weinberg, "An automated laser system for eye surgery," *IEEE Eng. Med. Biol.*, pp. 24–29, Dec. 1989.

[6] S. F. Barrett, C. H. G. Wright, M. R. Jerath, R. S. Lewis II, B. C. Dillard, H. G. Rylander III, and A. J. Welch, "Computer-aided retinal photocoagulation system," *J. Biomed. Opt.*, vol. 1, pp. 83–91, Jan. 1996.

[7] L. A. Margulies, "An analysis of retinal lesion formation during photocoagulation with an argon laser," Master's thesis, The University of Texas at Austin, 1985.

[8] M. S. Markow, *The Preliminary Development of a Robotic Laser System Used for Ophthalmic Surgery.* Ph.D. dissertation, The University of Texas at Austin, 1987.

[9] E. J. Engelken, *Influence of Visual and Auditory Stimuli on Saccadic Eye Movement.* Ph.D. dissertation, The University of Texas at Austin, 1987.

[10] M. R. Jerath, "A software package for the analysis of laser induced retinal lesions," Master's thesis, The University of Texas at Austin, 1989.

[11] A. J. Seltzer, "Design and implementation of a laser-tissue interaction observer," Master's thesis, The University of Texas at Austin, 1990.

[12] S. Ghaffari, *The Design of a 2-Dimensional Optical Image Correlator and Its Application in Image Tracking.* Ph.D. dissertation, The University of Texas at Austin, 1990.

[13] Y. Yang, *Automatic Control of the Extent of Laser Induced Coagulation.* Ph.D. dissertation, The University of Texas at Austin, 1990.

[14] M. R. Jerath, *Real Time Control of Laser Induced Retinal Lesions.* Ph.D. dissertation, The University of Texas at Austin, 1992.

[15] S. F. Barrett, *Digital Tracking and Control of Retinal Images.* Ph.D. dissertation, The University of Texas at Austin, 1993.

[16] W. Weinberg, R. Birngruber, and B. Lorenz, "The change in light reflection of the retina during therapeutic laser-photocoagulation," *IEEE J. Quant. Elect.*, vol. QE-20, no. 12, pp. 1481–1489, 1984.

[17] Y. Yang, A. J. Welch, and H. G. Rylander III, "Rate process parameters of albumen," *Lasers Surg. Med.*, vol. 11, pp. 188–190, 1991.

[18] W. J. Geeraets, R. C. Williams, M. Ghosh, W. T. Ham, D. Guerry, F. Schmidt, and R. Ruffin, "Light reflectance from the ocular fundus," *Arch. Ophthalmol.*, vol. 69, pp. 612–617, 1963.

[19] O. Pomerantzeff, G. J. Wang, M. Pankratov, and J. Schneider, "A method to predetermine the correct photocoagulation dosage," *Arch. Ophthalmol.*, vol. 101, pp. 949–953, 1983.

[20] K. P. Pflibsen, F. C. Delori, O. Pomerantzeff, and M. M. Pankratov, "Fundus reflectometry for photocoagulation dosimetry," *Appl. Opt.*, vol. 28, pp. 1084–1096, 1989.

[21] J. H. Inderfurth, R. D. Ferguson, M. B. Frish, and R. Birngruber, "Dynamic reflectometer for control of laser photocoagulation on the retina," *Lasers Surg. Med.*, vol. 15, pp. 54–61, 1994.

[22] W. F. Ganong, *Review of Medical Physiology.* Appleton & Lange, 16th ed., 1993.

[23] D. G. Vaughan, T. Asbury, and P. Riordan-Eva, *General Ophthalmology.* Appleton & Lange, 13th ed., 1992.

[24] O. Pomerantzeff, R. H. Webb, and F. C. Delori, "Image formation in fundus cameras," *Invest. Ophthalmol. Vis. Sci.*, vol. 18, pp. 630–637, June 1979.

[25] A. M. Mansour, "Measuring fundus landmarks," *Invest. Ophthalmol. Vis. Sci.*, vol. 31, pp. 41–42, Jan. 1990.

[26] H. A. Quigley, A. E. Brown, J. D. Morrison, and S. M. Drance, "The size and shape of the optic disk in normal human eyes," *Arch. Ophthalmol.*, vol. 108, pp. 51–57, Jan. 1990.

[27] F. W. Newell, *Ophthalmology: Principles and Concepts.* The C. V. Mosby Company, 6th ed., 1986.

[28] E. A. Boettner, "Spectral transmission of the eye," tech. rep., The University of Michigan, July 1967. Prepared for USAF School of Aerospace Medicine, Brooks AFB, TX, under Contract AF41(609)-2966.

[29] W. Bloom and D. W. Fawcett, *A Textbook of Histology.* W. B. Saunders, 8th ed., 1962.

[30] American National Standards Institute, *American National Standard for Safe Use of Lasers*, ANSI Z136.1-1993.

[31] R. Sekuler and R. Blake, *Perception.* McGraw-Hill, 3rd ed., 1994.

[32] D. Marr, *Vision.* W. H. Freeman, 1982.

[33] R. H. S. Carpenter, *Movements of the Eyes.* London: Pion Limited, 1988.

[34] R. W. Ditchburn, *Eye Movements and Visual Perception.* Oxford, England: Clarendon Press, 1973.

[35] W. Kosnik, J. Fikre, and R. Sekuler, "Visual fixation stability in older adults," *Invest. Ophthalmol. Vis. Sci.*, vol. 27, pp. 1720–1725, Dec. 1986.

[36] J. D. Enderle and J. W. Wolf, "Time-optimal control of saccadic eye movements," *IEEE Trans. Biomed. Eng.*, vol. BME-34, pp. 43–55, 1987.

[37] E. Hecht, *Optics.* Addison-Wesley, 2nd ed., 1987.

[38] F. L. Pedrotti and L. S. Pedrotti, *Introduction to Optics.* Prentice Hall, 2nd ed., 1993.

[39] M. Born and E. Wolf, *Principles of Optics: Electromagnetic Theory of Propagation, Interference, and Diffraction of Light.* Pergamon Press, 6th (corrected) ed., 1986.

[40] M. V. Klein and T. E. Furtak, *Optics.* John Wiley & Sons, 2nd ed., 1986.

[41] A. J. Welch and M. J. C. van Gemert, eds., *Optical-Thermal Response of Laser Irradiated Tissue.* Plenum Press, 1995.

[42] A. J. Welch and M. J. C. van Gemert, "Lasers in medicine," in Waynant and Ediger [108], ch. 24.

[43] A. Ishimaru, *Wave Propagation and Scattering in Random Media*, vol. 1. Academic Press, 1978.

[44] V. P. Gabel, R. Birngruber, and F. Hillenkamp, "Visible and near infrared light absorption in pigment epithelium and choroid," *Excerpta Medica*, pp. 658–662, 1979. Series 450 (International Congress).

[45] H. G. Rylander III, "personal communication." The University of Texas at Austin.

[46] D. C. Gause and G. M. Weinberg, *Exploring Requirements: Quality Before Design.* Dorset House, 1989.

[47] G. M. Weinberg, *Rethinking Systems Analysis and Design.* Dorset House, 1988.

[48] G. M. Weinberg and D. Weinberg, *General Principles of System Design.* Dorset House, 1988.

[49] C. H. G. Wright, *A Unified Design for the Image Processing, Tracking, and Control of a Real-Time Robotic Laser System for Ophthalmic Surgery.* Ph.D. research proposal, The University of Texas at Austin, Jan. 1995.

[50] S. F. Barrett, M. R. Jerath, H. G. Rylander III, and A. J. Welch, "Digital tracking and control of retinal images," *Opt. Eng.*, vol. 33, pp. 150–159, Jan. 1994.

[51] M. R. Jerath, D. Kaisig, H. G. Rylander III, and A. J. Welch, "Calibrated real-time control of lesion size based on reflectance images," *Appl. Opt.*, vol. 32, pp. 1200–1209, Mar. 1993.

[52] M. R. Jerath, R. Chundru, S. F. Barrett, H. G. Rylander III, and A. J. Welch, "Reflectance feedback control of photocoagulation in vivo," *Arch. Ophthalmol.*, vol. 111, pp. 531–534, Apr. 1993.

[53] M. S. Markow, H. G. Rylander III, and A. J. Welch, "Real-time algorithm for retinal tracking," *IEEE Trans. Biomed. Eng.*, vol. 40, pp. 1269–1281, Dec. 1993.

[54] R. Duncan, ed., *Extending DOS: A Programmer's Guide to Protected-Mode DOS.* Addison-Wesley, 2nd ed., 1992.

[55] P. van der Linden, *Expert C Programming.* PTR Prentice-Hall, 1994.

[56] P. Hipson, *Advanced C.* Sams Publishing, 1992.

[57] S. F. Barrett, C. H. G. Wright, E. D. Oberg, B. A. Rockwell, C. P. Cain, M. R. Jerath, H. G. Rylander III, and A. J. Welch, "Integrated computer-aided retinal photocoagulation system," in *Proceedings of the 1996 SPIE International Symposium on Biomedical Optics (SPIE 2673-32)*, (San Jose, CA), Feb. 1996.

[58] S. F. Barrett, C. H. G. Wright, E. D. Oberg, R. D. Ferguson, B. A. Rockwell, C. P. Cain, H. G. Rylander III, and A. J. Welch, "Development of an integrated automated retinal surgical laser system," in *Proceedings of the 33rd Annual Rocky Mountain Bioengineering Symposium*, (Colorado Springs, CO), pp. 215–224, Apr. 1996.

[59] J. Fulcher, *An Introduction to Microcomputer Systems: Architecture and Interfacing.* Addison-Wesley, 1989.

[60] R. E. Haskell, *Introduction to Computer Engineering: Logic Design and the 8086 Microprocessor.* Prentice-Hall, 1993.

[61] W. L. Rosch, *The Winn Rosch Hardware Bible.* Brady, 1989.

[62] J. Morrissey, "Handling large still images now: PCI bus board impact," *Advanced Imaging*, pp. 38–42, Feb. 1995.

[63] M. Byerly, "Host-based imaging duels dedicated systems," *Laser Focus World*, pp. 153–156, Mar. 1996.

[64] MuTech Corporation, *M-Vision 1000 Technical Reference Manual (Version 2.0)*, 1996.

[65] S. Lathe, "10 things to consider when considering frame grabbers," *Advanced Imaging*, pp. 22–23, 76, Jan. 1996.

[66] A. W. Davis, "The PCI frame grabber on-board memory debate," *Advanced Imaging*, pp. 24–25, Jan. 1996.

[67] S. F. Barrett, "personal communication." United States Air Force Academy.

[68] Data Translation, Incorporated, *User Manual for DT2801 Series*, 1983.

[69] National Instruments Corporation, *AT-MIO-16 User Manual*, October 1993 ed.

[70] P. A. Darnell and P. E. Margolis, *Software Engineering in C.* Springer-Verlag, 1988.

[71] D. E. Knuth, *The Art of Computer Programming*, vol. 1–3. Addison-Wesley, 2nd ed., 1981.

[72] A. V. Aho, J. E. Hopcroft, and J. D. Ullman, *The Design and Analysis of Computer Algorithms.* Addison-Wesley, 1974.

[73] E. Horowitz and S. Sahni, *Fundamentals of Computer Algorithms.* Computer Science Press, 1978.

[74] N. D. Birrell and M. A. Ould, *A Practical Handbook for Software Development.* Cambridge University Press, 1985.

[75] M. A. Weiss, *Data Structures and Algorithm Analysis in C.* Benjamin/Cummings Publishing, 1993.

[76] J. Sanchez and M. P. Canton, *PC Programmer's Handbook.* McGraw-Hill, 2nd ed., 1994.

[77] D. Thielen and B. Woodruff, *Writing Windows Virtual Device Drivers.* Addison-Wesley, 1994.

[78] K. Crouse, *The Windows Programming Puzzle Book.* John Wiley & Sons, 1994.

[79] M. Goodwin, *User Interfaces in C.* MIS Press, 1989.

[80] MuTech Corporation, *M-Vision 1000 Software Development Guide.*

[81] R. F. Ferraro, *Programmer's Guide to the EGA, VGA, and Super VGA Cards.* Addison-Wesley, 3rd ed., 1994.

[82] SciTech Software, *MegaGraph Graphics Library Reference Manual, Version 2.0*, September 1995.

[83] B. E. A. Saleh and M. C. Teich, *Fundamentals of Photonics.* John Wiley & Sons, 1991.

[84] C.-L. Chen, *Elements of Optoelectronics and Fiber Optics.* Irwin, 1996.

[85] J. B. Pawley, ed., *Handbook of Biological Confocal Microscopy.* Plenum Press, 2nd ed., 1995.

[86] R. H. Webb and G. W. Hughes, "Scanning laser ophthalmoscope," *IEEE Trans. Biomed. Eng.*, vol. BME-28, pp. 488–492, July 1981.

[87] R. H. Webb, "Manipulating laser light for ophthalmology," *IEEE Eng. Med. Biol.*, pp. 12–16, Dec. 1985.

[88] R. H. Webb, "Optics for laser rasters," *Appl. Opt.*, vol. 23, pp. 3680–3683, Oct. 1984.

[89] R. H. Webb, G. W. Hughes, and F. C. Delori, "Confocal laser scanning ophthalmoscope," *Appl. Opt.*, vol. 26, pp. 1492–1499, Apr. 1987.

[90] A. Rosenfeld and A. C. Kak, *Digital Picture Processing*, vol. 1 and 2. Academic Press, 2nd ed., 1982.

[91] R. C. Gonzalez and R. E. Woods, *Digital Image Processing.* Addison-Wesley, 1992.

[92] K. R. Castleman, *Digital Image Processing.* Prentice Hall, 1979.

[93] W. K. Pratt, *Digital Image Processing.* John Wiley & Sons, 2nd ed., 1991.

[94] J. C. Russ, *The Image Processing Handbook.* CRC Press, 2nd ed., 1995.

[95] R. M. Haralick and L. G. Shapiro, *Computer and Robot Vision*, vol. 1 and 2. Addison-Wesley, 1992.

[96] Y. LeGrand and S. G. El Hage, *Physiological Optics.* Springer-Verlag, 1980.

[97] N. Drasdo and C. W. Fowler, "Non-linear projection of the retinal image in a wide-angle schematic eye," *Brit. J. Ophthalmol.*, vol. 58, pp. 709–714, 1974.

[98] J. W. Goodman, *Introduction to Fourier Optics.* McGraw-Hill, 1968.

[99] D. Shotton, ed., *Electronic Light Microscopy: Techniques in Modern Biomedical Microscopy.* Wiley-Liss, 1993.

[100] R. H. Webb and C. K. Dorey, "The pixelated image," in Pawley [85], ch. 4, pp. 55–67.

[101] K. R. Castleman, "Resolution and sampling requirements for digital image processing, analysis, and display," in Shotton [99], ch. 3, pp. 71–94.

[102] I. T. Young, "Quantitative microscopy," *IEEE Eng. Med. Biol.*, vol. 15, no. 1, pp. 59–66, 1996.

[103] A. V. Oppenheim and R. W. Schafer, *Digital Signal Processing.* Prentice Hall, 1975.

[104] A. Papoulis, *Systems and Transforms with Applications in Optics.* McGraw-Hill, 1968.

[105] L. J. Pinson, *Electro-Optics.* John Wiley & Sons, 1985.

[106] W. J. Smith, *Modern Optical Engineering.* McGraw-Hill, 2nd ed., 1990.

[107] C. L. Wyatt, *Electro-Optical System Design.* McGraw-Hill, 1991.

[108] R. W. Waynant and M. N. Ediger, eds., *Electro-Optics Handbook.* McGraw-Hill, 1994.

[109] S. Inoué, *Video Microscopy.* Plenum Press, 1986.

[110] R. D. Guenther, *Modern Optics.* John Wiley & Sons, 1990.

[111] V. Ronchi, *Optics: The Science of Vision.* Dover, 1991. Republication of 1957 New York University Press edition.

[112] F. W. Campbell and R. W. Gubisch, "Optical and retinal factors affecting visual resolution," *J. Physiol.*, vol. 181, pp. 576–593, 1965.

[113] F. W. Campbell and R. W. Gubisch, "Optical quality of the eye," *J. Physiol.*, vol. 186, pp. 558–578, 1966.

[114] M. A. Bronstein, M. A. Mainster, O. Pomerantzeff, C. L. Trempe, C. L. Schepens, M. P. Avila, and J. Schneider, "High magnification fundus photoggraphy with the macula-disk camera," *Ophthalmol.*, pp. 189–191, Aug. 1982. Instrument and Book Supplement.

[115] F. A. Young and D. N. Farrer, "Visual similarities of nonhuman and human primates," in *Medical Primatology 1970* (E. I. Goldsmith and J. Moor-Jankowski, eds.), (Basel, Switzerland), pp. 316–328, S. Karger, 1971.

[116] F. A. Rosell, "Imaging detectors," in Waynant and Ediger [108], ch. 18.

[117] K. B. Benson and J. Whitaker, *Television Engineering Handbook.* McGraw-Hill, revised ed., 1992.

[118] F. T. S. Yu and I. C. Khoo, *Principles of Optical Engineering.* John Wiley & Sons, 1990.

[119] C. E. Shannon, "A mathematical theory of communication," *Bell Syst. Tech. J.*, vol. 27, pp. 623–656, Oct. 1948. Second of two parts.

[120] L. W. Couch II, *Digital and Analog Communication Systems.* Macmillan, 4th ed., 1993.

[121] J. D. Gibson, *Principles of Digital and Analog Communications.* Macmillan, 2nd ed., 1993.

[122] Panasonic Corporation, *GP-MF602 CCD Camera Specifications*, 1995.

[123] J. G. Proakis and D. G. Manolakis, *Digital Signal Processing.* Macmillan, 2nd ed., 1992.

[124] A. V. Oppenheim and R. W. Schafer, *Discrete-Time Signal Processing.* Prentice Hall, 1989.

[125] J. G. Proakis, C. M. Rader, F. Ling, and C. L. Nikias, *Advanced Digital Signal Processing.* Macmillan, 1992.

[126] B. Jähne, *Digital Image Processing: Concepts, Algorithms, and Scientific Applications.* Springer-Verlag, 3rd ed., 1995.

[127] E. Peli and B. Schwartz, "Enhancement of fundus photographs taken through cataracts," *Ophthalmology*, vol. 94(S), pp. 10–13, 1987.

[128] C. H. G. Wright, E. J. Delp, and N. C. Gallagher, "Nonlinear target enhancement algorithms to counter the hostile nuclear environment," *IEEE Trans. Aerosp. Elect. Syst.*, vol. AES-26, pp. 122–145, Jan. 1990.

[129] C. H. G. Wright, E. J. Delp, and N. C. Gallagher, "Morphological based target enhancement algorithms to counter the hostile nuclear environment," in *Proceedings of the 1989 IEEE International Conference on Systems, Man, and Cybernetics*, (Cambridge, MA), Nov. 1989.

[130] C. H. G. Wright, "A study of target image enhancement algorithms to counter the hostile nuclear environment," Master's thesis, Purdue University, 1988.

[131] G. R. Cooper and C. D. McGillem, *Modern Communications and Spread Spectrum.* McGraw-Hill, 1986.

[132] J. S. Bendat and A. G. Piersol, *Random Data: Analysis and Measurement Procedures.* John Wiley & Sons, 2nd ed., 1986.

[133] D. Marr and E. Hildreth, "Theory of edge detection," *Proc. Royal Soc. London,* vol. B-207, pp. 187–217, 1980.

[134] J. Canny, "A computational approach to edge detection," *IEEE Trans. Patt. Anal. Mach. Intel.*, vol. PAMI-8, pp. 679–698, Nov. 1986.

[135] H. L. Tan and E. J. Delp, "Edge detection by cost minimization," Tech. Rep. TR-EE 88-49, Purdue University, Dec. 1988.

[136] D. P. Wornson, G. W. Hughes, and R. H. Webb, "Fundus tracking with the scanning laser ophthalmoscope," *Appl. Opt.*, vol. 26, pp. 1500–1504, Apr. 1987.

[137] T. Bantel, D. Ott, and M. Rueff, "Global tracking of the ocular fundus pattern imaged by scanning laser ophthalmoscopy," *Int. J. Biomed. Comput.*, vol. 27, pp. 59–69, 1990.

[138] R. D. Ferguson, C. H. G. Wright, S. F. Barrett, H. G. Rylander III, and A. J. Welch, "Hybrid tracking and control system for computer-aided retinal surgery," in *Proceedings of the 1996 SPIE International Symposium on Biomedical Optics (SPIE 2673-09)*, (San Jose, CA), Feb. 1996.

[139] C. H. G. Wright, R. D. Ferguson, S. F. Barrett, H. G. Rylander III, and A. J. Welch, "Hybrid eye tracking for computer-aided retinal surgery," in *Proceedings of the 33rd Annual Rocky Mountain Bioengineering Symposium*, (Colorado Springs, CO), pp. 225–235, Apr. 1996.

[140] C. H. G. Wright, R. D. Ferguson, H. G. Rylander III, A. J. Welch, and S. F. Barrett, "A hybrid approach to retinal tracking and laser aiming for photocoagulation," *J. Biomed. Opt.* (in review).

[141] General Scanning, Inc., *Operating Manual for Driver Amplifiers: A-102 and AX-200.*

[142] A. Ludwiszewski, *Standards for Oscillatory Scanners.* General Scanning, Inc., 1993.

[143] W. H. Press, S. A. Teukolsky, W. T. Vetterling, and B. P. Flannery, *Numerical Recipes in C.* Cambridge University Press, 2nd ed., 1992.

[144] J. M. Hammersley and D. C. Handscomb, *Monte Carlo Methods.* London: Methuen, 1964.

[145] N. Metropolis, A. W. Rosenbluth, M. N. Rosenbluth, A. H. Teller, and E. Teller, "Equation of state calculations by fast computing machines," *J. Chem. Physics*, vol. 21, pp. 1087–1092, June 1953.

[146] S. Kirkpatrick, C. D. Gelatt, and M. P. Vecchi, "Optimization by simulated annealing," *Science*, vol. 220, pp. 671–680, May 1983.

[147] V. Cerny, "Thermodynamical approach to the traveling salesman problem: An efficient simulation algorithm," *J Optimiz. Theory App.*, vol. 45, pp. 41–51, Jan. 1985.

[148] M. P. Vecchi and S. Kirkpatrick, "Global wiring by simulated annealing," *IEEE Trans. Comput.-Aided Design*, vol. CAD-2, pp. 215–222, Oct. 1983.

[149] A. A. El Gamal, L. A. Hemachandra, I. Shperling, and V. K. Wei, "Using simulated annealing to design good codes," *IEEE Trans. Inf. Theory*, vol. IT-33, pp. 116–123, Jan. 1987.

[150] P. Carnevali, L. Coletti, and S. Patarnello, "Image processing by simulated annealing," *IBM J. Res. Dev.*, vol. 29, pp. 569–579, Nov. 1985.

[151] W. E. Smith, H. H. Barrett, and R. G. Paxman, "Reconstruction of objects from coded images by simulated annealing," *Opt. Lett.*, vol. 8, pp. 199–201, Apr. 1983.

[152] A. B. Brotz, M. H. Kalos, and J. L. Lebowitz, "A new algorithm for Monte Carlo simulation of Ising spin systems," *J. Comput. Physics*, vol. 17, pp. 10–18, 1975.

[153] I. Z. Fisher, "Applications of the Monte Carlo model in statistical physics," *Soviet Physics Uspekhi*, vol. 2, pp. 783–1012, June 1960.

[154] A. Papoulis, *Probability, Random Variables, and Stochastic Processes.* McGraw-Hill, 3rd ed., 1991.

[155] M. Keijzer, S. L. Jacques, S. A. Prahl, and A. J. Welch, "Light distributions in artery tissue: Monte carlo simulations for finite diameter laser beams," *Lasers Surg. Med.*, pp. 148–154, 1989.

[156] S. A. Prahl, *Light Transport in Tissue.* Ph.D. dissertation, The University of Texas at Austin, 1988.

[157] N. Maharajh, "Use of reflectance for the real time feedback control of photocoagulation," Master's thesis, The University of Texas at Austin, 1996.

[158] E. J. Engelken, K. W. Stevens, W. J. McQueen, and J. D. Enderle, "Application of robust data processing methods to the analysis of eye movements," in *Proceedings of the 33rd Annual Rocky Mountain Bioengineering Symposium*, (Colorado Springs, CO), pp. 7–11, Apr. 1996.

[159] C. H. G. Wright, J. K. Barton, H. G. Rylander III, and A. J. Welch, "Anomalous reflectance of retinal lesions," *Lasers Surg. Med.*, 1996. (in review).

[160] G. L. LeCarpentier, M. Motamedi, L. P. McMath, S. Rastegar, and A. J. Welch, "Continuous wave laser ablation of tissue: Analysis of thermal and mechanical events," *IEEE Trans. Biomed. Eng.*, vol. 40, pp. 188–201, Feb. 1993.

[161] A. J. Welch, J. A. Pearce, K. R. Diller, G. Yoon, and W. F. Cheong, "Heat generation in laser irradiated tissue," *Trans. ASME*, vol. 111, pp. 62–68, 1989.

[162] S. Thomsen, "Pathologic analysis of photothermal and photomechanical effects of laser-tissue interactions," *Photochem. Photobiol.*, vol. 53, no. 6, pp. 825–835, 1991.

[163] A. J. Welch, M. Motamedi, S. Rastegar, G. LeCarpentier, and D. Jansen, "Laser thermal ablation," *Photochem. Photobiol.*, vol. 53, no. 6, pp. 815–823, 1991.

[164] F. Partovi, J. A. Izatt, R. M. Cothren, C. Kitrell, J. E. Thomas, S. Strikwerda, J. R. Kramer, and M. S. Feld, "A model for thermal ablation of biological tissue using laser radiation," *Lasers Surg. Med.*, vol. 7, pp. 141–154, 1987.

[165] T. G. van Leeuwen, E. D. Jansen, M. Motamedi, C. Borst, and A. J. Welch, "Pulsed laser ablation of soft tissue," in Welch and van Gemert [41], ch. 21, pp. 709–763.

[166] J. A. Pearce and S. Thomsen, "Rate process analysis of thermal damage," in Welch and van Gemert [41], ch. 17, pp. 561–606.

[167] H. S. Carslaw and J. C. Jaeger, *Conduction of Heat in Solids*. Oxford University Press, 2nd ed., 1959.

[168] A. J. Welch, E. H. Wissler, and L. A. Priebe, "Significance of blood flow in calculations of temperature in laser irradiated tissue," *IEEE Trans. Biomed. Eng.*, vol. 27, pp. 164–166, Mar. 1980.

[169] J. W. Valvano and J. A. Pearce, "Temperature measurements," in Welch and van Gemert [41], ch. 15, pp. 489–534.

[170] F. P. Incropera and D. P. DeWitt, *Fundamentals of Heat and Mass Transfer.* John Wiley & Sons, 3rd ed., 1990.

[171] S. F. Cleary, "Laser pulses and the generation of acoustic transients in biological material," in *Laser Applications in Medicine and Biology* (M. L. Wohlbarst, ed.), ch. 3, pp. 175–219, Plenum Press, 1977.

[172] A. A. Oraevsky, "Laser-induced acoustic and shock waves in ocular tissues," Tech. Rep. AL/OE-TR-1995-0044, Armstrong Laboratory, Brooks AFB, TX, May 1995.

[173] C. H. G. Wright, "Tracking the moving retina: A hybrid digital/analog approach," in *Fourteenth Annual Houston Conference on Biomedical Engineering Research*, (Houston, TX), Houston Society for Engineering in Medicine and Biology, Feb. 1996.

[174] C. H. G. Wright, S. F. Barrett, M. R. Jerath, H. G. Rylander III, and A. J. Welch, "Retinal robotic laser system," in poster session at *1994 Gordon Conference on Lasers in Biology and Medicine*, (Meriden, NH), July 1994.

[175] S. F. Barrett, C. H. G. Wright, M. R. Jerath, R. S. Lewis, B. C. Dillard, H. G. Rylander III, and A. J. Welch, "Automated retinal robotic laser system instrumentation," in *Proceedings of the 1995 SPIE International Symposium on Biomedical Optics (SPIE 2396)*, (San Jose, CA), Feb. 1995. Invited paper.

[176] S. F. Barrett, C. H. G. Wright, H. G. Rylander III, and A. J. Welch, "Automated placement of retinal laser lesions *in vivo*," in *Proceedings of the SPIE 1995 International Symposium on Lasers and Applications (SPIE 2374)*, (San Jose, CA), Feb. 1995.

[177] S. F. Barrett, C. H. G. Wright, M. R. Jerath, R. S. Lewis II, B. C. Dillard, H. G. Rylander III, and A. J. Welch, "Automated retinal robotic laser system," in *Proceedings of the 32nd Annual Rocky Mountain Bioengineering Symposium*, (Copper Mountain, CO), Apr. 1995.

[178] R. G. Wilson, *Fourier Series and Optical Transform Techniques in Contemporary Optics.* John Wiley & Sons, 1995.

[179] E. L. Dereniak and D. G. Crowe, *Optical Radiation Detectors.* John Wiley & Sons, 1984.

[180] H. W. Ott, *Noise Reduction Techniques in Electronic Systems.* John Wiley & Sons, 1976.

[181] F. C. Delori, E. S. Gragoudas, R. Francisco, and R. C. Pruett, "Monochromatic ophthalmoscopy and fundus photography," *Arch. Ophthalmol.*, vol. 95, pp. 861–868, May 1977.

[182] A. E. Elsner, S. A. Burns, F. C. Delori, and R. H. Webb, "Quantitative reflectometry with the SLO," in *Scanning Laser Ophthalmoscopy and Tomography* (J. E. Nasemann and R. O. W. Burke, eds.), ch. 10, pp. 109–121, Berlin: Quintessenz Verlag, 1990.

[183] A. E. Elsner, S. A. Burns, G. W. Hughes, and R. H. Webb, "Reflectometry with a scanning laser ophthalmoscope: Noninvasive assessment of the visual system," *Appl. Opt.*, vol. 31, pp. 3697–3711, July 1992.

[184] D. Shotton, "An introduction to digital image processing and image display in electronic light microscopy," [99], ch. 2, pp. 39–70.

[185] L. G. Brown, "A survey of image registration techniques," *ACM Comput. Surv.*, vol. 24, pp. 325–376, Dec. 1992.

[186] A. V. Cideciyan, "Registration of ocular fundus images," *IEEE Eng. Med. Biol.*, vol. 4, pp. 52–58, Jan. 1995.

[187] D. I. Barnea and H. F. Silverman, "A class of algorithms for fast digital image registration," *IEEE Trans. Comput.*, vol. C-21, pp. 179–186, Feb. 1972.

[188] M. Svedlow, C. D. McGillem, and P. E. Anuta, "Image registration: Similarity measure and processing method comparisons," *IEEE Trans. Aerosp. Elect. Syst.*, vol. AES-14, no. 1, pp. 141–149, 1978.

[189] E. Peli, R. A. Augliere, and G. T. Timberlake, "Feature-based registration of retinal images," *IEEE Trans. Med. Imaging*, vol. MI-6, pp. 272–278, Sept. 1987.

[190] C. H. G. Wright, G. P. Heckert, and T. E. Bleier, "Near-term approach to data relay for satellites under test," *IEEE Trans. Aerosp. Elect. Syst.*, vol. AES-30, pp. 778–786, July 1994.

[191] M. L. Meade, *Lock-In Amplifiers: Principles and Applications.* London, UK: Peregrinus Ltd, 1983.

[192] G. F. Marshall, ed., *Laser Beam Scanning: Opto-Mechanical Devices, Systems, and Data Storage Optics.* Marcel Dekker, 1985.

[193] G. F. Marshall, ed., *Optical Scanning.* Marcel Dekker, 1991.

[194] D. Kleppner and R. J. Kolenkow, *An Introduction to Mechanics.* McGraw-Hill, 1973.

[195] P. A. Tipler, *Physics.* Worth Publishers, 2nd ed., 1982.

[196] J. J. D'Azzo and C. H. Houpis, *Linear Control System Analysis and Design.* McGraw-Hill, 3rd ed., 1988.

[197] H. Pender and W. A. Del Mar, eds., *Electrical Engineers' Handbook.* John Wiley & Sons, 4th ed., 1949.

Vita

Cameron H. G. Wright was born in Quincy, Massachusetts, on January 21, 1956, the son of Dorothy L. Wright and Frederick H. G. Wright. He grew up in the Cape Cod region and graduated from Plymouth-Carver High School in 1973. He then spent over six years in the U.S. Navy as an intelligence analyst and an electronics technician, serving in a wide variety of overseas locations.

In 1983 he graduated with a BSEE (summa cum laude) from Louisiana Tech University, and proceeded to the U.S. Air Force Officer Training School, Lackland AFB, TX, from which he graduated first in his class with highest honors. Lieutenant Wright then served three years as a design engineer for the cockpit electronics of high performance aircraft at the Avionics Laboratory, Wright-Patterson AFB, OH. Following this assignment, he attended and graduated with highest honors from the U.S. Air Force Squadron Officers School at Maxwell AFB, AL.

Selected for an Air Force graduate school scholarship, he proceeded to Purdue University where he received the MSEE in 1988. At Purdue, he met and married Robin M. Rawlings of Indianapolis, IN. Captain Wright then served three years as a senior engineer and division chief for satellite communications, command, and control at Air Force Space Division, Los Angeles AFB, CA, and coordinated space research and test programs at Onizuka AFB, CA, Vandenberg AFB, CA, Falcon AFB, CO, Peterson AFB, CO, Cheyenne Mountain (HQ NORAD), CO, Patrick AFB, FL, and other sites worldwide. During this time he qualified as a registered Professional Engineer, and was licensed in California. Following this assignment, he

was chosen as an instructor on the faculty of the U.S. Air Force Academy, Department of Electrical Engineering, where he taught and performed research for over two years.

Selected for another Air Force graduate school scholarship, he proceeded to the University of Texas at Austin where he received the Ph.D. in 1996. He is a Senior Member of the IEEE, a Life Member of the Air Force Association, a member of ASEE, AFCEA, and holds an advanced certification in Toastmasters International. He has been elected to the honor societies Eta Kappa Nu, Tau Beta Pi, Phi Kappa Phi, Omicron Delta Kappa, and Pi Mu Epsilon, and was listed in recent editions of *Who's Who in Science and Engineering* and *Who's Who in the South and Southwest.* Major Wright will now return to the U.S. Air Force Academy as an Assistant Professor of Electrical Engineering.

Permanent Address: 19420 Doewood Drive
Monument, CO 80132

This dissertation was typeset by the author using LaTeX 2_ε and *Scientific Word*.[1]

[1] LaTeX 2_ε is a document preparation system developed by Leslie Lamport as a special version of Donald Knuth's TeX program. TeX is a trademark of the American Mathematical Society. *Scientific Word* is a Windows-based front-end to LaTeX 2_ε written by TCI Software Research.